

UC Davis

UC Davis Electronic Theses and Dissertations

Title

Mechanical Characterization of Slab/Base Interactions for Concrete Pavement Structures

Permalink

<https://escholarship.org/uc/item/0qr1w2x1>

Author

Paniagua Fernandez, Fabian

Publication Date

2023

Peer reviewed|Thesis/dissertation

Mechanical Characterization of Slab/Base Interactions
for Concrete Pavement Structures

By

FABIAN PANIAGUA FERNANDEZ
DISSERTATION

Submitted in partial satisfaction of the requirements for the degree of

DOCTOR OF PHILOSOPHY

in

Civil And Environmental Engineering

in the

OFFICE OF GRADUATE STUDIES

of the

UNIVERSITY OF CALIFORNIA

DAVIS

Approved:

John Harvey, Chair

Angel Mateos

Alejandro Martinez

Committee in Charge

2023

ABSTRACT

This dissertation provides an in-depth mechanical characterization of slab/base interaction for concrete pavement structures considering the viscoelastic properties of asphalt base under both traffic and environmental loading and different environmental conditions.

Concrete pavement structures can be divided into jointed plain concrete pavement (JPCP) for thicker concrete layers or a short jointed plain concrete pavement - concrete overlay on asphalt (SJPCP-COA) for thinner concrete layers. Good performance for concrete pavements relies on the bonding between the concrete and the base layer. The literature shows that JPCP over lean concrete bases (LCB) results in poorer transverse cracking performance than JPCP over asphalt bases. The literature regarding slab/base interactions and the role of the interphase and composite structures with concrete on top of asphalt is scarce. Additionally, current mechanistic-empirical design procedures over-simplify the slab-base interactions. Hence, several gaps and questions about slab/base interactions for concrete pavements were found and are answered in this dissertation.

The goal of this study is to investigate and understand the slab/base interactions, including the bonding of concrete to different bases/interlayers, and how to reduce concrete pavement shear and tensile stresses and strains that cause cracking and, therefore, reduce the cost of the structures. This research developed a laboratory testing framework to address mechanisms of failure related to the base of concrete pavements under testing conditions that replicated temperatures, frequency of loading, and loading modes observed in the field by using available laboratory testing machines and a newly developed device were used to test specimens in shear,

tension, and compression. Full-scale test slabs were constructed to analyze different pavement structures under the effect of the environment and falling weight deflectometer load, and the sections were modeled using material properties obtained from the laboratory testing to replicate the behavior observed in the falling weight deflectometer (FWD) testing and study the debonding process of composite structures under the effect of environment loads.

Thirteen laboratory testing procedures in tension and shear were determined adequate for asphalt and composite specimens testing based on the available testing equipment and the development of a new testing device. The shear and tensile tests were frequency sweep, creep, and ramp tests. Additionally, a compressive dynamic modulus was also done. Three testing procedures were already developed and had their corresponding American Society for Testing Materials (ASTM) or American Association of Highway and Transportation Officials (AASHTO) standards, while the other ten were developed under this research project. Nine of those tests were used in the first phase of testing in which a hot mix asphalt (HMA) and a gap-graded rubberized hot mix asphalt (RHMA-G) were extensively characterized under testing conditions that replicated field conditions. A testing protocol consisting of tensile hanging creep, compressive dynamic modulus, and tensile ramp test was narrowed down from the initial 13 tests. It was determined to be enough to characterize the asphaltic base materials and bonding properties precisely while being time-efficient and budget-friendly. Additionally, the final testing phase introduced a test to capture the water-induced damage. Any well-established laboratory or agency can easily replicate all four selected tests.

Material stiffness properties and damage parameters were obtained from the laboratory tests, which determined that temperature and humidity negatively impact the strength of the base

materials and, by extension, will also impact the slab/base interaction. Moisture conditioning specimens at 60 °C (140 °F) cause a decrease in the strength of the asphalt material by 11% for HMA specimens and 16% for RHMA-G specimens. Laboratory strength tests conducted at different temperatures determined that temperature increases reduced the material strength and caused the material to behave softer, increasing the deformation to reach a 50 percent integrity between 40 and 100 percent more when testing at 40 °C than when testing at 25 °C.

The literature review showed that JPCP over LCB cracks 2.8 times more than JPCP over HMA bases. A full-scale test track, including four sections, was built to study and better understand the effects of different bases and interlayers for concrete pavements in addition to laboratory experiments. Three of the sections were built over LCB with different interlayer materials. One of the sections was prepared with curing compound, a typical interlayer material widely used in the state of California; another section was built with geotextile as an interlayer, an alternative currently allowed by Caltrans but not commonly used. The third interlayer used was microsurfacing, an interlayer alternative proposed by this research to improve the performance of concrete pavements over LCB. The fourth and last section was built with an RHMA-G base, which is not used as a base but is currently used as a pavement surface, which was also proposed as an alternative to conventional HMA bases. The sections were instrumented with vibrating wire strain gages and thermocouples at different depths. Multiple FWD tests were conducted to analyze the structures under different temperatures and drying shrinkage gradients besides the data recorded from the sensors.

Based on the FWD, it was determined that the deflections in the section of JPCP over LCB are three times the deflections in the sections of JPCP over RHMA-G, which means that less area of

the concrete slab is in contact with the base and will cause a higher cracking potential. The two new concrete pavement alternative base/interlayers proposed in this research project outperformed the two alternatives currently allowed by Caltrans. The results obtained support the field observations of poor transverse and longitudinal cracking performance of JPCP over LCB, typically with curing compound, which has already been reported, but there was no clear explanation of the reason behind this until now. The curing compound and geotextile prevent the layers from bonding and do not allow the base to follow the concrete slab deformations due to temperature and moisture gradients.

Based on corner deflections from full-scale test sections and laboratory testing, it is concluded that RHMA-G can be used as a base layer for concrete pavements. An additional benefit of using this type of mix as a base is to fulfill Caltrans desire of using rubber in the paving industry. As of right now, it is only used in the surface layer, but the use of rubber can also be expanded to base layers of concrete pavements. From the laboratory experimental design, it was seen that the interphase in both RHMA-G and HMA composite specimens is not the weakest point in the structure. Placing microsurfacing between the lean concrete base and concrete slabs is considered to be an ideal interlayer. It provides the road paving industry with a new material to be used as an interphase when dealing with concrete pavements, but further investigation in field pilot projects should be conducted. It is an alternative that is cheaper to place than widely used geotextile and produces almost the same behavior as having an RHMA-G base. This outcome is ideal since it still supports the use of lean concrete bases in concrete pavements since they can use the same paving equipment and plants but causes the section to perform similarly to concrete pavements placed on top of asphalt bases. Allowing structures with lean concrete

bases to perform similarly to sections with asphalt layers may be a solution to the current issues faced in the state of California, where concrete over LCB layers is cracking at a much faster rate than concrete pavements placed over HMA layers. Based on those results, it is suggested to have RHMA-G base and microsurfacing interlayer in pilot projects.

Lastly, a FEM modeling framework was developed to model the JPCP sections that were built and analyzed. Stiffness laboratory tests provided a detailed characterization of the materials, and the damage initiation and damage evolution laws were obtained from laboratory test models. Two different models for full-scale concrete sections were created with the material parameters from the laboratory testing and material models. First, a complex dynamic model, including asphalt viscoelastic behavior, long-term action of ambient loads, and progressive damage on the interphase, was used to study the performance of the structure and bonding condition under environmental loads. Second, a simplified static model with elastic materials behavior, a preestablished debonding area between the PCC and base obtained from the complex dynamic model, and equivalent static loads to study the performance of the structure under FWD loads.

The damage initiation and damage evolution laws for the materials required for the development of full-scale pavement models were obtained from the tensile hanging damage test and shear ramp test models. Using the complex dynamic model and the simplified static model, it was concluded that the environmental loads have a significant impact on pavement performance, reducing the overall stiffness due to interphase damage and resulting in higher FWD deflections than those observed with an undamaged interphase. Higher deflections result from curled concrete slabs with less base support, which will increase the tensile strains at the bottom and, therefore, increase the cracking potential of the slabs.

ACKNOWLEDGEMENTS

I am incredibly grateful with life and God for letting me finish an important step in my academic career. What a fantastic journey it was, but thankfully, it is done.

It would not have been possible without the love, support, guidance, and lessons taught by my parents, Jose Joaquin Paniagua Luna and Marlene Fernandez Jimenez. This milestone also belongs to you two. Dad, I wish you were here to celebrate, but you can do it on my behalf up in heaven. *Gracias Papi, gracias Mami!*

A special thanks goes to my wife, Melissa, thank you for being so supportive and understanding through the time we have been together. Sharing with you the last two years of this journey made it more accessible. My achievements are also yours; thank you, love!

Thankful for having been able to share the M.Sc. and Ph.D. journey with my twin brother Julio. All the classes, homework, lab work, and research were always easier when working together, thanks!

I sincerely thank my advisor, John Harvey. Thank you for all your support, guidance, and mentoring through my time at UC Davis. You allowed me to attend grad school at a world-renowned research facility, and I will always be grateful for it. You and Rita made my journey less complicated, being a home away from home, thank you both!

I want to thank Angel Mateos and Miguel Millan for endless hours of guidance, work, and knowledge transfer. Working with you two was an honor, and I will always be grateful for it.

Thanks to Alejandro Martinez, committee member, for the contributions and insightful comments.

This milestone was made possible by having great support from current and previous UCPRC Staff from the Davis and Berkeley facilities. I greatly appreciate all your help and support.

I want to thank all my fellow Grad Students for sharing this chapter in our lives together. To all those who were done before me, those who are finishing soon, and those who are just starting, thank you all!

Thanks to all the Undergraduate Students who helped me during different stages of my research journey. Thank you for your hard work and dedication.

Lastly, I want to thank me for believing in me, for all the hard work and effort, for never giving up, and for always wanting to succeed. Thanks, Fabian!

This dissertation is part of a research project sponsored by the California Department of Transportation (Caltrans). I am grateful for their support to research studies and for the intellectual knowledge exchange with individuals like Deepak Maskey, Dulce Rufino, and David Lim. The contents of this dissertation reflect the view of the author alone and do not necessarily reflect the official views or policies of Caltrans.

TABLE OF CONTENTS

ABSTRACT	II
ACKNOWLEDGEMENTS.....	VII
TABLE OF CONTENTS	IX
LIST OF FIGURES	XIII
LIST OF TABLES.....	XIX
LIST OF ABBREVIATIONS	XXI
LIST OF STANDARD METHODS AND SPECIFICATIONS.....	XXIII
CONVERSION TABLE	XXIV
1. INTRODUCTION	1
1.1 Background	1
1.1.1 Types of Pavement	1
1.1.1.1 Flexible Pavements	1
1.1.1.2 Rigid Pavements.....	5
1.1.1.2.1 Bases for Rigid Pavements	7
1.1.1.3 Composite Pavements	8
1.1.1.3.1 HMA Layer	11
1.1.1.3.2 PCC Slab	12
1.1.1.3.3 Interphase.....	12
1.1.2 Loading Scenarios	14
1.1.3 Distresses.....	15
1.1.4 Overall	20
1.2 Goal	22
2. LITERATURE SURVEY	23
2.1 Performance Studies	23
2.2 Distress Mechanisms.....	31
2.3 Properties of the Materials	34
2.4 Testing	35
2.4.1 Laboratory testing	35
2.4.2 Field testing	41
2.5 Composite Pavement Design.....	48
2.6 Summary of Findings from Literature Review	50
2.7 Problem Statement.....	52
3. PROBLEM STATEMENT AND STUDY METHODOLOGY.....	53
3.1 Gaps and Questions to be Answered.....	53
3.2 Objectives and Tasks	54
3.3 Structure and Content.....	56
4. LABORATORY TESTING METHODOLOGIES	58
4.1 Goal and Objectives	58
4.2 Introduction.....	58
4.3 Critical Field Conditions.....	60
4.4 Machine Characteristics and Limitations.....	62
4.4.1 Superpave Shear Tester (SST).....	64
4.4.2 Universal Testing Machine (UTM)	65
4.4.3 Tensile Hanger Device (TH).....	67
4.4.4 Asphalt Mixture Performance Tester (AMPT)	68
4.4.5 Uniaxial Loader Device (UL).....	70
4.5 Testing Conditions.....	71

4.5.1	Temperature	71
4.5.2	Humidity	76
4.6	Laboratory Tests	77
4.6.1	Shear Frequency Sweep	79
4.6.1.1.	Input Parameters	80
4.6.1.2.	From Standard	81
4.6.1.3.	Summary	81
4.6.2	Shear Creep	81
4.6.2.1.	Input Parameters	82
4.6.2.2.	Parameter Determination	82
4.6.2.3.	Summary	83
4.6.3	Shear Ramp.....	84
4.6.3.1.	Input Parameters:	85
4.6.3.2.	Parameters Determination	85
4.6.3.3.	Summary	85
4.6.4	Tensile Creep	85
4.6.4.1.	Input Parameters	86
4.6.4.2.	Parameters Determination	87
4.6.4.3.	Summary	87
4.6.5	Tensile Ramp	87
4.6.5.1.	Input Parameters:	88
4.6.5.2.	Parameters Determination	88
4.6.5.3.	Summary	89
4.6.6	Tensile Hanging Creep	89
4.6.6.1.	Input Parameters	90
4.6.6.2.	Summary	91
4.6.7	Tensile Hanging Damage	91
4.6.7.1.	Input Parameters	92
4.6.7.2.	Summary	92
4.6.8	Compressive Dynamic Modulus	93
4.6.8.1.	Input Parameters	94
4.6.8.2.	From Standard	94
4.6.8.3.	Summary	94
4.6.9	Indirect Tensile Cracking Test (IdealCT)	94
4.6.9.1.	Input Parameters and Standard	95
4.6.9.2.	Summary	95
5.	FULL-FACTORIAL TESTING RESULTS.....	96
5.1	Goal and Objectives	96
5.2	Materials Tested	96
5.3	Stiffness Test Results and Analysis	97
5.3.1	Shear Frequency Sweep	98
5.3.2	Shear Creep	102
5.3.3	Tensile Creep	107
5.3.4	Tensile Hanging Creep	110
5.3.5	Compressive Dynamic Modulus	114
5.3.6	Stiffness Data for Modeling	118
5.3.7	Stiffness Tests Summary	121
5.4	Strength Test Results and Analysis	125
5.4.1	Tensile Hanging Damage	130
5.4.2	Tensile Ramp	132
5.4.3	Shear Ramp.....	134
5.4.4	Strength Test Summary	136

5.5	Recommendations	137
6.	TESTING PROTOCOL FOR MATERIAL AND BONDING CHARACTERIZATION	139
6.1	Goal and Objectives	139
6.2	Materials Tested	139
6.3	Stiffness Test Results and Analysis of Asphalt Specimens	140
6.3.1	Tensile Hanging Creep	141
6.3.2	Compressive Dynamic Modulus	142
6.3.3	Stiffness Tests Summary	143
6.4	Strength Test Result and Analysis	144
6.4.1	Tensile Ramp of Asphalt Specimens	145
6.4.2	Tensile Ramp Tests of Composite Specimens	148
6.4.3	Strength Tests Summary	151
6.5	Water Induced Damage Test Results and Analysis of Asphalt Specimens	152
6.5.1	Indirect Tensile Cracking Test (IdealCT)	152
7.	FULL-SCALE COMPOSITE PAVEMENT SECTIONS	155
7.1	Goal and Objectives	155
7.2	Test Track Design	155
7.3	Instrumentation	157
7.4	Construction of the Test Track	158
7.4.1	Construction of the Lean Concrete Base	158
7.4.2	Construction of the RHMA-G Base	160
7.4.3	Construction of the Interlayers	161
7.4.3.1.	Curing Compound	162
7.4.3.2.	Geotextile	163
7.4.3.3.	Microsurfacing	164
7.4.4	Construction of the Concrete Slabs	165
7.5	QC/QA Testing of Materials Used	167
7.5.1	Summary Results for LCB	168
7.5.2	Summary Results for PLC	170
7.6	Test Track Monitoring	172
7.6.1	Slabs Curling/Warping	172
7.6.2	FWD Deflections	175
7.6.3	Coring of Microsurfacing Section	179
7.6.3.1.	Summary of Findings	184
8.	MODELING FRAMEWORK	186
8.1	Goal and Objectives	186
8.2	Constitutive parameters	186
8.3	Cohesive elements	189
8.4	Material parameters obtained from testing	190
8.4.1	Tensile Hanging Damage test	191
8.4.2	Shear Ramp Test	197
8.4.3	Full model damage properties	201
8.4.4	Combined model for tension and shear damage	203
8.4.5	Compression model for the viscoelastic solids	207
8.5	Models	209
8.5.1	Complex model	210
8.5.1.1.	Curing compound section	211
8.5.1.2.	RHMA-G section	212
8.5.2	Simplified debonded model	214
8.5.2.1.	Curing compound section	214
8.5.2.2.	RHMA-G section	215
8.5.3	Material model properties	217

8.6	FEM modeling application to a full-scale test track	219
8.6.1	Complex model: Structural response under ambient loading.....	219
8.6.1.1.	RHMA-G section	221
8.6.2	Simplified debonded model: Structural response under FWD loading	223
8.6.2.1.	Curing compound section	225
8.6.2.2.	RHMA-G section	227
8.6.2.2.1.	Influence of the variation of curvature	227
8.6.2.2.2.	Influence of the debonded band width	229
8.6.2.2.3.	Influence of the FWD load magnitude	234
9.	CONCLUSIONS AND RECOMMENDATIONS	235
9.1	Summary of Completed Tasks	235
9.2	Contributions to Knowledge	236
9.3	Recommendations for Future Work	243
	REFERENCES.....	244
	APPENDIX A.....	250
	Shear Fatigue.....	251
	Input Parameters	252
	From 4.58B HVS Sections:.....	252
	From Modeling.....	253
	Summary	260
	Shear Sine-Ramp	260
	Input Parameters	262
	From Modeling.....	262
	Summary	267
	Tensile Sine-Ramp	267
	Input Parameters	268
	From Modeling.....	269
	Summary	271
	Combined Sine-Ramp	272
	Input Parameters	273
	Summary	273
	APPENDIX B.....	275
	APPENDIX C.....	277
	APPENDIX D.....	280

LIST OF FIGURES

FIGURE 1-1. GRADATION CHART FOR HMA MIXES,.....	2
FIGURE 1-2. TEMPERATURE-TIME SUPERPOSITION FOR MASTER CURVES PROCESS	5
FIGURE 1-3. UPWARD/DOWNWARD MOVEMENT OF CONCRETE SLABS.....	6
FIGURE 1-4. CONCRETE VERTICAL AND HORIZONTAL MOVEMENTS.....	7
FIGURE 1-5. BONDED COA PAVEMENT STRUCTURE.....	8
FIGURE 1-6. SYSTEM DIAGRAM	21
FIGURE 2-1. CRACKING PERFORMANCE OF STRUCTURES WITH DIFFERENT BASES [6]	24
FIGURE 2-2. MEAN CRACK LENGTH OF TRANSVERSE CRACKING PER SECTION FOR TWO CLIMATIC ZONES [20].....	25
FIGURE 2-3. MEAN TRANSVERSE CRACK LENGTH PER SECTION OVER TIME FOR THREE DIFFERENT BASE TYPES [20].....	26
FIGURE 2-4. STRAIN MEASUREMENTS IN HVS TEST SECTION [14].....	28
FIGURE 2-5. HVS TESTING PLAN [14]	28
FIGURE 2-6. TENSILE STRENGTH TEST OF COMPOSITE SPECIMENS	30
FIGURE 2-7. FREQUENCY SWEEP TEST OF COMPOSITE SPECIMENS	30
FIGURE 2-8. DIFFERENTIAL DRYING SHRINKAGE IN SJPCP-COA SLABS AT THE CORNERS [23].....	32
FIGURE 2-9. SJPCP-COA COMMON DISTRESSES	33
FIGURE 2-10. SAMPLE SPECIMEN AND TEST LAYOUT OF MODIFIED TENSILE EXPERIMENT [30].....	38
FIGURE 2-11. WST TEST SET UP AND SPECIMEN [32].....	39
FIGURE 2-12. LOAD-DISPLACEMENT CURVES OF WEDGE SPLITTING TEST [32].....	40
FIGURE 2-13. PULL-OFF TEST SCHEMATIC [35]	41
FIGURE 2-14. AVERAGE SHEAR STRENGTH AT DIFFERENT BREAK LOCATIONS [36].....	43
FIGURE 2-15. FABAC FATIGUE DEVICE AND TEST SECTIONS [37].....	44
FIGURE 2-16. MOISTURE-RELATED SHRINKAGE IN THE UNRESTRAINED SHRINKAGE BEAMS [23].....	46
FIGURE 2-17. SCANNER IMAGES FOR CONCRETE PENETRATION ANALYSIS.....	48
FIGURE 2-18. CRACKED SLABS PREDICTION [41].....	49
FIGURE 4-1. CONCRETE MOVEMENTS DUE TO TEMPERATURE VARIATION (ΔT).....	59
FIGURE 4-2. EXAMPLE OF THERMOCOUPLES READINGS AT DIFFERENT DEPTHS OF THE PAVEMENT [21].....	61
FIGURE 4-3. TESTING MACHINES	64
FIGURE 4-4. SHEAR SPECIMEN DIAGRAM.....	65
FIGURE 4-5. TENSILE SPECIMEN DIAGRAM	66
FIGURE 4-6. HANGING TEST SPECIMEN DIAGRAM.....	68
FIGURE 4-7. AMPT SPECIMEN DIAGRAM	69
FIGURE 4-8. IDEAL CT SPECIMEN DIAGRAM	70
FIGURE 4-9. CALTRANS PAVEMENT CLIMATE REGIONS	72

FIGURE 4-10. INTERPHASE TEMPERATURE HISTOGRAM. NOMENCLATURE: WEATHER REGION-PCC THICKNESS IN MM.....	75
FIGURE 4-11. MIST DEVICE	76
FIGURE 4-12. SHEAR FREQUENCY SWEEP TEST DIAGRAM.....	79
FIGURE 4-13. LVER REPRESENTATION	80
FIGURE 4-14. SHEAR CREEP TEST DIAGRAM	82
FIGURE 4-15. SHEAR CREEP TEST RESULT	83
FIGURE 4-16. SHEAR RAMP TEST DIAGRAM	84
FIGURE 4-17. TENSILE CREEP TEST DIAGRAM	86
FIGURE 4-18. TENSILE RAMP TEST DIAGRAM.....	88
FIGURE 4-19. TENSILE HANGING CREEP TEST DIAGRAM	90
FIGURE 4-20. TENSILE HANGING DAMAGE TEST DIAGRAM	92
FIGURE 4-21. COMPRESSIVE DYNAMIC MODULUS TEST DIAGRAM	93
FIGURE 4-22. INDIRECT TENSILE CRACKING TEST DIAGRAM	95
FIGURE 5-1. HMA SHEAR DYNAMIC MODULUS TEST RESULT EXAMPLE	100
FIGURE 5-2. AVERAGE HMA AND RHMA-G SHEAR DYNAMIC MODULUS TEST PLOTS.....	101
FIGURE 5-3. AVERAGE SHEAR DYNAMIC MODULUS MASTER CURVES	101
FIGURE 5-4. SHEAR CREEP TEST PLOT EXAMPLE	103
FIGURE 5-5. AVERAGE HMA AND RHMA-G SHEAR CREEP TEST SUMMARY.....	106
FIGURE 5-6. AVERAGE SHEAR CREEP DYNAMIC MODULUS MASTER CURVES SUMMARY	106
FIGURE 5-7. TENSILE CREEP TEST PLOT EXAMPLE.....	108
FIGURE 5-8. AVERAGE HMA AND RHMA-G TENSILE CREEP TEST.....	109
FIGURE 5-9. AVERAGE TENSILE CREEP DYNAMIC MODULUS MASTER CURVES SUMMARY.....	110
FIGURE 5-10. TENSILE HANGING CREEP TEST PLOT EXAMPLE	112
FIGURE 5-11. AVERAGE HMA AND RHMA-G TENSILE HANGING CREEP TEST	114
FIGURE 5-12. AVERAGE TENSILE HANGING CREEP DYNAMIC MODULUS MASTER CURVES	114
FIGURE 5-13. HMA COMPRESSIVE DYNAMIC MODULUS TEST EXAMPLE	117
FIGURE 5-14. AVERAGE HMA AND RHMA-G COMPRESSIVE DYNAMIC MODULUS TEST.....	117
FIGURE 5-15. AVERAGE COMPRESSIVE DYNAMIC MODULUS MASTER CURVES	118
FIGURE 5-16. GENERALIZED MAXWELL MODEL	119
FIGURE 5-17. APPROACH FOR DETERMINING THE PARAMETERS OF THE ASPHALT VISCOELASTIC MODEL [23, EDITED]	121
FIGURE 5-18. RHMA-G STIFFNESS SUMMARY PLOTS COMBINING RESULTS FROM DIFFERENT TESTS FOR SHEAR AND TENSION/COMPRESSION	122
FIGURE 5-19. HMA STIFFNESS SUMMARY PLOTS COMBINING RESULTS FROM DIFFERENT TESTS FOR SHEAR AND TENSION/COMPRESSION	123
FIGURE 5-20. RHMA-G AND HMA MASTER CURVES FOR MODELING	124

FIGURE 5-21. STRENGTH TEST ANALYSIS EXAMPLES.....	128
FIGURE 5-22. INTEGRITY PLOT EXAMPLES.....	129
FIGURE 5-23. INTEGRITY CURVES FOR TENSILE HANGING DAMAGE TEST.....	131
FIGURE 5-24. SUMMARY OF INTEGRITY CURVES FOR TENSILE HANGING DAMAGE TEST FOR HMA AND RHMA-G MIXES	132
FIGURE 5-25. SUMMARY OF INTEGRITY CURVES FOR TENSILE RAMP TEST FOR HMA AND RHMA-G MIXES.....	133
FIGURE 5-26. SUMMARY OF INTEGRITY CURVES FOR SHEAR RAMP TEST FOR HMA AND RHMA-G MIXES.....	135
FIGURE 6-1. 4.88HMA TENSILE CREEP TEST SUMMARY.....	142
FIGURE 6-2. TENSILE HANGING CREEP MASTER CURVE COMPARISON	142
FIGURE 6-3. COMPRESSIVE DYNAMIC MODULUS MASTER CURVES SUMMARY	143
FIGURE 6-4. MASTER CURVES FROM THE COMPRESSIVE DYNAMIC MODULUS TEST FOR THE TWO RHMA-G MIXES ANALYZED.....	144
FIGURE 6-5. SUMMARY OF INTEGRITY CURVES FOR TENSILE RAMP TEST OF RHMA-G AND HMA SPECIMENS.....	146
FIGURE 6-6. ASPHALT SPECIMENS TENSILE RAMP FAILURES OF RHMA-G AND HMA SPECIMENS	147
FIGURE 6-7. SUMMARY OF INTEGRITY CURVES FOR TENSILE RAMP TEST OF COMPOSITE RHMA-G AND HMA SPECIMENS.....	149
FIGURE 6-8. COMPOSITE SPECIMENS TENSILE RAMP FAILURES FOR RHMA-G AND HMA SPECIMENS	150
FIGURE 6-9. DRY IDEALCT PLOTS FOR RHMA-G AND HMA SPECIMENS.....	153
FIGURE 6-10. AVERAGE INDIRECT TENSILE CRACKING TEST RESULTS FOR RHMA-G AND HMA SPECIMENS	153
FIGURE 7-1. TEST TRACK LAYOUT.....	157
FIGURE 7-2. TEST SECTION INSTRUMENTATION LAYOUT, TOP VIEW.....	158
FIGURE 7-3. LCB CONSTRUCTION	159
FIGURE 7-4. CURING COMPOUND APPLICATION ON LCB	160
FIGURE 7-5. RHMA-G PAVING	161
FIGURE 7-6. SECTION WITH CURING COMPOUND BOND BREAKER, BEFORE PLC PAVING.....	162
FIGURE 7-7. SECTION WITH GEOTEXTILE BOND BREAKER, BEFORE PLC PAVING	163
FIGURE 7-8. MICROSURFACING PAVING.....	164
FIGURE 7-9. PLC CONSTRUCTION	165
FIGURE 7-10. CURING COMPOUND APPLICATION ON PLC	166
FIGURE 7-11. FULL DEPTH CUTTING OF TRANSVERSE JOINTS ON PLC	167
FIGURE 7-12. LCB COMPRESSIVE STRENGTH RESULTS.....	169
FIGURE 7-13. LCB MODULUS OF ELASTICITY RESULTS	169
FIGURE 7-14. PLC COMPRESSIVE STRENGTH RESULTS.....	170
FIGURE 7-15. PLC MODULUS OF ELASTICITY RESULTS	171
FIGURE 7-16. PLC MODULUS OF RUPTURE RESULTS	171
FIGURE 7-17. CALCULATION OF ϵ_{MEAN} AND ϵ_{DIFF}	172
FIGURE 7-18. STRAIN ϵ_{MEAN} AT THE CORNER OF THE SLABS	174
FIGURE 7-19. EXAMPLE OF DAILY VARIATION OF STRAIN AND TEMPERATURE AT THE CORNERS OF THE SLABS	174

FIGURE 7-20. FWD EVALUATION LOCATIONS	176
FIGURE 7-21. EXAMPLE OF FWD EVALUATION @ SECTION WITH CURING COMPOUND; AUG-19, 2022	177
FIGURE 7-22. SUMMARY OF FWD EVALUATIONS @ 70 kN (15,750 LBF) LOADING	179
FIGURE 7-23. CORE LOCATIONS IN THE MICROSURFACING SECTION	180
FIGURE 7-24. CLOSE UP PICTURES OF CORES 1 THROUGH 8	181
FIGURE 7-25. MICROSURFACING THICKNESS, CORES1 THROUGH 8 FROM TRANSITION SLAB	182
FIGURE 7-26. CLOSE UP PICTURES OF CORES A THROUGH F	183
FIGURE 7-27. MICROSURFACING THICKNESS, CORES A THROUGH F FROM TEST SLAB	184
FIGURE 8-1. TRACTION-SEPARATION EVOLUTION LAWS OF THE COHESIVE ELEMENT CONSIDERED IN THIS RESEARCH	187
FIGURE 8-2. HANGING TEST SETUP AND MODEL	191
FIGURE 8-3. DISPERSION OF HANGING TEST RESULTS FOR TWO SETS OF YOL113RHMA-G TESTS	193
FIGURE 8-4. DAMAGE PROPERTIES FITTING. R3 CASE (NO NEED OF SCALING)	195
FIGURE 8-5. YOL113RHMA-G TENSILE HANGING DAMAGE TEST COMPARED TO DIFFERENT DAMAGE MODELS, COHESIVE LAYER THICKNESS OF 10 MM	196
FIGURE 8-6. TENSILE HANGING DAMAGE TEST RESULTS COMPARED TO ABAQUS VISCOELASTIC AND DAMAGE MODEL, COHESIVE LAYER THICKNESS OF 10 MM	197
FIGURE 8-7. STT SHEAR TEST SETUP AND MODEL.....	198
FIGURE 8-8. CONCEPTUAL BEHAVIOR OF DIFFERENT COHESIVE LAYER THICKNESSES IN THE DAMAGE RANGE	199
FIGURE 8-9. SHEAR STRESS-TIME RESULTS TO BE USED AS A REFERENCE FOR THE DAMAGE PROPERTIES FITTING	200
FIGURE 8-10. SHEAR STRESS-DISPLACEMENT RESULTS FOR DIFFERENT COHESIVE LAYER THICKNESS	201
FIGURE 8-11. HANGING TEST STRAIN-TIME RESULTS FOR DIFFERENT SPECIMEN THICKNESSES.....	202
FIGURE 8-12. SHEAR TEST STRESS-TIME RESULTS FOR DIFFERENT SPECIMEN THICKNESSES	202
FIGURE 8-13. COMPARISON OF MODEL RESULTS INTERCHANGING DAMAGE EVOLUTION LAWS FOR HANGING AND SHEAR TESTS	205
FIGURE 8-14. TENSILE AND SHEAR STRAIN COMPARISON FOR DETERMINING THE CRITICAL DAMAGE INITIATION LAW	206
FIGURE 8-15. SIMPLIFIED PROCESS OF THE TENSION FAILURE OF THE VISCOELASTIC SOLID AND LATER RE-CONTACT WITH THE ELASTIC TWIN SOLID UNDER COMPRESSION.....	208
FIGURE 8-16. SCHEMATIC OF THE PAVEMENT MODEL SECTION INCLUDING THE DIFFERENT COHESIVE LAYERS AND COINCIDENT MINIMUM-COMPRESSION COMPONENTS.....	208
FIGURE 8-17. DESCRIPTION OF THE JPCP OVER LCB SECTION (UNSCALED).....	211
FIGURE 8-18. DISASSEMBLED REPRESENTATION OF THE 3D FINITE ELEMENT MODEL OF THE JPCP LCB SECTION.....	212
FIGURE 8-19. DESCRIPTION OF THE JPCP OVER RHMA-G SECTION (UNSCALED).....	213
FIGURE 8-20. DISASSEMBLED REPRESENTATION OF THE 3D FINITE ELEMENT MODEL OF THE JPCP OVER RHMA-G SECTION.....	213
FIGURE 8-21. SIMPLIFIED MODEL. ASPHALT-JPCP INTERPHASE COMPOSED OF A BONDED ZONE AND A B-WIDE DEBONDED BAND	216
FIGURE 8-22. DISASSEMBLED REPRESENTATION OF THE 3D SIMPLIFIED FINITE ELEMENT MODEL OF THE JPCP OVER RHMA-G SECTION.....	216
FIGURE 8-23. STRAIN VARIATION AT THE CORNER OF THE CONCRETE SLAB	220

FIGURE 8-24. TIME VARIATION OF APPLIED LOADS TO THE MODEL	221
FIGURE 8-25. EVOLUTION OF THE DAMAGE THROUGH THE SCALAR STIFFNESS DEGRADATION OF THE INTERPHASE, CONSIDERING THE APPLICATION OF SELF-WEIGHT, LONG-TERM SHRINKAGE, AND DAILY TEMPERATURE VARIATION. CENTER NODE OF THE FRONTAL EDGE. RHMA-G SECTION.....	222
FIGURE 8-26. STIFFNESS DEGRADATION BANDS IN RHMA-G SECTION WITH CONSTANT CURVATURE	223
FIGURE 8-27. ASSUMED LAWS OF SLAB CURVATURE VARIATION: CONSTANT, LINEAR, AND PARABOLIC CURVATURES	224
FIGURE 8-28. FWD AND MODELING COMPARISON, CURING COMPOUND SECTION, F=70 kN (15,750 LBF) FWD AT SLAB'S CORNER ..	226
FIGURE 8-29. FWD AND MODELING COMPARISON, CURING COMPOUND SECTION, F=70 kN (15,750 LBF) FWD AT SLAB'S CENTER ...	227
FIGURE 8-30. FWD AND MODELING COMPARISON, RHMA-G SECTION, F=70 kN (15,750 LBF) FWD AT SLAB'S CORNER.....	228
FIGURE 8-31. FWD AND MODELING COMPARISON, RHMA-G SECTION, F=70 kN (15,750 LBF) FWD AT SLAB'S CENTER	229
FIGURE 8-32. SENSITIVITY ANALYSIS OF THE FWD TEST WITH DIFFERENT DEBONDING BANDWIDTHS. RHMA-G SECTION WITH LINEAR CURVATURE. FWD AT SLAB'S CORNER. F=70 kN (15,750 LBF)	230
FIGURE 8-33. DEFLECTION EVOLUTION WITH DIFFERENT LOADING STEPS AND COMPARISON OF DIFFERENT AMBIENT LOAD MAGNITUDES. RHMA-G SECTION, B=200 MM (8 IN.), WITH LINEAR CURVATURE. FWD AT SLAB'S CORNER. F=70 kN (15,750 LBF)	231
FIGURE 8-34. DEFLECTION EVOLUTION OF DIFFERENT LOAD CASES AND LOAD MAGNITUDES. RHMA-G SECTION, B=200 MM (8 IN.), WITH LINEAR CURVATURE	233
FIGURE 8-35. SENSITIVITY ANALYSIS OF THE FWD TEST WITH DIFFERENT FWD LOAD MAGNITUDES. RHMA-G SECTION WITH LINEAR VARIATION OF CURVATURE. FWD AT SLAB'S CORNER	234
FIGURE A- 1. FEM MODELS AXIS REPRESENTATION	250
FIGURE A- 2. SHEAR FATIGUE TEST DIAGRAM	251
FIGURE A- 3. DEFLECTION INFLUENCE LINES UNDER THE HVS WHEEL.....	252
FIGURE A- 4. UNDEFORMED SJPCP-COA SECTION OF 1.8 x 1.8 M (6 x 6 FT) SLABS	254
FIGURE A- 5. SHEAR STRAIN UNDER MOVING LOAD FOR SJPCP-COA SECTIONS, 0 M CORRESPONDS TO THE JOINT	255
FIGURE A- 6. SHEAR STRAIN UNDER MOVING LOAD IN A 1.8 x 1.8 M (6 x 6 FT) SECTION, 0 M CORRESPONDS TO JOINT	256
FIGURE A- 7. SHEAR STRAIN ENVELOPE ALONG TRANSVERSE JOINT, 1.8 x 1.8 M (6 x 6 FT) SLAB. 0 MM CORRESPONDS TO EDGE.....	257
FIGURE A- 8. DAMAGING MECHANISMS UNDER THE CONCRETE JOINT	258
FIGURE A- 9. SUMMARY OF SHEAR STRAIN ENVELOPE ALONG TRANSVERSE JOINT FOR 1.8 x 1.8 M (6 x 6 FT) SLAB	259
FIGURE A- 10. SINE-RAMP STRESS VS TIME PLOT	261
FIGURE A- 11. SHEAR SINE-RAMP TEST DIAGRAM	262
FIGURE A- 12. UNDEFORMED SJPCP-COA SECTION OF 3.6 x 3.6 M (12 x 12 FT) SLABS	263
FIGURE A- 13. DEFORMED SJPCP-COA SECTION UNDER ENVIRONMENTAL LOADS	264
FIGURE A- 14. TOTAL SHEAR STRAIN ALONG CRITICAL PATH, SLAB 3.6 x 3.6 M (12 x 12 FT)	265
FIGURE A- 15. TOTAL SHEAR STRAIN ALONG CRITICAL PATH, SLAB 1.8 x 1.8 M (6 x 6 FT)	266
FIGURE A- 16. TENSILE SINE-RAMP TEST DIAGRAM.....	268

FIGURE A- 17. TOTAL VERTICAL STRAIN ALONG CRITICAL PATH, SLAB 3.6 X 3.6 M (12 X 12 FT)	269
FIGURE A- 18. TOTAL VERTICAL STRAIN ALONG CRITICAL PATH, SLAB 1.8 X 1.8 M (6 X 6 FT)	271
FIGURE A- 19. COMBINED SINE-RAMP TEST DIAGRAM	273

LIST OF TABLES

TABLE 1-1. CONCRETE PAVEMENT DISTRESSES	16
TABLE 2-1. INITIAL TESTING PROTOCOL	35
TABLE 3-1. OBJECTIVES AND TASKS.....	55
TABLE 4-1. SST MACHINE LIMITS AND CHARACTERISTICS	64
TABLE 4-2. UTM MACHINE LIMITS AND CHARACTERISTICS.....	65
TABLE 4-3. TENSILE HANGER DEVICE LIMITS AND CHARACTERISTICS	67
TABLE 4-4. AMPT MACHINE LIMITS AND CHARACTERISTICS	68
TABLE 4-5. UNIAXIAL LOADER DEVICE LIMITS AND CHARACTERISTICS	70
TABLE 4-6. SUMMARY OF VARIABLES ANALYZED	73
TABLE 4-7. SUMMARY OF MATERIAL PROPERTIES.....	74
TABLE 4-8. MIST DEVICE CHARACTERISTICS.....	77
TABLE 4-9. TESTING PROCEDURES SUMMARY.....	78
TABLE 5-1. ASPHALT MIXES PROPERTIES	97
TABLE 5-2. SHEAR DYNAMIC MODULUS TEST DATA EXAMPLE AND CALCULATIONS.....	99
TABLE 5-3. SHEAR CREEP TEST DATA EXAMPLE	102
TABLE 5-4. SHEAR CREEP TEST PROCESSED DATA EXAMPLE.....	105
TABLE 5-5. TENSILE CREEP TEST DATA EXAMPLE.....	107
TABLE 5-6. TENSILE CREEP TEST PROCESSED DATA EXAMPLE.....	108
TABLE 5-7. TENSILE HANGING CREEP TEST DATA EXAMPLE	111
TABLE 5-8. TENSILE HANGING CREEP TEST PROCESSED DATA EXAMPLE	112
TABLE 5-9. COMPRESSIVE DYNAMIC DATA TEST RESULT EXAMPLE AND CALCULATIONS.....	115
TABLE 5-10. RHMA-G AND HMA YOUNG’S MODULUS SUMMARY VALUES	125
TABLE 5-11. RHMA-G AND HMA SHEAR MODULUS SUMMARY VALUES	125
TABLE 5-12. STRENGTH TESTING CONDITIONS.....	126
TABLE 5-13. STRAIN LEVELS AT 50 PERCENT INTEGRITY FOR TENSILE RAMP TEST COMPARED FOR HMA AND RHMA-G	134
TABLE 5-14. STRAIN LEVELS AT 50 PERCENT INTEGRITY FOR SHEAR RAMP TEST COMPARED FOR HMA AND RHMA-G	136
TABLE 5-15. STRAIN LEVELS AT 50 PERCENT INTEGRITY FOR DIFFERENT TEST FOR HMA AND RHMA-G	137
TABLE 6-1. ASPHALT MIXES PROPERTIES FOR FINAL TESTING.....	140
TABLE 6-2. TESTED SPECIMENS IN THE INDIRECT TENSILE CRACKING TEST	152
TABLE 7-1. PLC MIX DESIGN FOR 0.76 M ³ (1 YD ³).....	165
TABLE 8-1. ELASTIC PROPERTIES OF THE COHESIVE ELEMENTS.....	188
TABLE 8-2. COHESIVE DAMAGE APPROACHES TO THE HANGING TEST	196
TABLE 8-3. COHESIVE DAMAGE APPROACHES TO SST SHEAR TEST.....	200

TABLE 8-4. COHESIVE DAMAGE APPROACHES FOR THE COMPLEX MODEL OF ASPHALT.....	203
TABLE 8-5. MATERIAL PROPERTIES OF THE ELEMENTS IN THE PAVEMENT MODELS	217
TABLE A- 1. STRAIN VALUES AT THE POINT OF MAXIMUM SHEAR STRAIN IN SLAB 3.6 X 3.6 M (12 X 12 FT).....	264
TABLE A- 2. STRAIN VALUES AT THE POINT OF MAXIMUM SHEAR STRAIN IN SLAB 1.8 X 1.8 M (6 X 6 FT).....	266
TABLE A- 3. STRAIN VALUES AT THE POINT OF MAXIMUM VERTICAL STRAIN IN SLAB 3.6 X 3.6 M (12 X 12 FT)	269
TABLE A- 4. STRAIN VALUES AT THE POINT OF MAXIMUM VERTICAL STRAIN IN SLAB 1.8 X 1.8 M (6 X 6 FT)	270
TABLE D- 1. MATERIAL PROPERTIES OF THE ELEMENTS IN THE PAVEMENT MODELS, ENGLISH UNITS	280

LIST OF ABBREVIATIONS

AASHTO	American Association of State Highway and Transportation Officials
AB	Aggregate Base
AC	Asphalt Concrete
AMPT	Asphalt Mixture Performance Tester
ASTM	American Society for Testing and Materials
CalME	California Mechanistic Empirical Design Guide
Caltrans	California Department of Transportation
CC	Curing Compound
CH	Calcium Hydroxide
CIR	Cold in-place Recycling
CRM	Crumb Rubber Modifier
CSA	Calcium-sulfo-aluminate
C-S-H	Calcium Silica Hydrate
CTE	Coefficient of Thermal Expansion
D	Desert
DM	Dynamic Modulus
DOT	Department of Transportation
FEM	Finite Element Methods
FWD	Falling Weight Deflectometer
GEO	Geotextile
GMM	Generalized Maxwell model
HCl	Hydrochloric Acid
HMA	Hot Mix Asphalt
HVS	Heavy Vehicle Simulator
ICC	Internal Curing Concrete
IOMD	Interphase Opening Measuring Devices
ITZ	Interfacial Transition Zone
IV	Inland Valley
JDMD	Joint Opening Measuring Devices
JPCP	Jointed Plain Concrete Pavement
LCB	Lean Concrete Base
LVDT	Linear Variable Differential Transformer
LVER	Linear Viscoelastic Region
MIC	Microsurfacing
MOE	Modulus of Elasticity
MOR	Modulus of Rupture

NCHRP	National Cooperative Highway Research Program
NMAS	Nominal Maximum Aggregate Size
PCC	Portland Cement Concrete
PG	Performance Grade
PLC	Portland Limestone Cement
RAP	Reclaimed Asphalt Pavement
RHMA	Rubberized Hot Mix Asphalt
RHMA-G	Gap-Graded Rubberized Hot Mix Asphalt
SC	South Coast
SJPCP-COA	Short Jointed Plain Concrete Pavement – Concrete Overlay on Asphalt
SRA	Shrinkage Reducing Admixture
SST	Superpave Shear Tester
TSL	Traction-Separation Law
UCPRC	University of California Pavement Research Center
UL	Uniaxial Loader
UTM	Universal Testing Machine
VWSG	Vibration Wire Strain Gage
WST	Wedge Splitting Test

LIST OF STANDARD METHODS AND SPECIFICATIONS

AASHTO T320	Standard Method of Test for Determining the Permanent Shear Strain and Stiffness of Asphalt Mixtures Using the Superpave Shear Tester (SST)
AASHTO T378-22	Standard Method of Test for Determining the Dynamic Modulus and Flow Number for Asphalt Mixtures Using the Asphalt Mixture Performance Tester (AMPT)
ASTM C39/C39M-21	Standard Test Method for Compressive Strength of Cylindrical Concrete Specimens
ASTM C78/C78M-21	Standard Test Method for Flexural Strength of Concrete (Using Simple Beam with Third-Point Loading)
ASTM C309-19	Standard Specification for Liquid Membrane-Forming Compounds for Curing Concrete
ASTM C403/C403M-08	Standard Test Method for Time of Setting of Concrete Mixtures by Penetration Resistance
ASTM C469/C469M-22	Standard Test Method for Static Modulus of Elasticity and Poisson's Ratio of Concrete in Compression
ASTM C595/C595M-23	Standard Specification for Blended Hydraulic Cements
ASTM C989/989M-22	Standard Specification for Slag Cement for Use in Concrete and Mortars
ASTM D7870/D7870M-20	Standard Practice for Moisture Conditioning Compacted Asphalt Mixture Specimens by Using Hydrostatic Pore
ASTM D8225-19	Standard Practice for Determination of Cracking Tolerance Index of Asphalt Mixture Using the Indirect Tensile Cracking Test at Intermediate Temperature

CONVERSION TABLE

SI* (MODERN METRIC) CONVERSION FACTORS				
APPROXIMATE CONVERSIONS TO SI UNITS				
Symbol	When You Know	Multiply By	To Find	Symbol
LENGTH				
in.	inches	25.40	millimeters	mm
ft.	feet	0.3048	meters	m
yd.	yards	0.9144	meters	m
mi.	miles	1.609	kilometers	km
AREA				
in ²	square inches	645.2	square millimeters	mm ²
ft ²	square feet	0.09290	square meters	m ²
yd ²	square yards	0.8361	square meters	m ²
ac.	acres	0.4047	hectares	ha
mi ²	square miles	2.590	square kilometers	km ²
VOLUME				
fl. oz.	fluid ounces	29.57	milliliters	mL
gal.	gallons	3.785	liters	L
ft ³	cubic feet	0.02832	cubic meters	m ³
yd ³	cubic yards	0.7646	cubic meters	m ³
MASS				
oz.	ounces	28.35	grams	g
lb.	pounds	0.4536	kilograms	kg
TEMPERATURE (exact degrees)				
°F	Fahrenheit	(F-32)/1.8	Celsius	°C
FORCE and PRESSURE or STRESS				
lbf	pound-force	4.448	newtons	N
lbf/in ²	pound-force per square inch	6.895	kilopascals	kPa
APPROXIMATE CONVERSIONS FROM SI UNITS				
Symbol	When You Know	Multiply By	To Find	Symbol
LENGTH				
mm	millimeters	0.03937	inches	in.
m	meters	3.281	feet	ft.
m	meters	1.094	yards	yd.
km	kilometers	0.6214	miles	mi.
AREA				
mm ²	square millimeters	0.001550	square inches	in ²
m ²	square meters	10.76	square feet	ft ²
m ²	square meters	1.196	square yards	yd ²
ha	hectares	2.471	acres	ac.
km ²	square kilometers	0.3861	square miles	mi ²
VOLUME				
mL	milliliters	0.03381	fluid ounces	fl. oz.
L	liters	0.2642	gallons	gal.
m ³	cubic meters	35.31	cubic feet	ft ³
m ³	cubic meters	1.308	cubic yards	yd ³
MASS				
g	grams	0.03527	ounces	oz.
kg	kilograms	2.205	pounds	lb.
TEMPERATURE (exact degrees)				
°C	Celsius	1.8C + 32	Fahrenheit	°F
FORCE and PRESSURE or STRESS				
N	newtons	0.2248	pound-force	lbf
kPa	kilopascals	0.1450	pound-force per square inch	lbf/in ²

1. INTRODUCTION

1.1 Background

Roads are paved to enable easier transportation of people and goods, keeping in mind that the structure needs to be strong enough to support traffic and environmental loads, provide a good ride quality with a smooth wearing surface, have a safe skid-resistant surface, and must provide durability to not deteriorate at early ages.

1.1.1 Types of Pavement

Pavement structures can often be classified as flexible pavements or rigid pavements. Composite structures made of a combination of rigid and flexible pavement are also built. A 25 percent of interstates, freeways, and expressways in the United States were paved with rigid structures, according to the Federal Highway Administration (FHA) in the Highway Statistics report from 2020 [1], 52 percent were paved with asphalt structures, and the remaining 23 percent were paved with composite structures.

1.1.1.1. *Flexible Pavements*

Flexible pavements are primarily made of a combination of asphaltic material and aggregates. Asphalt is known to be a viscoelastic material whose properties are controlled by temperature and time of loading (alternatively by dynamic frequency). At low temperatures and high frequencies (short loading times), the asphalt will behave more elastically, while under high temperatures and low frequencies, it will tend to behave more like a viscous fluid. Asphalt layers are usually constructed on top of granular unbound layers and the existing subgrade.

The most commonly used surface layer materials are hot mix asphalt (HMA) and gap-graded rubberized hot mix asphalt (RHMA-G), which has environmental advantages over conventional HMA [2]. Other bituminous treatments for surface and base layers also exist and are widely used, such as microsurfacing, slurry seal, chip seal, and fog seal. Aggregate gradation will determine the type of HMA. Dense, open, and gap graded are the most common gradations and their gradations are shown in Figure 1-1 plotted with sieve sizes raised to the 0.45 power to indicate maximum density. In the US, since the 1960s, rubber has been used as a modifier of HMA. This has environmental advantages, as it eliminates waste tires, but it has also been found to extend pavement life through better resistance to reflective cracking [2].

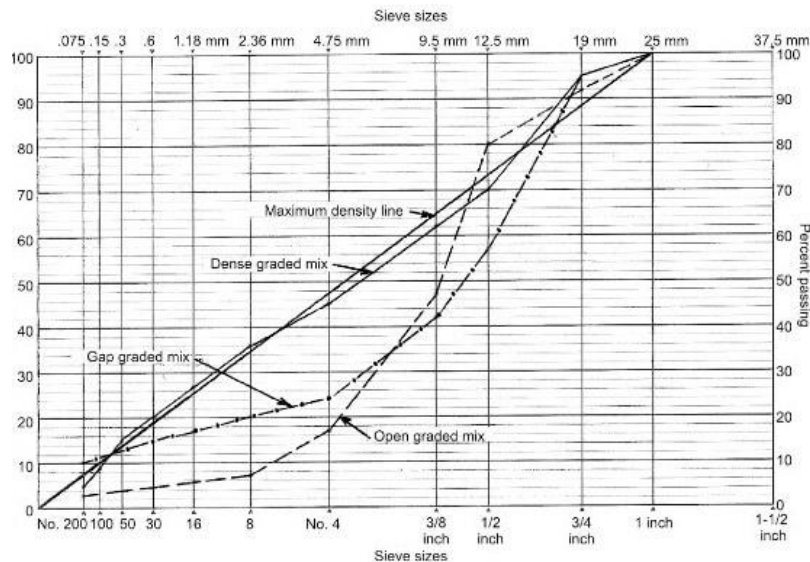


Figure 1-1. Gradation chart for HMA mixes,
Obtained from: <https://theconstructor.org/transportation/types-bitumen-mixes-pavements/16034/>

The stiffness properties of asphaltic materials can be determined in the laboratory, but only a small frequency range is analyzed at each chosen temperature. The test is often performed at four different temperatures: 4, 21, 38, and 54 °C (40, 70, 100, and 130 °F). The method of reduced variables, also called the time-temperature superposition principle, is applied once the data

points for each temperature are obtained. The method shifts the data relative to the frequency or time of loading after selecting a reference temperature. The shifting will reduce the data to a single curve that covers a wider range of frequencies and is usually called the master curve, which follows the shape of a sigmoidal function [3]. The process requires a shift factor and the calculation of the reduced frequencies. The following equations summarize the process:

$$\log(aT) = C_1 * (Temp - T_r) \quad \text{Equation 1}$$

Where,

aT	Shift factor
C1	Calibration coefficient
Temp	Test temperature
Tr	Reference temperature

$$Freq\ red = Freq * 10^{\log(aT)} \quad \text{Equation 2}$$

Where,

Freq red	Reduced frequency
Freq	Frequency
aT	Shift factor

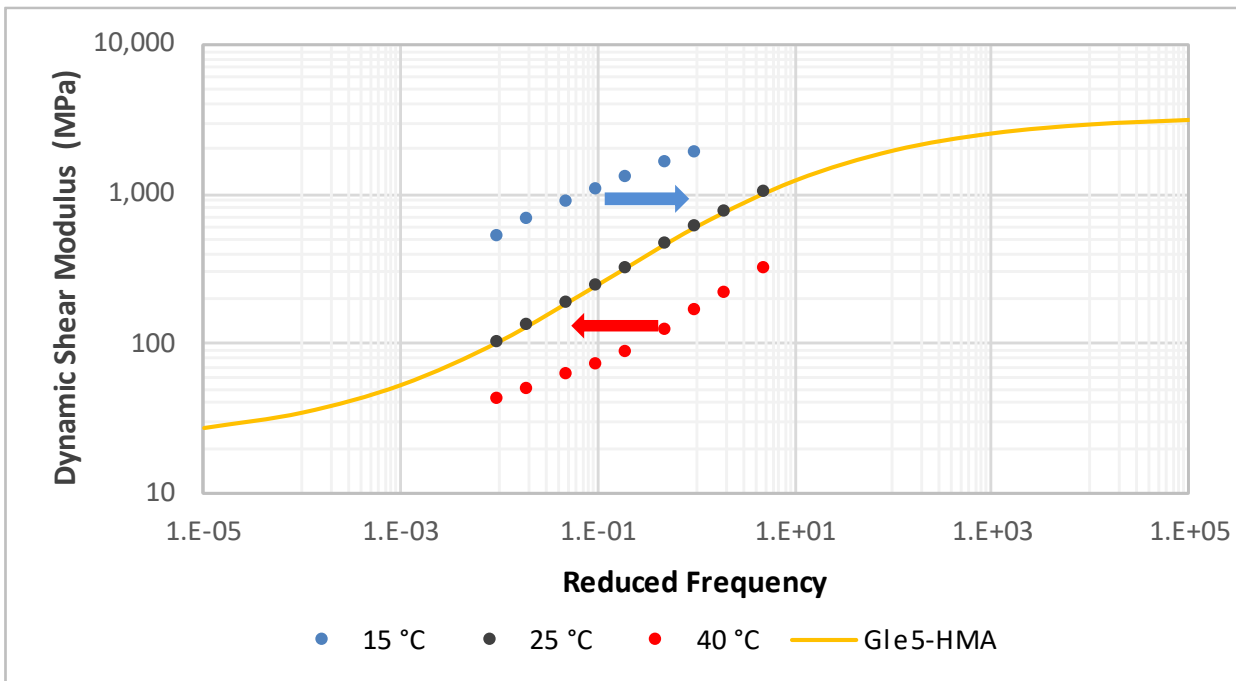
$$MC DM = 10^{\left(\delta + \frac{\alpha}{1 + e^{\beta + \gamma \cdot \log(\text{Frequency})}}\right)}$$

Equation 3

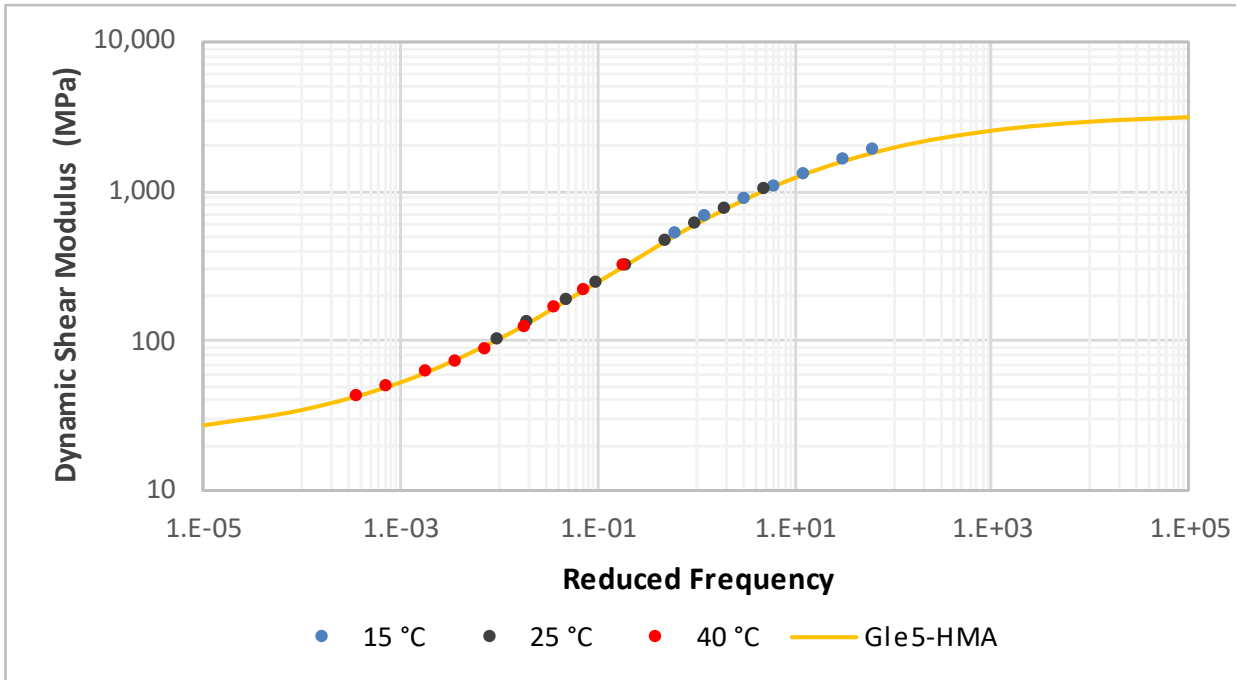
Where,

- MC DM Master curve dynamic modulus
- δ Minimum value of MC DM
- $\delta + \alpha$ Maximum value of MD CD
- β, γ Shape describing parameters

Figure 1-2 illustrates the process, the first figure shows the data points obtained for each of the frequencies at three different temperatures, and the second image shows the result after the lateral shifting is done. In this case, the shifting was performed using 25 °C (77 °F) as the reference temperature.



a) Frequency sweep datapoint at each temperature



b) Shifted data points around reference temperature of 25 °C (77 °F)

Figure 1-2. Temperature-time superposition for master curves process

1.1.1.2. Rigid Pavements

Rigid pavements are primarily composed of aggregate, water, and a cementitious material and are placed on top of a bound (cement or asphalt) base and one or more unbound layers. Rigid pavements are stiffer than flexible ones due to the high modulus of elasticity of the concrete. The most common cementitious material in the state of California is portland cement Type II/V but in other states it is portland cement Type I. If higher early strengths are desired, portland cement type III or calcium-sulfo-aluminate (CSA) can be used. Both type III cement and CSA can meet the design strength 4-10 hours after the pour, which can be beneficial when dealing with reduced road closing times. The ability to fulfill high early strengths is also related to the use of concrete admixtures to accelerate concrete reactions. Reinforcing mechanisms can be used to provide higher strengths and better performance of the structure under the traffic and

environmental loads depending on the thickness and type of rigid pavement. Some of the most common reinforcing methods used in concrete pavements are deformed steel at the longitudinal joints, smooth steel dowels for load transfer efficiency at the transverse joints, and fibers blended in the mix to resist crack propagation. Concrete slabs are exposed to changes in temperature and humidity, which will vary with depth, producing gradients in the slab. The temperature changes occur on a daily basis and are also seasonal throughout the year. Drying shrinkage in concrete slabs is caused by the nature of the concrete in addition to environmental conditions. Drying shrinkage occurs as the concrete ages due to the loss of capillary water in the structure. It tends to be higher at the top of the structure since it is in contact with the environment, while the bottom is in contact with the base or subgrade. The temperature and shrinkage gradients produce upward and downward movements of the corners and center of the slab. Upward movements of the corners happen when the temperature is cooler on top and when the top is drier than the bottom, which is also called night-time curling. Downward movements of the corners occur when the temperature is warmer on the top of the slab, and it is also called day-time curling. Deformed slabs for both conditions are shown in Figure 1-3.

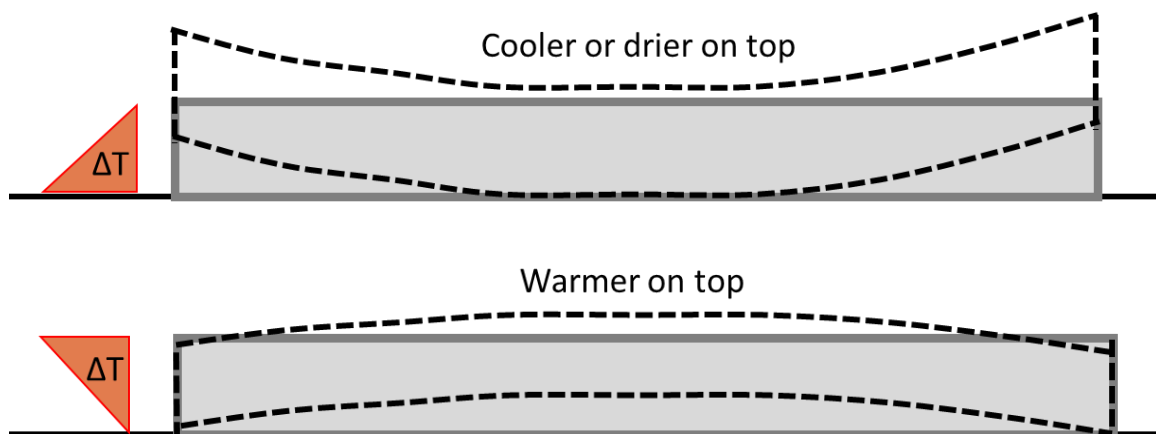


Figure 1-3. Upward/downward movement of concrete slabs

1.1.1.2.1. Bases for Rigid Pavements

The base in a rigid pavement is supposed to support the concrete layer and transfer the loads to the underneath layers. Due to the effect of traffic and environmental loads, the base ideally should behave soft under environmental loads and stiff under traffic loads. Stiff behavior under traffic loads will allow the structure to carry more loads and spread it down. Soft behavior during environmental loads will allow it to creep and follow the concrete upward/downward movements at the edges and corners and the horizontal movements due to expansion and contraction, as can be seen in Figure 1-4. Having these behaviors will provide a reduction in the stresses of the structure, mainly on the interphase, which is the contact plane between the base and the concrete slabs.

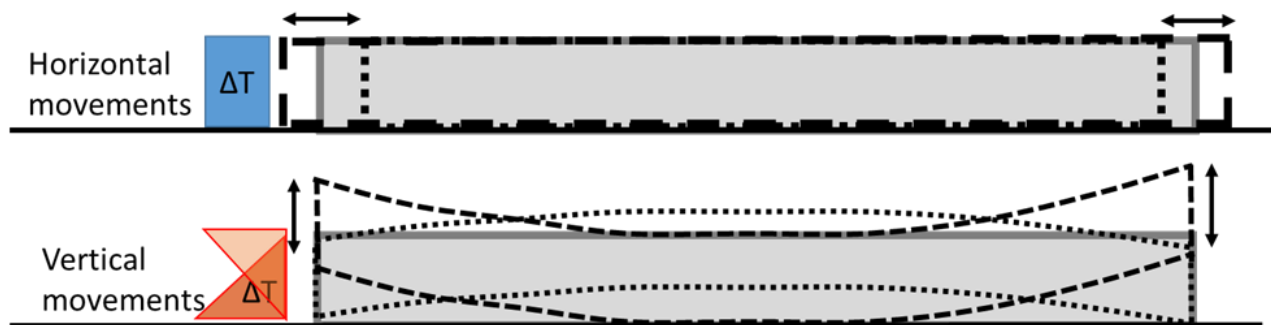


Figure 1-4. Concrete vertical and horizontal movements

The two most common bases for concrete pavements are lean concrete base (LCB) and HMA Type A, according to Caltrans' Concrete Pavement Guide [4] and Highway Design Manual [5]. LCB, as a base for jointed plain concrete pavements (JPCP), has 2.8 times the cracking than asphalt bases based on a statistical evaluation of concrete pavement performance in California from 30 years of data [6]. However, LCB offers advantages in terms of construction logistics. Compared to HMA, LCB also offers the possibility of using lower-quality aggregates, including greater

percentages of recycled materials. The poorer performance of LCB compared to HMA bases is likely related to the low capacity of deformation (high stiffness) of LCBs.

1.1.1.3. Composite Pavements

Composite pavements are structures containing flexible and rigid pavement. Traditionally, placing an asphalt layer over concrete layers is more commonly used, but placing a concrete layer on top of an old asphalt layer is also done to extend the life of an already deteriorated asphalt pavement. Studies [7, 8, 9] extensively covered construction processes and performance of composite structures of asphalt concrete overlays on concrete.

This research only focuses on composite structures where a concrete layer is placed on top of an asphalt layer, and a typical pavement section is shown Figure 1-5. It consists of a conventional asphalt pavement layer with a PCC layer on top. Different surface techniques can be used in the asphalt layer to improve the bonding between the HMA and PCC layers since, typically, the asphalt pavement structure will be in a deteriorated condition.

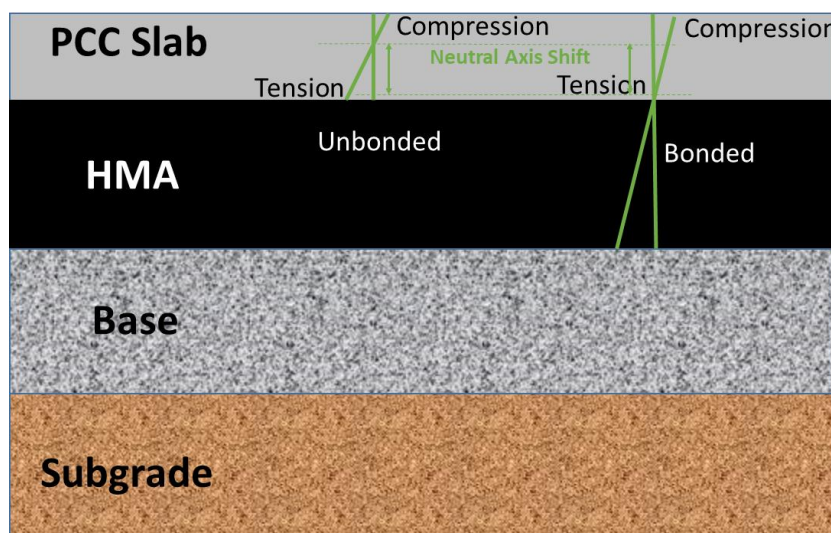


Figure 1-5. Bonded COA Pavement Structure

Bonded short jointed plain concrete pavement-concrete overlay of asphalt (SJPCP-COA) is a composite pavement that consists of a 100 to 175 mm (4 to 7 in.) thick concrete overlay placed on an existing flexible asphalt concrete (AC) pavement. The structures are considered ultra-thin whitetopping if the slabs are under 100 mm (4 in.) thick and conventional concrete pavement if the thickness is beyond 175 mm (7 in.). This technique was previously called thin whitetopping and bonded concrete overlays on asphalt, but the name has been changed now to short jointed plain concrete pavement - concrete overlay of asphalt because it better describes the structures and adapts to current pavement terminology used in different states and agencies.

The bonding between the two layers determines the success of a bonded SJPCP-COA structure. The section will work as a composite structure, and the stresses are transferred more efficiently to the underneath layers when full bonding is obtained. The bending resistance of the bonded concrete and asphalt layers depends on the stiffness (E) and the thickness (h) of the layers, and it is proportional to Eh^3 . The structure needs to be designed so that the neutral axis is shifted to the bottom of the PCC layer or even into the top of the HMA layer. If the structure is bonded and the bending resistance is appropriately designed, such a shift of the neutral axis causes a decrease in the tensile stresses in the PCC overlay, as can also be seen in the diagrams of Figure 1-5. The decrease in the tensile stresses will allow the structure to carry more load repetitions when calculating the fatigue life using Darter and Barenberg [10] concrete fatigue equation (Equation 4). In this equation, a decrease in the tensile stress in the structure will be reflected in an increase in the total amount of allowable load repetitions. The concrete layer will not be able to transfer the stresses to the layers below, and the rate of damage will increase if no bonding occurs.

$$\log_{10} N = 17.61 - 17.61 * \left(\frac{\sigma}{MR} \right) \quad \text{Equation 4}$$

Where σ is the tensile stress at the bottom of the concrete layer, and MR is the modulus of rupture of the concrete. The smaller the ratio σ /MR is, the bigger the amount of load repetitions the structure can withstand.

Bonded composite structures have been used in Canada, Belgium, France, and Japan, as well as Minnesota, Colorado, Iowa, Missouri, Virginia, Indiana, Montana, and Kentucky [11]. It will potentially provide the California Department of Transportation (Caltrans), local governments, and the concrete industry with an alternative for rehabilitation of pavements with reduced construction closure times, allowing night-time and weekend construction windows in which only asphalt overlays are currently able to compete. The suitability for night and weekend closures depends on the concrete mix and cement type.

The nature of the bonding between asphalt layers and concrete slabs can either be a mechanical bond, a chemical bond, or a combination of both types. Mechanical bonds would be due to material properties and interconnections that occur when the concrete is cast on the asphalt, such as mechanical friction due to aggregate interlock and penetration of concrete into the asphalt. The chemical bond would be due to internal interactions and attractions between molecules that enable the formation of new compounds.

When dealing with these types of composite structures, the three main components to take into consideration are the HMA layer base, PCC slab, and interphase between the asphalt and the

concrete. The base and subgrade from the original structure will remain the same for the SJPCP-COA and will not be analyzed in this project.

1.1.1.3.1. HMA Layer

Having asphalt materials as a base layer for the PCC slab is beneficial since its viscoelastic behavior will tend to be close to that of an 'ideal base' for concrete pavement, which will behave as a solid or as a viscous fluid depending on the type of load and temperature. Distressed asphalt mix layers are good candidates for application of SJPCP-COA except for those that are in a heavily distressed condition. The thickness can vary depending on the existing structure, but according to Vandebossche and Sachs (2013) [12], a minimum thickness of 75 to 100 mm (3 to 4 inches) of asphalt layer should be left so that the structures perform adequately.

Distresses are allowed when dealing with old HMA layers, but bonded SJPCP-COA is not recommended to be used in the case that severe structural damage is present, such as stripping of HMA layers, moisture damage, poor drainage, and extensive cracking. These distresses must be avoided since the structure will be affected by moisture deterioration and reflection into the concrete slab, which will cause full bonding to be hardly obtained. Colorado Department of Transportation (DOT) [13] has done several studies using a new HMA layer before placing the concrete slabs, but they recommend not placing a new HMA prior to concrete paving since they have observed in field projects that the concrete does not bond well to new asphalt layers. On the other hand, the UCPRC [14] observed that using a new layer of rubberized gap-graded hot mix asphalt (RHMA-G) can be a better base layer for the SJPCP-COA and even a relatively new conventional HMA had good bonding between both layers. Undercompaction and high air voids at the surface of the RHMA-G could have led to the success of the new RHMA-G layer in California.

The good performance of the RHMA-G as a base could also be due to the high workability of the concrete mixes, which may have contributed to the concrete slurry penetrating into the RHMA-G layer.

1.1.1.3.2. PCC Slab

Reinforcement is usually not used since it is a thin layer ranging between 100 to 175 mm (4 to 7 in.), and it is supposed to be bonded to the underneath asphalt layer. However, some literature supports the use of fibers in bonded COA to provide more strength and improve load transfer efficiency [15, 16]. Conventional types of PCC can be used, such as Type II and Type III, but other cementitious materials can also be utilized, for example, CSA. Even though Type III and CSA cements are not commonly used for concrete pavement, working with these materials will produce concrete mixes with high early strengths and faster setting time that can be beneficial during shorter construction windows. The opening time for concrete mixes done with Type III and CSA cement is usually 4 hours, while Type II cement can provide opening strengths in as fast as 10 hours. Achieving 4-hour or 10-hour opening times for Type III and Type II cement concrete, respectively, requires the use of concrete admixtures to accelerate the setting time and reduce the amount of water used in the mix. CSA mixes also require the use of admixtures to accelerate and stabilize the chemical reactions, and it is able to reach opening strengths in under 4 hours.

1.1.1.3.3. Interphase

Different procedures are usually applied to the asphalt layer to achieve adequate bonding between the two layers and are the currently recommended techniques in industry guidelines. Milling, micro-milling, grinding, shot blasting, and sweeping are some of the techniques that are commonly used to eliminate or diminish surface distresses and to provide a rougher surface by

leaving some exposed aggregate to ensure good bonding. According to Vandenbossche [12], block cracking, top-down cracking, fatigue cracking, rutting, and corrugations of the asphalt layer are distresses that are typically removed during milling processes. Failing to address asphalt distresses before placement of the overlay will reflect the distresses into the concrete slab and provide insufficient or partial bonding, causing the structure to fail prematurely.

Similarly to the concrete and asphalt layer, the bond will deteriorate with the application of loads. The loading will be a combination of traffic and environmental loads that will act on the pavement at different times of loading. It is essential to provide adequate bonding and strength for the structure to be capable of withstanding load applications throughout the life of the pavement.

It is recommended to use either milled old asphalt layers or new unmilled asphalt layers when choosing the asphalt base for a SJPCP-COA, based on the Colorado experience when dealing with BCOA structures [17]. This matches what was also found by Mateos [14] in the HVS report. Milling along with an adequately clean surface will reduce the strain levels by approximately 25 percent when dealing with old asphalt layers. Additional patching is required before concrete paving after the milling process if the asphalt layer has open surfaces. It is advised not to mill the surface if new asphalt layers are to be used since it was observed that the strain level would increase by approximately 50 percent when milling new asphalt layers prior to the placement of the concrete slabs.

The use of a bond breaker is required when dealing with unbonded bases. The bond breaker causes both layers to move independently, reducing reflective cracking and providing flexibility for slab curling due to temperature differences between the top and bottom of the pavement

surface. Caltrans allows the contractor to select from various materials to be used as a bond breaker, such as asphalt binder, curing compound, polyethylene film, curing paper, or geosynthetics, depending on the type of base material [4].

1.1.2 Loading Scenarios

Flexible and rigid pavements have similar loading scenarios, which can be divided into two main load types: environmental loads and traffic loads. Environmental loads are those related to changes in temperature and humidity that affect the pavement structure, and traffic loads are caused by vehicle movements. These two types of loads have different loading times and numbers of applications during the design life of a pavement structure. While traffic loads have short loading times and many applications, environmental loads have long loading times and fewer applications. Laboratory experiments can be performed to reproduce each loading scenario so that both conditions can be studied. Additionally, repeated loading can be used to analyze the damage evolution due to repetitive load applications. Composite structures exposed to traffic and environmental loads can fail in the asphalt layer or the interphase between the concrete and the asphalt. Understanding the behavior and performance of the interphase is a critical point in this research since good performance relies on adequate bonding between the layers.





Repeated application of traffic and environmental loads tend to damage the pavement over time, which will cause a reduction in the functionality of the structure and a reduction in ride quality for the users. Changes in humidity and temperature can negatively impact the structure. These loads would tend to curl up or down the corners of the concrete slab, increasing the debonding

susceptibility, which, in addition to traffic loading, will increase the rate of damage to the structure.



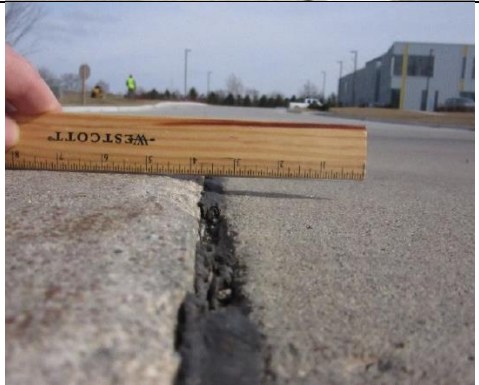

1.1.3 Distresses

This research is limited to distresses for rigid pavements and composite structures with a rigid layer on top. Tensile stresses and strains are what crack concrete, and tensile and shear properties are what control the support given to the slab by the asphalt and the interphase. Those stresses and strains are caused by cycles of temperature change driving thermal expansion and contraction and relative humidity changes driving drying shrinkage change, both operating at frequencies of daily and annual cycles. Stresses and strains are also caused by heavy traffic repetitions operating at frequencies controlled by the speed of traffic. The two types of stresses and strains interact to create the total stress and strain time histories for the pavement and its individual phases of interest in this study: the concrete slabs, the asphalt base, and the asphalt/concrete interphase. The following table summarizes the most common distresses, possible causes, and an image for reference [18].




Table 1-1. Concrete pavement distresses


Distress	Causes	Image
Plastic shrinkage cracking	Low humidity and windy conditions after construction	
Surface wear	Traffic loading applications and possibly poor aggregates	
Surface delamination	Construction issues	
Alkali-silica reaction cracking	The presence of alkali hydroxide in the cement, silica in the aggregate, and water in the pavement structure	

Distress	Causes	Image
Drying shrinkage cracking	Loss of moisture from the slab after hardening	
Transverse cracking	Temperature changes and poor support from underlying layers, excessive slab length, lack or poor saw cutting, and traffic loading	
Diagonal cracking	Temperature changes, poor support from underlying layers, and traffic loading	
Longitudinal cracking	Temperature and moisture changes in concrete, excessive slab widths, poor saw cutting, poor support from underlying layers, and traffic loading	

Distress	Causes	Image
Corner cracking	Poor support and traffic loading	
Spalling	Poor consolidation, temperature changes, freeze-thaw, and poor aggregate quality	
Faulting	Load transfer loss, cracking, pumping, traffic loading, presence of water	
Blowups	Upward movement of corners, temperature changes, presence of incompressible material in joints, presence of water, and poor drainage	

Note: Images from Ayers [18]

Distress	Causes	Image
Asphalt-asphalt debonding	Construction issues, traffic loading, and environmental loading	
Asphalt crushing/debonding at corners	Combination of environmental loading and traffic loading	
Asphalt cracking below the transverse joint	Environmental loads	

Distress	Causes	Image
Loss of bonding	Construction issues, traffic loading, and environmental loading	
Note: Images from Mateos [14]		

1.1.4 Overall

There are still significant gaps that need to be filled even though the SJPCP-COA technique has been improving since the mid-1990s, according to Harrington [19]. The slab-base interaction and the role and performance of the interphase between concrete and asphalt are the main gaps that this study will fill. A better understanding of the bonding, characterizing its properties and performance, will also lead to the determination of the ideal base and interphase preparation required for concrete pavements.

The diagram in Figure 1-6 summarizes the whole system used in the development of this research and will be referred to in different sections.

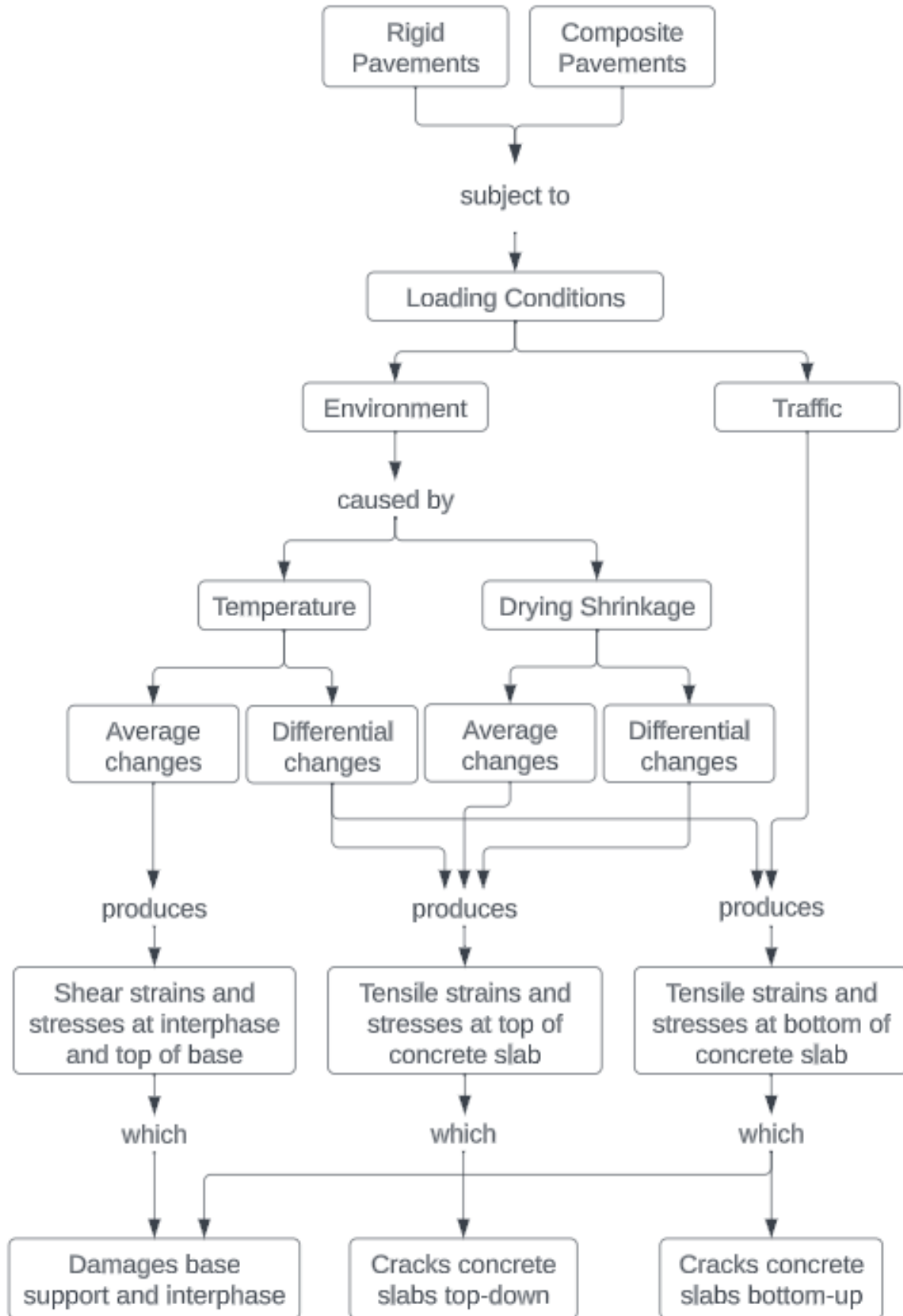


Figure 1-6. System diagram

1.2 Goal

The goal of this study is to investigate and understand the slab/base interactions, including the bonding of concrete to different bases/interlayers, and how to reduce concrete pavement shear and tensile stresses and strains that cause cracking and, therefore, reduce the cost of the structures. It is also intended to keep the functionality of the structure by optimizing bases and finding the best possible base and interlayer for concrete pavements, regarding materials and surface preparation that will allow the structure to properly carry traffic and environmental loads, particularly in dry environments. Such an ideal base will apply for SJPCP-COA and JPCP pavements, for which currently allowed bases are very limited, and the performance could be improved.

2. LITERATURE SURVEY

2.1 Performance Studies

Saboori [6] calibrated the transverse cracking model for JPCP in California and performed a statistical evaluation of concrete pavement performance from 30 years of data. The variables that were considered when doing the simulations were slab thickness, joint spacing, shoulder type, climate region, load spectra, and annual average daily truck traffic. Five different base types were used: aggregate base (AB), asphalt-treated permeable base (ATPB), cement-treated base (CTB), hot mix asphalt (HMA), and lean concrete base (LCB). A summary plot is shown in Figure 2-1, and it indicates that LCB as a base for jointed plain concrete pavements (JPCP) has 2.8 times the cracking probability than using asphalt bases [6]. The cracking probability observed for LCB was around 51%, while the cracking probability for HMA was around 18%. Only LCB and HMA are analyzed in this discussion since they are the only two base types allowed by Caltrans as a concrete pavement base, but it is interesting to note that both the aggregate base and the cemented-treated base had a cracking probability, which was lower than the one obtained for the LCB and the HMA, which can be helpful in other states or countries that allow different base types for concrete pavements. The asphalt-treated permeable base, on the other hand, had a cracking probability higher than the HMA but still lower than the LCB.

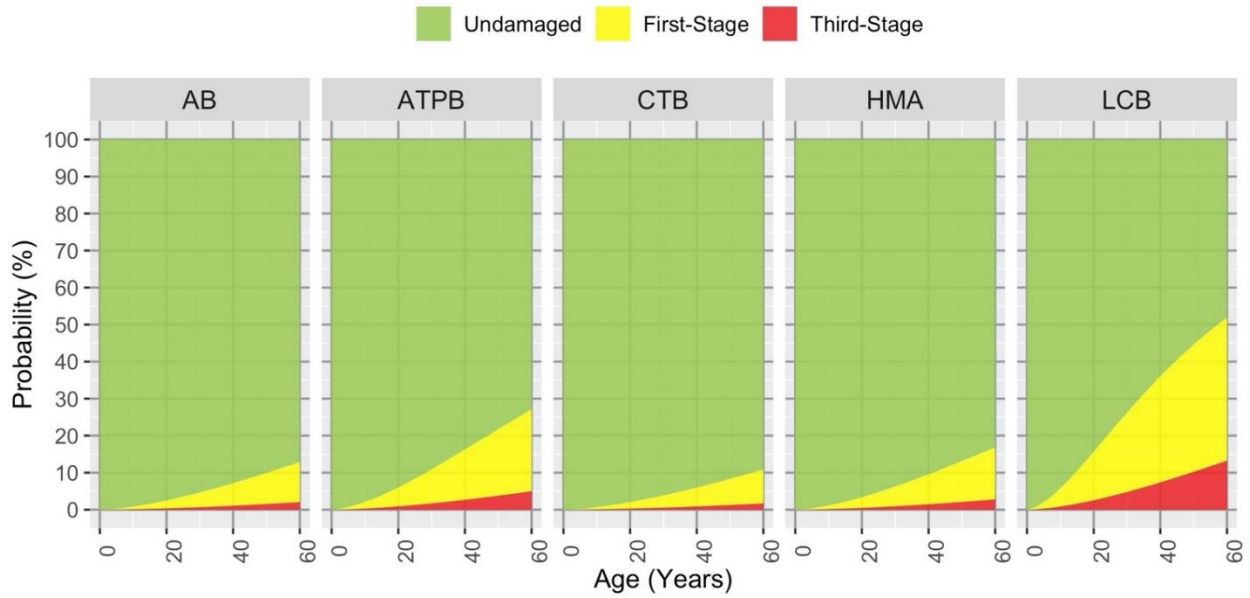


Figure 2-1. Cracking performance of structures with different bases [6]

The FHWA under the Long-Term Pavement Performance (LTPP) Strategic Study of Structural Factors for Rigid Pavements (SPS-2) [20] analyzed sections built between 1992 and 1999. Initially, all sections were analyzed, and it was followed by a detailed comparison of sections in Arkansas and Arizona to study the effects deeply in a wet and dry zone. Sections in the dry weather of Arizona cracked sooner and more extensively than the sections in Arkansas as can be seen in Figure 2-2. This behavior was observed in both longitudinal and transverse cracking, even though only the plot for transverse cracking is shown below. A similar behavior would be observed in California since it also has dry weather.

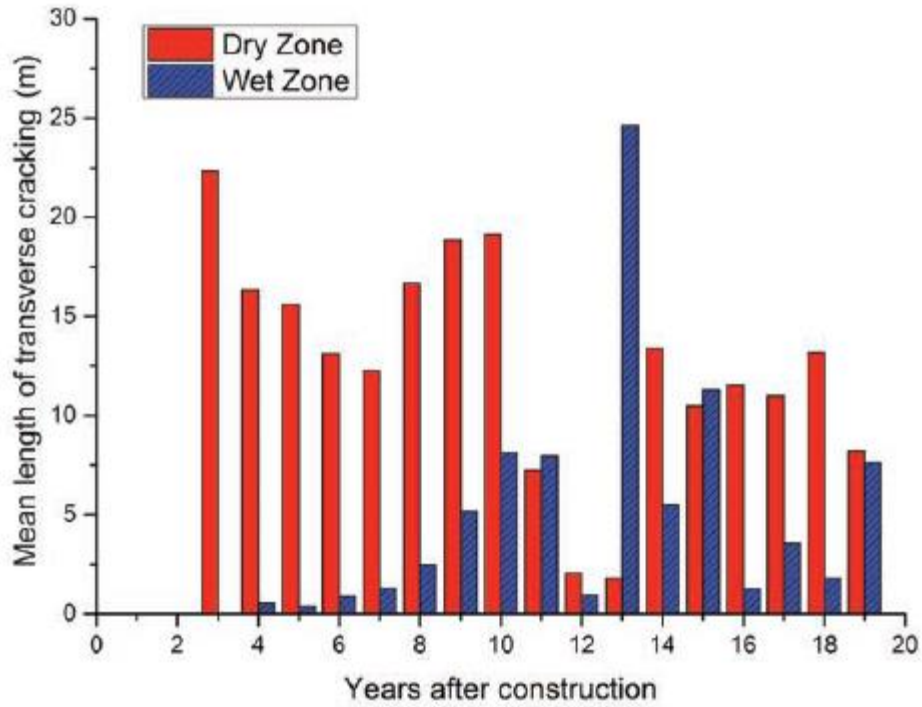


Figure 2-2. Mean crack length of transverse cracking per section for two climatic zones [20]

The SPS-2 sections had three different types of bases: dense-graded aggregate base (DGAB), lean concrete base (LCB), and permeable asphalt-treated base (PATB). Transverse and longitudinal cracking of concrete structures over LCB occurred faster and more extensively than in concrete sections over DGAB and PATB. Figure 2-3 shows the plot for transverse cracking, but a similar result was observed in longitudinal cracking.

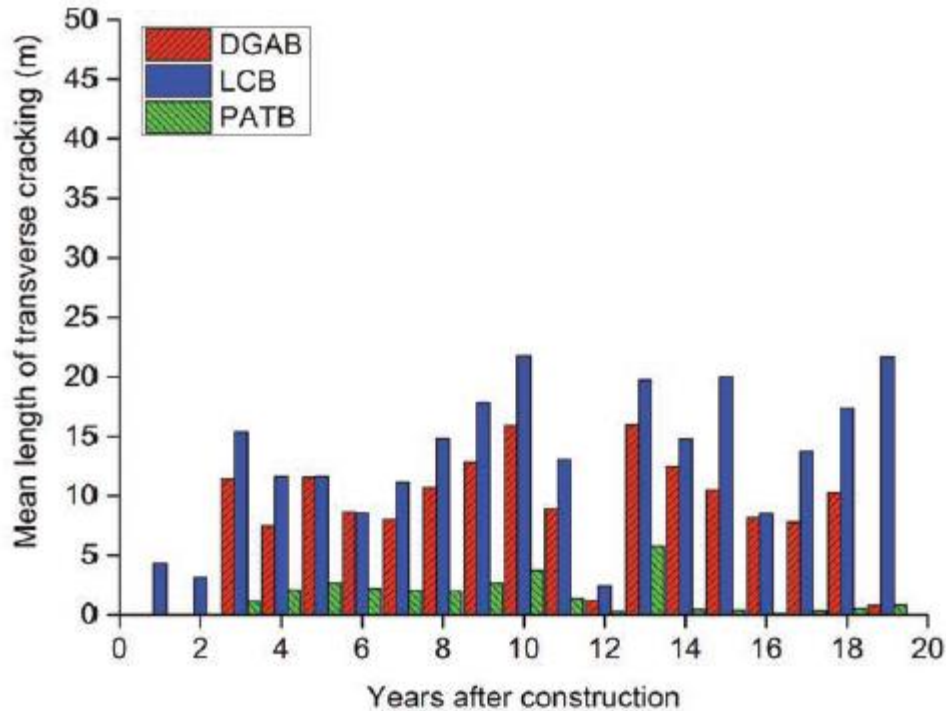


Figure 2-3. Mean transverse crack length per section over time for three different base types [20]

The University of California Pavement Research Center (UCPRC) built a real-scale bonded SJPCP-COA test track [21]. It was suspected that bonding between the two layers would be critical for the performance of the pavement test sections. Therefore, different materials and interphase conditions were analyzed at the test track, and extensive laboratory testing was performed. The analyzed variables were the following:

- Concrete: type II/V, type II/V with lightweight aggregate, type III, and CSA.
- Asphalt layer: old HMA and a new rubberized gap-graded mix (RHMA-G).
- Interphase preparation: sweeping, milling, and micromilling.
- Concrete slab size: 1.8 x 1.8 m, 2.4 x 2.4 m, and 3.6 x 3.6 m (6 x 6 ft, 8 x 8 ft, and 12 x 12 ft).
- Concrete slab thickness: 115 and 152.4 mm (4.5 and 6 in.).

- Asphalt thickness: 61 and 120 mm (2.4 and 4.7 in.).

The heavy vehicle simulator (HVS) report [14] contains strain measurements for the different sections that were tested. The results for section J are shown in Figure 2-4. This section had 3.6 x 3.6 m (12 x 12 ft) slabs with type II/V concrete, and it was tested for approximately 375,000 repetitions. A dual wheel applied the load, and the repetitions were distributed in the following way: 15,000 repetitions of 40 kN (9,000 lbf) in dry condition, 15,000 repetitions of 60 kN (13,500 lbf) in dry condition, 70,000 repetitions of 80 kN (18,000 lbf) in dry condition, 70,000 repetitions of 80 kN (18,000 lbf) in wet condition, 70,000 repetitions of 100 kN (22,500 lbf) in wet condition, and 135,000 repetitions of 100 kN (22,500 lbf) in wet condition. Such loading sequence can be observed in Figure 2-5.

Figure 2-4 shows the measured strains under traffic loads at three different depths in the SJPCP-COA structure through the testing period. The black dots correspond to measurements at the bottom of the rubberized asphalt mix, the solid green dots correspond to the measurements at the bottom of the PCC, and the green and white dots correspond to the strains at the top of the PCC. The plot suggests that bonding was not adequately achieved during the construction. The lack of adequate bonding can be seen from the fact that the strain at the bottom of the asphalt layer (black dots) is almost the same as the strain at the bottom of the PCC slab (green solid dots). The bottom of the asphalt layer should show more tension than the bottom of the PCC slab since the whole section would be bending as a composite under an ideal bonded scenario. Another aspect that can be observed is that around 250,000 repetitions, the bond started to deteriorate at a faster rate, and the asphalt strain curve decreased drastically, showing less than a third of the tensile strain recorded at the bottom of the PCC.

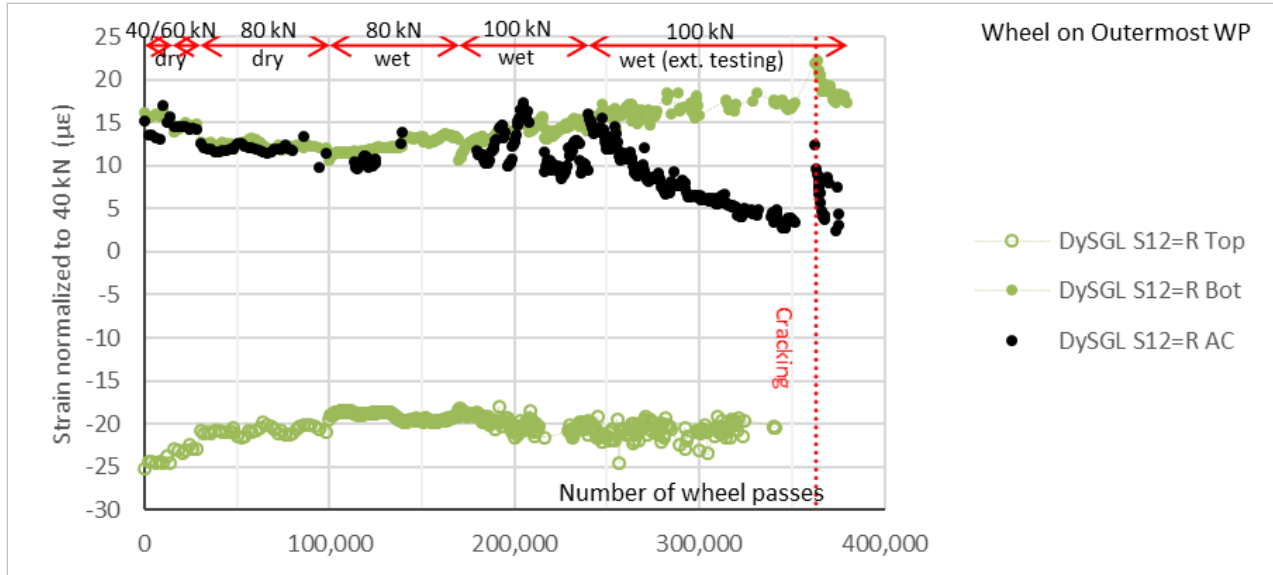
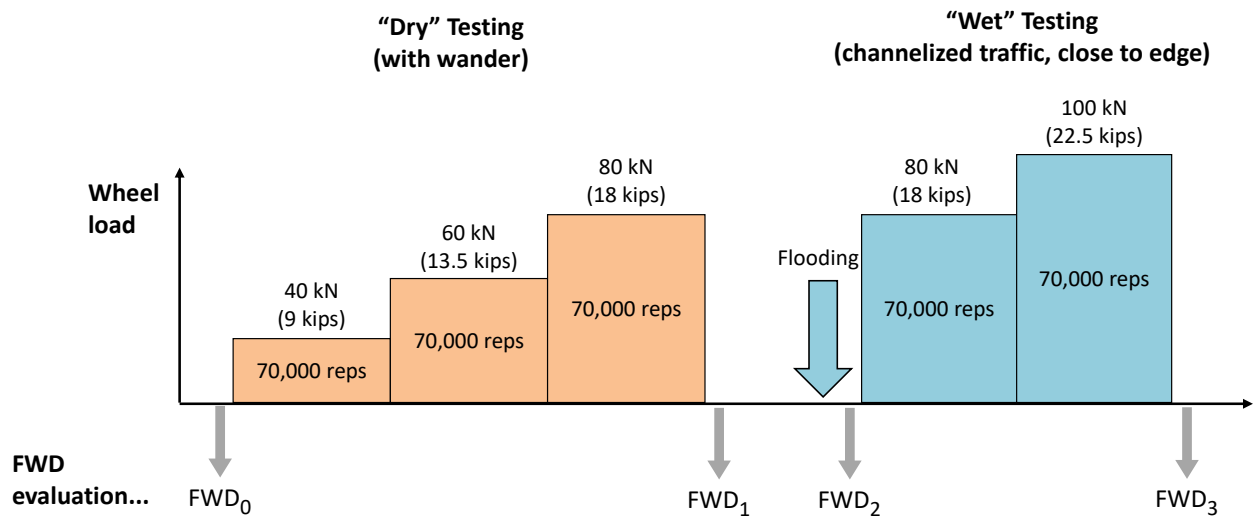


Figure 2-4. Strain measurements in HVS test section [14]



During HVS Testing:

- Continuous recording of the structural response (response under the HVS wheel)
- Periodic surveys during HVS maintenance halts

Figure 2-5. HVS testing plan [14]

Various laboratory tests were also performed on composite specimens. Tests included shear fatigue, shear stiffness, tensile creep, and tensile strength. Two different temperatures, 25 and 40 °C (77 and 104 °F), and two moisture conditions, wet and dry, were analyzed. Both water

conditioning and temperature tend to reduce the strength of the composite specimens as can be observed in Figure 2-6 and Figure 2-7. The results shown in Figure 2-6 are for the tensile strength of multiple specimens: three specimens at a temperature of 25 °C (77 °F) and dry condition, one specimen at 25 °C (77 °F) and wet condition, and two specimens at a temperature of 40 °C (104 °F) and dry condition. All the specimens were made with Type II/V cement placed on top of a gap-graded rubberized hot mix asphalt (RHMA-G). It can be observed that the addition of water caused a drop of approximately 33 percent of the strength, and the increase in temperature caused a drop of 80 percent. Figure 2-7 summarizes the results of the frequency sweep test performed in the same type of structure as mentioned in the previous test. Three temperatures were used so the shear master curve could be calculated when doing the test under dry conditions. Under wet conditions, it was only performed at 25 °C (77 °F) since it was only intended to get a direct comparison at one temperature. Besides, moisture-conditioned specimens become weaker, and it is more difficult to handle them; increasing the testing temperatures would have probably resulted in the failure of the specimen even before testing. Moisture conditioning of the specimens also caused a reduction in the dynamic shear modulus, similar to the reduction mentioned previously on the tensile strength.

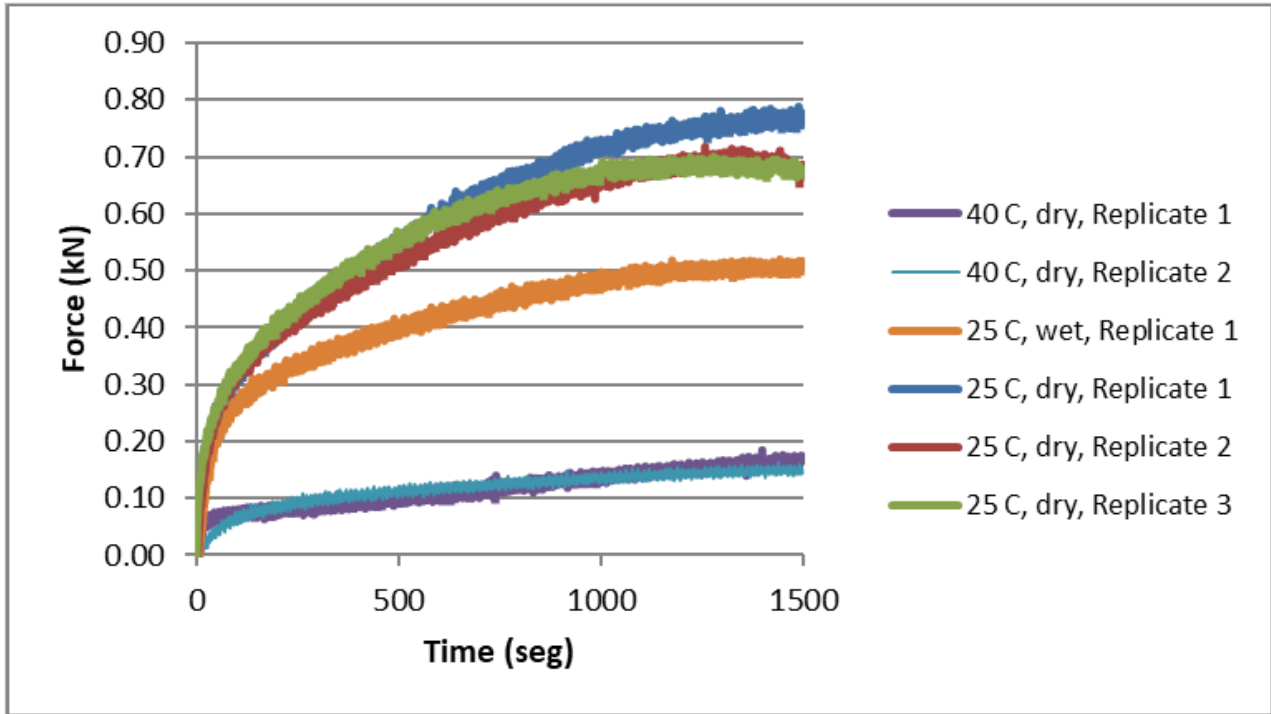


Figure 2-6. Tensile strength test of composite specimens

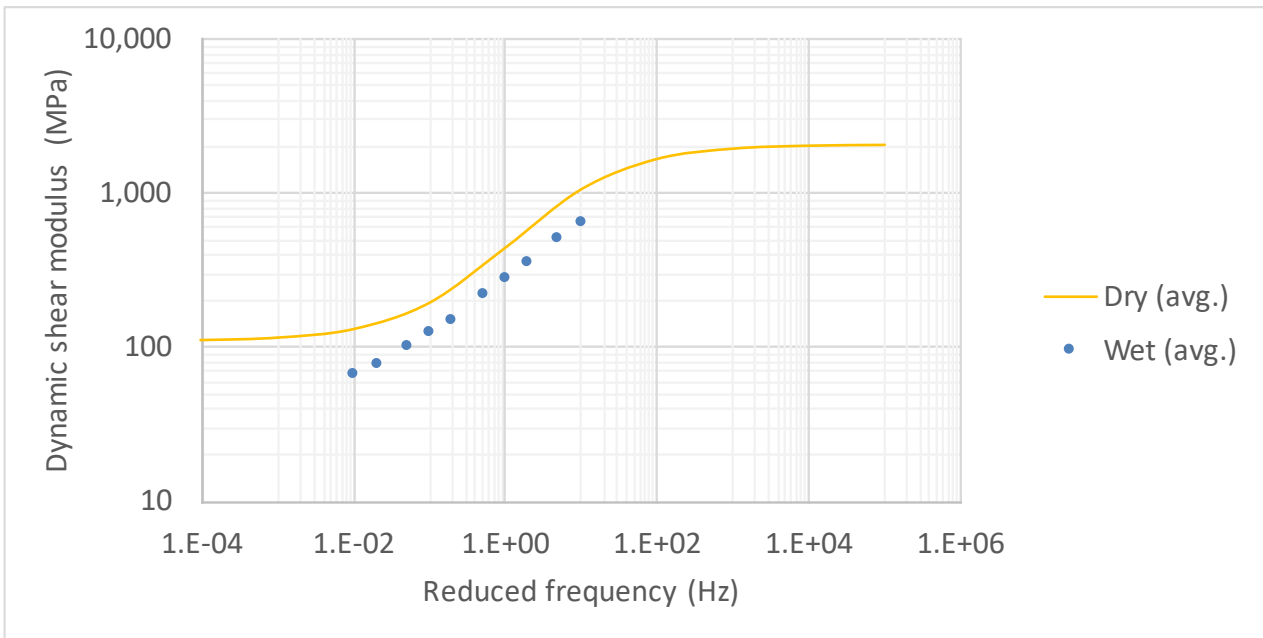


Figure 2-7. Frequency sweep test of composite specimens

2.2 Distress Mechanisms

Pavement structures are exposed constantly to traffic and environmental loads. Environmental loads are those related to changes in humidity and temperature and can produce an important impact on the structure. These loads would tend to curl up or down the corners of the concrete slab, increasing the debonding susceptibility. According to Pouteau et al. (2002) [22], the weakest section of the bond occurs near the shrinkage cracks in the PCC slab where the higher stress concentration is happening. From previous experience in the UCPRC [23], high differential drying shrinkage was measured at the corners of the concrete slabs, as shown in Figure 2-8. Such loading produced deterioration in both the slab and the interphase due to the upward movement of the concrete slabs in the corners. This movement caused the interphase to be in tension, and the tensile strength of the interphase was much lower than its compressive strength. The differential shrinkage in the slabs was obtained by subtracting the measurements of the bottom strain gage to the top strain gage.

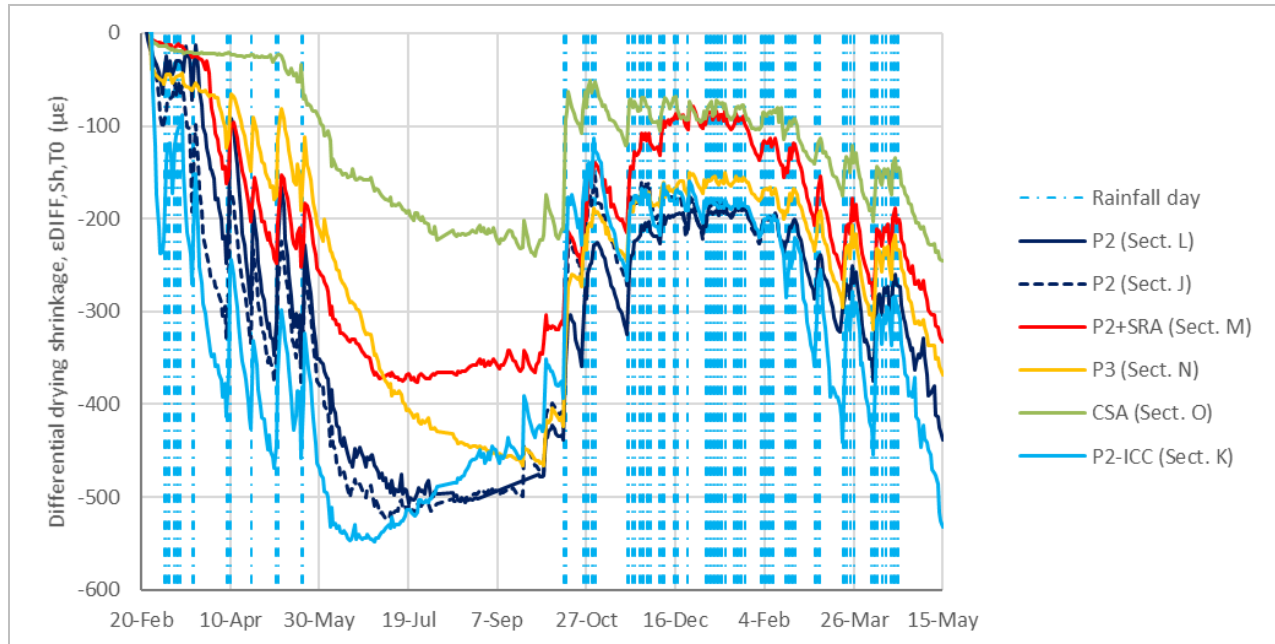
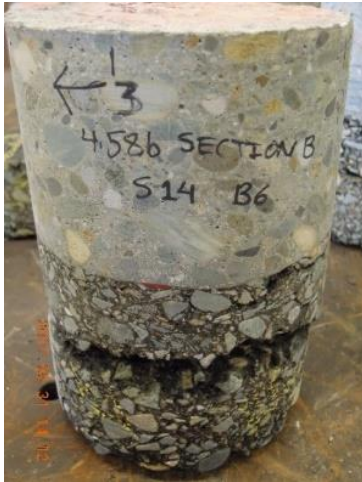


Figure 2-8. Differential drying shrinkage in SJPCP-COA slabs at the corners [23]

The bonding condition of the test sections was analyzed by extracting cores after the HVS testing was performed [14]. Approximately ten cores were extracted from each of the sections, and the bonding condition and distress mechanisms are summarized as follows:

- Asphalt-asphalt debonding between lifts in sections that were built on top of an old asphalt layer, which was built in two lifts, while it did not happen in sections built on top of a new RHMA-G.
- Asphalt crushing/debonding at the corners of the structures done with HMA and RHMA-G.
- Asphalt cracking below transverse joints of the concrete was observed only in sections built on top of old HMA.
- Asphalt failure along the perimeter of all the slabs, the asphalt delamination was found to reach between 150 and 450 mm (6 to 18 in.) from the edge.

Figure 2-9 shows extracted unbonded cores for each of the distresses previously mentioned. Damage mechanisms cause the structures to fail under different distresses such as: corner cracking, mid-slab cracking, joint faulting, and joint spalling [24, 25].



a) Asphalt-asphalt debonding



b) Asphalt crushing / debonding at corners



c) Asphalt cracking below the transverse joint



d) Band delamination around 3.6 x 3.6 m (12 x 12 ft) slab perimeter



e) Asphalt surface damage after the milling process



f) Weak bonding to micromilled asphalt

Figure 2-9. SJPCP-COA common distresses

The distresses observed above are due to the combination of traffic and environmental loads in most of the cases since the cores were only extracted from sections in which the HVS had been

performed. Asphalt cracking below the transverse joint likely occurred due to only environmental loads before the sections were tested under traffic loading, but there was no record of it. Asphalt cracking below the transverse joint happened due to the shear strains caused by the expansion and contraction of the concrete slab. All the other distresses are likely to have occurred due to a combination of tensile and shear strains and stresses in the structures.

2.3 Properties of the Materials

Heath [26] investigated shrinkage and thermal cracking of fast-setting hydraulic cement concrete pavement in Palmdale, California. Concrete thickness was an analysis variable, one section was built for each of the following thicknesses: 100, 150, and 200 mm. The sections were instrumented with thermocouples, strain gages, and joint displacement measuring devices. The authors concluded that the initial strain in the slab was likely due to thermal contraction of the concrete after construction. The increase of strains at the top of the structure after two months was the result of drying shrinkage and not thermal contraction anymore. The stresses caused by the combination of the drying shrinkage and the night-time temperature gradients exceeded the concrete strength and caused transverse cracking. Laboratory testing was performed to study the stress and stiffness properties additionally to the field slabs.

Different studies [14, 21 and 26] suggest the importance of analyzing the strength and stiffness properties of the pavement structures. Section 2.4 summarizes the available testing methodologies found in the literature and Table 2-1 summarizes the properties of interest for each type of material under different loading conditions and how to potentially measure such properties.

Table 2-1. Initial testing protocol

Property	Tests		
	Asphalt-Treated Base	Cement-Treated Base	Bonding of Composite Specimens
Stiffness under rapid loading	Dynamic Modulus	Modulus of Elasticity	Dynamic Modulus
Stiffness under slow loading	Not available	Modulus of Elasticity	Not available
Creep compliance	Not available	Not required	Not available
Capacity to deform under slow loading	Not available	Not required	Not available
Fatigue life	Not available	Not required	Not available
Erosion resistance	Raveling test with water conditioning	Raveling test with water conditioning	Raveling test with water conditioning
Early-age rutting/raveling resistance	Not available	Not required	Not required
Resistance to water-induced damage	Dry and post-conditioning test	Not required	Dry and post-conditioning test

Testing frameworks for measuring the properties that were labeled as “Not available” will have to be determined from the literature review (Section 2.4) or be developed under this research framework. Those listed as “Not required” are based on previous experience and due to material properties, but the condition can be changed during the research project.

2.4 Testing

2.4.1 Laboratory testing

Brand and Roesler (2017) [27, 28] worked with several chemical oxidative treatments to determine the effects on the interfacial cement-asphalt bond in concrete mixes made with reclaimed asphalt pavement (RAP) aggregates, not concrete placed on asphalt. The first part of the research [27] focused on the interfacial transition zone (ITZ), which is defined as a region with

a thickness of around 50 μm that surrounds the aggregate. The ITZ is characterized by its higher porosity, lower density, lower calcium silica hydrate (C-S-H) content, lower unhydrated cement content, larger calcium hydroxide (CH) crystals, and higher ettringite content relative to the bulk paste [27, 29]. Samples with and without RAP were prepared and analyzed with a high-definition microscope in which each pixel measured 0.2 x 0.2 μm . The major finding consisted of a higher porosity content and larger ITZ within the samples prepared with RAP aggregates. These factors caused reductions in the concrete strength and modulus when compared against samples without the addition of RAP. The hypothesis tested in the second part of the research [28] was that the interfacial bond energy between the asphalt and cement could be improved by chemical interaction after pre-treating or pre-activating the aggregates. The procedures followed were soaking RAP samples in chemical substances or adding chemical substances to the concrete at the time of mixing. The chemical additives were chosen based on the ability to oxidize the asphalt since it was hypothesized that an oxidized asphalt would bond better with inorganic cementitious materials. Some of the chemical substances used to soak RAP aggregate for 15 minutes were HNO_3 , H_2SO_4 , HF, and NaOH, while HCl, H_2O_2 , and chromic acid were mixed in the concrete. Testing of surface free energy was done to analyze if the treatment improved the strength and dynamic modulus properties. Hydrochloric acid (HCl), maleic anhydride, chromic acid, and nitric acid (HNO_3) increased the theoretical interfacial bond energy between asphalt and cement, which proved the hypothesis that the interfacial bond energy between the asphalt and cement can be improved by chemical interaction. Besides Brand and Roesler [27, 28], no other source has been found that analyzes the possible chemical bond between asphalt and concrete. Even though it provides valuable information on how to chemically improve the bonding between the

asphalt and the cement, adding chemical solutions to the mix or soaking the aggregates before mixing is unrealistic to implement in real life in field projects.

An investigation of the failure behavior of concrete-asphalt specimens was performed at the University of Rhode Island [30]. The author, as well as previous research done [31], expected that the combination of imperfect construction and load application would contribute to interfacial debonding and cracking between the two materials. Uniaxial tension mode test and mixed mode tension test were performed on prismatic composite specimens, Figure 2-10 shows a specimen for uniaxial tension. The difference between the uniaxial tension mode test and the mixed mode test is the orientation of the crack, instead of having a horizontal interphase, the interphase is at a 30° angle in the specimens tested under the mixed mode test. The specimen preparation included the addition of teflon tape to the asphalt surface to create an interfacial crack of desired size. It was found that the failure initiated at the pre-built crack and the crack normally propagated into the asphalt material in the uniaxial tension mode test at 20 °C (68 °F), which indicates that the interphase is somewhat stronger than the asphalt itself. Two conclusions were drawn after testing specimens at two different ages under the uniaxial test: the crack propagation path comes closer to the interphase in older specimens, and the strength measured at 200 days was approximately twice that of the one measured at 30 days. The idea behind performing a test with an interphase at a 30° angle was to replicate the shear load component that happens in the field due to the acceleration and stopping forces that vehicles can cause to the structure. For the mixed mode tension test, the first crack was also usually in the asphalt near the surface, but the second crack propagated deeper into the asphalt due to non-symmetric specimens. The non-symmetric condition caused the interphases to have smaller deformations than those obtained

in the uniaxial tension test. The total deformation decreased from approximately 4.6 to 1.25 mm (0.18 to 0.05 in.) when analyzing the mix mode scenario.

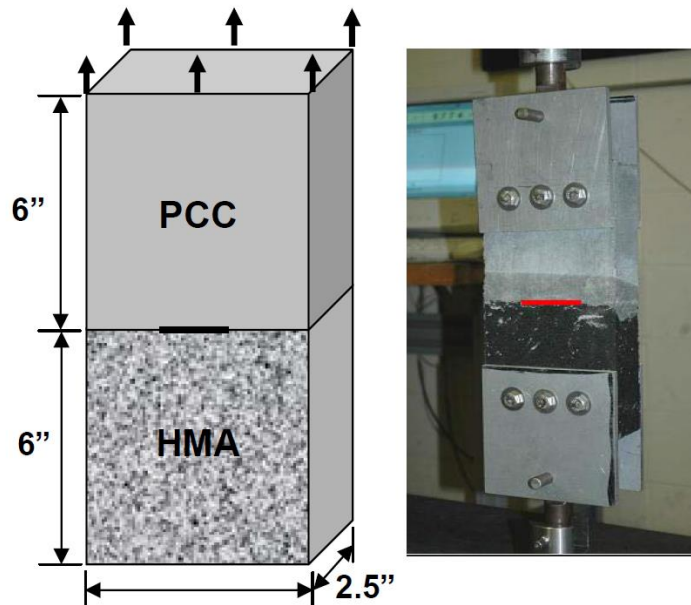


Figure 2-10. Sample specimen and test layout of modified tensile experiment [30]

In his doctoral thesis [32], Feng Mu investigated the interphase debonding of composite specimens and the effects that it has on the critical stresses of the overlay. Current SPCP-COA design procedures only allow one of two options: 1) bonded or 2) debonded [33, 34], although it is known that the bonding will vary over time. Instead, an adjustment factor is included to account for the debonding when calculating the fatigue damage of the structure. Wedge splitting tests (WST) of composite specimens were conducted based on the hypothesis that mode I failure (tension) would be the most critical condition in the SJPCP-COA structure. Figure 2-11 shows the equipment and a test sample used in the WST. Surface preparation and notch depth were the two main variables analyzed. The depth of the notch starter varied from 9 to 43 mm (0.35 to 1.70 in.) among the tested specimens, and two asphalt surfaces were included in the study: milled and

unmilled HMA. The author found that the performance of the bond is directly related to the surface preparation of the asphalt layer. It was determined that milled surfaces would tend to have better bonding based on the WST, in which the milled specimens had a greater splitting force than the unmilled specimens. A summary of the results obtained for two milled and two unmilled samples tested at a loading rate of 0.5mm/min (0.02 in./mm) is shown in Figure 2-12.

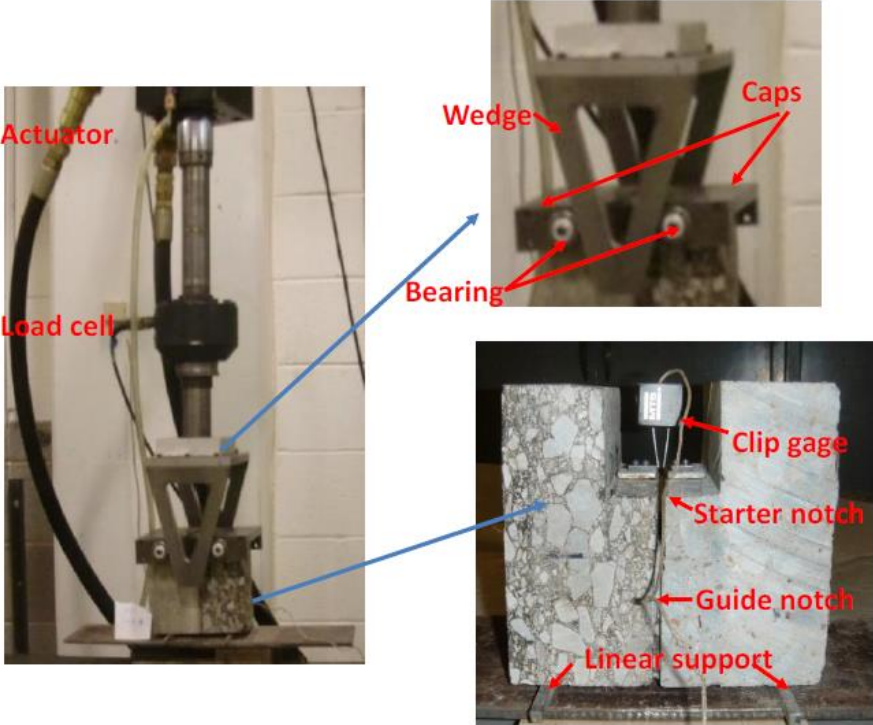


Figure 2-11. WST test set up and specimen [32]

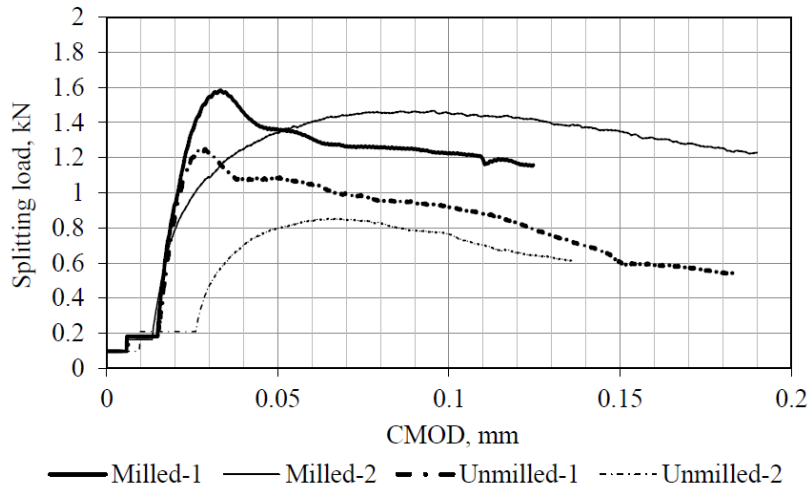


Figure 2-12. Load-displacement curves of wedge splitting test [32]

The Center for Transportation Research at the University of Texas at Austin [35] researched techniques and procedures for bonded concrete overlays. Several methods were proposed for quality assurance of composite pavement projects, some of them being field tests and other laboratory tests. The suggested laboratory test for checking the strength of the bond is based on ASTM C 1042, which is a standard test used to determine the strength of epoxies used with concrete. The specimens have the interphase at a 30° angle like what was done by Sadd [30], but with the difference that this is a cylindrical specimen. The direction of loading is another difference, in this case, the load is applied in compression, and it is expected to have the specimen fail along the interphase or close to it. A destructive field test was also suggested to evaluate the bonding in situ. The procedure consisted of drilling to extract a core but stopping the coring process slightly under the interphase depth. A circular steel plate was then glued to the top of the core, and this was where the tensile force was applied by means of a hydraulic or mechanical device to cause a failure in the asphalt layer or at the interphase. Figure 2-13 shows the schematic of the pull-off test. Lastly, a non-destructive way of evaluating the integrity and

bonding condition of the structure can be performed by using an impact echo, which is a device that uses mechanical waves that travel through the structure, and a signal transducer will capture the reflected waves in the surface. The depth at which the discontinuities happen can be calculated from the speed of the waves and how much time it takes the waves to get back to the signal transducer.

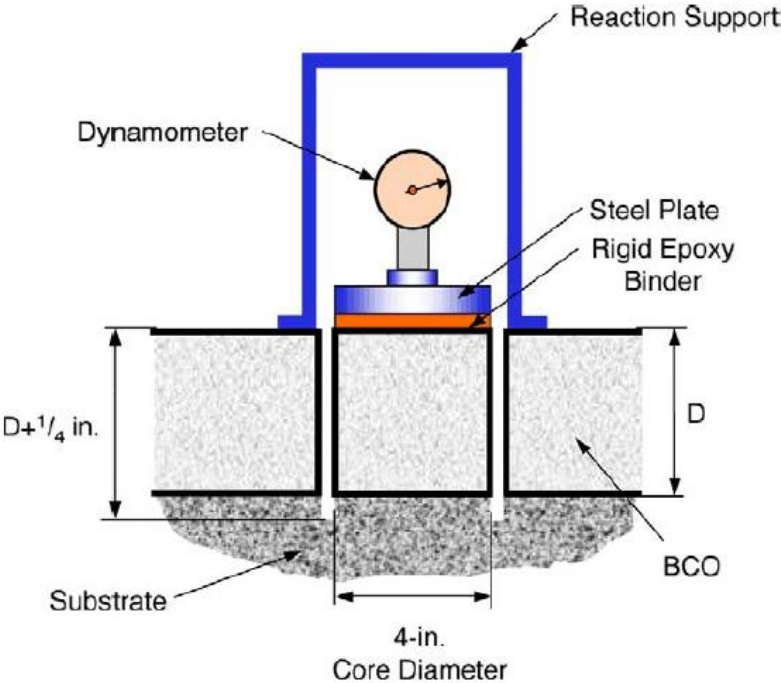


Figure 2-13. Pull-off test schematic [35]

2.4.2 Field testing

Cable J et al. (2001) [36] investigated the interphase bonding condition of concrete overlays over time. Different AC surface preparation treatments, such as milling, patch-only cold in-place recycling (CIPR), PCC thickness, synthetic fiber reinforcement usage, and joint spacing, were analyzed. The sections were instrumented with thermocouples, and strain gages at the

interphase. Immediately after the construction, all the test sections were bonded. The research approach consisted of monitoring strain and temperature data from the sensors, falling weight deflectometer (FWD) tests, direct shear strength of extracted cores, and visual distress inspection. Shear strength testing (IOWA 406-C) was done to measure the interphase bond over 3 and 5 years quantitatively. The cores were extracted from slabs in the outer wheel path in each of the sections. It was found that milled surfaces did better than patch only and CIPR and that a high percentage of cores failed in the AC approximately one inch below the interphase, indicating that the AC is often weaker than the interphase. The strength of the cores failing at the interphase was about 2 to 3 times more than the strength of similar cores failing in the asphalt layer. This behavior was observed at 3 and 5 years, meaning that the bond relationship with surface preparation is retained over the evaluation period of 5 years. The shear strength test data suggests that the interphase strength tends to increase with time while the asphalt strength tends to decrease, as can be seen in Figure 2-14. Based on the findings, a fundamental theory for bonding and bonding degradation was not developed.

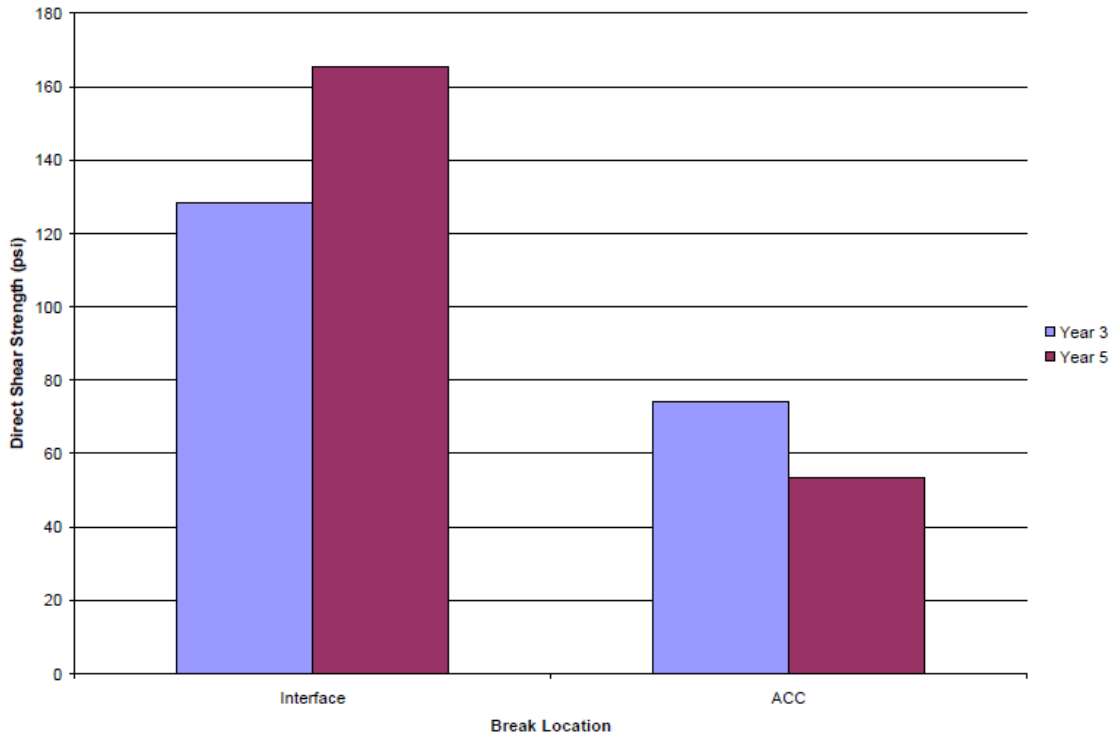


Figure 2-14. Average shear strength at different break locations [36]

A full-scale accelerated pavement test on SJPCP-COA was conducted in France [37]. The equipment used was the FABAC fatigue device, shown in Figure 2-15, that applies the load along 2 m (6.56 ft) of test track without lateral wandering. One million cycles were applied in each of the nine sections, and cores were extracted at the end of the test to analyze the bonding condition of the pavement structure visually. Three variables were analyzed: temperature conditions, wheel position, and interphase treatments. The range of temperatures for the experiment was from 5 to 30 °C (41 to 86 °F), depending on the season. Three interphases were analyzed: shot blasted, delaminated interphase, and no treatment. Temperature and wheel position were the variables that had a more severe effect on the bonding life of the composite pavement. It was observed that there was more damage near the slab joints when the

temperature was the maximum, and the most critical loading position was when the load was placed near the joint. Even though surface preparation did not provide much difference, it was established by the authors that a shot-blasted surface could stop and delay the debonding of the structure, mostly during higher temperatures. Laboratory testing of composite specimens was also carried out to determine which structure combination provides the best bonding between both layers. The laboratory experiments performed previously by Pouteau [38] also concluded that a shot-blasted asphalt layer could prevent and delay de-debonding in the structure, similar to what was found in the full-scale testing. No theory was formulated regarding factors that improve or deteriorate bonding, although recommendations were provided.

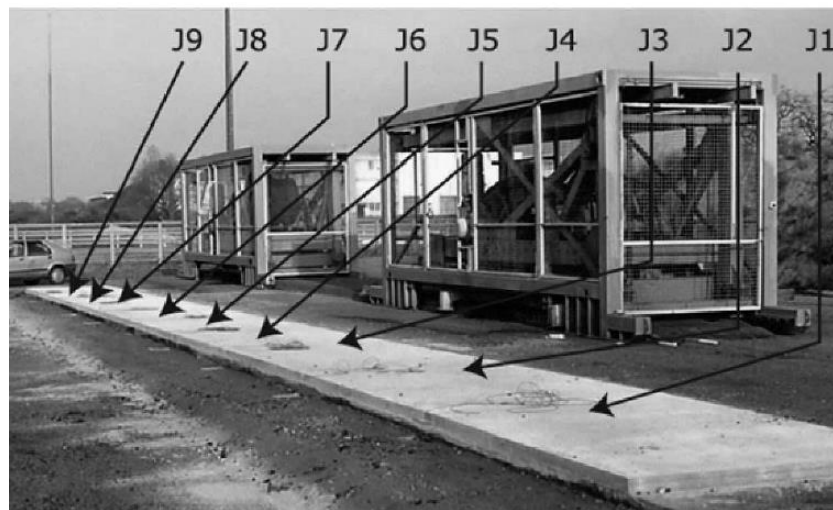


Figure 2-15. FABAC fatigue device and test sections [37]

The Louisiana Transportation Research Center [39] evaluated SJPCP-COA under accelerated loading. Three test sections with varying concrete thickness of 50, 100, and 150 mm (2, 4, and 6 in.) were analyzed. All sections had a 75 mm (3 in.) asphalt layer over 212.5 mm (8.5 in.) crushed stone, and 250 mm (10 in.) cemented treated base. The sections were evaluated with an

ATLaS30, which is a heavy load simulator with a dual wheel load, and as expected, the thicker the concrete slab, the longer the pavement life. It was found that most load-induced cracks happened along the wheel path after the accelerated pavement test was performed. In-situ bond strength tests were performed in all three sections in both loaded and unloaded areas using a PROCEQ tensile bond device tester (pull-off test). The testing procedure followed in this project is the same as the one that was followed by Trevino [35]. The primary conclusion drawn from the pull-off test corresponds to a strength decrease between 33-60 percent when comparing the strength of loaded areas to unloaded areas in which the thinner sections have a higher decrease. An additional forensic trench analysis was done in each of the sections in which a transverse trench slab of 1.2 to 0.3 m (4 ft x 1 ft) was extracted. The major conclusions after the visual inspections were:

- Majority of cracks are bottom-up cracking.
- All concrete joints were deployed along the PCC thickness.
- The trench slab came out with the concrete bonded to the asphalt completely.

The UCPRC did a three-year study of SJPCP-COA structures [14, 21, 23] to develop improved guidelines and designs for bonded concrete overlay on asphalt. A total number of 15 test sections were built with 560 sensors, primarily embedded in the concrete, for tracking the structure responses to environmental and traffic loading. The instrumentation included dynamic strain gages, static strain gages, moisture sensors, thermocouples, relative humidity sensors, interphase opening measuring devices (IOMD), and joint displacement measuring devices (JDMD). Unrestrained shrinkage beams were also cast and kept next to the pavement structure to be exposed to the same environmental conditions as the test track. The moisture-related

shrinkage of the unrestrained beams and the differential drying shrinkage of the concrete slabs showed high values; nonetheless, there were no cracks under environmental loads. Moisture-related shrinkage values of up to $800 \mu\epsilon$ were measured, as can be seen in Figure 2-16. The concrete type that showed the highest values is conventional type II/V portland cement. Internal curing concrete (ICC) and shrinkage-reducing admixtures (SRA) had a positive effect of reducing the total amount of shrinkage, as can be seen in the light blue and red curves, respectively.

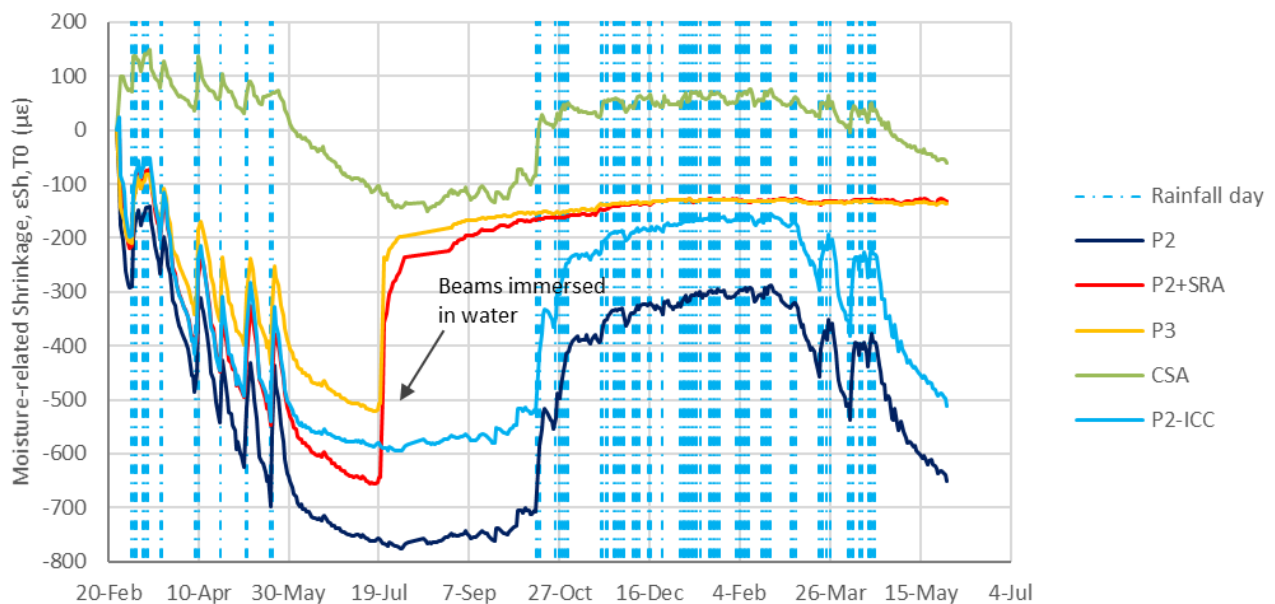
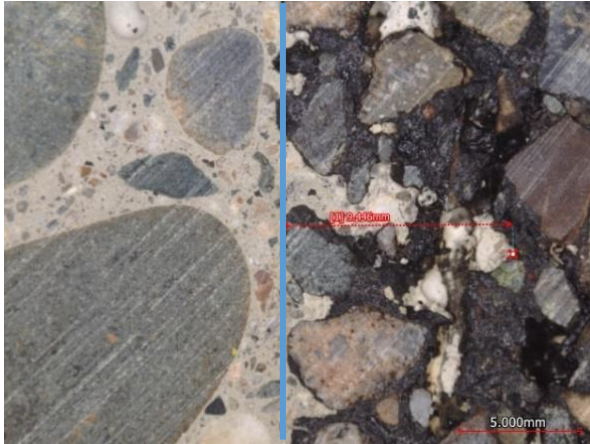


Figure 2-16. Moisture-related shrinkage in the unrestrained shrinkage beams [23]

Strain gages at two different concrete depths were placed to capture the curling and warping movements of the concrete slabs. Differential shrinkage, the difference in strain between the top and bottom of the slab, of concrete test slabs presented values in the same order of magnitude as was presented in Figure 2-8. Type II/V portland cement slabs presented one of the highest shrinkage values, and the internal curing concrete did not provide any reduction similarly to what was observed in the unrestrained shrinkage beams. The results from Figure 2-8 and Figure 2-16

are of great importance for the bonding condition of the SJPCP-COA structures since it has been observed that the shrinkage will cause very high deformations to the concrete slab and the rate of damage to the bond between the concrete and the asphalt will be increased. Having shrinkage values like the ones shown above makes it hard to understand how the debonding changes in time and space within the slab. Therefore, tensile stresses in the slab will vary, and the performance of the structure is going to be affected by the change in the bonding condition.

When analyzing the different asphalt layers that were used, it was found that the RHMA-G base for the SJPCP-COA structure provided the best performance in these experiments, but one reason for such good behavior might have been the under-compaction of the layer. It was expected to have between 3-9 percent of air voids, and the actual obtained value was 11 percent. It was also found that the concrete slurry penetrated the base layer several millimeters, and it was checked with a 3D Measurement System Sensor. High-definition images were taken to thin composite specimens, which allowed the penetration depths to be measured. Having an RHMA-G as a base provided 2 to 5 times more penetration of the slurry into the base compared to conventional HMA, and two test results can be observed in Figure 2-17 which the penetration decreases from 9.45 mm to 2.29 mm (0.37 to 0.09 in.) when the base is changed from RHMA-G to milled old HMA. This is an important finding since having greater penetration of the concrete will result in better interlock and bonding conditions between both layers, but also, having higher air void content can negatively impact the performance of the RHMA-G layer and the whole structure.



a) CSA cement on top of RHMA-G, depth of penetration of 9.45 mm (0.37 in.).



b) Type II/V cement on top of milled HMA, depth of penetration of 2.29 mm (0.09 in.).

Figure 2-17. Scanner images for concrete penetration analysis

2.5 Composite Pavement Design

Pavement ME and BCOA-ME are the two SJPCP-COA most used design software for composite structures. Although the two software are widely used, there are some restrictions and limitations. Neither design mechanism takes into consideration specific properties of the asphalt material, such as viscoelasticity, flow capacity, and creep. The existing HMA layer is assigned a damaged dynamic modulus that corresponds to 65 percent of the original value after 30 sections were analyzed [40]. Additionally, both design procedures were initially designed not to allow for the partial bond condition since there is no debonding model for SJPCP-COA structures. Pavement ME did not consider gradual changes in bond or built-in curl over the pavement service life and the influence of these changes on pavement performance [41]. BCOA-ME considers that the structures are always bonded by providing full contact friction between both layers. It assumes that the PCC slabs and HMA layer work as a composite slab, even though it is understood that the bonding will tend to deteriorate with time [12].

Khazanovich and Tompkins (2017) [41] in the National Cooperative Highway Research Program (NCHRP) Report 01-51 introduced a simplified friction deterioration model in the JPCP transverse cracking model that accounts for partial bonding conditions between the slab and the base on a monthly basis. The deterioration model is based on the coefficient of friction (Λ) between the slabs and the base layer, which is converted into the non-dimensional coefficient of friction (Λ^*). The model requires the input of the initial non-dimensional friction (L^*) and a friction degradation parameter (C_f) to calculate the monthly values of non-dimensional friction. The modified JPCP transverse cracking model was able to adequately predict the percentage of slabs cracked transversely, as can be seen in Figure 2-18. In this case, two different initial non-dimensional frictions were used, but the dimensional friction increase from 0.1 to 1,000 was not able to predict the cracking observed. Overall, the prediction of some level of cracking, even though highly dependent on the dimensional friction, is an improvement when compared to AASHTO M-E design software that predicts no cracking over the entire design life of a structure.

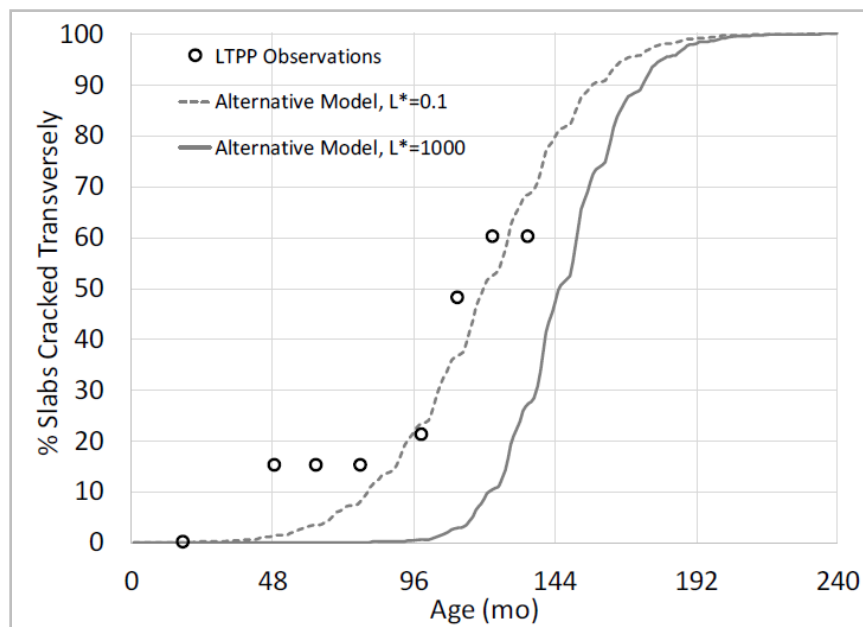


Figure 2-18. Cracked slabs prediction [41]

2.6 Summary of Findings from Literature Review

Nature of bonding

- The nature can be due to mechanical or chemical processes, but no theory explains the bonding. Up to date, only one source was found that analyzed the chemical bonding, and it was established that chemical oxidative processes with certain substances could slightly improve the interfacial bond energy between concrete mortar and asphalt due to physicochemical interaction. Application of chemical compounds to the aggregates or mixes in real life is not likely to occur; hence, it will not be studied in this research.

Surface preparation

- Different surface treatments can be applied to the old HMA and new RHMA-G layers prior to casting the PCC slabs, but how to consistently obtain good bonding and how to measure the bonding has not been determined. Old HMA sections seem to perform better after milling is done, while it has been found that milling has an adverse effect on new RHMA-G sections

Effects of loading on bond stresses

- Environmental and traffic loads will tend to deteriorate the bonding condition of a composite structure. Temperature and wheel position are critical variables that will also deteriorate the bonding condition of a composite structure.
- The evolution of bonding with time and space under traffic and environmental loads is not clear. But it is a fact that older structures will tend to have more debonding, and the perimeter of the slabs is most likely going to be the most deteriorated zone.

- There is no framework for understanding the debonding processes occurring in the pavement structures and how it affect the performance, only the beginning of models.

Effects of water and temperature on bonding condition

- Based on laboratory and field data, asphalt concrete strength is often weaker than the interphase bond strength, and the strength decreases with increases in temperature and the presence of water in the pavement structure or test specimens. The age of the structure has been found to affect the bonding condition in some cases but not in others.

Other findings

- An ideal base for concrete pavements would behave stiff under traffic loading but behave soft under environmental loading, enabling it to handle both load types properly.
- JPCP over LCB has been determined to have up to 2.8 times more cracking than JPCP over HMA.
- Interphase performance and behavior of the bond are not fully understood and do not show consistent results through time and space and between projects, which causes a loss of functionality and a decrease in the ride quality for the users.
- Current bonded SJPCP-COA design procedures do not allow partially bonded slabs, and no debonding model exists for these structures.
- Design methods do not account for the viscoelastic nature of the asphalt base and the interphase, and there are no degradation models under traffic and environmental loading.

- Multiple SJPCP-COA sections and laboratory testing have been performed, but no theory or framework has been developed regarding bonding and bonding degradation and how these affect the pavement distresses and deterioration of the structure.

2.7 Problem Statement

There is a considerable lack of knowledge in the literature regarding the role and performance of the slab/base interaction, including the bonding of concrete on top of asphalt layers, which results in not having specified an ideal base for concrete pavement. Pavement deterioration and a decrease in ride quality result from a lack of knowledge of the slab/base interaction. Besides, the design of SJPCP-COA and full-scale concrete pavement on asphalt bases does not consider the viscoelastic nature of the asphalt base and interphase, the flow and creep capacity of asphalt, and partial bonding is not allowed since there exists no debonding model.

It is also not known how to consistently get good bonding considering different surface preparations, base types, environmental variables, slab size, and traffic loads. Therefore, there is no well-developed procedure to evaluate base materials and bonding properties experimentally.

3. PROBLEM STATEMENT AND STUDY METHODOLOGY

3.1 Gaps and Questions to be Answered

Based on the literature review and previous experience in SJPCP-COA projects, it was observed that the literature regarding slab/base interactions and composite structures with concrete on top of asphalt is scarce. Hence, several gaps and questions about slab/base interactions for concrete pavements have been found, which will be answered in this study. The findings can be applicable to thinner concrete overlays as well as concrete pavements in general.

1. Determine a testing methodology based on available laboratory testing protocols to characterize the material and bonding properties of different structures.
 - i. Which are the available tests for asphalt materials to characterize them for use as a base for concrete pavements?
 - ii. Can the same tests be applicable to composite specimens?
2. Narrow down a testing protocol that enables material and bonding characterization with an efficient amount of effort and time.
 - i. Is there any set of tests that can characterize the material properties without having to do a full testing factorial?
 - ii. Can these tests be easily replicated by any other testing laboratory or agency?
3. The factors affecting the concrete bonding to asphalt mixes under traffic and environmental loading are not clear.
 - i. Which is the effect of temperature and humidity on the material and slab/base properties?

- ii. What variables control the material and slab/base properties?
- 4. Current bases for concrete pavements in California are limited to HMA and LCB.
 - i. What is the performance of the currently allowed bases?
 - ii. Is there any other base material or interlayer that can be used to increase the performance of concrete pavements?
- 5. Determine a modeling framework based on laboratory experiments
 - i. Can a FEM model explain SJPCP-COA performance?
 - ii. How does the debonding influence the performance of the SJPCP-COA under environmental and FWD loads?
- 6. Recommendations for materials or surface preparation of the asphalt layer that provide better bonding and work as an ideal base for concrete pavements is not available.
 - i. Based on laboratory testing, real-scale slabs, and modeling, which are the ideal base materials and/or surface preparation techniques for concrete structures?

3.2 Objectives and Tasks

Objectives, tasks, and deliverables are shown in the following table.

Table 3-1. Objectives and Tasks

<u>Objective</u>	<u>Task</u>	<u>Deliverable</u>
1) Develop a comprehensive literature review to understand the actual status of the topic	I) Synthesize what is desired in a base for concrete in terms of properties under different loading conditions II) Determine testing protocols performed in asphalt and composite specimens based on performance studies, distress mechanisms, and material properties	Summary of performance studies, distress mechanisms, material and base properties, testing, and composite pavement design
2) Determine testing methodologies that can be performed under this research project	III) Determine applicable tests and analysis procedures used for composite specimens and composite pavement structures	Detailed list of tests, equipment, and testing conditions to apply, as well as possible alternative tests
3) Analyze factors controlling and affecting the material integrity	IV) Testing of asphalt specimens produced with different materials and under various test conditions	Results of stiffness and strength material properties, and analysis and conclusions about the performance
4) Develop a testing protocol for composite specimens that can be replicated elsewhere	V) Determine a set of laboratory tests that enables materials and bonding characterization VI) Testing of asphalt and composite specimens under the new testing protocol	Set of laboratory tests easy to be performed by any other laboratory or agency, results, and analysis for two different composite structures
5) Characterize full-scale composite structure sections prepared with different bases and interlayers	VII) Instrumentation, construction, and long-term monitoring of four full-scale instrumented sections following current Caltrans designs and possible alternatives for improving rigid pavement performance VIII) Analysis of sensor data, additional testing performed, and forensic analysis	Documentation of instrumentation, construction, and performance of full-sized composite structures

<u>Objective</u>	<u>Task</u>	<u>Deliverable</u>
6) Develop a model that replicates laboratory tests and performance of full-scale slabs considering debonding	IX) By means of finite element method (FEM), replicate the behavior of specimens tested in the laboratory and estimate material properties to be used in pavement structure models X) Develop a complex viscoelastic model including damage properties to study the debonding process of composite pavement structures due to environmental loads XI) Develop a simplified elastic model with a predefined debonding level to study the loading results of composite structures with FWD	FEM models based on laboratory testing are able to replicate field slab behavior under environmental and FWD loads, analysis of results, and conclusions of how the debonding influences the performance
7) Recommendations and finalizing project	XII) Develop recommendations for implementation XIII) Dissertation writing	Dissertation with a chapter documenting all the recommendations

3.3 Structure and Content

The subsequent chapters of this dissertation are structured as follows:

- Chapter 4 discusses the laboratory testing methodologies used for composite specimens as well as the stress and strain levels at which the tests are performed. This chapter fulfills Task III and sets the testing framework required in Task IV. Different testing conditions are explained, and machine characteristics and limitations are covered. Additionally, the materials and mix designs used are described.
- Chapter 5 summarizes the testing results of asphalt materials that can be used as a base for concrete pavement. This chapter fulfills Task IV. The testing is focused on shear and tensile direction since it is considered to be the most representative of the type of stresses and strains that JPCP and SJPCP-COA structures are likely to experience on the field. A final recommendation of a reduced test factorial is provided.

- Chapter 6 describes the testing results using the reduced protocol for asphalt and composite specimens that was defined in Chapter 5. This chapter fulfills Tasks V and VI.
- Chapter 7 documents the instrumentation and construction of a full-scale test track. It provides results for the initial performance from data obtained from FWD tests and embedded sensors. This chapter fulfills Tasks VII and VIII.
- Chapter 8 documents the debonding framework based on laboratory testing and field data to replicate stress in the structures using FEM. This chapter fulfills Tasks IX, X, and XI. FEM was used to determine how the changes in stress due to debonding affect the performance of the structure.
- Chapter 9 summarizes the conclusions and recommendations and fulfills Tasks XII and XIII.

4. LABORATORY TESTING METHODOLOGIES

4.1 Goal and Objectives

The goal of this chapter is to understand the basic mechanics of the materials and interphase and characterize the engineering properties of asphalt, concrete, and interphases of different pavement structures under selected testing conditions that match the ranges expected to occur in the field. The testing conditions, such as temperature and frequency of loading, are based on modeling and field measurements from a full-scale laboratory test track. Laboratory tests were performed to simulate the interaction of these properties under complex field loading conditions, which is a combination of strain and stresses caused by environment and traffic loads, as was shown in Figure 1-6.

4.2 Introduction

Stresses and strains in the pavement structure depend on factors such as applied load, frequency and magnitude of the loads, loading location in the structure, temperature gradients, humidity gradients, and material properties such as the viscoelastic nature of the asphalt layer. The environmental and traffic loading on JPCP and SJPCP-COA pavements create complex stress/strain conditions in the slab/base and interphase, which includes tensile, shear, and compressive components. Since the cracking failure of asphaltic materials is controlled by tension and shear rather than compression, tensile and shear stresses/strains are the critical conditions for this analysis. Shear loading in the asphalt layer and the interphase between the asphalt and PCC is mainly caused by the expansion and contraction of the overlying PCC due to uniform temperature changes in the slab that the asphalt layer is bonded to, while tensile loading is

typically caused by the upward and downward movement of the PCC slab that the asphalt is bonded to, which are caused by vertical temperature and humidity gradients in the concrete slab. Such movements can be seen in Figure 4-1.

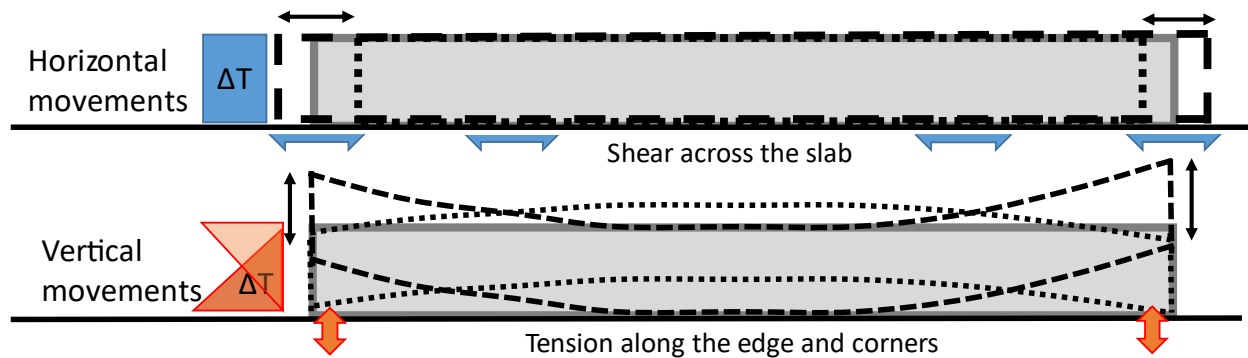


Figure 4-1. Concrete movements due to temperature variation (ΔT)

Consequently, tensile and shear laboratory tests were chosen to characterize the asphalt base materials and the bonding condition between the PCC and the asphalt, including the interphase between them. Compressive dynamic modulus was also performed to obtain the stiffness properties of the asphalt structures, which is an important design parameter and is required in the modeling of composite structures since it gives an idea of the embedment of the concrete as it compresses the asphalt. This test provides an important material property even though it was stated that compression is not the controlling cracking failure mechanism. The specimens were also tested under frequency sweep, creep, and ramp-type loading to characterize the properties that were stated in Table 2-1. Moisture susceptibility was analyzed using a cracking resistance test of dry and moisture-conditioned specimens. In addition to the tests mentioned above, four fatigue-applicable tests were determined under this research project to be useful for material and bonding characterization and are detailed in Appendix A. The tests are repeated load testing

to replicate traffic loads and short- and long-term environmental loads acting on the structure, shear and tensile tests are shown, but also a combined test, which includes the simultaneous application of shear and tensile loads.

4.3 Critical Field Conditions

Field stresses, temperatures, and frequencies of loading need to be estimated to understand better the field mechanisms shown in Figure 1-6 and be able to determine a testing protocol following the properties of interest shown in Table 2-1.

Caltrans maximum axle weight allowance corresponds to 89 kN (20,000 lbf), but the values are often higher than the maximum legal limits. The contact stress at the surface of the pavement can be in the range of 600 to 900 kPa (87 to 129 psi), depending on the tire configuration, tire pressure, and the magnitude of the load. Based on Mateos [14], it was observed a difference of up to 60 $\mu\epsilon$ between the top and bottom sections of the concrete slab during the application of an HVS on SJPCP-COA sections. The magnitude of the strain difference is directly related to the degree of bonding happening in the structure, the strain magnitude difference was more significant when the slab was properly bonded to the base and smaller when there was a lack or loss of bonding through testing.

Environmental loads had a more significant impact on the strain level at the concrete slab, as can be observed in Mateos [21]. The strain level depended on the time of the year, it was close to 500 $\mu\epsilon$ during the summer season and around 150 $\mu\epsilon$ during the winter season.

The frequency of loading depends on the type of load that is analyzed. While traffic loading has short loading times and many load applications, environmental loads have long loading times and

few load applications. Traffic loads can occur at a frequency of as much as 20 Hz depending on the truck speed and axle configuration, in which 20 Hz is assuming a speed of 105 km/h (65 mph) and an axle spacing of 1.5 m (5 ft). Environment loads occur on daily and yearly variations. Daily changes correspond to a frequency of loading of 1.16E-05 Hz, while yearly changes correspond to a frequency of 3.17E-08 Hz.

The laboratory testing should be performed at a similar temperature to those that a composite structure is exposed to in the field. The depth of interest is around where the interphase is located since it is hypothesized that it is the weakest section of the structure, and it is where the failures should happen. Mateos [21] determined that the temperatures of an interphase at a depth of 115 mm (4.5 in) had a maximum of 44 °C (111 °F) and a minimum of 3 °C (37.5 °F) over an analysis period of 15 months as it is shown in Figure 4-2.

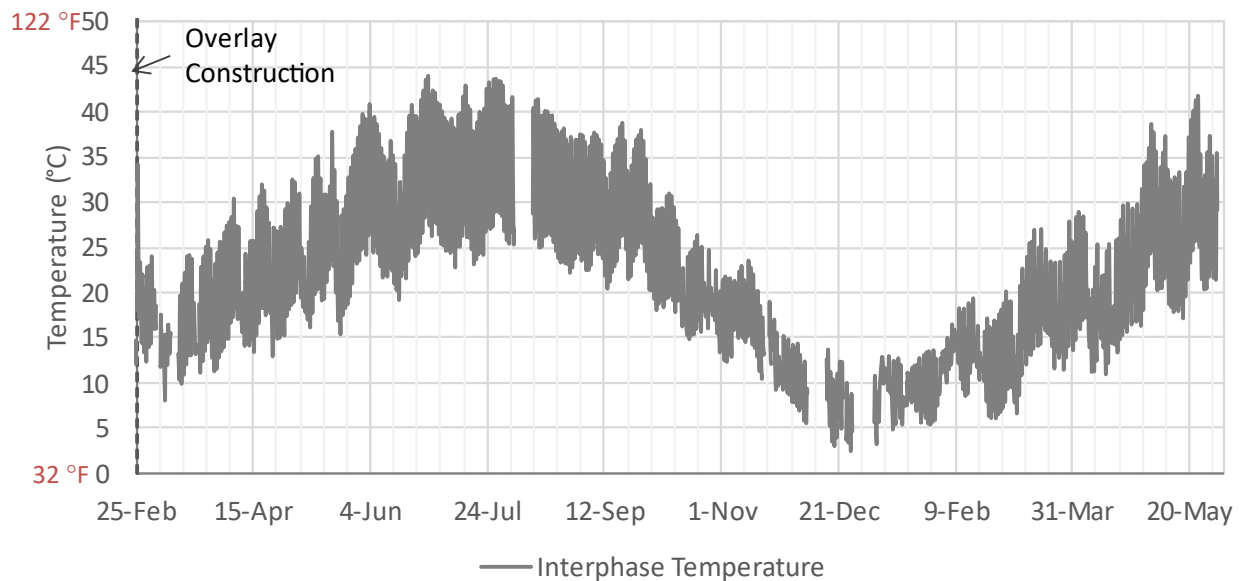


Figure 4-2. Example of thermocouples readings at different depths of the pavement [21]

4.4 Machine Characteristics and Limitations

Five different testing devices were used in this research project: a Superpave Shear Tester (SST), a Universal Testing Machine (UTM), a Tensile Hanger (TH), an Asphalt Mixture Performance Tester (AMPT), and a Uniaxial Loader (UL). All five machines are shown in Figure 4-3.

The SST and UTM machines were used to perform the shear and tensile tests, respectively. The SST can perform tensile testing, but due to time constraints, the UTM was used for the tensile testing. Detailed characteristics and limits for each machine are provided below. Since the machines require electricity and hydraulic systems to run, testing time cannot be very long because it is risky to expect the hydraulic and electric systems to perform properly for extended periods of time. Therefore, the maximum testing time for each device was selected to be 30 hours.

The AMPT and the UL machines also use electricity and hydraulics systems but are intended for testing procedures that do not require extended periods of time. The TH device is the only one that does not require electricity or hydraulics systems for the loading since the weights are applied mechanically. Such a characteristic enables the TH device to perform long-lasting tests with a maximum duration of 10 days.

The specimens used in UTM, SST, and TH were glued to aluminum platens that are used to be held by the machine. A 6-minute quick set epoxy glue with a shear strength of 6.9 MPa (1000 psi) is applied to both faces of the specimen, and a gluing fixture makes sure the specimen does not move while the glue is setting. Additionally, LVDT holders and targets are also attached to the specimens. The specimens are ready to be tested once glued and cured for 24 hours at room

temperature. The glue provided an additional limitation to the testing procedures. From previous experience, it has been seen that the glue does not behave properly when testing is performed at temperatures higher than 45 °C (113 °F). The glue becomes softer, and the likelihood for the specimen to debond from the platens increases when testing over such temperature.



a) Superpave Shear Tester (SST)



b) Universal Testing Machine (UTM)



c) Asphalt Mixture Performance Tester (AMPT)



d) Uniaxial Loader (UL)



e) Tensile Hanger (TH)

Figure 4-3. Testing machines

4.4.1 Superpave Shear Tester (SST)

Table 4-1 summarizes the limits and characteristics of the SST machine.

Table 4-1. SST machine limits and characteristics

	Min	Max	Unit
Axial load cell	0.1 (22)	22.2 (5,000)	kN (lbf)
Shear load cell	0.1 (22)	22.2 (5,000)	kN (lbf)
LVDT displacement	-2.5 (-0.1)	2.5 (0.1)	mm (in.)
Frequency range	0.01	10	Hz.
Testing time	0.02	30	hours
Temperature	15 (59)	55 (131)	°C (°F)
Specimen diameter	150 (6)	150 (6)	mm (in.)
Loads	Axial – tension and compression Shear – bidirectional		
Loading system	Hydraulics		
Type of loading	Creep, ramp, sinusoidal		
Holding method	Platens glued to specimens		
Glue curing time	24 hours		

Figure 4-4 shows a diagram of the shear specimens with the loading platens on both faces of the specimens that are used to be held by the machine. It also shows a representation of the loads

that the machine applies: a horizontal shear that can be applied in both directions and an axial load that can be applied in compression or tension.

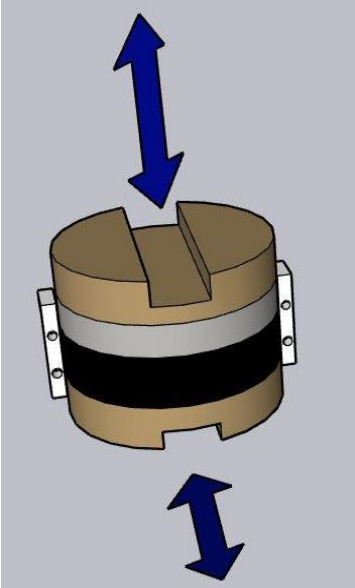


Figure 4-4. Shear specimen diagram

4.4.2 Universal Testing Machine (UTM)

Table 4-2 summarizes the limits and characteristics of the UTM machine.

Table 4-2. UTM machine limits and characteristics

	Min	Max	Unit
Axial load cell	0.1 (22)	130 (29,250)	kN (lbf)
LVDT displacement	-2.5 (-0.1)	±2.5 (0.1)	mm (in.)
Frequency range	0.01	2	Hz.
Testing time	0.02	30	hours
Temperature range	-10 (14)	50 (122)	°C (°F)
Specimen diameter	100 (4)	100 (4)	mm (in.)
Load	Axial – tension and compression		
Type of loading	Creep, ramp, sinusoidal		
Loading system	Hydraulics		
Holding method	Platens glued to specimens		
Glue curing time	24 hours		

Figure 4-5 shows a diagram of the tensile specimens with the loading platens that need to be glued to both faces of the specimens to be held by the machine. It also shows a representation of the load that can be applied by the machine: axial load in tension.

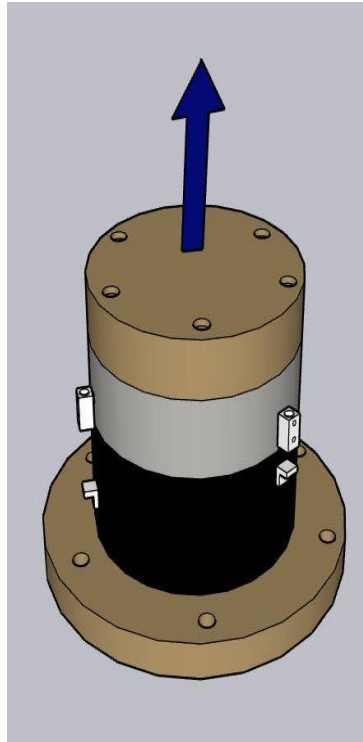


Figure 4-5. Tensile specimen diagram

4.4.3 Tensile Hanger Device (TH)

Table 4-3 summarizes the limits and characteristics of the TH device.

Table 4-3. Tensile hanger device limits and characteristics

	Min	Max	Unit
Weight limit	0.25 (0.55)	32 (70)	kg (lb)
LVDT displacement	-6 (-0.24)	6 (0.24)	mm (in.)
Temperature range	20 (68)	30 (86)	°C (°F)
Specimen diameter	100 (4)	100 (4)	mm (in.)
Load	Axial – tension		
Type of loading	Ramp		
Loading system	Mechanical		
Holding method	Platens glued to specimens		
Glue curing time	24 hours		

Figure 4-6 shows a diagram of the hanging test specimen with the loading platens that need to be glued to be held in the testing frame and to hold the additional weights. It also shows a representation of the load that is applied. The difference between this test and the UTM test is the specimen orientation, in this test the specimen is placed concrete side down since the loading procedure comes from self-weight and it can include additional hanging weight.

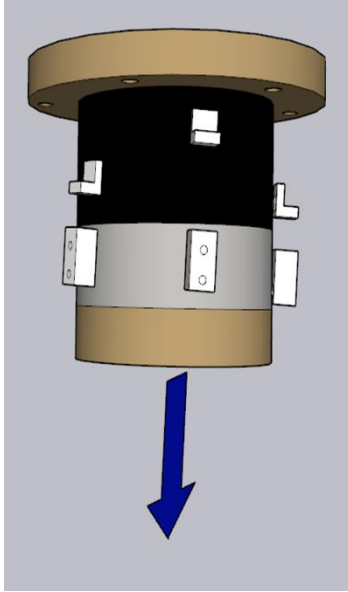


Figure 4-6. Hanging test specimen diagram

4.4.4 Asphalt Mixture Performance Tester (AMPT)

Table 4-4 summarizes the limits and characteristics of the AMPT machine.

Table 4-4. AMPT machine limits and characteristics

	Min	Max	Unit
Axial load cell	-20 (-4,500)	20 (4,500)	kN (lbf)
LVDT displacement	-0.5 (-0.02)	0.5 (0.02)	mm (in.)
Frequency range	0.01	25	Hz.
Temperature range	-25 (-13)	80 (176)	°C (°F)
Specimen diameter	100 (4)	100 (4)	mm (in.)
Load	Axial – compression		
Type of loading	Sinusoidal		
Loading system	Hydraulics		
Holding method	None		

Figure 4-7 shows a diagram of the AMPT specimen with a representation of the compressive load that is applied. This device is only used on asphalt specimens and does not require the use of any platens to hold the specimen.

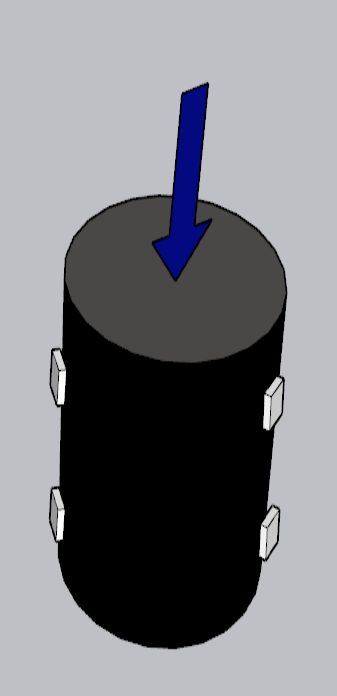


Figure 4-7. AMPT specimen diagram

4.4.5 Uniaxial Loader Device (UL)

Table 4-5 summarizes the limits and characteristics of the UL machine.

Table 4-5. Uniaxial Loader device limits and characteristics

	Min	Max	Unit
Axial load cell	0.1 (22)	50 (11,250)	kN (lbf)
LVDT displacement	0	50 (2)	mm (in.)
Specimen diameter	150 (5)	150 (5)	mm (in.)
Loading rate	48 (1.89)	52 (2.05)	mm/min (in./min)
Load	Axial – tension		
Type of loading	Ramp		
Loading system	Hydraulics		
Holding method	None		

Figure 4-8 shows a diagram of the specimen used in the uniaxial loader with a representation of the load that is applied. This device is only used on asphalt specimens and does not require the use of any platens to hold the specimen.

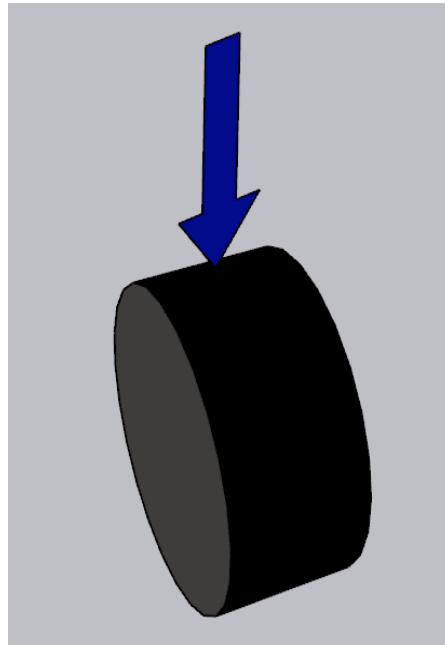


Figure 4-8. Ideal CT specimen diagram

4.5 Testing Conditions

The laboratory testing cannot be performed by replicating the field conditions due to the machine limits and characteristics that were previously mentioned. The magnitude of the stresses or strains used in the laboratory tests are independently described in each of the tests, which are shown in section 4.6. Temperatures and humidity conditions suggested for the testing, taking into consideration the equipment capabilities, are shown in this section. Overall, the field conditions cannot be fully replicated under laboratory conditions. Hence, the chosen conditions are the best approximation that was possibly done within the limitations provided by each of the testing equipment.

4.5.1 Temperature

The temperature history of three climate regions of California spanning most of the conditions in the state was analyzed to determine the range of temperatures at which the different tests were going to be performed. Figure 4-9 shows the nine California climate regions used for pavement design and asset management [42]. A red rectangle is drawn around the three climate regions that were selected for this study, which are Inland Valley, Desert, and South Coast. The representative cities for each region are Fresno, Daggett, and Los Angeles, respectively. These three sections provide a representative spread of the temperatures in the State, and most other climate regions can be interpolated from these three. The analysis process consisted of the determination of the temperatures in the interphase based on the surface temperature of the structures.

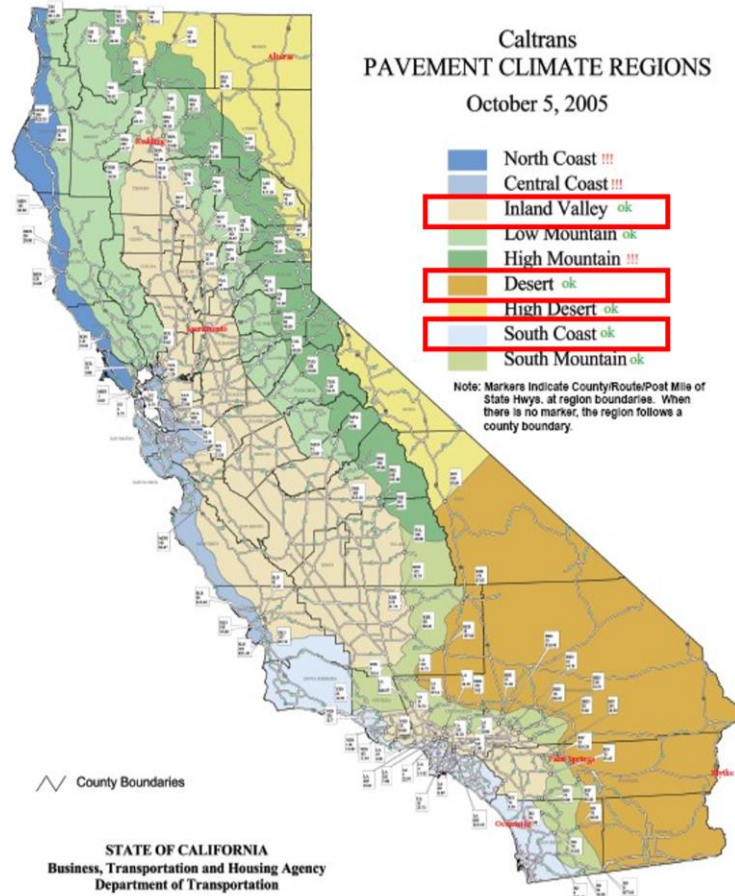


Figure 4-9. CALTRANS Pavement Climate Regions

The temperatures for the three climate regions were obtained using the 1-D Temperature Model developed for the California Mechanistic-Empirical Design Guide (CalME) [43] which depends on the heat capacity, conductivity, and thermal diffusivity of all the layers. The CalME temperature model was used to populate a database with hourly nonlinear PCC temperature profiles for a period of 10 years. The model reports the temperatures at 11 depths of the concrete layer. The average hourly temperature at each analyzed depth was calculated once the database was populated, and a histogram was performed to analyze the range of temperatures.

Pavement structures with different thicknesses of concrete and asphalt layers were analyzed to obtain the temperature at the interphase between the concrete and the base. This location in

the structure is considered to provide the most accurate temperature for testing since it is assumed that the failure is likely to occur at the top of the asphalt layer near the interphase between both layers. Since SJPCP-COA usually consists of concrete layers of 100 to 180 mm (4 to 7 in.), three different thicknesses were chosen: 100, 140 and 180 mm (4, 5.5 and 7 in.). The thickness of the RHMA layers was set to 0, 50, and 100 mm (0, 2, and 4 in.). All the structures had a 125 mm (5 in.) old HMA layer and a 305 mm (12 in.) aggregate base underneath the RHMA layer. Table 4-6 summarizes all the variables analyzed. A total of 27 sections were evaluated, which correspond to the combination of three climate regions, three PCC thicknesses, and three RHMA thicknesses.

Table 4-6. Summary of variables analyzed

Variable	Values
Climate Region	Inland Valley (IV)
	Desert (D)
	South Coast (SC)
PCC Thickness, mm (in.)	100 (4)
	140 (5.5)
	180 (7)
RHMA thickness, mm (in.)	0 (0)
	50 (2)
	100 (4)
Old HMA thickness, mm (in.)	125 (5)
AB thickness, mm (in.)	305 (12)
Temperature	Average
Depth	Interphase

A summary of the properties of the material used as an input in the model for each of the layers is shown in Table 4-7.

Table 4-7. Summary of material properties

Layer	Conductivity k ($Wm^{-1}K^{-1}$)	Heat Capacity c_p ($Jkg^{-1}K^{-1}$)	Density ρ (kgm^{-3})	Thermal Diffusivity α (mm^2h^{-1})	E (MPa)
PCC	1.5	1,016	2,800	1,898.2	28,000
RHMA	0.896	875	2,200	1,638.6	3,000
HMA	1.15	921	2,200	1,997.8	3,500
AB	1.55	820	1,950	3,490.2	150

A histogram for interphase temperature distribution was obtained for each of the structures. Figure 4-10 shows a summary histogram for all the analyzed sections, and it is determined that the average interphase temperature is in the range between 10 and 45 °C (50 and 113 °F) through the ten years of data. Each pavement structure is labeled with the initials of the weather region and the thickness of the PCC layer in mm. During the analysis, it was observed that the thickness of the RHMA layer did not influence the temperature at the interphase between the PCC and the asphalt, which is why in Figure 4-10, only the data for 9 out of the 27 structures is shown.

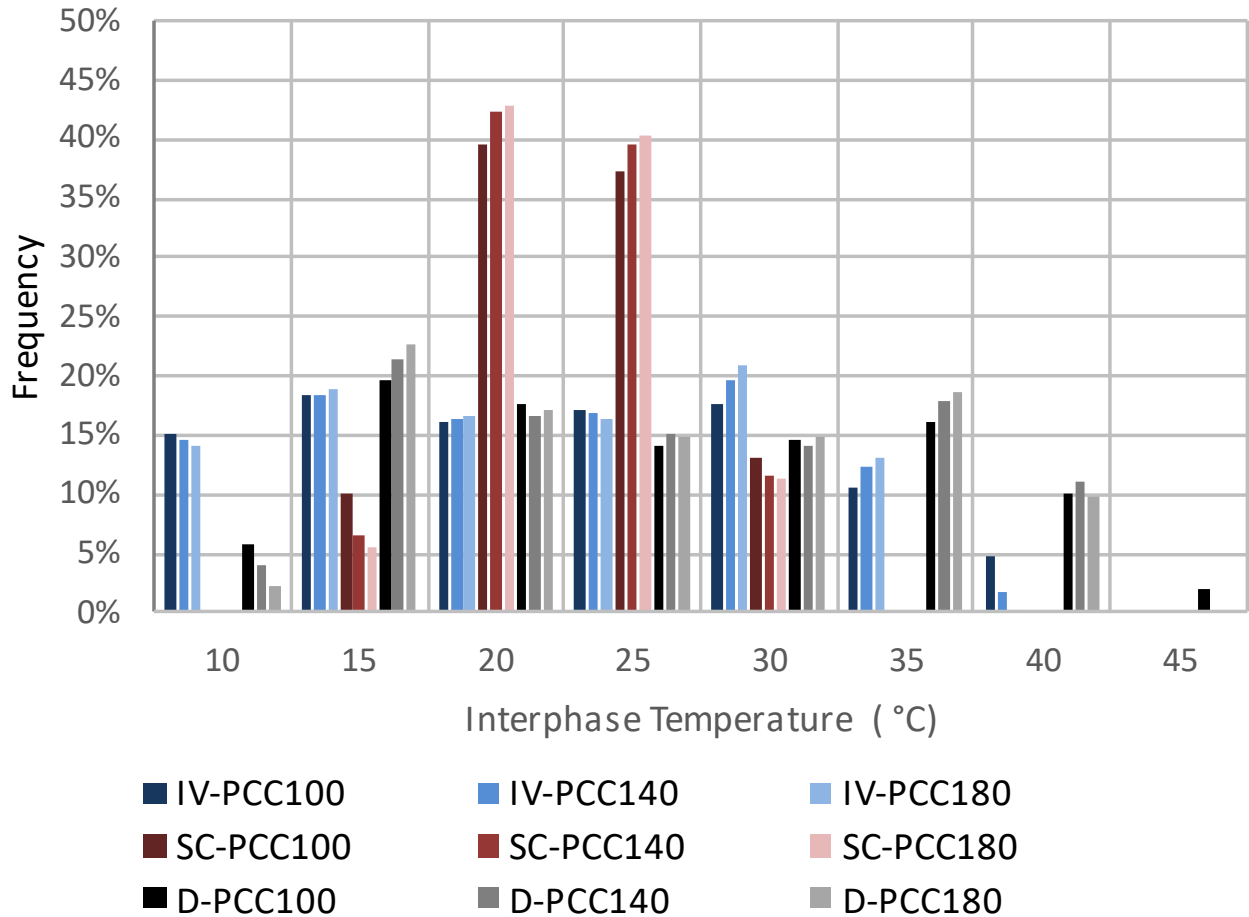


Figure 4-10. Interphase temperature histogram. Nomenclature: weather region-PCC thickness in mm

Figure 4-10 suggest that there is a strong agreement between the temperatures obtained through the analysis of 10 years of temperature data and the temperature recorded in pavement sections in Davis for 15 months. The minimum and maximum temperatures that will likely happen at the interphase of the SJPCP-COA structure are slightly out of the limits for the shear machine. Since the temperature system is the restricting issue, the minimum temperature at which the tests can be done is 15 °C (59 °F), and the maximum is 40 °C (104 °F). Besides these two temperatures, a third value was selected in between the two extremes: 25 °C (77 °F).

4.5.2 Humidity

Moisture conditioning of asphalt specimens was used to determine the moisture susceptibility that different mixes can have by using hydrostatic pore pressure in a conditioning chamber like the one shown in Figure 4-11. Such a device is commonly called MiST. After the specimens were conditioned, a dry set of specimens and a conditioned set of specimens were tested to determine the effects of the water conditioning. The process followed is described in ASTM D7870 [44] and consists of 3,500 pressurizing cycles to force water into the specimens. The tank is full of water at 50 to 60 °C (122 to 140 °F), and a bladder expands to create a pressure of 0.28 MPa (40 psi) every cycle. The device characteristics are summarized in Table 4-8.



Figure 4-11. MiST device

Table 4-8. MiST device characteristics

Pressure	0.28 (40)	MPa (psi)
Temperature	50 to 60 (122 to 140)	°C (°F)
Cycles	3,500	cycles
Time	4.5	hours
Specimens	2-3	samples

4.6 Laboratory Tests

This section describes all the laboratory procedures that were used for this thesis based on the testing capabilities that were available or could be developed as part of this study. A detailed explanation of the testing parameters is provided for those tests that are performed under this project. Additional test procedures for fatigue analysis were developed under this research framework and were used in the initial phases but were not required for the final characterization. Those tests are detailed in Appendix A in case there is a future need to expand the current study or application to a new research project.

Table 4-9 summarizes basic information for all the testing procedures initially considered based on the properties that were initially described in Table 2-1. The following subsections provide details for each test and how the stress/strain testing parameters were defined.

Table 4-9. Testing procedures summary

Device	Test	Property	Conditions	Used in final testing	Replicates
SST	Frequency sweep	Stiffness under rapid loading	15, 25 and 40 °C	Yes	3
	Creep	Creep compliance	15, 25 and 40 °C	Yes	3
	Fatigue	Fatigue life	15, 25 and 40 °C	No	3
	Sine-ramp	Fatigue life	25 °C	No	3
	Ramp	Capacity to deform under slow loading	15, 25 and 40 °C	Yes	3
	Combined Sine-ramp	Fatigue life	25 °C	No	3
UTM	Creep	Creep compliance	15, 25 and 40 °C	Yes	3
	Ramp	Capacity to deform under slow loading	15, 25 and 40 °C	Yes	3
	Sine-ramp	Fatigue life	25 °C	No	3
TH	Creep	Stiffness under slow loading	25 °C	Yes	3
	Damage	Capacity to deform under slow loading	25 °C	Yes	3
AMPT	Frequency sweep	Stiffness under rapid loading	4, 15, 25, 40 and 54 °C	Yes	3
UL	Indirect tensile cracking test	Resistance to water-induced damage	Wet and dry 25 °C	Yes	3
NOTE: 4, 15, 25, 40, and 54 °C correspond to 40, 59, 77, 104, and 129 °F					

4.6.1 Shear Frequency Sweep

The shear frequency sweep test is performed in the SST machine. It is a deformation-controlled test used to determine the dynamic shear stiffness behavior of asphalt and composite specimens under different loading frequencies and temperatures. The interaction between loading time and temperature will determine how stiff or soft the material is, which describes how the structure behaves. For example, fast traffic loading during cold weather results in the stiffest behavior, while slow environmental loading during hot weather results in the softest behavior. This test covers frequencies for both environment and traffic loading happening on the field. A diagram for the test is shown in Figure 4-12.

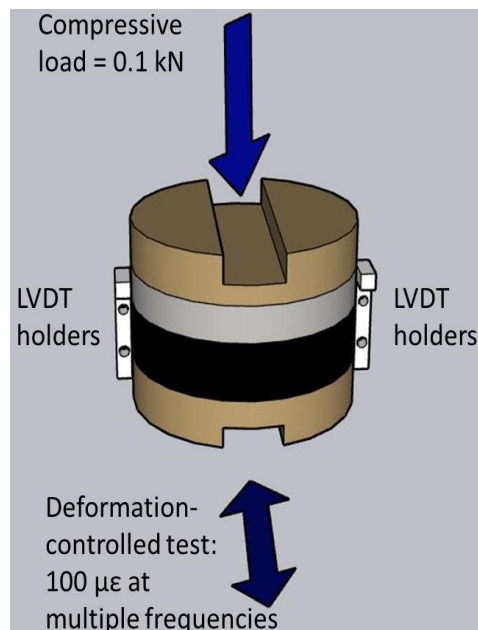


Figure 4-12. Shear frequency sweep test diagram

Four horizontal LVDTs are used to measure displacement at two different locations, interphase between the concrete and the asphalt and in the asphalt. One of the asphalt LVDTs is used through the test to control the deformation level. A compressive load is also shown in the figure

above, which is applied to ensure that the specimen always remains at constant height throughout the test, starting from slight compression prior to starting shear loading.

4.6.1.1. Input Parameters

The test requires the input of frequencies at which it is going to be performed and the peak-to-peak strain level. The strain level for this testing needs to be such that it does not cause any structural damage to the specimen. This means that the strain level must be within the linear viscoelastic region (LVER), which is the range where the stress and strain are proportional and the applied stress is considerably smaller than the failure stress. Figure 4-13 shows a strain versus modulus plot for two different materials with their LVER labeled. Additionally, the test needs to be performed at a minimum of three different temperatures to provide overlap between the stiffnesses of different frequencies to be able to apply the time-temperature superposition principle. The temperature-dependent properties of viscoelastic materials such as asphalt are determined using the superposition principle that was explained in Section 2.1 and is required to develop the shear stiffness master curve.

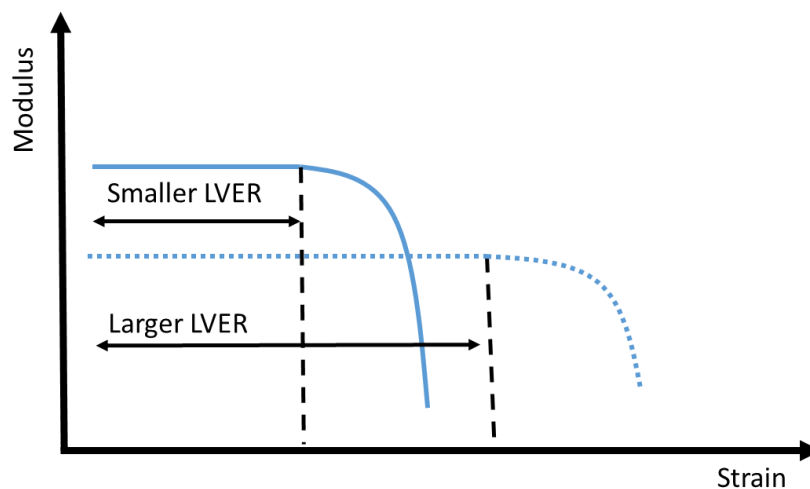


Figure 4-13. LVER representation

4.6.1.2. *From Standard*

AASHTO T320 Standard [45], in the shear frequency sweep at constant height subsection, determines for this test a peak-to-peak amplitude of 100 $\mu\epsilon$ at the following frequencies: 10, 5, 2, 1, 0.5, 0.2, 0.1, 0.05, 0.02 and 0.01 Hz. The number of cycles should be 50 for 10 and 5 Hz, 20 cycles for 2 and 1 Hz, 7 cycles for 0.5, 0.2, and 0.1 Hz, and 4 cycles for 0.05, 0.02 and 0.01 Hz.

Based on the testing conditions and input parameters defined above, the three temperatures previously chosen under testing conditions 15, 25, and 40 °C (59, 77, and 104 °F) ensure overlap between the stiffnesses of different frequencies.

4.6.1.3. *Summary*

The shear frequency sweep test was performed at:

- Strain level: 100 $\mu\epsilon$ peak-to-peak.
- Frequencies: 10, 5, 2, 1, 0.5, 0.2, 0.1, 0.05, 0.02 and 0.01 Hz.
- Temperatures: 15, 25, 40 °C (59, 77 and 104 °F).

4.6.2 Shear Creep

The shear creep test is performed in the SST machine. It is a load-controlled test used to characterize the asphalt and interphase stiffness of SJPCP-COA specimens under low constant load over extended periods of time. The idea of this test is to replicate the effect of environmental loads that have long loading times and low load levels without causing damage to the specimens. A testing diagram can be seen in Figure 4-14. The test includes a compressive load of 0.1 kN (22.5 lbf) for not allowing the specimen to go into tension.

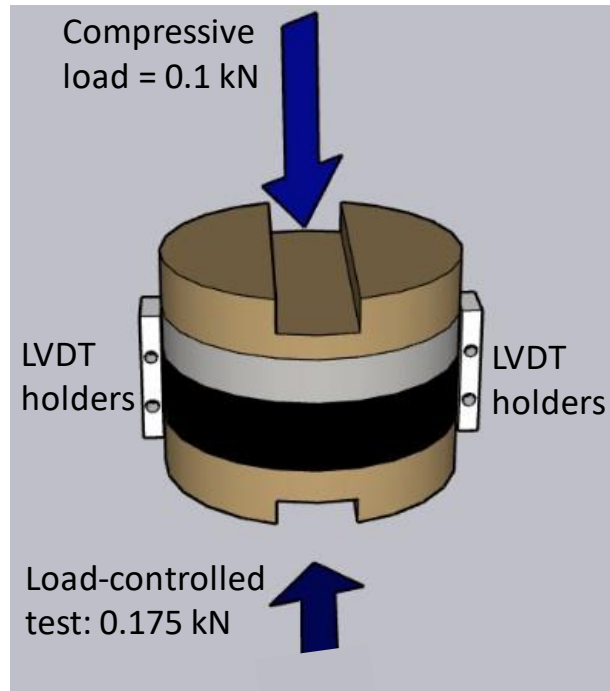


Figure 4-14. Shear creep test diagram

4.6.2.1. *Input Parameters*

The test requires two parameters to be defined: load and time of loading. The test consists of a quick loading ramp to achieve the specified load, followed by a loading time under the chosen load. The testing temperatures are the same as the ones explained under testing conditions: 15, 25, and 40 °C (59, 77, and 104 °F).

4.6.2.2. *Parameter Determination*

The creep test is intended to be performed in the range in which only recoverable damage is caused in the specimen so that the specimens can be reused for testing at different temperatures. Deformations under 0.1 percent are assumed to cause only recoverable creep since such deformation level will be in the LVER where the stress and strain are directly proportional. Based on previous experience (Figure 4-15) done under a constant load of 0.175 kN

(40 lbf) at 25 °C (77 °F), it can be assumed that a shear deformation of 1000 $\mu\epsilon$ would occur in approximately 4 hours.

The load level parameter needs to be determined for each particular type of mix in order to be at 1000 $\mu\epsilon$ or less at the end of the testing time, but it is expected to be in the vicinity of 0.175 kN (40 lbf) as is shown in Figure 4-15.

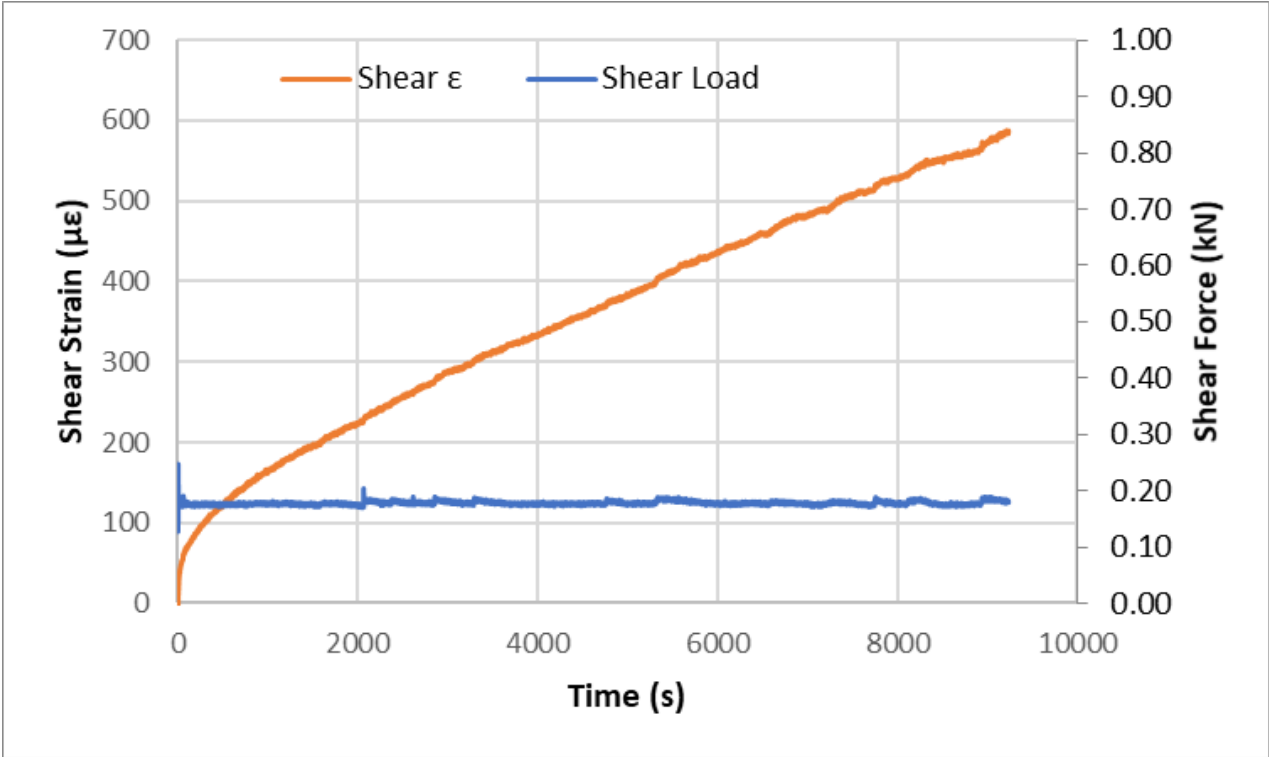


Figure 4-15. Shear creep test result

4.6.2.3. Summary

The shear creep test was performed at:

- Load level: approximately 0.175 kN (40 lbf).
- Maximum strain level: 1000 $\mu\epsilon$.
- Temperatures: 15, 25, 40 °C (59, 77 and 104 °F).

4.6.3 Shear Ramp

The shear ramp test is performed with the SST machine. It is a deformation-controlled test that is used to characterize the capacity to deform under slow loading using a constant deformation rate, but also to determine if the daily temperature variations happening in the field are critical for the bonding of the structure or if it is merely the shrinkage which is the most harmful.

A diagram for the test is shown in Figure 4-16. The diagram shows the unidirectional horizontal load that is applied, as well as the required LVDT holders. One of the asphalt LVDTs controls the deformation level of the test. A vertical load is also applied in this test to have the specimen under slight compression.

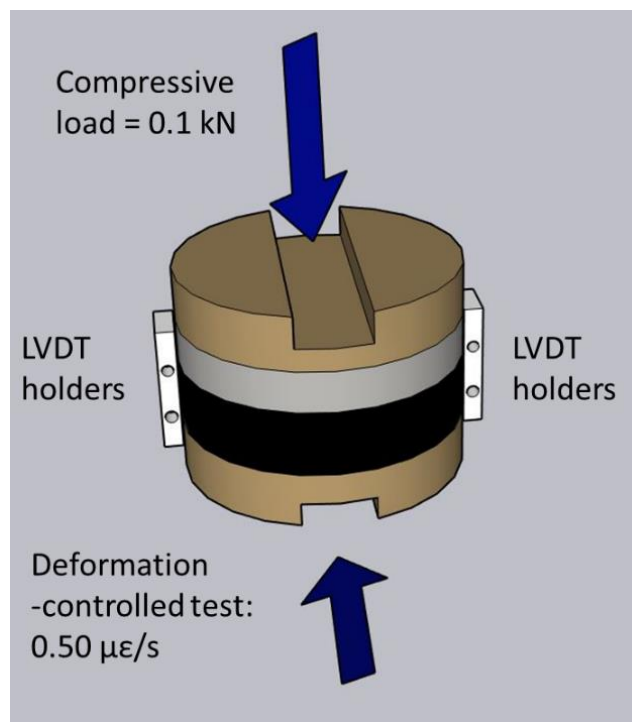


Figure 4-16. Shear ramp test diagram

4.6.3.1. *Input Parameters:*

The test is performed at a constant deformation rate and at three different temperatures. The testing temperatures are 15, 25, and 40 °C (59, 77, and 104 °F). The loading rate is explained in the following subsection.

4.6.3.2. *Parameters Determination*

The shear ramp test is intended to replicate the long-term shrinkage effect happening in the concrete slabs, which can be performed as a constant rate loading ramp. Since it is a strain-controlled test, the ramp rate will depend on the length of the test. The testing time is defined as 3 hours. Knowing that the end strain level must be 5,500 $\mu\epsilon$ [Figure A- 15], the corresponding strain rate is 0.50 $\mu\epsilon/s$.

4.6.3.3. *Summary*

The shear strength test was performed at:

- Ramp rate: 0.50 $\mu\epsilon/s$.
- Temperatures: 15, 25, 40 °C (59, 77 and 104 °F).

4.6.4 Tensile Creep

The tensile creep test is performed in the UTM machine. It is a load-controlled test used to characterize the stiffness of the asphalt and composite specimens under low constant load over extended periods of time. The idea of this test is to replicate the effect of environment loads that have long loading times and low load levels without causing permanent deformation on the specimens.

A diagram for this test is shown in Figure 4-17. Two LVDT positions are shown, and at the back of the specimen, there is one more LVDT. The diagram also shows the direction of the load that is used for this test.

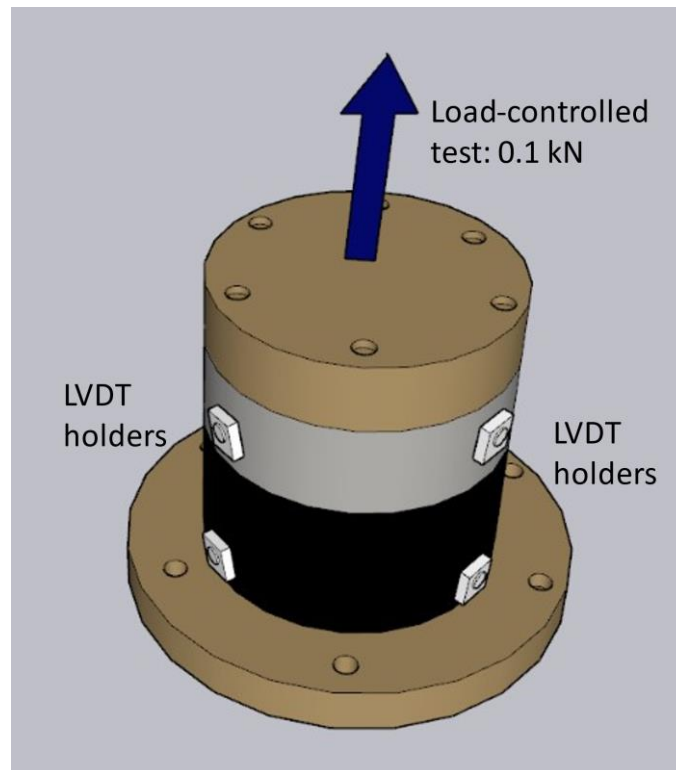


Figure 4-17. Tensile creep test diagram

4.6.4.1. Input Parameters

The only parameter required is the load level. The test consists of a quick loading ramp to achieve the specified load, followed by a loading time under the constant load, and the test is finalized with a quick unloading ramp. The tensile creep test complements the data obtained in the tensile hanging creep test by allowing tests to be performed in a shorter period of time under higher loading levels.

The test will be performed at the three temperatures that were explained at the beginning of this chapter: 15, 25, and 40 °C (59, 77, and 104 °F).

4.6.4.2. Parameters Determination

The creep test is intended to be performed in the range in which only recoverable damage is caused in the specimen so that the specimens can be reused for testing at different temperatures. Deformations under 0.1 percent are assumed to cause only recoverable creep. The loading level is determined by the machine's capability of holding small loads under extended periods of time, which is why a load of 0.1 kN (22.5 lbf) is chosen. Such load is 5 to 6 times the tensile hanging damage test load to speed up the deformation rate and reduce the testing time.

4.6.4.3. Summary

The tensile creep test was performed at:

- Load level: 0.1 kN (22.5 lbf).
- Maximum strain level: 1,000 $\mu\epsilon$.
- Temperatures: 15, 25, 40 °C (59, 77 and 104 °F).

4.6.5 Tensile Ramp

The tensile ramp test is performed in the UTM machine. It is a deformation-controlled test used to determine the capacity to deform under slow loading using asphalt and composite specimens under a constant deformation rate, but also to determine if the daily temperature variations happening in the field are critical for the structure or if it is merely the seasonal variation which is the most harmful.

A diagram for the test is shown in Figure 4-18. The diagram shows the unidirectional vertical load that is applied and two LVDT positions; at the back of the specimen, there is one more LVDT.

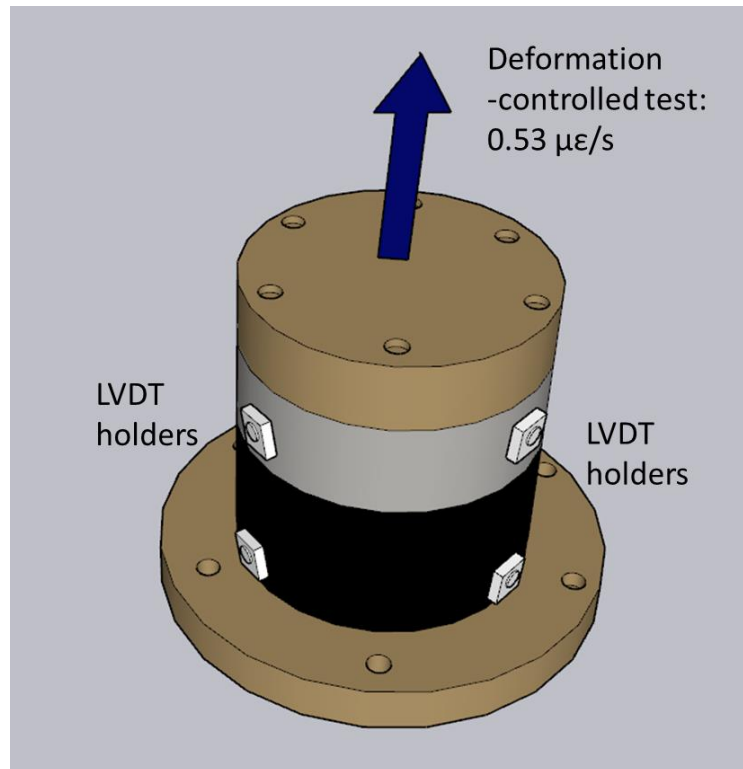


Figure 4-18. Tensile ramp test diagram

4.6.5.1. *Input Parameters:*

The test is performed at a constant deformation rate and at three different temperatures, which are 15, 25, and 40 °C (59, 77 and 104 °F).

4.6.5.2. *Parameters Determination*

The tensile ramp test is intended to replicate the long-term shrinkage effect happening in the concrete slabs, which can be performed as a constant rate loading ramp. Since it is a strain-controlled test, the ramp rate will depend on the length of the test. The testing time is defined

as 3 hours. Knowing that the end strain level must be 1,800 $\mu\epsilon$ [Figure A- 18], the corresponding strain rate is 0.167 $\mu\epsilon/s$.

4.6.5.3. Summary

The shear strength test was performed at:

- Ramp rate: 0.167 $\mu\epsilon/s$.
- Temperatures: 15, 25, 40 °C (59, 77 and 104 °F).

4.6.6 Tensile Hanging Creep

The tensile hanging creep test is performed in the tensile hanger (TH) device. It is a self-weight test used to characterize the tensile stiffness under slow loading of asphalt and composite specimens under a constant load over an extended period of time. Additional weight can also be added in case the test needs to be performed faster. An upside-down asphalt or composite specimen is hung with LVDTs that track the elongation at two different points, close to the interphase and as far as possible from the interphase. The creep compliance for each type of structure is calculated, which corresponds to the rate at which strain increases for a constant applied stress.

Figure 4-19 shows a diagram for the tensile hanging creep test. The asphalt side of the specimen is glued to a platen that is connected to the frame where the specimens hang, while the concrete side is glued to a platen that allows additional weight to be added. Three LVDTs can be seen on this side of the specimen, two for the interphase and one for the asphalt. Behind the specimen, there are three more LVDTs, two for the asphalt and one for the interphase. The total

displacement at the interphase and the asphalt is obtained by averaging the three LVDTs measuring at each location.

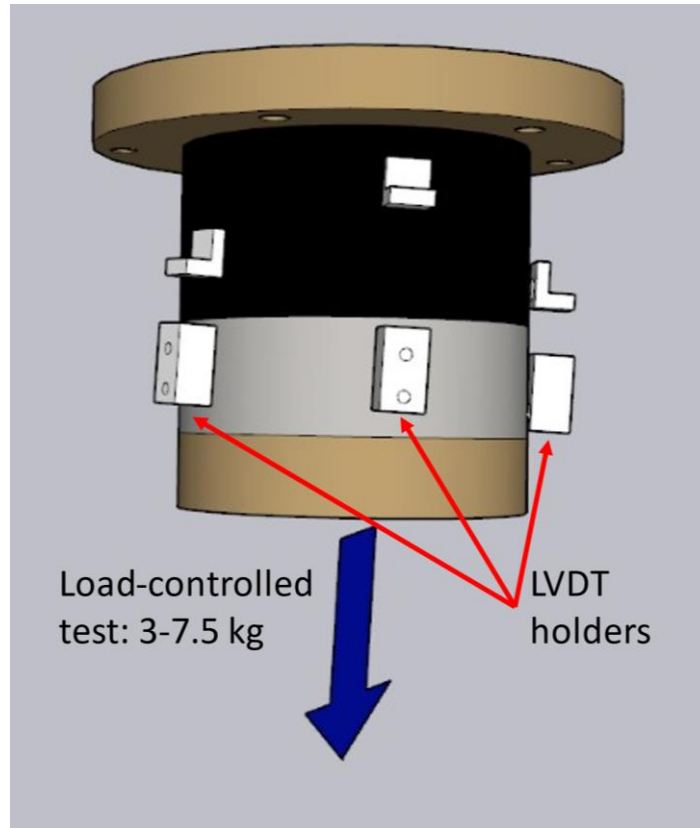


Figure 4-19. Tensile hanging creep test diagram

4.6.6.1. Input Parameters

The only input parameter for this test is the load that is applied. Based on previous testing performed, it is known that in order to obtain 5,000 to 10,000 $\mu\epsilon$ after seven days, it is required to hang an additional load of 3 to 7.5 kg (6.6 to 16.5 lb), which corresponds to 0.004 to 0.009 MPa (0.54 to 1.36 psi), depending on the material being tested. Conventional HMA is usually closer to the higher-end load, while when testing RHMA-G specimens, it is closer to the lower-

end load. The test setup is inside a room with a controlled temperature of 25 °C (77 °F) and controlled humidity of 50 percent.

4.6.6.2. *Summary*

The tensile hanging test was performed at:

- Load level: 3 to 7.5 kg (6.6 to 16.5 lb).
- Testing time: 7 days.
- Temperatures: 25 °C (77 °F).

4.6.7 Tensile Hanging Damage

The tensile hanging damage test is performed in the TH device. It is a hanging-weight test used to characterize the capacity to deform under slow loading of asphalt and composite specimens under a constant load over an extended period of time. Additional weight is added to perform the test at a faster damage rate. This test is an alternative to the tensile ramp that was explained in section 4.6.5. An upside-down composite specimen is hung with LVDTs that track the elongation at two different points, close to the interphase and as far as possible from the interphase. Figure 4-20 shows a diagram for the tensile hanging damage test. The only difference when comparing it to the tensile hanging creep test is the magnitude of the load that is applied to the bottom plate. Three LVDTs can be seen on this side of the specimen, two for the interphase and one for the asphalt. Behind the specimen, there are three more LVDTs, two for the asphalt and one for the interphase. The total displacement at the interphase and the asphalt is obtained by averaging the three LVDTs measuring at each location.

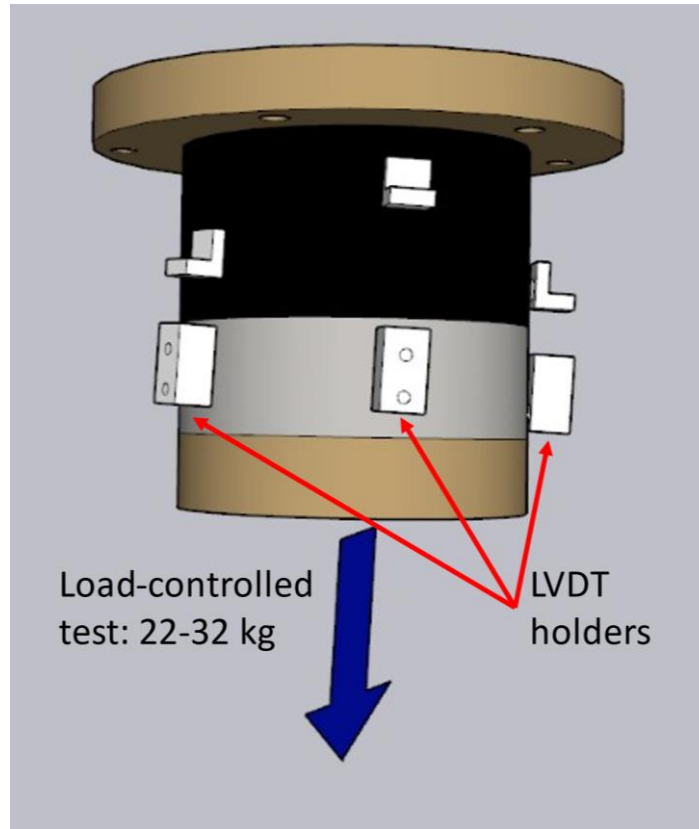


Figure 4-20. Tensile hanging damage test diagram

4.6.7.1. *Input Parameters*

The only input parameter for this test corresponds to the load that is applied. Based on previous testing performed, it is known that three days is enough to have the specimens fail with 22 to 32 kg (48.5 to 70.5 lb) of added weight, which corresponds to a stress of 0.027 to 0.400 MPa (3.98 to 5.80 psi). Conventional HMA is usually closer to the higher-end load, while when testing RHMA-G specimens, it is closer to the lower-end load. The test setup is inside a room with a controlled temperature of 25 °C and a controlled humidity of 50 percent.

4.6.7.2. *Summary*

The tensile hanging test was performed at:

- Load level: 22 to 32 kg (48.5 to 70.5 lb).
- Testing time: 3 days.
- Temperatures: 25 °C (77 °F).

4.6.8 Compressive Dynamic Modulus

The compressive dynamic modulus test is performed in the AMPT machine. It is a deformation-controlled test used to determine the dynamic shear stiffness behavior of asphalt specimens under different loading frequencies and temperatures. The interaction between loading time and temperature determines how stiff or soft the structure behaves. This test covers frequencies for both environment and traffic loading happening on the field. A diagram for the test is shown in Figure 4-21. Three vertical LVDTs are used to measure displacement, but only two locations can be seen in the diagram.

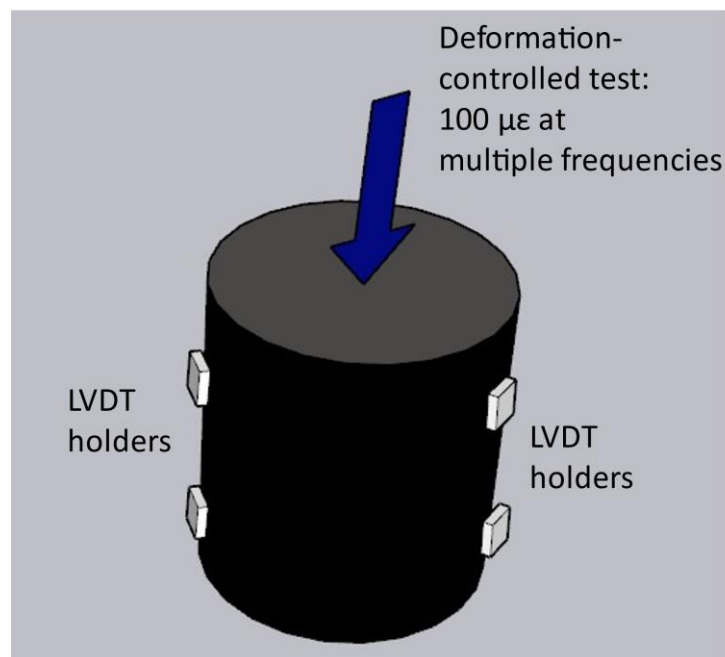


Figure 4-21. Compressive dynamic modulus test diagram

4.6.8.1. *Input Parameters*

This test needs to be performed at least at a minimum of three different temperatures to provide overlap between the stiffnesses at different frequencies to be able to apply the time-temperature superposition principle. Since 15, 25, and 40 °C (59, 77, and 104 °F) are used for all the other tests, it will also be used in this one with the addition of 4 and 54 °C (40 and 129 °F) to expand the temperature testing range. It also requires a set of frequencies and the strain level at which it is performed, which are given by the standard testing procedure.

4.6.8.2. *From Standard*

AASHTO T378-22 [46] in the dynamic modulus test determines that the peak-to-peak strain for unconfined specimens needs to be within 75 and 125 $\mu\epsilon$. The typical frequency range used for the test is between 0.1 and 25 Hz.

4.6.8.3. *Summary*

The compressive dynamic modulus test was performed at:

- Strain level: 100 $\mu\epsilon$ peak-to-peak.
- Frequencies: 25, 10, 5, 1, 0.5, 0.1 Hz.
- Temperatures: 4, 15, 25, 40 and 54 °C (40, 59, 77, 104, and 129 °F).

4.6.9 Indirect Tensile Cracking Test (IdealCT)

The indirect tensile cracking test is performed in the uniaxial loader (UL) device. It is a deformation-controlled test used to determine the cracking resistance of asphalt specimens. This test was chosen to analyze the moisture effect by testing a set of dry specimens and a set of

moisture-conditioned specimens. The process followed for the moisture conditioning was explained in section 4.5.2. A diagram for the test is shown in Figure 4-22.

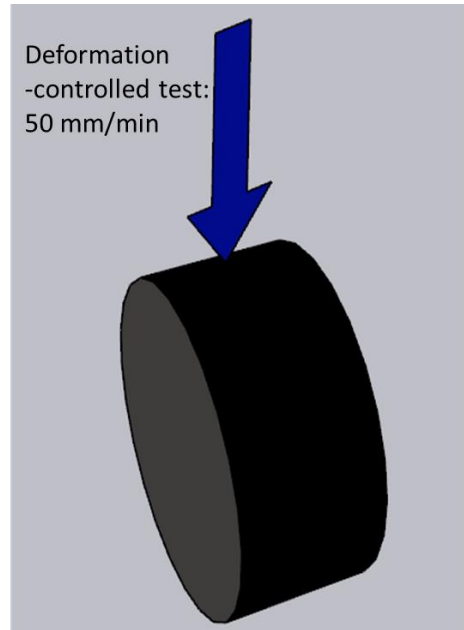


Figure 4-22. Indirect tensile cracking test diagram

4.6.9.1. *Input Parameters and Standard*

The only required input parameter for the indirect tensile cracking test is the loading rate of 50 ± 2 mm/min (2 ± 2 in./min), as shown in ASTM D8225-19 [47]. The test is performed in an open testing device where the temperature is not controlled since the test lasts 1 minute.

4.6.9.2. *Summary*

The indirect tensile cracking test was performed at:

- Loading rate: 50 ± 2 mm/min (2 ± 0.079 in./min).
- Temperature: room temperature.
- Moisture conditions: dry and wet.

5. FULL-FACTORIAL TESTING RESULTS

5.1 Goal and Objectives

The goal of this chapter was to apply the testing procedures determined in Chapter 4 to asphalt specimens created with two different materials, HMA and RHMA-G, under different testing conditions to simulate traffic and environment loads occurring in the field. The testing is focused on shear and tensile direction since it is considered to be the most representative of the types of stresses and strains that JPCP and SJPCP-COA structures are likely to experience in the field. A reduced testing factorial is recommended for future testing.

5.2 Materials Tested

Two different asphalt materials were tested as a first step to determine the properties of base materials for concrete pavements. The literature review discussed bases allowed for concrete pavement by the State of California, which is why HMA was one of the materials that was tested. An RHMA-G mix was also analyzed since, based on previous experience at the UCPRC [7], it seemed to perform better than the HMA, and it could be used as a base material, although it is currently not used. Table 5-1 summarizes the major characteristics of each mix, and copies of the mix designs are attached in Appendix B for detailed information.

Table 5-1. Asphalt mixes properties

	Mixes	
	Gle5	Yol113
Mix Type	HMA	RHMA-G
NMAS, mm (in.)	19 (3/4)	12.5 (1/2)
Binder	PG64-16	PG64-16 w/CRM
Rubber	No	Yes
Virgin Binder, %	3.85	7.5 including CRM
RAP	Yes	No
Notes= NMAS: nominal maximum aggregate size, RAP: reclaimed asphalt pavement, CRM: crumb rubber modifier		

The asphalt specimens tested were prepared using a gyratory compactor with a compacting temperature and pressure of 138 °C (280 °F) and 600 kPa (87 psi) for Gle5, and 152 °C (306 °F) and 825 kPa (120 psi) for Yol113. The difference in compacting temperature and pressure is due to the presence of rubber in RHMA-G mixes. The specimens were placed in a temperature-controlled room after they were compacted until it was time to get tested.

The results in this chapter are the first phase of testing that was performed to determine which tests capture the material properties most efficiently. Results are presented in two sets. First, the results for all the stiffness tests are shown, and in the following subsection, the results for all the strength tests are discussed. Stiffness and strength properties of the materials are required for the development of FEM (finite element method) models that are covered in Chapter 8.

5.3 Stiffness Test Results and Analysis

A total of five different tests were used to characterize the stiffness of asphaltic materials: two tests in shear, two tests in tension, and one test in compression. The tests have different loading times, which provide a stiffness characterization of the materials over a frequency range that is

within the range mentioned in section 4.3. The tensile hanging creep test has the longest testing time, about 5 to 7 days.

Since there are two asphalt mixes and usually three or more replicates, for each test method, the result for one sample is detailed with the corresponding data analysis process, and then a summary result for both is shown afterward.

5.3.1 Shear Frequency Sweep

The shear frequency sweep test was performed at three different temperatures with ten frequencies at each temperature, which produced a total of 30 stiffness values with different temperature-frequency combinations. The time-temperature superposition principle converted the frequencies at each temperature into a reduced frequency value. The output of the test provided the frequency (Freq), temperature (Temp), dynamic modulus (DM), and phase angle (ϕ). The time-temperature shift factor, reduced frequencies, and master curve dynamic modulus were calculated once the reference temperature (T_r) was picked with the equations shown in section 2.1. The reference temperature was 25 °C since it is the middle temperature at which the tests were done. The process required the minimization of the error between the test result dynamic modulus (DM) and the master curve dynamic modulus (MC DM). Table 5-2 shows the data for an HMA specimen test. The top two rows show the calibration parameters required for the calculation of the master curve and the summation of the error, which is minimized during the process.

Table 5-2. Shear dynamic modulus test data example and calculations

δ	1.369	B	-0.877	C1	-0.114		Error
α	2.210	γ	-0.745	Tr (°C)	25		3.76E-02
Freq	Temp (°C)	DM (MPa)	Phi	log(aT)	Freq red	MC DM (MPa)	Error DM
10.00	15.0	#N/A	#N/A	1.143	1.39E+02	2,554	#N/A
5.00	15.0	#N/A	#N/A	1.143	6.95E+01	2,334	#N/A
2.00	15.0	#N/A	#N/A	1.143	2.78E+01	2,016	#N/A
1.00	15.0	1,921	22.9	1.143	1.39E+01	1,761	1.42E-03
0.50	15.0	1,633	24.9	1.143	6.95E+00	1,504	1.29E-03
0.20	15.0	1,286	27.6	1.143	2.78E+00	1,176	1.51E-03
0.10	15.0	1,074	29.9	1.143	1.39E+00	949	2.88E-03
0.05	15.0	872	32.2	1.143	6.95E-01	748	4.40E-03
0.02	15.0	656	35.2	1.143	2.78E-01	530	8.55E-03
0.01	15.0	504	37.1	1.143	1.39E-01	402	9.54E-03
10.00	25.0	1,821	28.4	0.000	10.000	1,638	2.11E-03
5.00	25.0	1,444	30.5	0.000	5.000	1,383	3.50E-04
2.00	25.0	1,064	33.8	0.000	2.000	1,065	9.66E-08
1.00	25.0	846	36.0	0.000	1.000	850	3.45E-06
0.50	25.0	652	38.5	0.000	0.500	664	5.77E-05
0.20	25.0	460	41.1	0.000	0.200	466	2.92E-05
0.10	25.0	352	42.2	0.000	0.100	351	7.43E-07
0.05	25.0	271	42.8	0.000	0.050	264	1.13E-04
0.02	25.0	188	42.8	0.000	0.020	182	1.78E-04
0.01	25.0	142	42.6	0.000	0.010	139	9.26E-05
10.00	40.0	451	42.8	-1.715	0.193	459	5.82E-05
5.00	40.0	342	43.4	-1.715	0.096	346	3.44E-05
2.00	40.0	236	45.0	-1.715	0.039	237	6.65E-06
1.00	40.0	177	46.8	-1.715	0.019	179	4.11E-05
0.50	40.0	126	46.8	-1.715	0.010	137	1.46E-03
0.20	40.0	89	41.1	-1.715	0.004	99	2.01E-03
0.10	40.0	75	39.4	-1.715	0.002	79	6.74E-04
0.05	40.0	64	36.3	-1.715	0.001	65	3.95E-05
0.02	40.0	52	34.4	-1.715	0.000	52	1.23E-05
0.01	40.0	42	31.9	-1.715	0.000	45	7.59E-04

Notes: The first four columns are the data output, and the second four columns are the calculations required to obtain the master curve. Freq: Frequency, Temp: Temperature, DM: Dynamic Modulus, Freq Red: Reduced Frequency, MC DM: Master Curve Dynamic Modulus

The dynamic modulus plot and Black diagram are obtained after the previous calculations and are shown in Figure 5-1. The Black diagram shows the relationship between the dynamic modulus and phase angle.

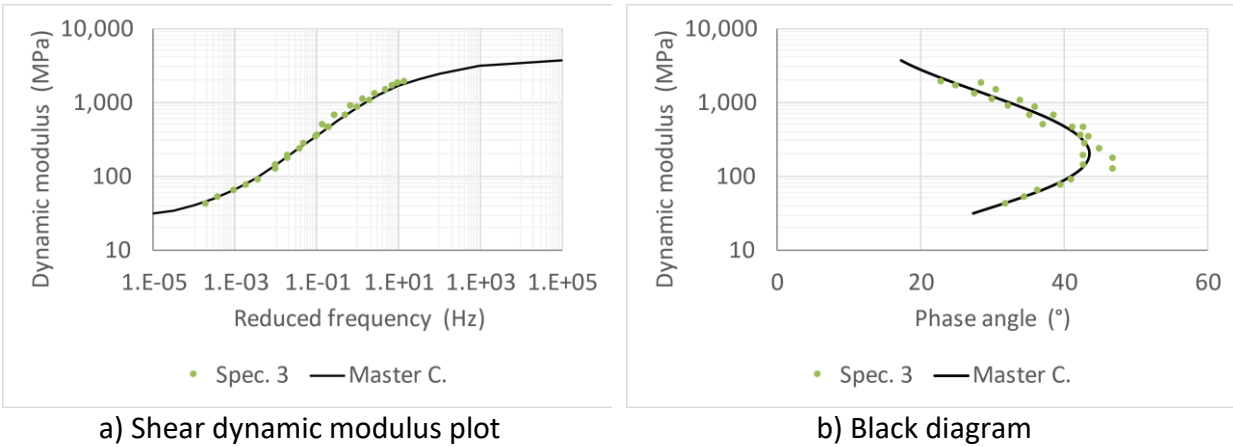


Figure 5-1. HMA shear dynamic modulus test result example

The exact process was followed for three replicate tests of HMA and RHMA-G mixes, and the summary results are shown in Figure 5-2. Figure 5-3 presents a summary plot of the master curves obtained for each of the mixes. The HMA mix is, in general, a stiffer mix over the whole frequency range. The softer behavior of the RHMA-G could be beneficial when used as a base for JPCP and bonded SJPCP-COA pavement structures since a lower stiffness under slow loading will allow the base to accommodate the slab movements.

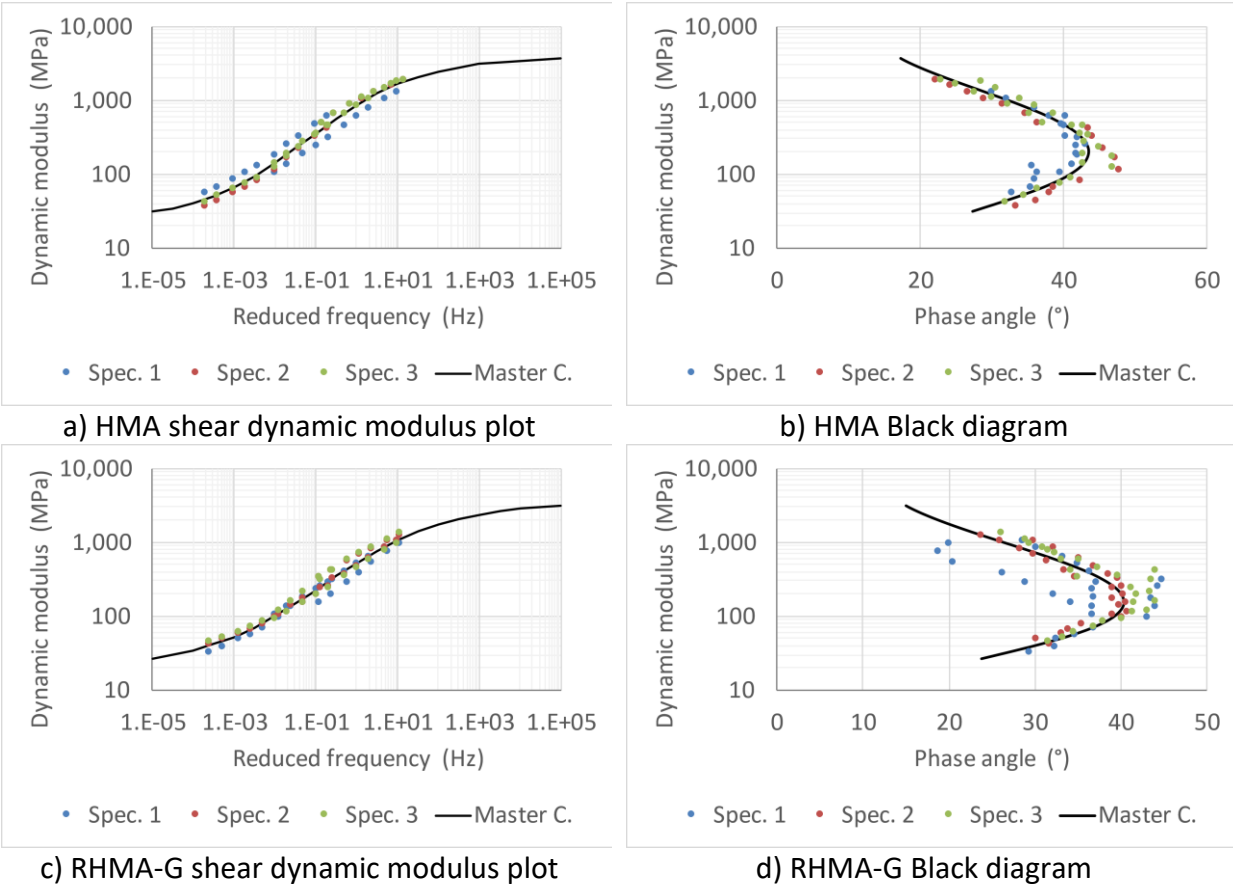


Figure 5-2. Average HMA and RHMA-G shear dynamic modulus test plots

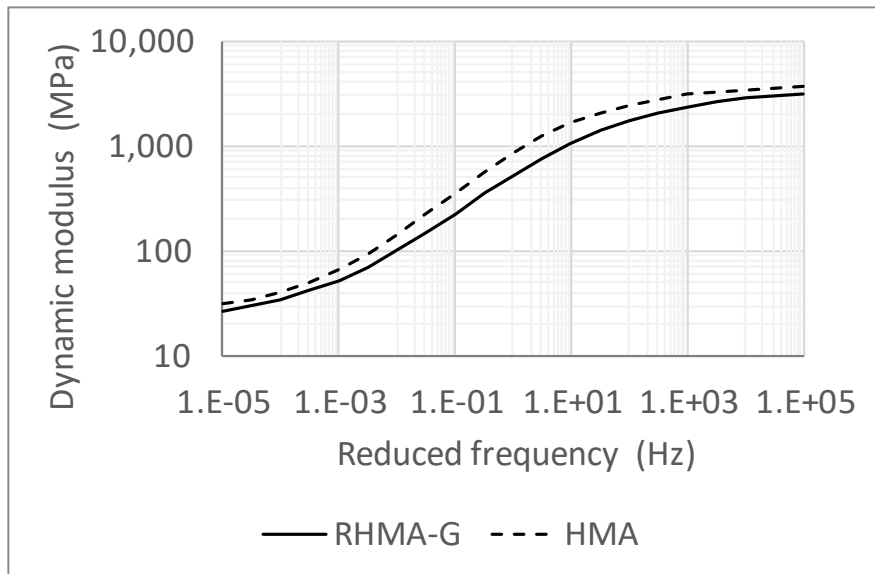


Figure 5-3. Average shear dynamic modulus master curves

5.3.2 Shear Creep

The shear creep test was performed at three different temperatures for each of the specimens since it is a non-destructive test. An additional step needed to be made to produce results similar to those shown for the shear frequency sweep test. The outcome of this test provides time-stamped data for shear stroke displacement, shear load, the reading of four LVDTs, and temperature. A sample of the data is shown in Table 5-3, which corresponds to a RHMA-G sample tested at 25 °C (77 °F). The LVDTs measure at two different depths of the asphalt to eliminate any displacement that occurred in the glue used between the specimen and platens. The distance between both measuring depths is 30 mm.

Table 5-3. Shear creep test data example

			Asph1	Int1	Asph2	Int2	
			LVDT1	LVDT2	LVDT3	LVDT4	
Time	Sh Stroke	Sh Load	Ax LVDT	LVDT 2	Sh LVDT	LVDT 4	Temp
	mm	kN	mm	mm	mm	mm	°C
2021-10-25 13:10:02.662	-0.151	-0.040	0.041	-0.018	-0.016	0.111	25.1
2021-10-25 13:10:02.762	-0.151	-0.040	0.041	-0.018	-0.016	0.111	25.1
2021-10-25 13:10:02.862	-0.151	-0.040	0.041	-0.018	-0.016	0.111	24.9
2021-10-25 13:10:02.962	-0.151	-0.040	0.040	-0.018	-0.016	0.111	25.1
2021-10-25 13:10:03.062	-0.151	-0.039	0.040	-0.018	-0.016	0.111	25.1
2021-10-25 13:10:03.162	-0.150	-0.042	0.041	-0.018	-0.016	0.111	25.2
2021-10-25 13:10:03.262	-0.149	-0.041	0.040	-0.018	-0.016	0.111	25.0
2021-10-25 13:10:03.362	-0.151	-0.041	0.041	-0.018	-0.016	0.111	25.1
2021-10-25 13:10:03.462	-0.152	-0.043	0.041	-0.018	-0.016	0.111	25.1
2021-10-25 13:10:03.562	-0.151	-0.044	0.041	-0.018	-0.016	0.111	25.1

Notes= Asph: Asphalt, Int: Interphase, Sh: Shear, Ax: Axial

Figure 5-4 shows the force and asphalt strain plotted over time for 50 seconds. The additional step mentioned before corresponds to the ϵ -Model curve shown in the figure, which is a model

that is fit to the test result. The explanation of how to obtain this model is shown below. It is a critical step in transforming the data into modulus and phase angle at different frequencies.

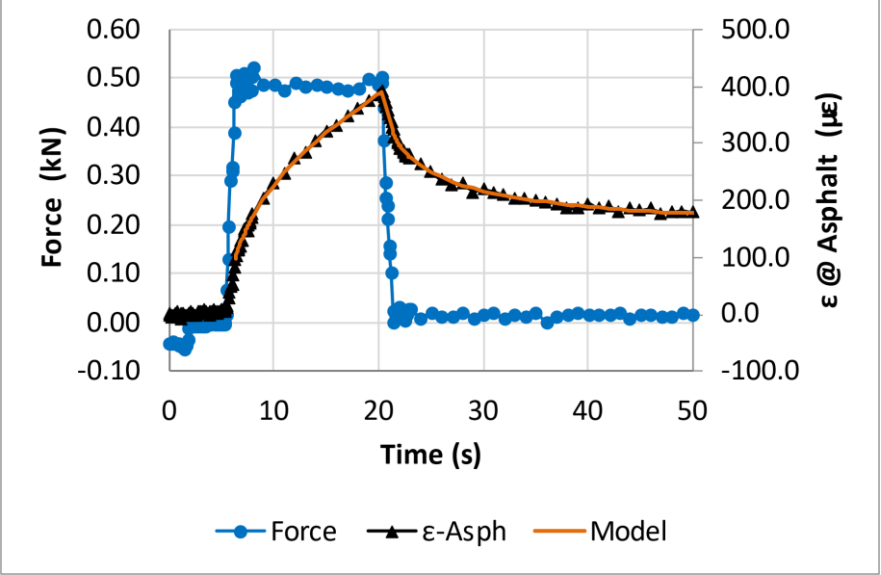


Figure 5-4. Shear creep test plot example

The model used to fit the strain data is a viscoelastic model in which the creep compliance follows the power law and has the following general equation:

$$\epsilon = J_0 + J_1 * (t - t_i)^n \tag{Equation 5}$$

Where,

- J0 Power law constant, consistency index
- J1 Power law constant, intercept
- t Time
- t_i Initial time
- n Power law behavior index

The model is applied for a given stress and temperature, and it is fitted to the test data by minimizing the error between the measured and predicted strain in the calculation by adjusting the viscoelastic parameters of the previous strain equation: J_0 , J_1 , and n . For this case, the values for the parameters were $J_0=394.7$, $J_1=3947.4$, and $n=0.464$. It can be seen in Figure 5-4 that the model is able to describe the test result very accurately. Therefore, it is considered that the process does not add any source of error to the calculations that follow.

Once the parameters (J_0 , J_1 , and n) were obtained, the next step was to calculate the components of the dynamic compliance with the equations shown below.

$$J_{real}^* = J_0 + J_1 * \Gamma(n + 1) * (2\pi * freq)^{-n} * \cos\left(\frac{n\pi}{2}\right) \quad \text{Equation 6}$$

$$J_{imag}^* = -J_1 * \Gamma(n + 1) * (2\pi * freq)^{-n} * \sin\left(\frac{n\pi}{2}\right) \quad \text{Equation 7}$$

$$J = \sqrt{J_{real}^{*2} + J_{imag}^{*2}} \quad \text{Equation 8}$$

$$Phi(J) = \tan^{-1}\left(\frac{J_{imag}^*}{J_{real}^*}\right) * \frac{180}{\pi} \quad \text{Equation 9}$$

Where J_0 , J_1 , and n are the parameters already explained, and $freq$ is the desired frequency at which the calculations were performed. Once the J -values were obtained, the next step was to obtain the dynamic modulus (DM) and phase angle (Φ), which finalizes the data conversion into a format matching the one shown in the shear frequency sweep test. The resulting data are summarized in Table 5-4.

$$DM = \frac{10^6}{J} \quad \text{Equation 10}$$

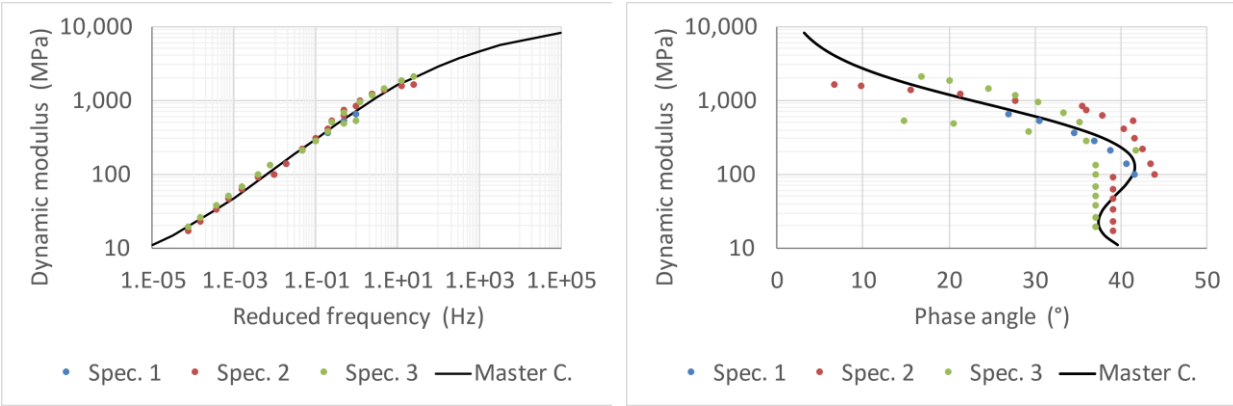
$$\Phi(DM) = -\Phi(J) \quad \text{Equation 11}$$

Table 5-4. Shear creep test processed data example

J0	73.5	freq.	J*(real)	J*(imag)	J	Phi(J)	DM (MPa)	Phi (DM)
J1	4911.3	1	1,582	-1235	2,007	-38.0	498.1	38.0
n	0.437	0.5	2,116	-1671	2,696	-38.3	370.8	38.3
		0.2	3,121	-2493	3,995	-38.6	250.3	38.6
		0.1	4,198	-3375	5,386	-38.8	185.6	38.8
		0.05	5,655	-4567	7,270	-38.9	137.6	38.9
		0.02	8,401	-6814	10,817	-39.0	92.4	39.0
		0.01	11,344	-9223	14,620	-39.1	68.4	39.1

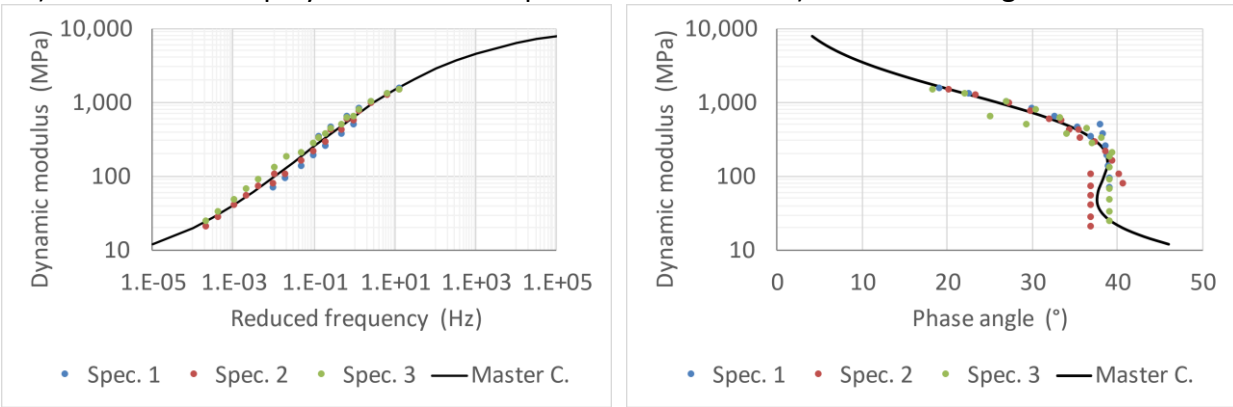
Following the same steps mentioned in the shear frequency sweep test, the following dynamic modulus plots and Black diagram were obtained for each of the mixes analyzed (Figure 5-5). The bottom part of the Black diagram does not follow the typical behavior since one of the simplifications that the creep compliance formula used in the power law model has is that it uses a constant phase angle. This behavior will later be adjusted when calculating the final master curves for FEM modeling.

Figure 5-6 presents a summary plot of the two master curves that were obtained. The HMA mix is stiffer at mid-range frequencies and has a similar stiffness to the RHMA-G mix at the top range of frequencies and at the lowest frequencies. The differences in stiffness are not as noticeable as they were in the previous test, but the RHMA-G mix still has a slightly softer behavior.



a) HMA shear creep dynamic modulus plot

b) HMA Black diagram



c) RHMA-G shear creep dynamic modulus plot

d) RHMA-G Black diagram

Figure 5-5. Average HMA and RHMA-G shear creep test summary

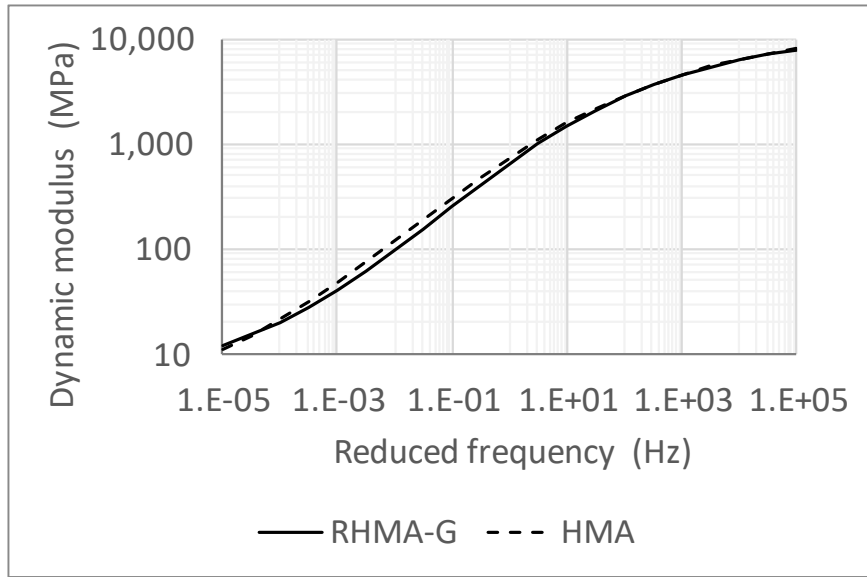


Figure 5-6. Average shear creep dynamic modulus master curves summary

5.3.3 Tensile Creep

The tensile creep test was performed at three different temperatures for each of the specimens since it is a non-destructive test. The tensile creep test data needed to be processed in the same way as the shear creep data. The outcome of this test provides time, actuator displacement, axial force, the reading of three LVDTs, and temperature. A sample of the data is shown in Table 5-5. The three LVDTs for this test measure over the same span, a total length of 100 mm (4 in.). Figure 5-7 shows the force and asphalt strain plotted over time for 50 seconds with the corresponding ϵ -Model curve, which was obtained following the same procedure that was explained in the previous test and shown in Equation 5. After minimizing the error between the measured and predicted strain, the viscoelastic parameters for this particular test were $J_0=421.8$, $J_1=1088.0$, and $n=0.621$.

Table 5-5. Tensile creep test data example

Time (s)	Actuator displ.	Axial force	LVDT1	LVDT2	LVDT3	Temp
	mm	kN	mm	mm	mm	°C
0.1	17.9082	-0.003	-0.110	-0.015	-0.084	24.6
0.2	17.9083	-0.007	-0.110	-0.015	-0.084	24.6
0.3	17.9080	-0.007	-0.110	-0.015	-0.084	24.6
0.4	17.9083	-0.007	-0.110	-0.015	-0.084	24.6
0.5	17.9085	-0.005	-0.110	-0.015	-0.084	24.6
0.6	17.9086	-0.005	-0.110	-0.015	-0.084	24.6
0.7	17.9084	-0.006	-0.109	-0.015	-0.084	24.6
0.8	17.9080	-0.007	-0.109	-0.015	-0.084	24.6
0.9	17.9082	-0.007	-0.109	-0.015	-0.084	24.6
1	17.9082	-0.014	-0.109	-0.015	-0.084	24.6

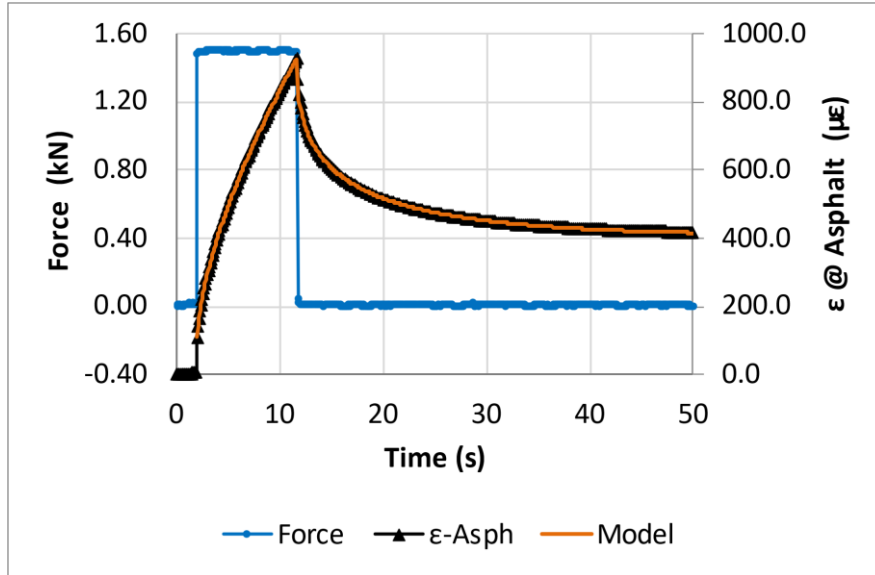


Figure 5-7. Tensile creep test plot example

Once the model was fitted and making use of Equation 6 through Equation 11 the dynamic modulus (DM) and phase angle (Phi) were obtained, which finalizes the data conversion into a format matching the one shown in the shear frequency sweep test. The resulting data are summarized in Table 5-6.

Table 5-6. Tensile creep test processed data example

J0	421.8	freq.	J*(real)	J*(imag)	J	Phi(J)	DM (MPa)	Phi (DM)
J1	1088.0	1	596	-257	649	-23.4	1,538	23.4
n	0.621	0.5	690	-396	796	-29.9	1,255	29.9
		0.2	896	-700	1,137	-38.0	879	38.0
		0.1	1,151	-1076	1,576	-43.1	634	43.1
		0.05	1,544	-1656	2,264	-47.0	441	47.0
		0.02	2,404	-2924	3,786	-50.6	264	50.6
		0.01	3,470	-4497	5,680	-52.4	176	52.4

The process was repeated for all three specimens of each of the mixes, and the dynamic modulus plots and Black diagram were obtained for each material as shown in Figure 5-8.

Figure 5-9 presents a summary plot of the two master curves that were obtained. The HMA mix is stiffer throughout the frequency range and has a greater difference with the RHMA-G at mid-range frequencies. The outcome is very similar to the one obtained in the shear creep test. Still, in this case, the difference seems to be larger, which indicates that the RHMA-G also has a softer behavior in the vertical direction, which would be an ideal behavior when the asphalt bases are exposed to stresses and strains caused by the curling and warping of concrete slabs as was mentioned in the system diagram shown in Figure 1-6.

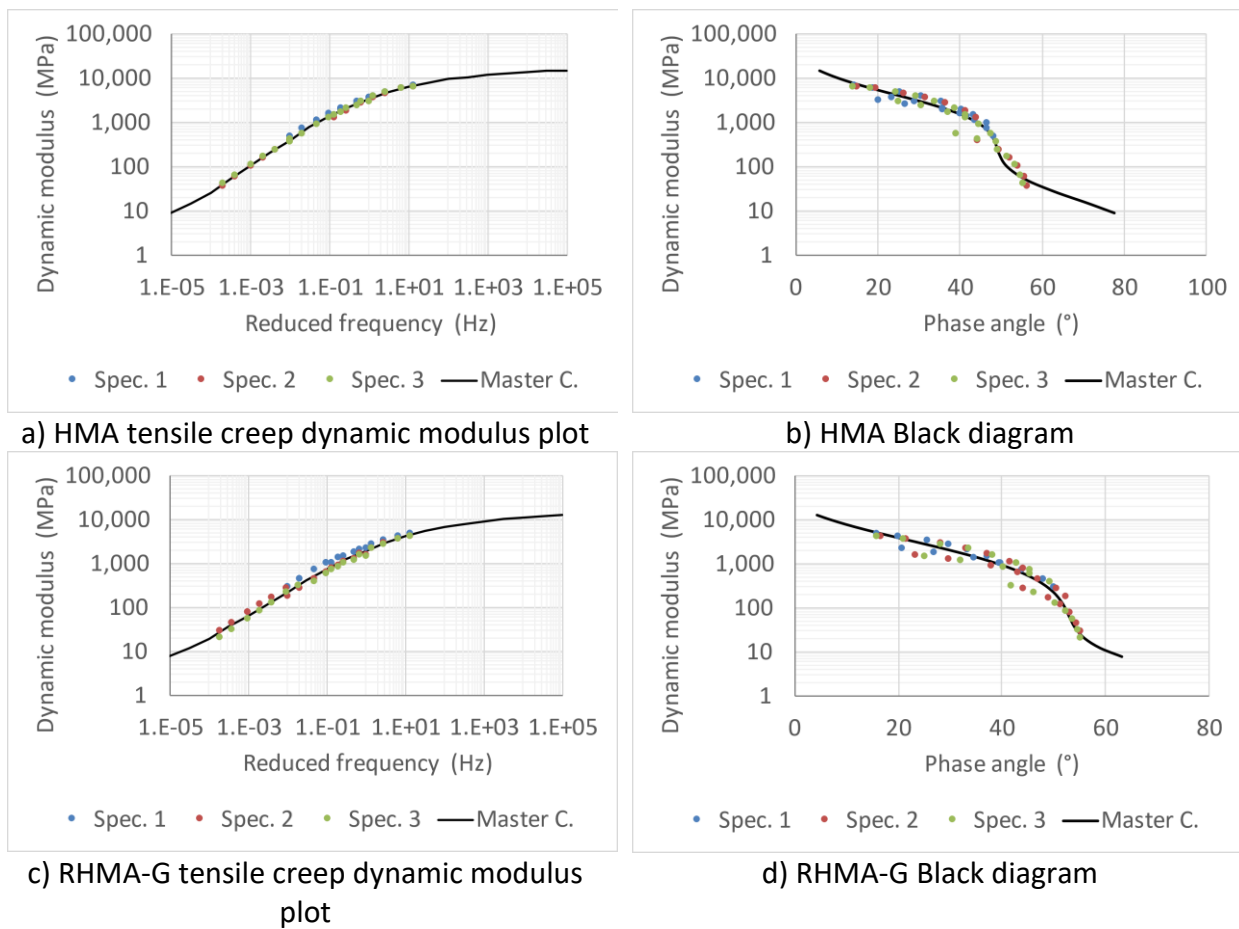


Figure 5-8. Average HMA and RHMA-G tensile creep test

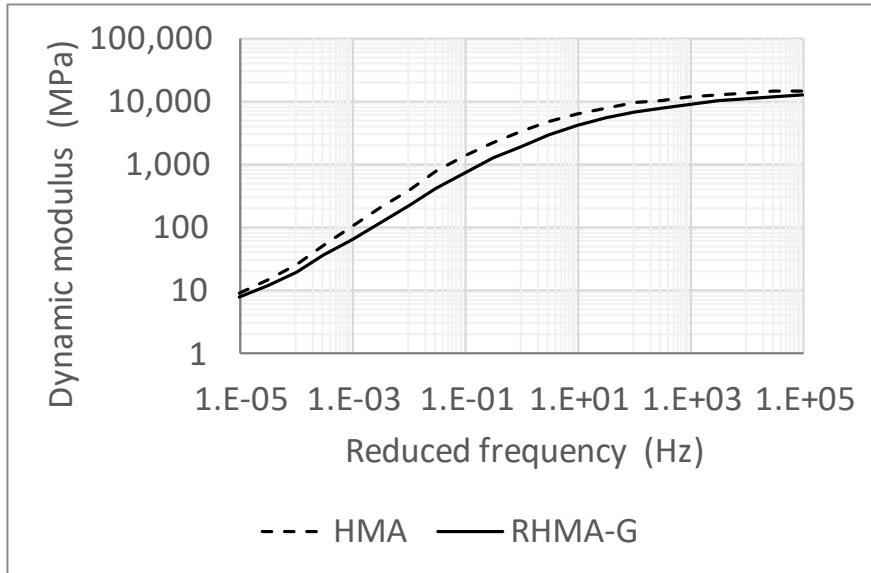


Figure 5-9. Average tensile creep dynamic modulus master curves summary

5.3.4 Tensile Hanging Creep

The tensile hanging creep test is the third and last creep test that was performed on the HMA and RHMA-G materials. This test was only performed at 25 °C (77 °F) since the testing frame sits inside a temperature-controlled room. The analysis process for this test consisted of the same steps followed to analyze the shear creep and tensile creep tests. The major difference between the tensile hanging creep test and the tensile creep test is the testing time; this test is meant to capture the material performance at very low frequencies. The average testing time of this test is between 5 and 10 days, and since it is a long test, the data is only recorded every 5 min. The outcome of this test provides time-stamped data for the 6 LVDTs used. The LVDTs are measuring at two different heights to avoid any possible displacements that occur in the glue used to connect the specimens to the platens. A sample of the data is shown in Table 5-7.

Table 5-7. Tensile hanging creep test data example

	Total1	Total2	Total3	Int1	Int2	Int3
	mm	mm	mm	mm	mm	mm
2021/10/19 12:50	0.000	0.000	0.000	0.000	0.000	0.000
2021/10/19 13:00	0.007	0.000	0.003	0.005	0.007	-0.001
2021/10/19 13:10	0.001	-0.002	0.013	0.006	0.006	0.000
2021/10/19 13:20	0.000	-0.001	0.016	0.005	0.008	-0.001
2021/10/19 13:30	0.013	-0.001	0.023	0.006	0.007	0.000
2021/10/19 13:40	0.006	0.002	0.026	0.005	0.008	0.000
2021/10/19 13:50	0.010	0.004	0.030	0.007	0.008	-0.001
2021/10/19 14:00	0.013	0.005	0.030	0.005	0.007	0.000
2021/10/19 14:10	0.003	0.019	0.034	0.005	0.009	-0.001
2021/10/19 14:20	0.004	0.029	0.039	0.006	0.008	0.000
Note= Int: Interphase						

Figure 5-10 shows the asphalt strain plotted over time for the duration of the test. Unlike the previous tests, the tensile hanging test does not record the applied load because it is just a hanging weight that is placed at the bottom plate. The figure also presents the corresponding ϵ -Model curve, which was obtained following Equation 5. The model can be used to describe the behavior of the force or strain as long as it follows a power function behavior, which is the case for the strain as well. After minimizing the error between the measured and predicted strain, the viscoelastic parameters for this test were $J_0=0$, $J_1=125.9$, and $n=0.621$.

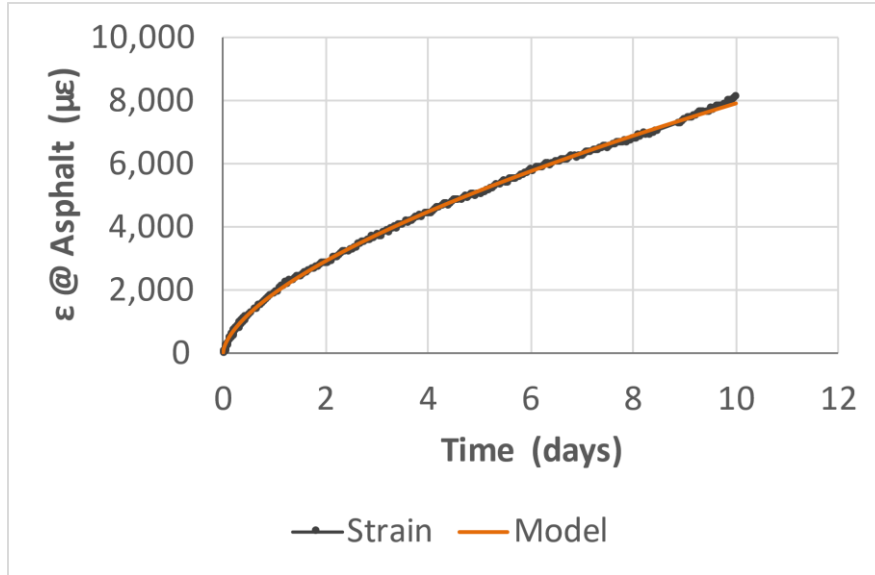


Figure 5-10. Tensile hanging creep test plot example

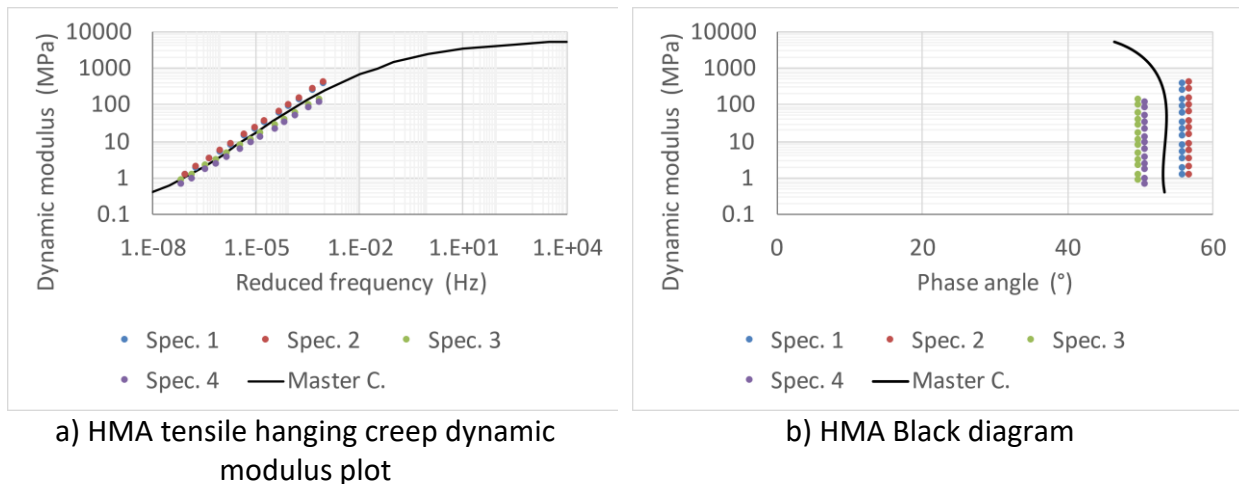
The dynamic modulus (DM) and phase angle (Phi) were obtained using Equation 6 through Equation 11, which finalizes the data conversion into a format matching the one shown in the shear frequency sweep test. The resulting data are summarized in Table 5-8 and compared to previous tests. It should be noted that the frequency range for the tensile hanging creep is lower.

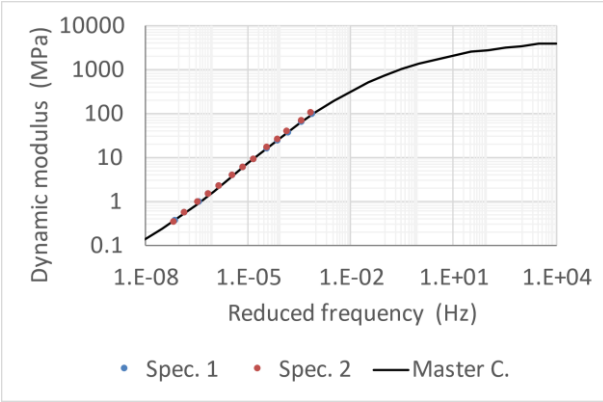
Table 5-8. Tensile hanging creep test processed data example

J0	0.0	freq.	J*(real)	J*(imag)	J	Phi(J)	DM (MPa)	Phi (DM)
J1	125.9	1.00E-03	1,474	-2,179	2,631	-55.9	380.1	55.9
n	0.621	5.00E-04	2,268	-3,351	4,047	-55.9	247.1	55.9
		2.00E-04	4,008	-5,922	7,151	-55.9	139.8	55.9
		1.00E-04	6,165	-9,109	10,999	-55.9	90.9	55.9
		5.00E-05	9,483	-14,012	16,920	-55.9	59.1	55.9
		2.00E-05	16,756	-24,759	29,896	-55.9	33.4	55.9
		1.00E-05	25,774	-38,084	45,986	-55.9	21.7	55.9
		5.00E-06	39,645	-58,581	70,735	-55.9	14.1	55.9
		2.00E-06	70,050	-103,508	124,983	-55.9	8.0	55.9
		1.00E-06	107,750	-159,215	192,249	-55.9	5.2	55.9
		5.00E-07	165,741	-244,905	295,717	-55.9	3.4	55.9
		2.00E-07	292,851	-432,726	522,507	-55.9	1.9	55.9
		1.00E-07	450,462	-665,618	803,718	-55.9	1.2	55.9

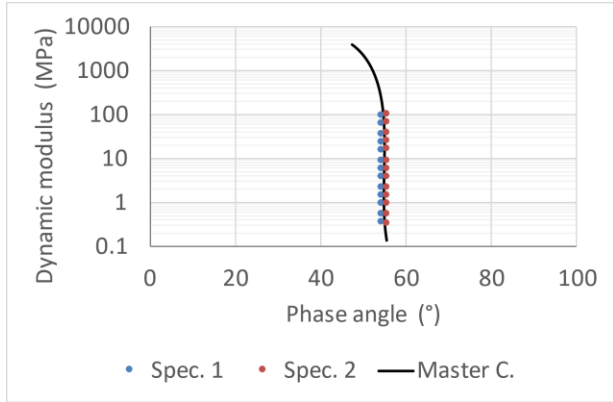
The process was repeated for all three specimens of each of the mixes, and the following dynamic modulus plots and Black diagrams were obtained for each material. Results are shown in Figure 5-11. As explained in the shear creep test, since the creep compliance formula of the power law model uses a constant phase angle, the results of the Black diagram are aligned in a vertical line for each of the specimens.

Figure 5-12 presents a summary plot of the two master curves that were obtained. The HMA mix is stiffer throughout the frequency range. The outcome indicates that the RHMA-G also has a softer behavior in the vertical direction, which could be beneficial when used as a base for concrete pavements. The base low creep vertical stiffness will allow more of the slab to be in contact with the base, reducing the amount of the slab that is in a cantilever condition, therefore reducing tensile stresses, which are critical for the structure as was shown in the system diagram of Figure 1-6.





c) RHMA-G tensile hanging creep dynamic modulus plot



d) RHMA-G Black diagram

Figure 5-11. Average HMA and RHMA-G tensile hanging creep test

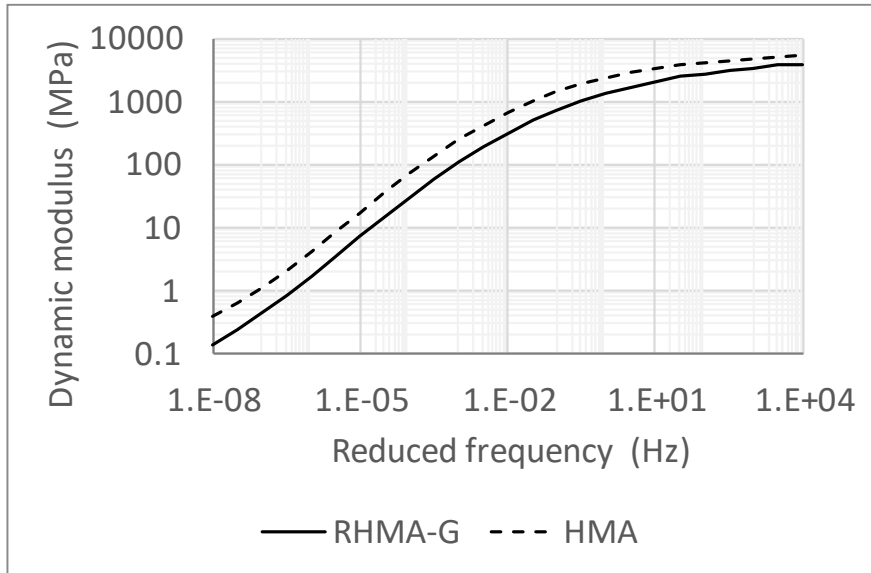


Figure 5-12. Average tensile hanging creep dynamic modulus master curves

5.3.5 Compressive Dynamic Modulus

The compressive dynamic modulus test was performed at five different temperatures and six different frequencies at each temperature, which resulted in a total of 30 stiffness values with different temperature-frequency combinations. Using the time-temperature superposition, a

reduced frequency was obtained for each of the data points, which enabled the data points to spread over a longer reduced frequency range. The output of the test provided the frequency (Freq), temperature (Temp), dynamic modulus (DM), and phase angle (phi). The shift factor, reduced frequencies, and master curve dynamic modulus were calculated once the reference temperature (T_r) was picked with the equations shown in section 2.1. The reference temperature was 25 °C since it is the middle temperature at which the tests were done. The process required the minimization of the error between the test result dynamic modulus and the master curve dynamic modulus. Table 5-9 shows the data for an HMA specimen tested, with the top two rows showing the calibration parameters required for the calculation of the master curve and the summation of the error, which is minimized during the process.

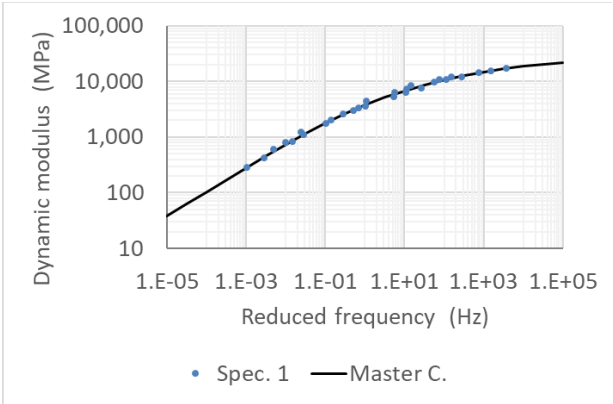
Table 5-9. Compressive dynamic data test result example and calculations

δ	0.020	β	-1.353	C1	-0.103		Error
α	4.477	γ	-0.394	Tr (°C)	25		2.32E-02
Freq	Temp (°C)	DM (MPa)	Phi	log(aT)	Freq red	MC DM (MPa)	Error DM
0.1	4.0	8530	16.0	2.162	1.45E+01	7,371	4.02E-03
0.5	3.9	10,891	13.0	2.179	7.55E+01	10,123	1.01E-03
1	3.8	11,977	12.0	2.186	1.53E+02	11,375	5.02E-04
5	3.9	14,468	10.0	2.177	7.52E+02	14,221	5.58E-05
10	3.9	15,591	9.4	2.174	1.49E+03	15,433	1.95E-05
25	3.9	17,032	8.5	2.172	3.72E+03	16,997	8.05E-07
0.1	15.0	4,423	23.8	1.033	1.08E+00	3,857	3.53E-03
0.5	14.9	6,329	20.0	1.043	5.52E+00	5,923	8.30E-04
1	14.8	7,258	18.6	1.047	1.11E+01	6,959	3.34E-04
5	14.8	9,620	15.4	1.051	5.62E+01	9,610	1.84E-07
10	14.8	10,726	14.3	1.051	1.13E+02	10,826	1.61E-05
25	14.8	12,291	12.8	1.052	2.82E+02	12,465	3.72E-05
0.1	24.9	1,785	29.3	0.008	1.02E-01	1,812	4.50E-05
0.5	24.8	2,977	26.6	0.021	5.25E-01	3,116	3.91E-04
1	24.8	3,588	25.7	0.021	1.05E+00	3,828	7.91E-04
5	24.8	5,398	22.3	0.026	5.30E+00	5,866	1.30E-03

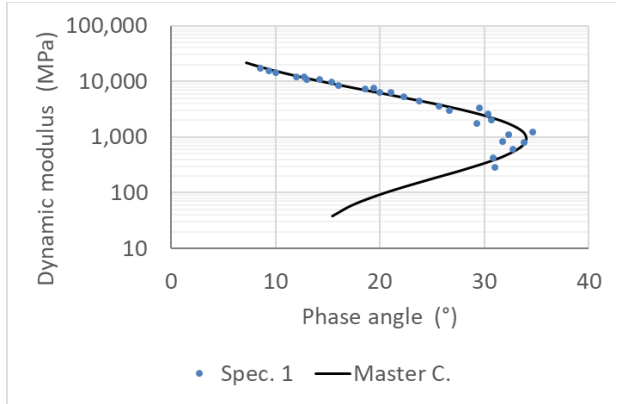
δ	0.020	β	-1.353	C1	-0.103		Error
α	4.477	γ	-0.394	Tr (°C)	25		2.32E-02
Freq	Temp (°C)	DM (MPa)	Phi	log(aT)	Freq red	MC DM (MPa)	Error DM
10	24.7	6,260	21.1	0.027	1.06E+01	6,890	1.74E-03
25	24.7	7,537	19.4	0.028	2.67E+01	8,351	1.98E-03
0.1	39.9	426	30.9	-1.539	2.89E-03	443	3.07E-04
0.5	39.9	830	31.8	-1.533	1.47E-02	871	4.34E-04
1	40.0	1,093	32.3	-1.541	2.88E-02	1,135	2.75E-04
5	40.0	2,062	30.7	-1.546	1.42E-01	2,037	2.94E-05
10	40.0	2,569	30.4	-1.548	2.83E-01	2,564	8.62E-07
25	40.0	3,380	29.5	-1.549	7.06E-01	3,408	1.27E-05
#N/A	#N/A	#N/A	#N/A	#N/A	#N/A	#N/A	#N/A
#N/A	#N/A	#N/A	#N/A	#N/A	#N/A	#N/A	#N/A
1	54.0	287	31.0	-2.985	1.04E-03	284	2.39E-05
5	54.1	604	32.8	-2.998	5.02E-03	560	1.06E-03
10	54.1	816	33.8	-3.002	9.95E-03	744	1.58E-03
25	54.2	1,212	34.6	-3.004	2.47E-02	1,071	2.89E-03
Note= Freq: Frequency, Temp: Temperature, DM: Dynamic Modulus, Freq Red: Reduced Frequency, MC DM: Master Curve Dynamic Modulus							

The dynamic modulus plot and Black diagram are obtained after the previous calculations and are shown in Figure 5-13. The Black diagram represents the relationship between the dynamic modulus vs phase angle, as can be seen in Figure 5-13b.

The same process was followed for three replicate tests of HMA and RHMA G mixes, and the summary results are shown in Figure 5-14.

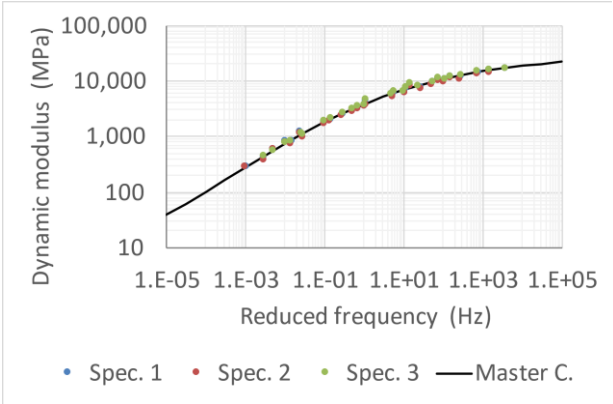


a) Dynamic modulus plot

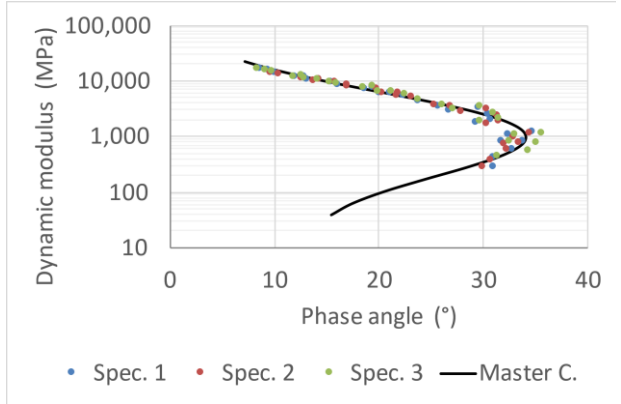


b) Black diagram

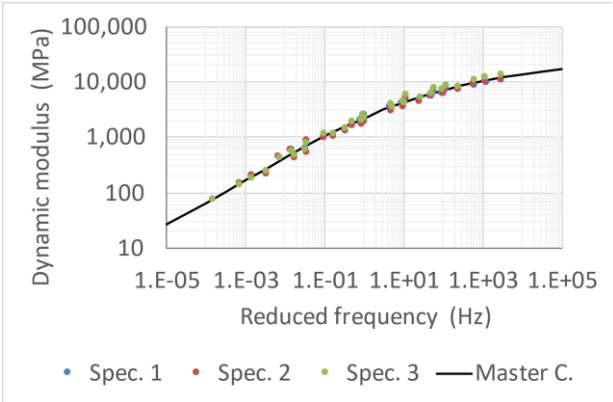
Figure 5-13. HMA compressive dynamic modulus test example



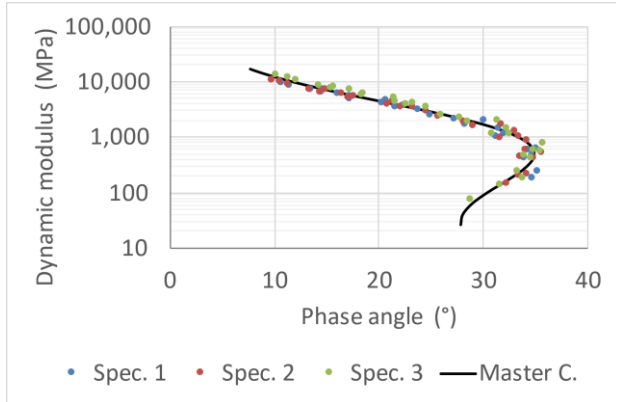
a) HMA dynamic modulus plot



b) HMA Black diagram



c) RHMA-G dynamic modulus plot



d) RHMA-G Black diagram

Figure 5-14. Average HMA and RHMA-G compressive dynamic modulus test

Figure 5-15 presents a summary plot of the two master curves that were obtained. The HMA mix is, in general, a stiffer mix over the whole frequency range, which is expected and matches the result obtained for the shear frequency sweep test. The softer behavior of the RHMA-G proves that it is a good candidate for use as a base for JPCP and bonded SJPCP-COA pavement structures since it will work as a cushion to absorb the slab deformations due to the lower stiffness under slow loading. The base low creep vertical (compressive) stiffness will allow more of the slab to be in contact with the base, reducing the amount of the slab that is in a cantilever condition, therefore reducing tensile stresses, which are critical for the structure as was shown in the system diagram of Figure 1-6.

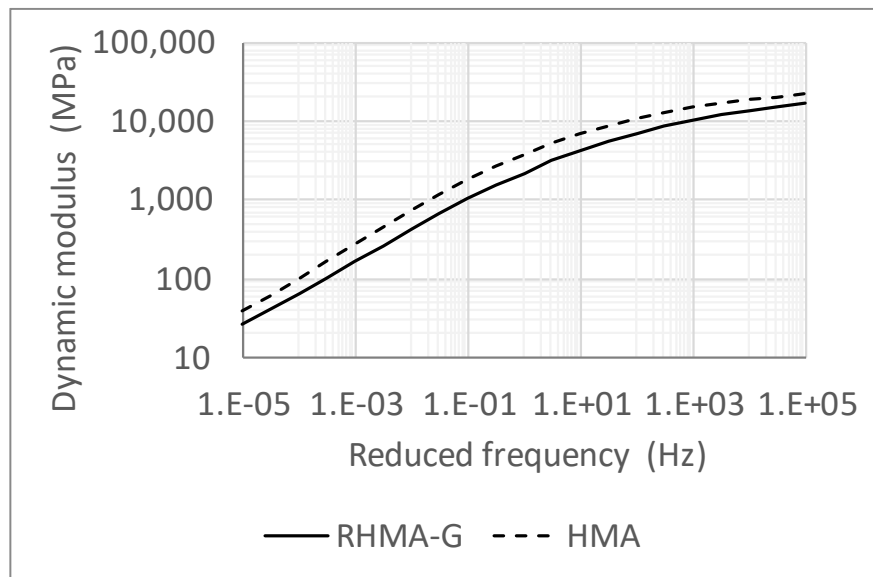


Figure 5-15. Average compressive dynamic modulus master curves

5.3.6 Stiffness Data for Modeling

The stiffness properties for the HMA and RHMA-G mixes were analyzed through five different tests, with each of them giving a characteristic dynamic modulus plot and a Black diagram. The FEM modeling that will be detailed in Chapter 8 considers the asphalt as a linear viscoelastic

material to account for the creep/relaxation capacity of the asphalt material. The software used for the FEM modeling was Abaqus and uses the Generalized Maxwell model (GMM), also known as Maxwell-Weichert model, as the linear viscoelasticity model. The GMM consists of a series of single Maxwell models placed in parallel, as can be observed in Figure 5-16. The viscoelastic materials are defined in Abaqus independently for shear and bulk stiffness, which means that two GMM models were defined for HMA and RHMA-G.

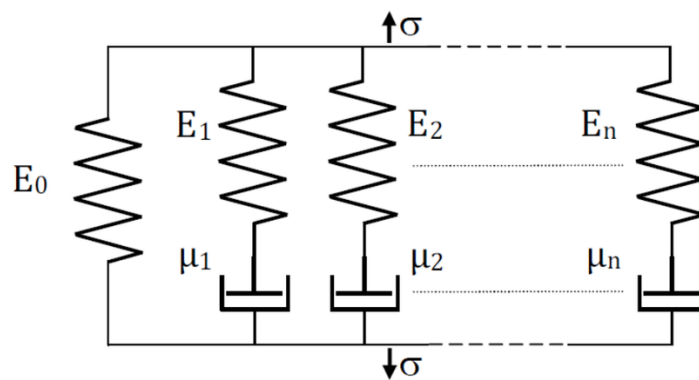


Figure 5-16. Generalized Maxwell model

The dynamic modulus plots and Black diagrams obtained in the tests summarized in sections 5.3.1 through 5.3.5 were used to determine the parameters of the GMM. The complex shear modulus (G^*) and the complex bulk modulus (K^*) need to be defined when using Abaqus' GMM; therefore, a simplification of the model was used. Most of the viscoelasticity of an asphalt mix is attributed to its shear stiffness. For this reason, a reasonable approach for modeling this material is assuming that its bulk modulus is linear elastic (constant versus frequency) while its shear modulus is linear viscoelastic [23, 48]. The bulk modulus (K^*) is defined as in linear elastic theory:

$$K^* = \frac{E_g}{3 * (1 - 2\nu_g)} \quad \text{Equation 12}$$

Where,

E_g Young's modulus at infinite frequency, maximum modulus

ν_g Poisson's ratio at infinite frequency, assumed to be 0.1

The bulk modulus (K^*) was obtained using the assumed Poisson's ratio at an infinite frequency of 0.1 and the maximum Young's modulus. The complex shear modulus (G^*) was calculated for each frequency after the bulk modulus (K^*) was obtained using the following equation:

$$G^* = \frac{3K^*E^*}{9K^* + E^*} \quad \text{Equation 13}$$

Where,

E^* Young's modulus at each frequency

K^* Bulk modulus, constant

Finally, the parameters for the GMM were obtained using the G^* . The model used consisted of 20 parallel elements following the distribution shown in Figure 5-16 and each element had a fixed relaxation time (G_i/η_i) and the G_i values were back-calculated. The chosen range for the relaxation times was between 10^{-6} and 10^8 seconds since that was the range of reduced frequencies of the laboratory tests. Figure 5-17 provides a summary of the steps mentioned above to obtain the parameters for the asphalt viscoelastic model.

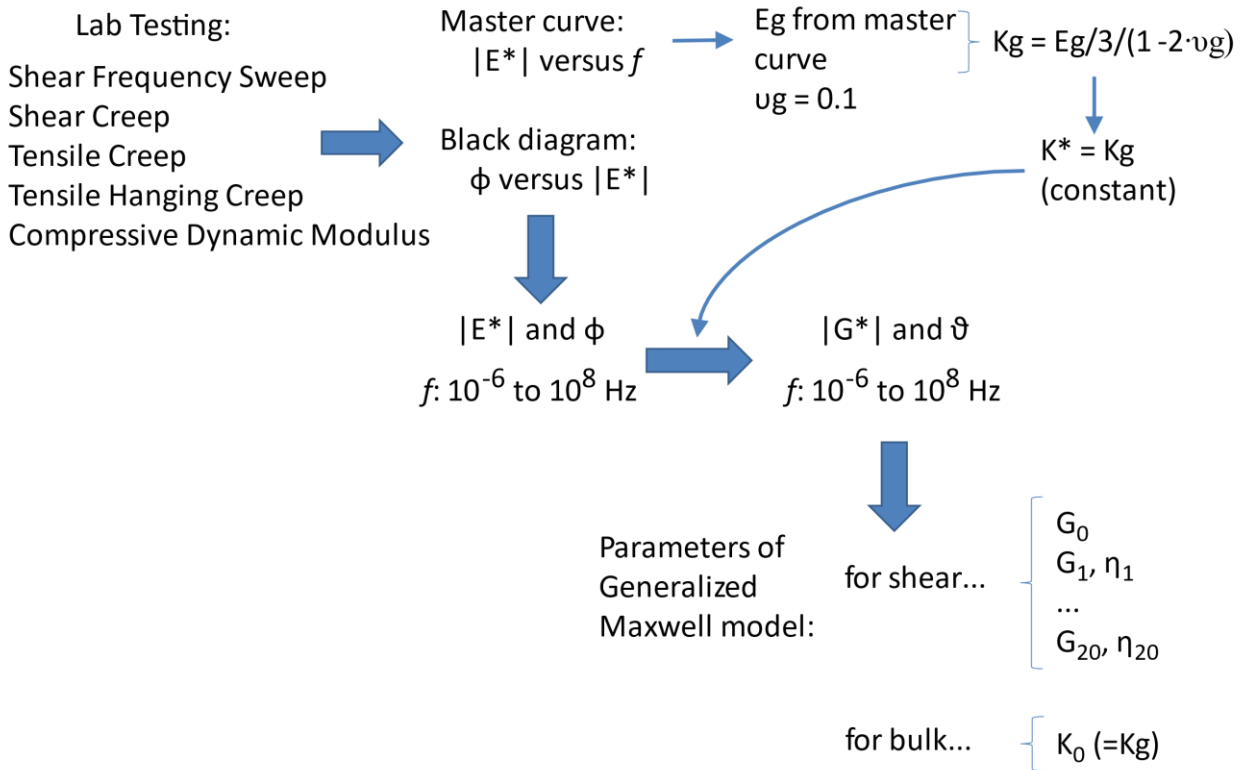
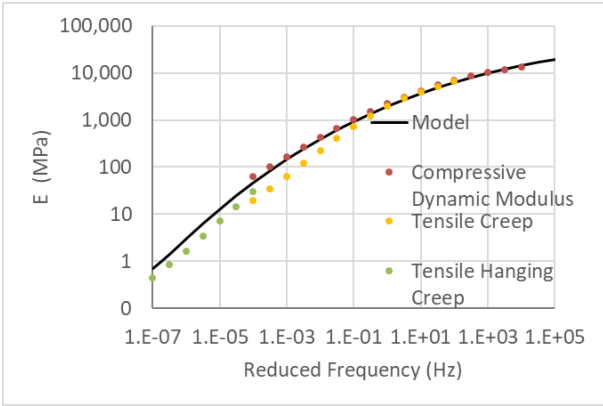


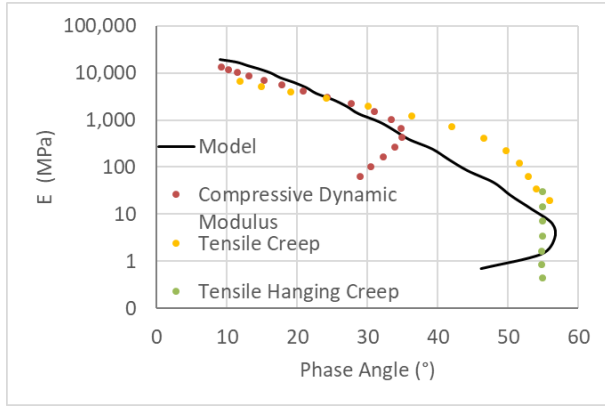
Figure 5-17. Approach for determining the parameters of the asphalt viscoelastic model [23, edited]

5.3.7 Stiffness Tests Summary

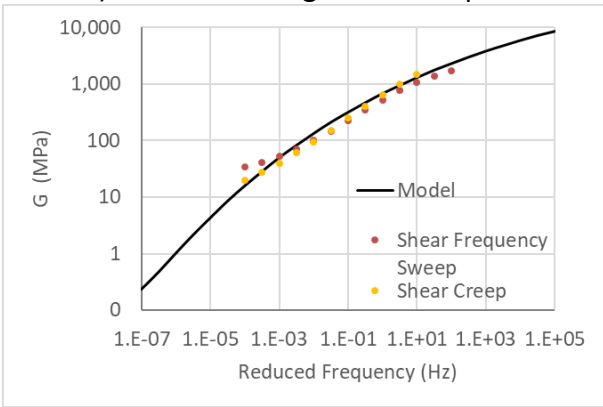
The summary plots for the master curves and black diagrams are shown in Figure 5-18 and Figure 5-19 for RHMA-G and HMA, respectively. As can be seen from the summary plots, the different test results for both materials follow the same trend, which allowed the master curves to describe the behavior of the materials with a very good agreement. This aspect is beneficial for FEM modeling since one set of parameters can adequately describe the material behavior across the range of stress states, times of loading, and temperatures needed to model concrete pavement on asphalt bases. The differences observed in modulus and phase angle within the different tests are due to the differences in testing temperature and loading frequencies used in each test.



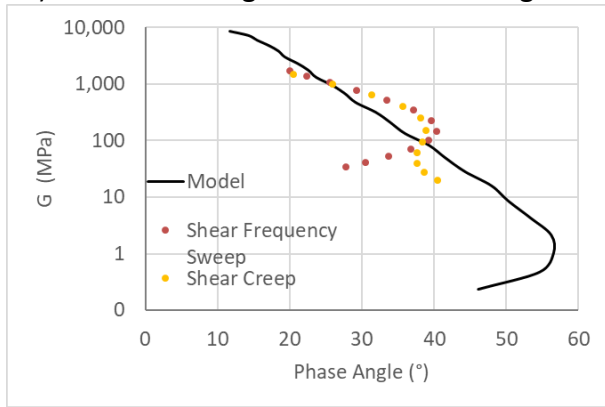
a) RHMA-G Young's modulus plot



b) RHMA-G Young's modulus Black diagram



c) RHMA-G shear modulus plot



d) RHMA-G shear modulus Black diagram

Figure 5-18. RHMA-G stiffness summary plots combining results from different tests for shear and tension/compression

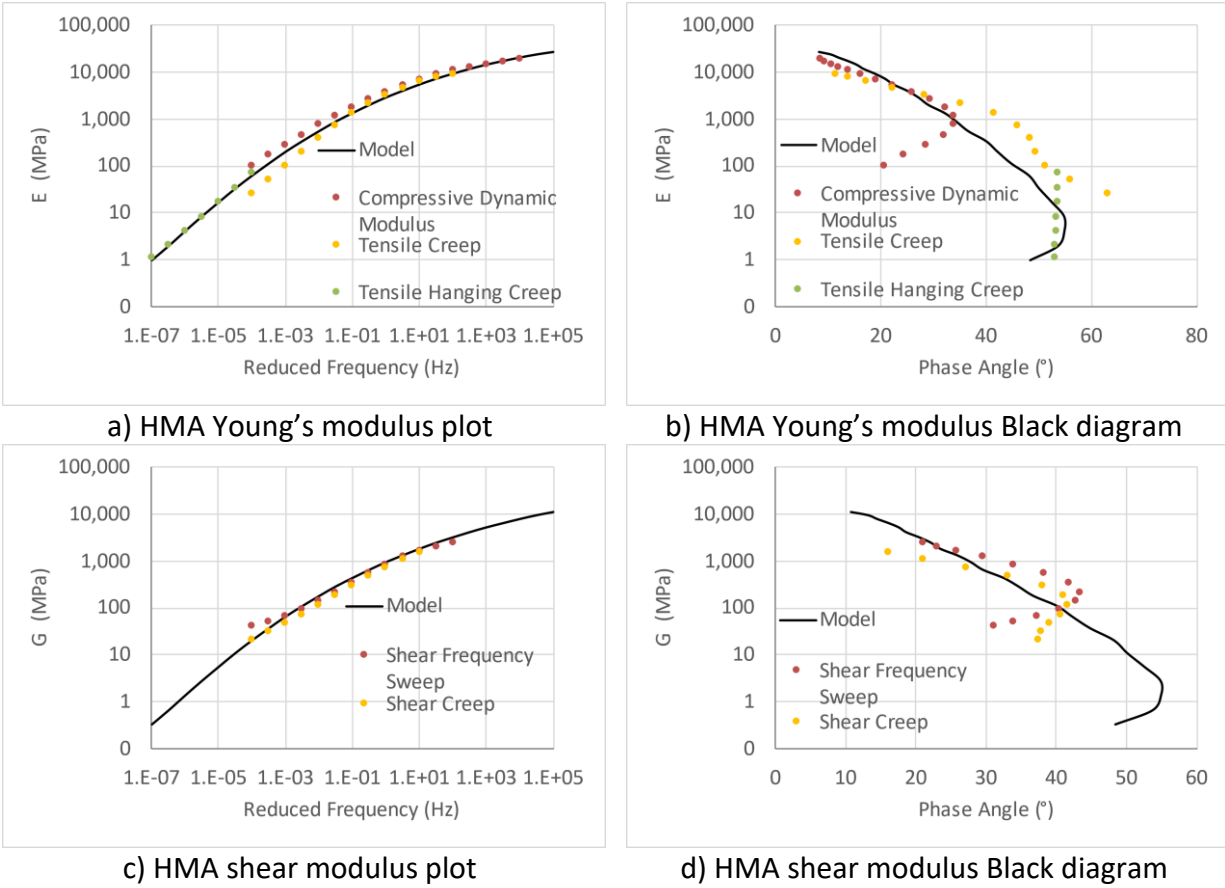
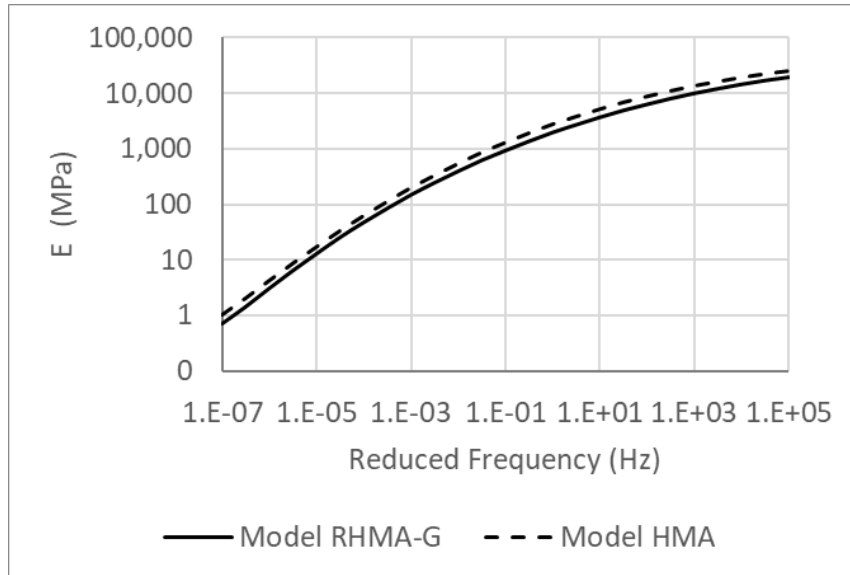


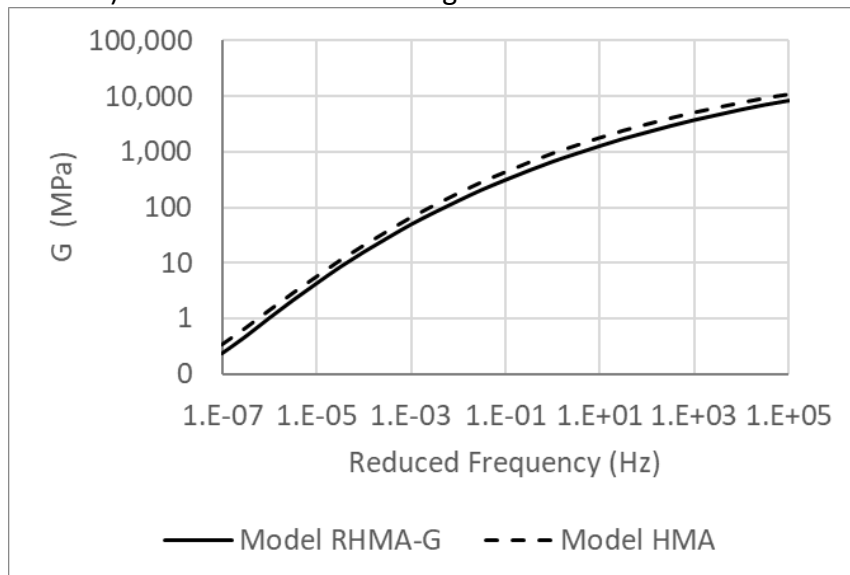
Figure 5-19. HMA stiffness summary plots combining results from different tests for shear and tension/compression

A summary plot for master curves is shown in Figure 5-20. The behavior observed in each test result is also included in the overall model, which includes all test data from five different stiffness tests. The RHMA-G mix has a lower Young's modulus and shear modulus compared to the HMA mix, which suggests that it can perform better as a base for JPCP and bonded SJPCP-COA since the material would have a softer behavior, allowing it to accommodate better the stresses and strains caused by the concrete slabs when exposed to temperature gradients and uniform temperature changes (illustrated in Figure 2-4). Having the ability to follow the concrete movements enables the structure to be better supported and enhances the ability to transfer the

loads to the layers beneath. Having said this, the RHMA-G seems to have the behavior of an ‘ideal base’ material for rigid pavements, as was mentioned in Sections 1.1.1.3 and 1.1.4.



a) RHMA-G and HMA Young's modulus master curve



b) RHMA-G and HMA shear modulus master curve

Figure 5-20. RHMA-G and HMA master curves for modeling

Table 5-10 and Table 5-11 contain values for Young’s modulus and shear modulus extracted from the previously shown master curves for several frequencies of interest to be able to compare the actual values for each type of mix. The HMA is, in general, stiffer than the RHMA-G for both Young’s modulus and shear modulus. The tables also show the percentual differences, which are between 32 and 45 percent in both cases.

Table 5-10. RHMA-G and HMA Young’s modulus summary values

Frequency		RHMA-G	HMA	Difference between HMA and RHMA-G
Maximum	1.00E+05	17179.5	22730.2	32%
Traffic loads	2.00E+01	3728.6	5271.6	41%
Daily environment loads	1.16E-05	12.9	17.2	33%
Minimum	1.00E-07	0.7	1.0	45%

Table 5-11. RHMA-G and HMA shear modulus summary values

Frequency		RHMA-G	HMA	Difference between HMA and RHMA-G
Maximum	1.00E+05	7149.2	9516.6	33%
Traffic loads	2.00E+01	1295.6	1839.0	42%
Daily environment loads	1.16E-05	4.3	5.7	33%
Minimum	1.00E-07	0.2	0.3	45%

5.4 Strength Test Results and Analysis

Three different tests were used to characterize the strength and capacity to deform under slow loading of asphaltic materials, with two tests in tension and one test in shear. The tests are tensile hanging damage, tensile ramp, and shear ramp. The duration of the tensile hanging damage test was about 1 to 3 days, while the duration of the tensile and shear ramp tests was limited to three hours for the fast test, 30 hours for the slow tensile ramp test, and 9 hours for the slow shear

ramp test. Initially, it was planned to only do the tensile ramp and shear ramp tests for a maximum duration of 3 hours since it uses hydraulic equipment, but after running some trials, it was determined that the UTM was able to perform tests of up to 30 hours and the SST was able to do up to 9 hours. A summary of all testing conditions is presented in Table 5-12.

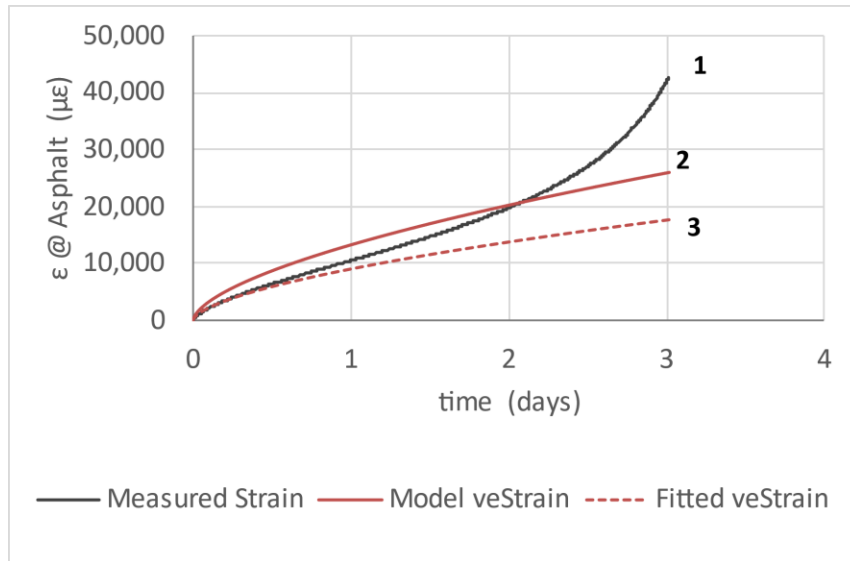
Table 5-12. Strength testing conditions

Test	Temperature, °C (°F)	Duration
Tensile Ramp	15 (59)	3 hrs
		30 hrs
	25 (77)	3 hrs
		30 hrs
	40 (104)	3 hrs
		30 hrs
Shear Ramp	15 (59)	3 hrs
		9 hrs
	25 (77)	3 hrs
		9 hrs
	40 (104)	3 hrs
		9 hrs
Tensile Hanging Damage	25 (77)	1-3 days

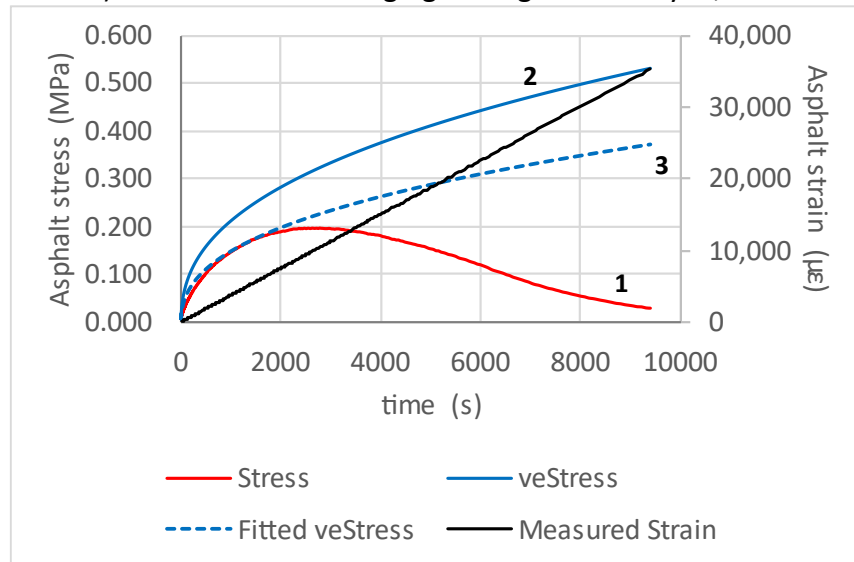
The analysis process followed in the three tests is the same; therefore, an explanation of the procedure will be provided, followed by the results for each test in the following subsections. The analysis relies on having previously analyzed the three creep tests that were explained in section 5.3. The viscoelastic parameters, J_0 , J_1 , and n , obtained in those tests were used to estimate a theoretical undamaged curve. The theoretical undamaged curve represents the behavior of the creep test, which assumes that no damage was caused since the tests were performed at deformations under 0.1 percent, which were assumed to cause only recoverable creep since such deformation level is in the LVER of the materials. The theoretical undamaged curve required a

fitting parameter to describe each test, and then the integrity parameter was calculated as the measured value divided by the fitted undamaged value. Figure 5-21a and Figure 5-21b show a couple of plots that were obtained following the process just mentioned, and the different curves were labeled with step numbers as follows:

1. Test result can be a strain curve from the tensile hanging damage test (load-controlled test) or a stress curve from the tensile ramp or shear ramp tests (deformation-controlled tests).
2. Model veStrain or model veStress, which corresponds to the theoretical undamaged curve using the viscoelastic parameters obtained from the creep tests. Since the viscoelastic parameters were obtained from the average of three or more tests, the Model veStrain or Model veStress is likely not to perfectly match the test result without a fitting parameter.
3. Fitted veStrain or fitted veStress, which corresponds to a fitting done to the veStrain or veStress, to describe each particular curve through the undamaged portion of the test.



a) RHMA-G tensile hanging damage test analysis, 25°C



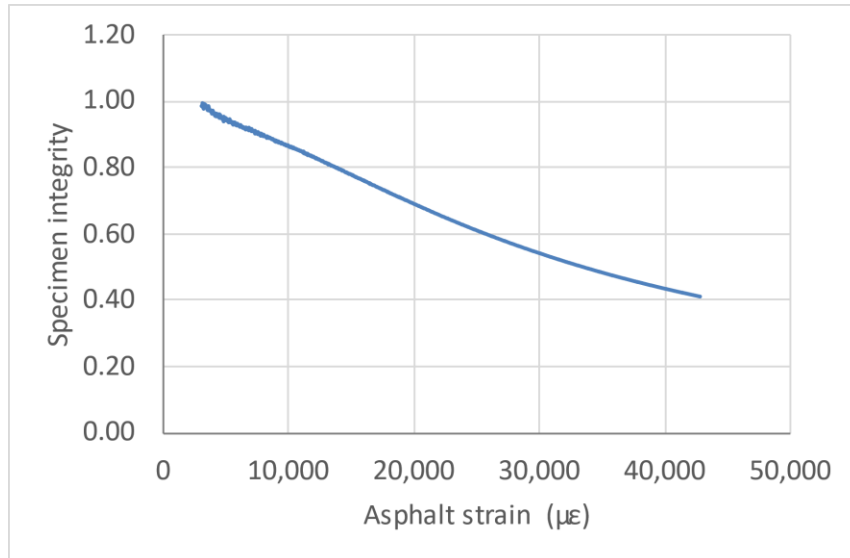
b) HMA tensile ramp test analysis, 25 °C

Figure 5-21. Strength test analysis examples

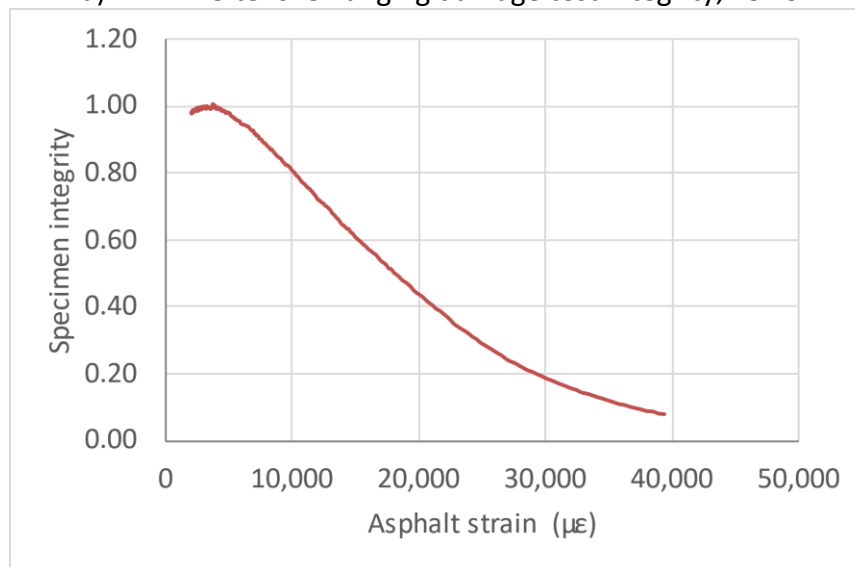
The final step of the analysis consisted of calculating the ratio of the measured value divided by the fitted undamaged value (Curve 1 divided by Curve 3), which is referred to as integrity. The integrity is a non-dimensional value given to every step of the test that describes the level of damage a specimen has, and it ranges from 1 (undamaged) to close to 0 (completely damaged). The integrity parameter was plotted against strain for the tensile hanging damage test and the

tensile ramp test and provides a direct relationship of what the strain level is for a given integrity.

The integrity plots for the two tests are shown in Figure 5-21 and Figure 5-22.



a) RHMA-G tensile hanging damage test integrity, 25 °C



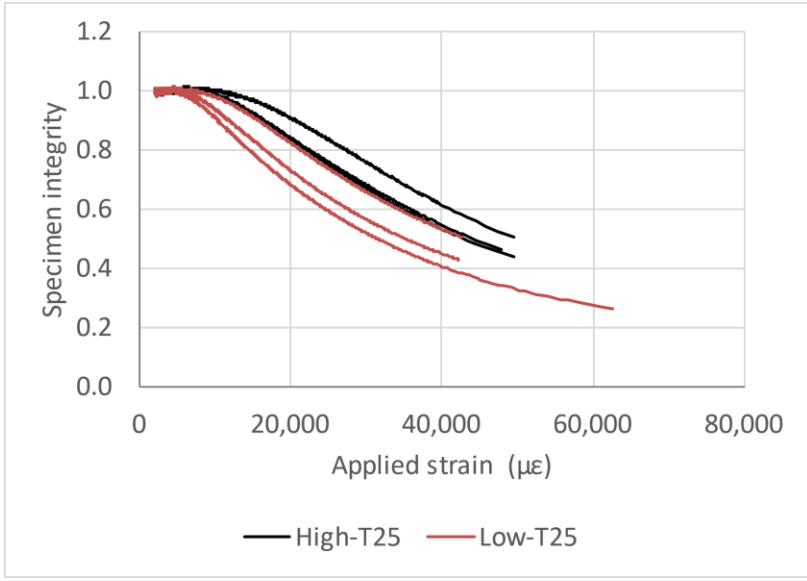
b) HMA tensile ramp test analysis, 25 °C

Figure 5-22. Integrity plot examples

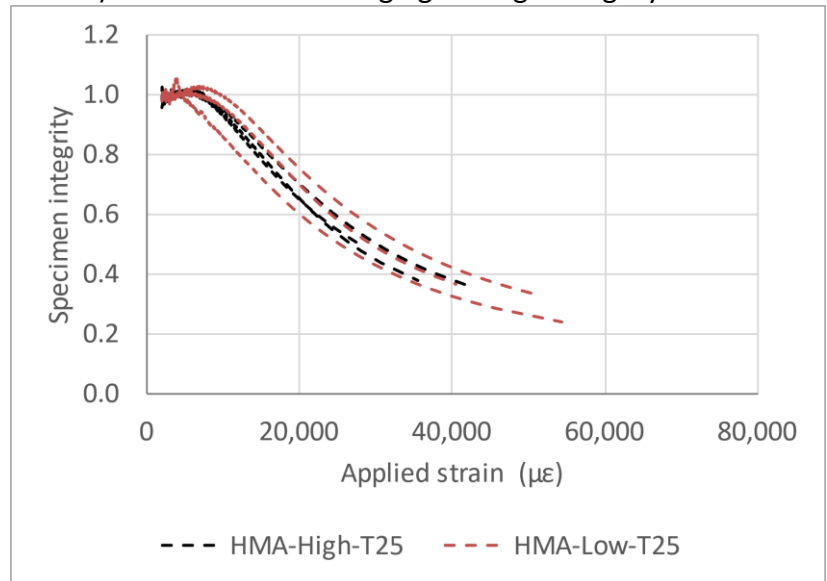
5.4.1 Tensile Hanging Damage

The tensile hanging damage test was done only at 25 °C (77 °C), as was previously shown in Table 5-12. The tests were done at two different load levels to reduce the testing time and study the effect of the loading magnitude on the material behavior. Initially, it was done at 17 and 22 kg (37.5 and 48.5 lb) for the RHMA-G and HMA, respectively. For the second set of tests, the loads were increased by 10 kg (22 lb), for a total of 27 and 32 kg (59.5 and 70.5 lb), respectively. The testing scenarios are referred to as low and high for the lower and higher load, respectively. Figure 5-23 shows the integrity curves obtained for the RHMA-G and HMA mixes. It can be seen from the plots that the load level does not affect the HMA mix, while for the RHMA-G, the effect is less conclusive since there appear to be a couple of tests that are clearly different while the others have similar behavior.

A summary plot is shown in Figure 5-24 to compare the differences between both mixes knowing that the HMA is a more brittle mix compared to the RHMA-G mix, which corresponds to its greater stiffness. The plot supports that idea since the integrity of an HMA specimen is lower than the integrity of an RHMA-G at a certain strain level. For example, at an integrity level of 0.5, the average strain for the HMA mix is close to 30,000 $\mu\epsilon$, while it is close to 43,000 $\mu\epsilon$ for the RHMA-G. This means that the RHMA-G mix can take, on average, 43 percent more vertical deformation than the HMA mix when reaching an integrity level of 50 percent, which can be beneficial when used as a base for concrete pavements and dealing with the curling and warping of concrete slabs due to the effect of vertical temperature and humidity gradients in the slabs as was previously shown in Figure 1-6.



a) RHMA-G tensile hanging damage integrity curves



b) HMA tensile hanging damage integrity curves

Figure 5-23. Integrity curves for tensile hanging damage test

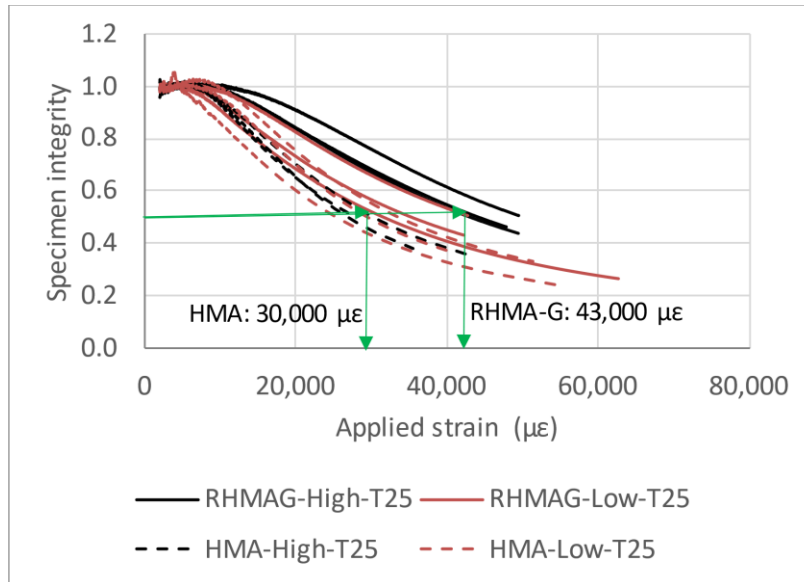
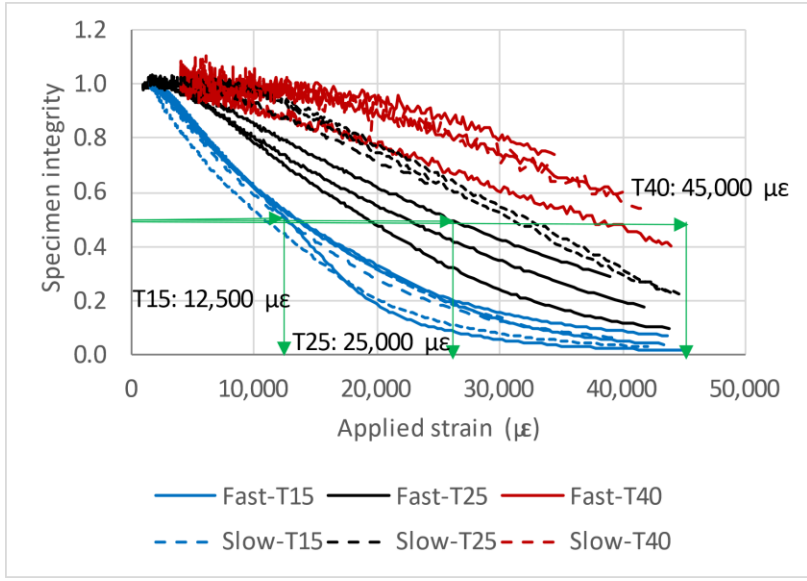


Figure 5-24. Summary of integrity curves for tensile hanging damage test for HMA and RHMA-G mixes

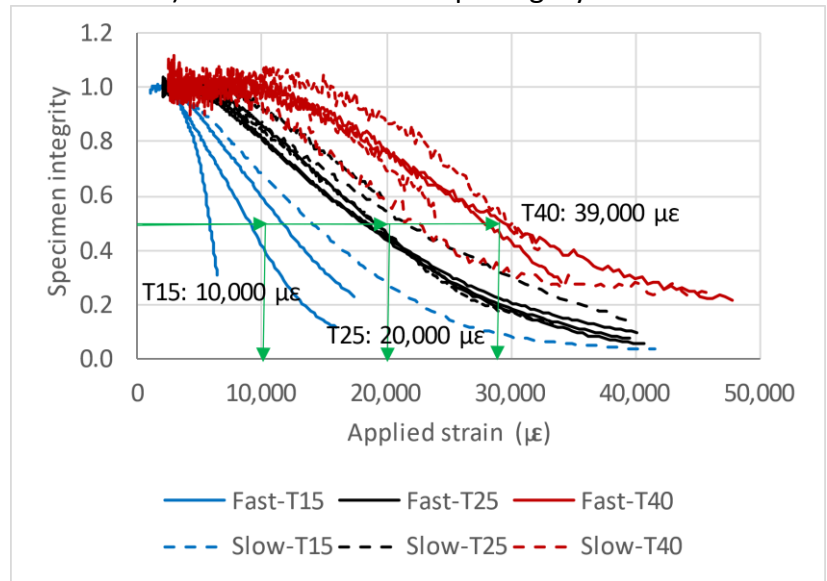
5.4.2 Tensile Ramp

The tensile ramp test was done at three temperatures: 15, 25, and 40 °C (59, 77, and 104 °F) as shown in Table 5-12. Two different testing times were used at each temperature: 3 and 30 hours. The testing scenarios are referred to as fast and slow for the 3 and 30 hours, respectively. Figure 5-25 shows the integrity curves obtained for the RHMA-G and HMA mixes.

It can be seen from the plots that the temperature variable had a noticeable effect on the integrity curves. For the RHMA-G mix, a 50 percent integrity was achieved at 45,000 μϵ at 40 °C (104 °F), at 25,000 μϵ at 25 °C (77 °F) and at 12,500 μϵ at 15 °C (59 °F). Similarly, for the HMA mix, it was achieved at 39,000 μϵ at 40 °C (104 °F), at 20,000 μϵ at 25 °C (77 °F) and at 10,000 μϵ at 15 °C (59 °F). Testing length only had an effect at 25 °C (77 °F) for the RHMA-G mix and at 15 °C (59 °F) for the HMA, at all other temperatures, the testing results suggested that there was no effect of the length of testing in the evolution of the integrity.



a) RHMA-G tensile ramp integrity curves



b) HMA tensile ramp integrity curves

Figure 5-25. Summary of integrity curves for tensile ramp test for HMA and RHMA-G mixes

When analyzing the deformation levels obtained for each temperature at an integrity of 50 percent, similar behavior was observed compared with the one seen in the tensile hanging damage test. On average, the RHMA-G mix takes between 15 and 25 percent more vertical strain than the HMA mix, depending on the temperature. Table 5-13 shows a summary of the results.

Table 5-13. Strain levels at 50 percent integrity for tensile ramp test compared for HMA and RHMA-G

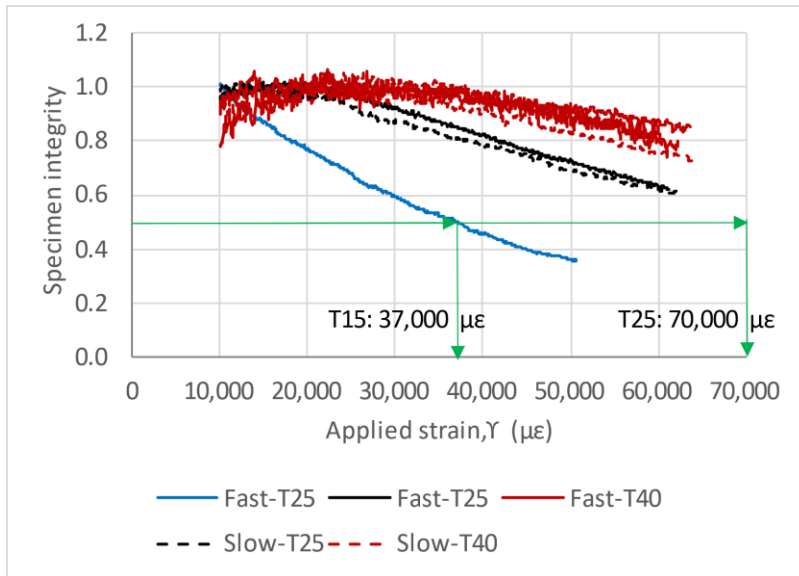
	T15	T25	T40
HMA	10,000	20,000	39,000
RHMA-G	12,500	25,000	45,000
Difference between HMA and RHMA-G	25%	25%	15%

5.4.3 Shear Ramp

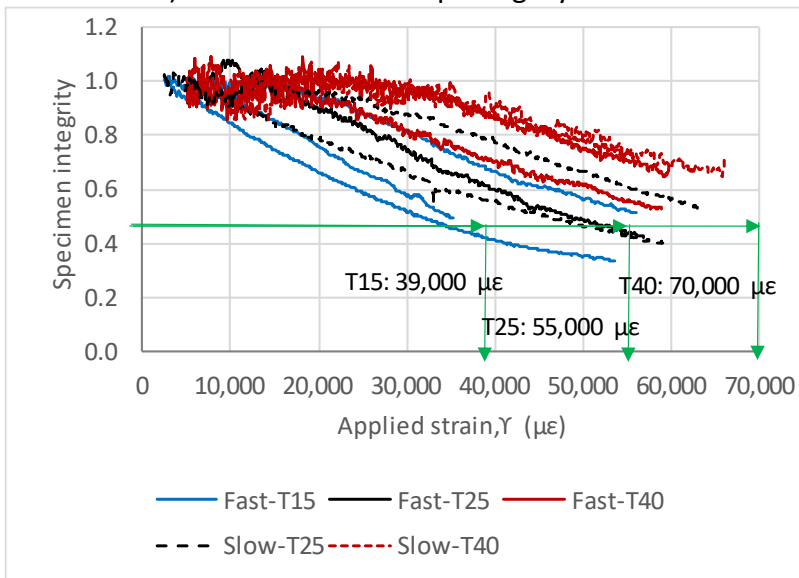
The testing protocol for the shear ramp test was the same one as the one explained previously for the tensile ramp. It was done at three temperatures: 15, 25, and 40 °C (59, 77, and 104 °F) and with two different testing times at each temperature: 3 and 9 hours, as it was shown in Table 5-12. The testing scenarios are referred to as fast and slow for the 3 and 9 hours, respectively. Figure 5-26 shows the integrity curves obtained for the RHMA-G and HMA mixes.

The SST device was not as reliable as the UTM machine used for the tensile ramp test. Some specimens got damaged when they were fixed to the machine or when the test was starting, probably due to issues in the hydraulic system. Hence, it was not possible to get three replicates for each testing condition, and in some cases, it was not possible to even get one replicate. For the RHMA-G specimens shown in Figure 5-26a, even though there were not many specimens tested, it was observed that the temperature has a noticeable effect on the strain level reached at an integrity of 50 percent, but there seemed not to be much difference when analyzing the fast and slow results at temperatures of 25 and 40 °C. The strain levels for the RHMA-G mix at 15 and 25 °C (59 and 77 °F) were 37,000 and 70,000, respectively, while at 40 °C (104 °F), it was estimated to be close to 97,500 $\mu\epsilon$ since such a large deformation level cannot be achieved during the test due to equipment limitations. The results obtained for the HMA mix, shown in Figure

5-26b, presented fewer differences between the sets of tests performed at different temperatures. A 50 percent integrity was achieved at 70,000 $\mu\epsilon$ at 40 °C (104 °F), at 55,000 $\mu\epsilon$ at 25 °C (77 °F) and at 39,000 $\mu\epsilon$ at 15 °C (59 °F). The testing length did not have an effect on the evolution of the integrity for both mixes.



a) RHMA-G shear ramp integrity curves



b) HMA shear ramp integrity curves

Figure 5-26. Summary of integrity curves for shear ramp test for HMA and RHMA-G mixes

A summary of the strain values at 50 percent integrity is presented in Table 5-14 and it shows that at temperatures of 25 and 40 °C, the RHMA-G has 27 and 39 percent, respectively, more shear strain than the HMA mix. Since there was only one valid test result for the RHMA-G mix at 15 °C (59 °F), the comparison suggests that the RHMA-G had 5 percent less strain than the HMA, which does not match what has been observed in the previous analysis, and it may just be due to the lack of replicate tests. Having the ability to carry more shear strain is ideal if used as a base for concrete pavements since it is known that the concrete will expand and contract with changes in temperature and humidity, causing shear strains and stresses in the interphase and HMA layers.

Table 5-14. Strain levels at 50 percent integrity for shear ramp test compared for HMA and RHMA-G

	T15	T25	T40
HMA	39,000	55,000	70,000
RHMA-G	37,000	70,000	97,500
Difference between HMA and RHMA-G	-5%	27%	39%

5.4.4 Strength Test Summary

A summary of the strain levels at 50 percent integrity for all the tests previously discussed is shown in Table 5-15. There is a clear behavior that the RHMA-G mix can take more strain to reach the same integrity level as the HMA in both tension and shear. This behavior, even though it is expected since HMA is a more rigid mix, confirms the initial thought that the RHMA-G mix can be used as a base for concrete pavements and may even behave better than the HMA. Being able to deform more (15 to 43 percent more) provides the RHMA-G an advantage when compared to the HMA as a rigid pavement base since it will be able to deform more than the HMA for the

same damage when the concrete slabs curl up or down and expand or contract due to shrinkage, temperature, and humidity effects.

Table 5-15. Strain levels at 50 percent integrity for different test for HMA and RHMA-G

	Tensile Hanging Damage	Tensile Ramp			Shear Ramp		
	T25	T15	T25	T40	T15	T25	T40
HMA	30,000	10,000	20,000	39,000	39,000	55,000	70,000
RHMA-G	43,000	12,500	25,000	45,000	37,000	70,000	97,500
Change	43%	25%	25%	15%	-5%	27%	39%

The tensile hanging damage test and the shear ramp test explained above will be replicated in FEM models to capture where the damage initiation and failure of the specimens are. These two parameters are required inputs for the full-scale models, details and explanations are shown in Chapter 8.

5.5 Recommendations

After finishing the first phase of testing, it was determined that the five tests used for the stiffness analysis provided a good agreement when characterizing HMA and RHMA-G mixes. Therefore, there is no need to perform all five tests to describe the behavior of the materials properly. For the following steps of this research and other projects, it is recommended to perform only the compressive dynamic modulus test and the tensile hanging creep test. The tensile hanging creep test may be more challenging to replicate since it was developed under this research project, but the testing frame and recording device are very simple and easy to implement in an already established testing or research facility. It is recommended to run the tensile hanging creep test

since it will characterize the material behavior at a frequency range that is not covered by any other test.

The characterization of the strength and capacity to deform under slow loading should be performed only using the tensile ramp test or tensile hanging damage test, but the final phase of testing, which will be presented in Chapter 6, will only include the use of the tensile ramp test as it produced similar results than the tensile hanging damage at a fraction of the time.

The shear frequency sweep test, shear creep test, and shear ramp test were very expensive and time-consuming since the equipment did not have good repeatability within samples and the hydraulic system was unreliable before and just after the specimens were set inside the machine, causing multiple specimens to fail even before the beginning of the test. Therefore, the use of the SST in future research is not recommended and will not be included in the last phase of testing. It should be noted that the SST equipment was built in 1998.

Future research following this testing protocol must verify that the temperature ranges used in this project are valid for their climate region. The range can be expanded, or additional temperature may be added to cover the expected temperature interval if more extreme temperatures are required.

A test to characterize the resistance to water-induced damage is recommended to be added to the testing protocol. For this research and the data presented in Chapter 6, the indirect tensile cracking test will be performed using dry specimens as well as moisture-conditioned specimens using the MiST device. Additional testing methodologies, shown in Appendix A, can also be used to characterize the mixes, but in the final steps were not included due to constraints.

6. TESTING PROTOCOL FOR MATERIAL AND BONDING CHARACTERIZATION

6.1 Goal and Objectives

The goal of this chapter was to apply the final testing protocol for asphaltic materials to be used as a base for rigid concrete pavements. The protocol has been developed and fine-tuned with the materials shown in Chapter 5. The materials tested in this chapter were also an HMA and RHMA-G mixes that were used for the construction of test sections at the UCPRC. Besides the testing of asphalt specimens, composite specimens were also prepared and tested to determine the properties of the interphase and to determine whether the interphase or the asphalt was the weakest point in the structure.

6.2 Materials Tested

The mixes analyzed in this chapter were used in two test sections built at the UCPRC. The HMA used was part of project number 4.88, which is why the name for it is 4.88HMA. The RHMA-G was used under project 4.76B, hence, it will be referred to as 4.76BRHMA-G. A summary of the properties for each of the mixes is shown in Table 6-1 and a copy of the mix designs is included in Appendix C for more detailed information. Compared to the mixes used in the last chapter, the HMA used in this chapter has a PG64-10 binder instead of a PG64-16 and has 0.35 percent more virgin binder by mass of mix. The only difference in the RHMA-G is the nominal maximum aggregate size, which is now 19 mm (3/4 in.) instead of 12.5 mm (1/2 in.).

Table 6-1. Asphalt mixes properties for final testing

	Mixes	
	4.88HMA	4.76BRHMA-G
Mix Type	HMA	RHMA-G
NMAS, mm (in.)	19 (3/4)	19 (3/4)
Binder	PG64-10	PG64-16 w/CRM
Rubber	No	Yes
Virgin Binder, %	4.21	7.5 including CRM
RAP	Yes	No

Besides asphalt specimens, composite specimens made of concrete on top of asphalt were also prepared and tested with the tensile ramp test. The concrete mix was produced with a portland limestone cement (PLC) with a design slump of 10 cm (4 in.) and a design compressive strength of 27.6 MPa (4,000 psi) at 28 days. The mix design is attached in Appendix C, and it is the same concrete mix that was used for the test sections that will be explained in Chapter 7. The composite specimen preparation followed the same initial step of preparing the asphalt specimens, and the concrete was cast on top over a moist asphalt surface. After casting, the specimens were cured for at least 28 days before testing.

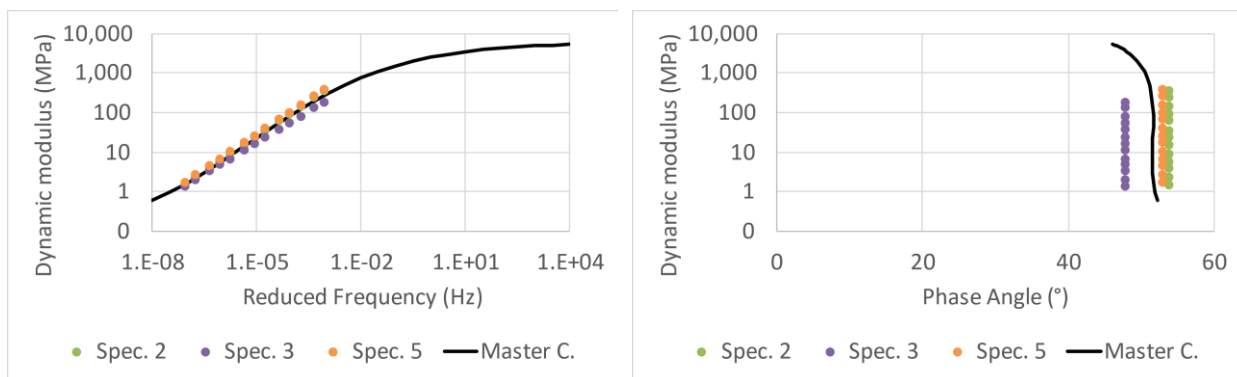
6.3 Stiffness Test Results and Analysis of Asphalt Specimens

The stiffness characterization of asphaltic materials was performed with the tensile hanging creep test and the compressive dynamic modulus test. The first test is in tension, and the second one is in compression. The tensile hanging creep test has a duration of 5 to 7 days, while the compressive dynamic modulus is done in approximately 10 minutes at each temperature. The temperatures at which these tests were performed are the same as the ones shown in Chapter 5: 4, 15, 25, 40, and 54 °C for the compressive dynamic modulus test and only at 25 °C for the

tensile hanging creep. The data processing for these tests followed the same procedure as the one explained in the previous chapter, so the process is not going to be explained again, and only the results are shown. For reference on how to process the data, section 5.3.4 and section 5.3.5 provide a detailed explanation of how it was done for the tensile hanging creep and compressive dynamic modulus respectively.

6.3.1 Tensile Hanging Creep

The tensile hanging creep test was only performed for the HMA specimens. When testing the RHMA-G specimens, the recording systems seemed not to be performing correctly when recording small deformations in the specimen. Several samples were attempted, but the system was not able to provide accurate and repeatable data. Five replicates were tested for the HMA mix, three of them were done with an additional weight of 3 kg (6.6 lb), while the other two were tested with an additional load of 7 kg (15.4 lb). Figure 6-1 shows the dynamic modulus plot and Black diagram obtained for the HMA mix. The master curve and Black diagram were fitted using the data from the three test replicates that were performed at 3 kg (6.6 lb) since the ones tested at 7 kg (15.4 lb) had a very premature failure, and the creep behavior of the specimens was hard to obtain.



a) HMA tensile hanging creep dynamic modulus plot

b) HMA Black diagram

Figure 6-1. 4.88HMA tensile creep test summary

When comparing the master curve obtained for the 4.88HMA material to the materials analyzed in section 5.3.4, it can be seen that the two HMA mixes behave similarly even though the current mix has a PG64-10 binder instead of a PG64-16 and has 0.35 percent more virgin binder. They also have the same aggregate size, which may contribute to similar behavior. Figure 6-2 shows the plot of the three master curves obtained from the tensile hanging creep test.

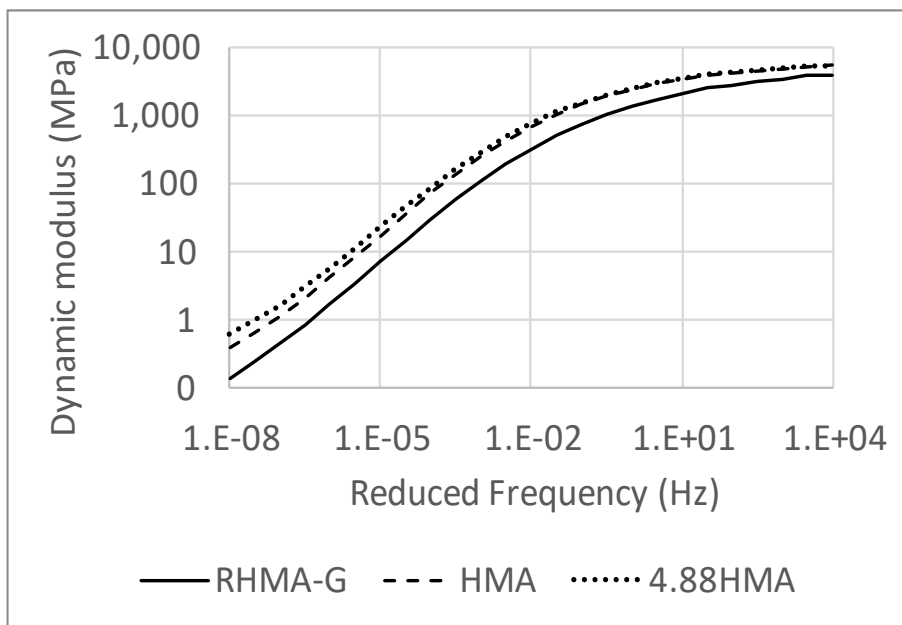


Figure 6-2. Tensile hanging creep master curve comparison

6.3.2 Compressive Dynamic Modulus

Four specimens were tested for each of the mixes at temperatures of 4, 15, 25, 40, and 54 °C (40, 59, 77, 104, and 129 °F). The data analysis process shown in section 5.3.5, which included the use of the time-temperature superposition, was also applied for the analysis of the 4.88HMA and

4.76BRHMA-G data. The results for both master curves are shown in Figure 6-3. The HMA mix results are stiffer than the RHMA-G mix at frequencies over 1.E-02, while the RHMA-G mix was stiffer at frequencies under 1.E-02. The behavior is likely to be due to the presence of rubber in the RHMA-G mix, which tends to flatten the behavior and makes the material less susceptible to changes in stiffness due to temperature changes.

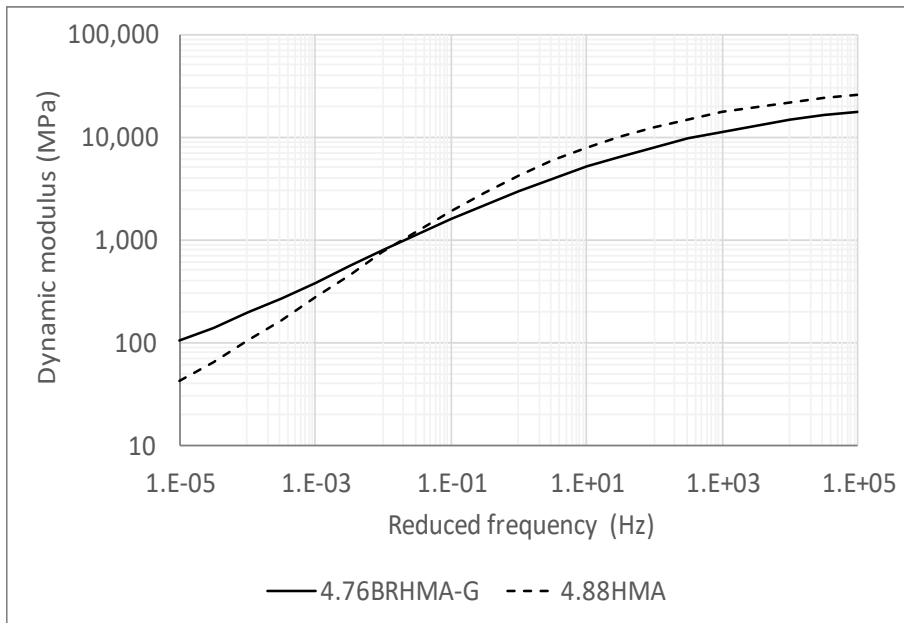


Figure 6-3. Compressive dynamic modulus master curves summary

6.3.3 Stiffness Tests Summary

Figure 6-4 shows the master curve obtained from the compressive dynamic modulus test for both RHMA-G mixes that have been analyzed. The 4.76BRHMA-G shows a stiffer behavior across the full range of analyzed frequencies. It is reasonable to assume that one of the reasons why the 4.76BRHMA-G mix with an aggregate size of 19 mm (3/4 in.) was stiffer than the RHMA-G material from Chapter 5 with an aggregate size of 12.5 mm (1/2 in.) is due to the aggregate size

difference. Other possible reasons for such differences can be the binder content and the binder source.

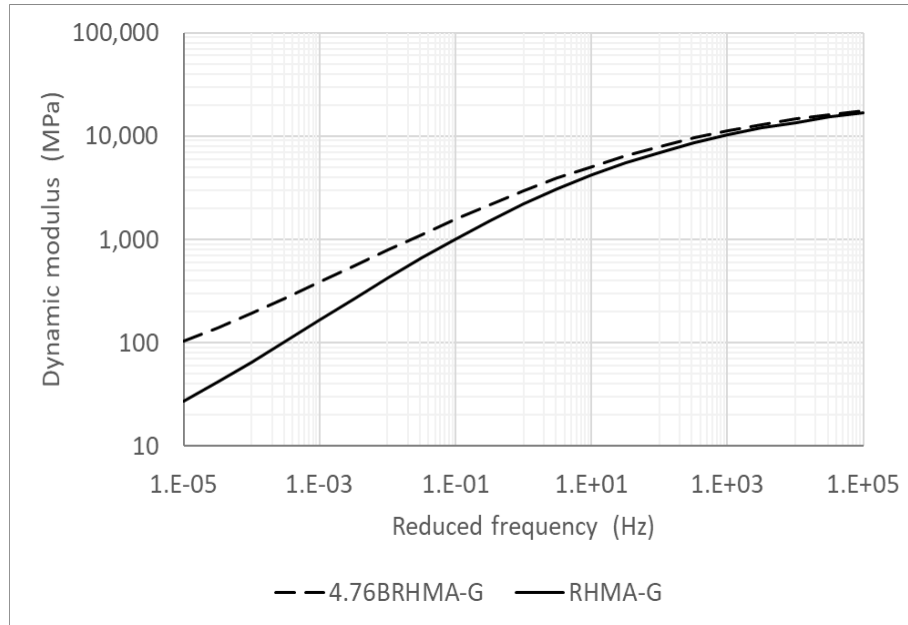


Figure 6-4. Master curves from the compressive dynamic modulus test for the two RHMA-G mixes analyzed

6.4 Strength Test Result and Analysis

The strength and the capacity to deform under slow loading of asphalt and composite specimens were analyzed with the tensile ramp test. For the second stage of testing, only the short 3-hour ramp was used, as opposed to the 3-hour and 30-hour ramps that were performed for the characterization in the previous chapter. Additionally, the testing temperature was only 25 °C (77 °F). The data processing for this test followed the same procedure as the one explained in the previous chapter, so the process is not going to be explained again, and only the results are shown. For reference on how to process the data, section 5.4.2 provides a detailed explanation of how it was done. Both sets of tests are shown in the following subsections.

The analysis of the tensile ramp tests requires the input of the viscoelastic parameters (J_0 , J_1 , and n) obtained from the tensile hanging creep, as was explained in section 5.4. Since the tensile hanging ramp test was only performed on the HMA specimens due to device inaccuracy when recording small strains in the RHMA-G, in this section, both the HMA and the RHMA-G were analyzed with the viscoelastic parameters obtained from the HMA specimens. The reason behind this decision relies on the fact that the maximum aggregate size of both mixes is the same, 19 mm (3/4 in.). This assumption is believed to provide an adequate approximation since the analysis process also requires the fitting of the viscoelastic stress to match the test result. The analysis was also performed with the viscoelastic parameters from the RHMA-G mix of Chapter 5 and comparable results were obtained.

6.4.1 Tensile Ramp of Asphalt Specimens

A total of 5 specimens were tested for each of the mixes. Figure 6-5 shows a summary of the integrity curves for both mixes. As can be seen from the plot, the RHMA-G mix requires a lower strain than the HMA mix to get to 50 percent integrity. This result is the opposite of what was observed in section 5.4.2 when analyzing the previous set of mixes. Differences in binder sources, binder contents, and aggregate sizes are some of the probable causes for this to happen. This result suggests that the RHMA-G mix with a 19 mm (3/4 in.) maximum aggregate size has a stiffer behavior, which can negatively impact the fatigue life of the structure.

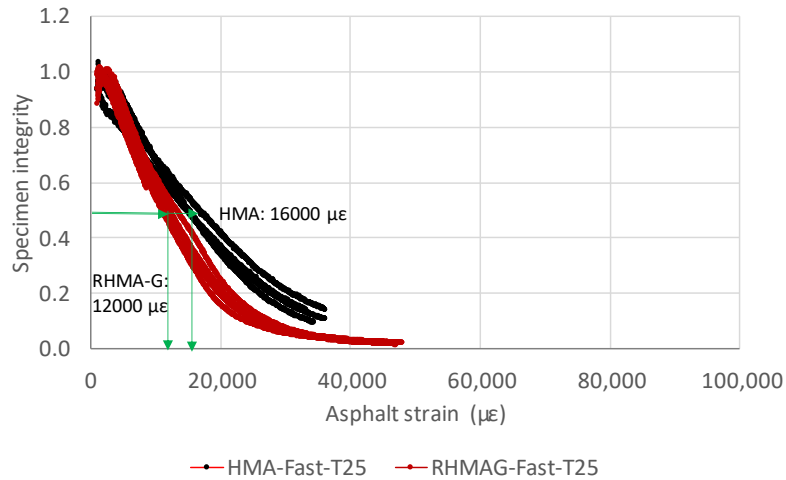


Figure 6-5. Summary of integrity curves for tensile ramp test of RHMA-G and HMA specimens

Since the tensile ramp test is a destructive laboratory procedure, the location of the failure in the specimens was recorded for each specimen. It was of interest to see whether the failure would occur near the ends of the specimens or somewhere in the middle. Figure 6-6 shows the failed specimens for both mixes, and it can be observed that the failure in all ten specimens happened far away from where the glue was applied in each of the faces. The failures in the specimens have been highlighted to be easily observed.



a) RHMA-G tensile ramp failures



b) HMA tensile ramp failures

Figure 6-6. Asphalt specimens tensile ramp failures of RHMA-G and HMA specimens

6.4.2 Tensile Ramp Tests of Composite Specimens

A total of 5 specimens were prepared for each of the mixes, but only 4 HMA and 5 RHMA-G were tested. The fifth HMA specimen could not be tested since there was an issue with the gluing process when preparing it. The testing of the asphalt and composite specimens was performed under the same procedure.

The only difference between both sets of specimens is the distance over which the LVDTs were measuring. For the asphalt specimens, the displacement is measured over a 100 mm span. For the composite specimens, the LVDT span was the same, but a portion of that span fell in the concrete, which, for this study, was assumed not to deform. Hence, the total asphalt thickness over which it was measured was only 50 mm (2 in.). Figure 6-7 shows the integrity versus strain plots for each of the specimens. A similar trend to the one observed in the previous test can be seen in this case. The average strain to get to a 50 percent integrity was again lower for the RHMA-G specimens when compared against the HMA specimens. Interestingly, the average strain to reach a 50 percent integrity obtained in the composite specimens was almost identical to one of the asphalt specimens shown in Figure 6-5. It can be concluded that the asphalt strain is relatively consistent along all the thicknesses of the layer. Such behavior is beneficial for the modeling assumptions that will be presented in Chapter 8.

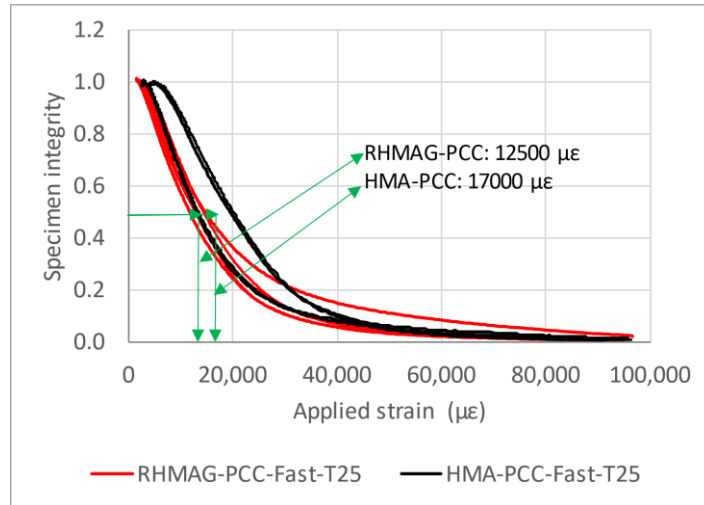
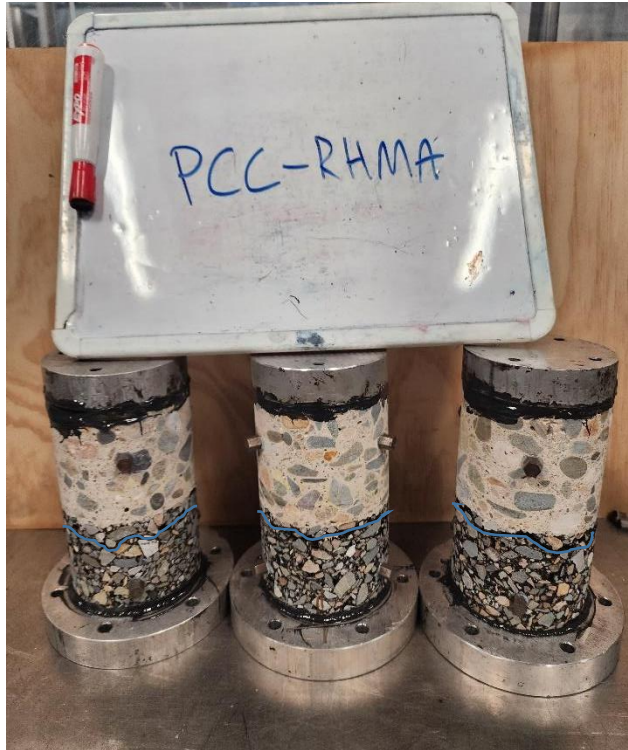
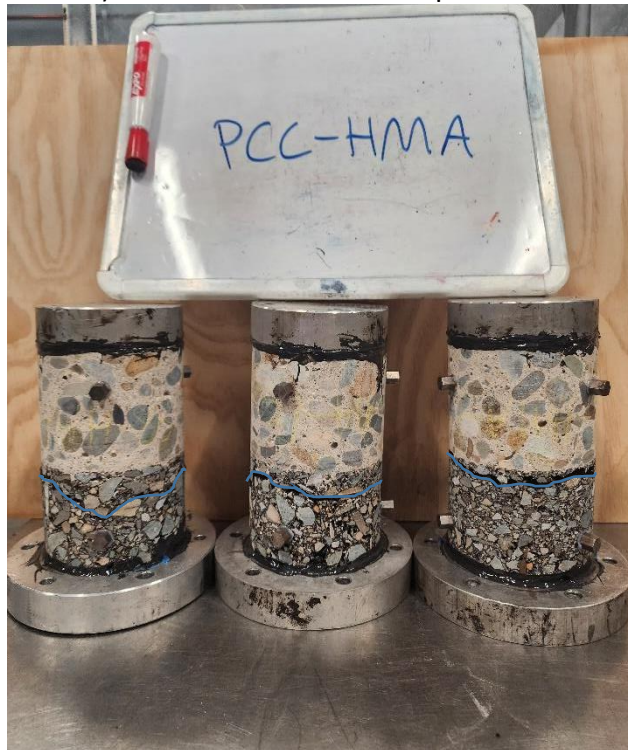


Figure 6-7. Summary of integrity curves for tensile ramp test of composite RHMA-G and HMA specimens

The failures of the composite specimens are shown in Figure 6-8, which have been highlighted to be easier to see. Only the failure of three specimens for each of the mixes was recorded since the platens to hold the specimens inside the testing equipment were required, and the specimens were taken apart right after testing. The failure in the six specimens that are shown, and in the other three that are not included in the picture, happened under the interphase between the concrete and the asphalt, in the asphalt, and not in the interphase. This result seconds the initial thought that the interphase was stronger than the asphalt itself, which likely happened because the concrete grout can penetrate into the asphalt layer, creating a thin hybrid layer composed of both concrete and asphalt mix.



a) PCC-RHMAG tensile ramp failures



b) PCC-HMA tensile ramp failures

Figure 6-8. Composite specimens tensile ramp failures for RHMA-G and HMA specimens

6.4.3 Strength Tests Summary

After having performed the tensile ramp test in asphalt and composite specimens for both HMA and RHMA-G mixes, the following conclusions were obtained:

- The repeatability of the tensile ramp test performed in the UTM machine was very high within replicates of the same material.
- Strain levels observed in asphalt and composite specimens suggest that only asphalt or composite specimens could be analyzed and still provide the information required. For simplicity, the asphalt material could be the only one to be tested, but it could lead to a lack of information in case the interphase is weaker than the asphalt. Hence, if only one set of specimens was selected to be tested, it is recommended to test the composite specimens since they provide information about both the asphalt and the interphase. If more asphalt materials are characterized and provide the same behavior, showing that the interphase is stronger than the asphalt layer, then it would be safe only to do the tensile ramp test of the asphalt since it would require less preparation effort and time.
- The interphase of the composite specimens did not provide a weak plane in the structure, the behavior of the composite specimen was governed by the behavior of the asphalt material itself.

6.5 Water Induced Damage Test Results and Analysis of Asphalt Specimens

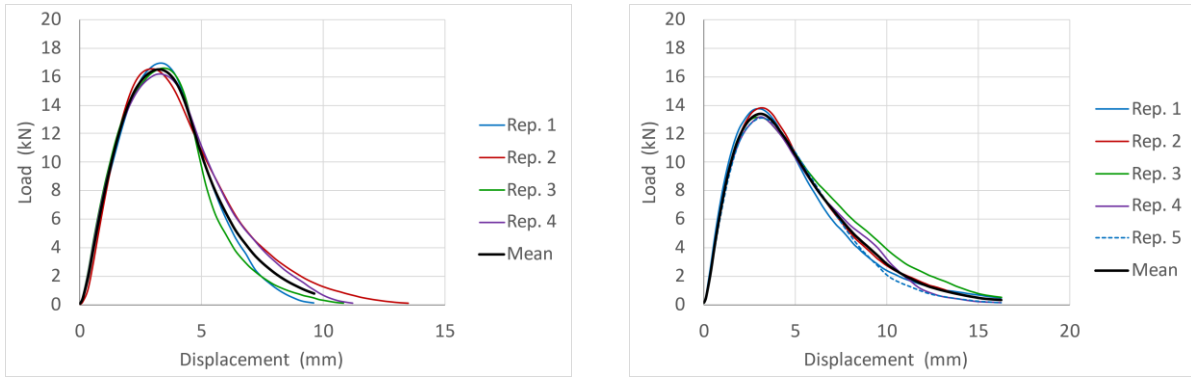
6.5.1 Indirect Tensile Cracking Test (IdealCT)

Moisture susceptibility of asphalt specimens was investigated using the indirect tensile cracking test of dry and moisture-conditioned specimens. The moisture conditioning was performed in a MiST device which was explained in section 4.4.2. The typical temperature at which the MiST conditioning is done is 60 °C (140 °F). The HMA mix was also conditioned at 50 °C (122 °F) to determine the effect of different conditioning temperatures. Table 6-2 summarizes the testing conditions and the number of specimens tested for each mix/condition combination.

Table 6-2. Tested specimens in the indirect tensile cracking test

Mix/Condition	Replicates
RHMA-G/dry	5
RHMA-G/MiST at 60 °C (140 °F)	3
HMA/dry	4
HMA/MiST at 50 °C (122 °F)	3
HMA/MiST at 60 °C (140 °F)	3

The test duration is 1 minute, and the outcome is a time-stamped load and displacement data points. Those data points were used to create a load vs. displacement plot to graphically show the strength of the material and the amount of displacement required for such strength. Figure 6-9 shows the load vs displacement curves for all the specimens that were performed under dry conditions, as well as the mean curve for all the replicates. The test provided very repeatable results for both types of materials, which is beneficial considering that it is a very easy and fast test to perform. The specimens tested after the MiST conditioning also provided repeatable results.



a) Dry HMA IdealCT results b) Dry RHMA-G IdealCT results
Figure 6-9. Dry IdealCT plots for RHMA-G and HMA specimens

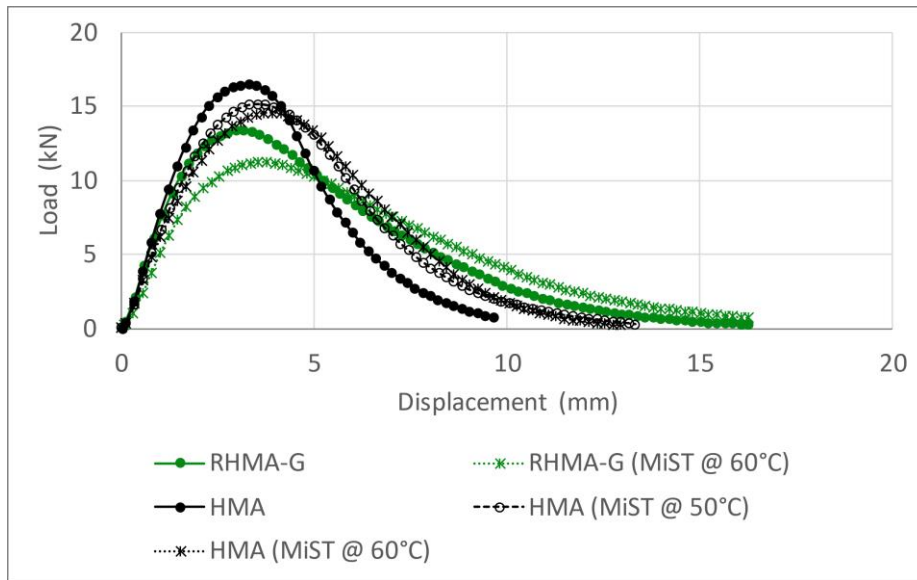


Figure 6-10. Average indirect tensile cracking test results for RHMA-G and HMA specimens

Each of the five mix/condition combinations was averaged, and the results are shown in Figure 6-10. The following conclusions can be drawn:

- HMA had a higher tensile cracking strength than the RHMA-G.
- The moisture conditioning produced a reduction in the strength of both mixes, as was hypothesized.

- Water conditioning at higher temperatures caused a bigger decrease in the strength when comparing temperatures of 50 and 60 °C (122 and 140 °F) on the HMA mix.
- HMA strength dropped 8.3 percent and 11.7 percent after 50 °C (122 °F) and 60 °C (140 °F) conditioning respectively compared to the dry condition.
- RHMA-G strength dropped 16.10 percent after 60 °C (140 °F) conditioning.

The use of a water-induced damage test should remain in the testing protocol for material and bonding characterization since water is known to increase the rate of damage and distress of rigid and composite pavements, as was shown in Section 1.1.3.

7. FULL-SCALE COMPOSITE PAVEMENT SECTIONS

7.1 Goal and Objectives

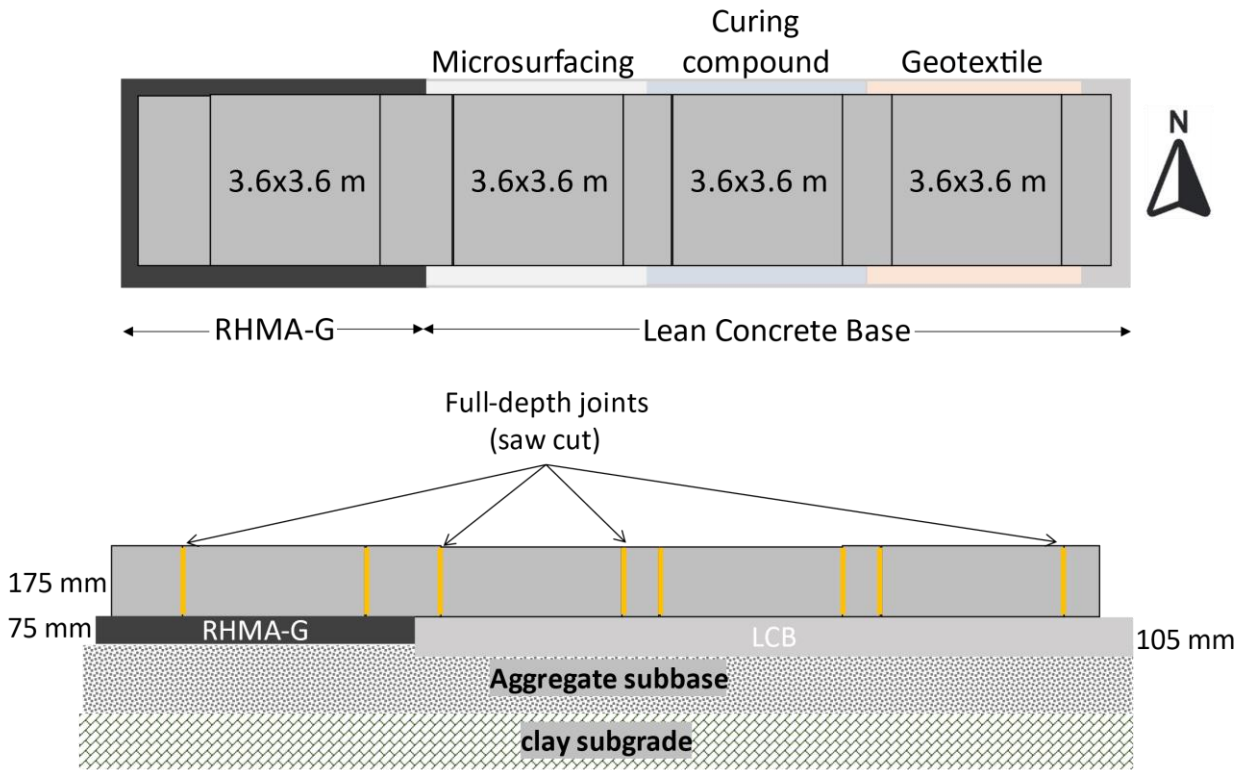
The goal of this chapter was to construct a test track to evaluate how the type of base and the interlayer impact the performance of the structure and the capacity of the slab to support loading under the effect of environmental loads. Currently, allowed bases and interlayer materials were tested, as well as new potential alternative materials. The sections were instrumented with thermocouples and strain gages to monitor the structures for 12 months. Additionally, FWD testing was performed to determine how the corner deflection changes versus the curvature of the slab and how the change varies from section to section since it was reported in the literature review that the cracking performance of JPCP pavements over LCB is 2.8 times worse than JPCP over HMA.

7.2 Test Track Design

Two base materials were used for the test track: the first one was an LCB, and the second one was an RHMA-G. In both cases, the materials were designed and built according to Caltrans Standard Specifications. An RHMA-G was selected instead of an HMA since preliminary laboratory testing indicated that the two mixes would perform similarly as a JPCP of SJPCP-COA base. Three different interlayers were used between the JPCP slabs and the LCB: curing compound, geotextile, and microsurfacing. The first two were selected and placed following Caltrans Standard Specifications (Section 36-2 “Base Bond Breaker”). The third one, the microsurfacing, was designed and placed following Caltrans Standard Specifications (Section 37-3 “Slurry Seals and Micro-Surfacings”), although it is not one of the “bond breaker” options

allowed by Caltrans. The concrete pavement was built with portland limestone cement as this type of cement will most likely replace ordinary portland cement due to its lower embodied carbon.

Only one slab per section was built due to space and budget limitations. This means that the sections are not provided with transverse joints, which may be regarded as a limitation to study jointed pavements. However, the use of single (isolated) slabs is not regarded as a limitation since the curling/warping is expected to be larger for single (isolated) slabs than for jointed slabs provided with doweled transverse joints since the dowels restrict slab curling/warping effect. Further, the corner deflections under FWD loading will be larger on a single slab than on jointed slabs, particularly if the transverse joints are provided with dowels. Consequently, the effect of the type of base and interlayer will be better captured on single (isolated) slabs than on jointed slabs. The thickness of the slab was 175 mm (7 in.), which is relatively thin for JPCP for heavy wheel loads with full-size slabs (3.6 m long and wide). The reason why a 175 mm (7 in.) thickness was selected was to ensure a high curling/warping of the slabs based on the depth-to-width ratio. Additional transition slabs were built between the test sections to ensure that the base and interlayers would extend well outside the test slab boundaries. The configuration of the test track is shown in Figure 7-1.



7.3 Instrumentation

The instrumentation installed in each of the four sections, shown in Figure 7-2, focuses on measuring the response to the ambient environment loading. The instrumentation of each slab includes:

- Two thermocouple rods are used to measure the temperature profile in the slabs and base through the depth of the pavement structure to capture the temperature gradients happening in the structure.
- Three pairs of GeoKon 4200 vibrating wire strain gages (VWSG) are located at the center of the slab and two corners. Each pair includes a VWSG at 25 mm (1 in.) from the top of the slab and another VWSG at 25 mm (1 in.) from the bottom of the slab to capture

relative differences in strain between the top and bottom of the slab due to the effect of environment loads.

The data from the sensors data was collected by a Campbell Scientific data acquisition system located by the test sections. Data was collected every 10 minutes, starting before the PLC construction.

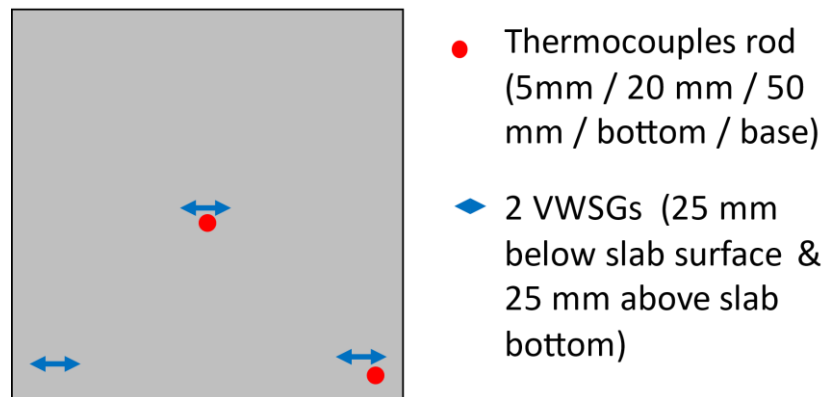


Figure 7-2. Test section instrumentation layout, top view

7.4 Construction of the Test Track

7.4.1 Construction of the Lean Concrete Base

The UCPRC team prepared the subbase in April 2022. The LCB was supplied by a local plant (Elite Ready Mix) and placed and consolidated by the paving contractor (Vanguard) on May 6, 2022. Figure 7-3 shows a picture from construction day. LCB cylindrical specimens were prepared during the construction and were tested in the laboratory, which is summarized in Section 7.4.

The LCB was cured (Figure 7-4) following Caltrans specifications, which include:

- 1st spray: 0.27 L/m² (1 gal/150 ft²).

- 2nd spray (less than 4 days after the construction; clean surface and apply 2nd spray):
0.20 L/m² (1 gal/200 ft²).

The curing compound was Type 2B (white-pigmented, resin-based), meeting the ASTM C309 specification [47]. The curing compound used for LCB curing was the same used as the bond breaker and also for curing the portland limestone cement concrete. The LCB was saw-cut every 6 m (20 ft). The cut depth was 35 mm (1.4 in.) which corresponds to one third of LCB thickness and the cuts matched the mid-slab locations.



Figure 7-3. LCB construction



Figure 7-4. Curing compound application on LCB

7.4.2 Construction of the RHMA-G Base

The RHMA-G was supplied by Teichert aggregates and placed and compacted by a local contractor (Helmert and Sons) on May 6, 2022. The paving equipment is shown in Figure 7-5.

Loose mix was sampled during the construction, and specimens were produced and tested in the laboratory. The RHMA-G used for the construction of the test sections is the one used in Chapter 6, where it was analyzed in different stiffness and strength tests. The RHMA-G had a 19 mm (3/4 in.) nominal maximum aggregate size and PG 64-16 base binder. The complete mix design is shown in Appendix C.



Figure 7-5. RHMA-G paving

7.4.3 Construction of the Interlayers

Three different interlayers were placed over the LCB layer after the two applications of curing compound were applied. A third application of curing compound, a layer of geotextile, and a microsurfacing layer well applied to the test slab and halfway into the transition slabs to ensure that the interlayers are applied underneath the area of the test slab.

7.4.3.1. Curing Compound

The “bond breaking” curing compound was applied the day before the concrete paving. Following Caltrans specifications, it consisted of a third spray application of 0.54 L/m² (1 gal/75 ft²). Type 2B (white-pigmented, resin-based), according to ASTM C309 [49], was used. The section with curing compound bond breaker, before PLC paving, is shown in Figure 7-6.



Figure 7-6. Section with curing compound bond breaker, before PLC paving

7.4.3.2. Geotextile

The geotextile was selected and placed following Caltrans Standard Specifications in Section 36-2, "Base Bond Breaker," and Section 96-1.02Q, "Geosynthetic Bond Breaker". It consisted of a nonwoven polypropylene geosynthetic, with a weight of 500 g/m² (14.7 oz/yd²). The section with the geotextile bond breaker, before PLC paving, is shown in Figure 7-7.



Figure 7-7. Section with geotextile bond breaker, before PLC paving

7.4.3.3. *Microsurfacing*

The microsurfacing was paved by VSS International on May 20, 2022. The application is shown in Figure 7-8. The microsurfacing had a Type II gradation with a nominal maximum aggregate size of 2.36 mm (0.093 in.) with polymer-modified emulsion, an asphalt binder content of 9% (by total weight of microsurfacing), and 1% portland cement. The microsurfacing followed Caltrans Standard Specifications Section 37-3, “Slurry Seals and Micro-Surfacings”. It was placed at a rate of 18 lb of dry aggregate per yd² (9.8 kg of dry aggregate per m²), which is roughly equivalent to a thickness of 10 mm (0.2 in.).



Figure 7-8. Microsurfacing paving

7.4.4 Construction of the Concrete Slabs

The PLC was supplied by the Cemex Perkins plant in Sacramento and was placed and consolidated by UC Davis Transportation of Parking Services with support from UCPRC staff on June 6, 2022. The paving process is shown in Figure 7-9. It consisted of a regular paving mix designed to provide 27.6 MPa (4,000 psi) compressive strength in 28 days. A summary of the PLC concrete mix design is shown in Table 7-1, and full details are provided in Appendix C.

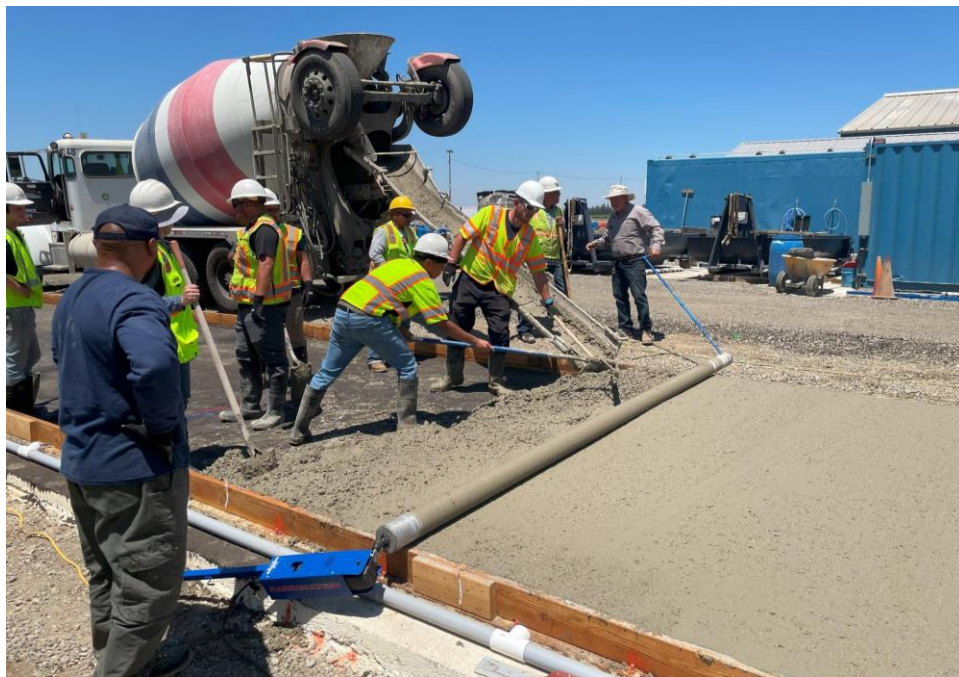


Figure 7-9. PLC construction

Table 7-1. PLC mix design for 0.76 m³ (1 yd³)

Material	Description	Design quantity
Coarse Aggregate	Gravel	
Fine Aggregate	Sand	596 kg (1313 lb)
Cement	Type 1L, ASTM C595 [50]	187 kg (413 lb)
Ground granulated blast furnace slag (GGBFS)	Slag, Grade 120, ASTM C989 [51]	80 kg (177 lb)
Water reducer	Master Glenium 7500	4 oz/cwt
Water		128 L (34.0 gal)

The PLC slab was consolidated with a vibrating rolling screed and finished with a trowel. No surface texturing was applied. The curing compound was a white-pigmented, resin-based curing compound meeting ASTM C309 [49] Type 2B specifications, applied at a nominal rate of 0.27 L/m² (1 gal/150 ft²). The application of the curing compound is shown in Figure 7-10.

The transverse joints were sawn to full depth once the PLC was hard enough to resist cutting without spalling. The cutting process is shown in Figure 7-11.



Figure 7-10. Curing compound application on PLC



Figure 7-11. Full depth cutting of transverse joints on PLC

7.5 QC/QA Testing of Materials Used

Laboratory specimens were prepared during the construction days to characterize the LCB and PLC mixes. For the LCB material, 150 x 300 mm (6 x 12 in.) cylinders for compressive strength and modulus of elasticity testing (MOE) were prepared. For the PCC material, 150 x 300 mm (6 x 12 in.) cylinders were prepared for modulus of elasticity testing, 100 x 200 mm (4 x 8 in.) cylinders were prepared for compressive strength, and 150 x 150 x 550 mm (6 x 6 x 22 in.) beams were prepared for flexural strength. All the testing was done following ASTM standards:

- ASTM C39/C39M-21: Standard Test Method for Compressive Strength of Cylindrical Concrete Specimens [52].
- ASTM C78/C78M-21: Standard Test Method for Flexural Strength of Concrete (Using Simple Beam with Third-Point Loading) [53].

- ASTM C469/C469M-22: Standard Test Method for Static Modulus of Elasticity and Poisson's Ratio of Concrete in Compression [54].

The testing protocol was established to test three replicate specimens in each test at the following ages:

- For LCB: 3, 7, 28, and 365 days.
- For PCC: 10, 28, 365 days.

The MOE test at 365 days of the LCB material could not be performed due to machine issues, and the PLC material was tested at 433 days instead.

The specimens were placed in a water tank containing 3 g/L (0.025 lb/gal) of calcium hydroxide until the corresponding testing times. MOE specimens that were reused for multiple testing ages were placed back into the tank after each test was performed.

7.5.1 Summary Results for LCB

The summary of the laboratory testing results done for the LCB material is shown in Figure 7-12 and Figure 7-13 for compressive strength and modulus of elasticity, respectively. As was mentioned above, the 1-year MOE testing was not performed due to machine complications, and the compressive strength was performed 37 days later. According to Caltrans, the compressive strength at seven days for the LCB to be acceptable has to be at least 3.65 MPa (530 psi). The current mix met that requirement with an average strength of 3.68 MPa (534 psi).

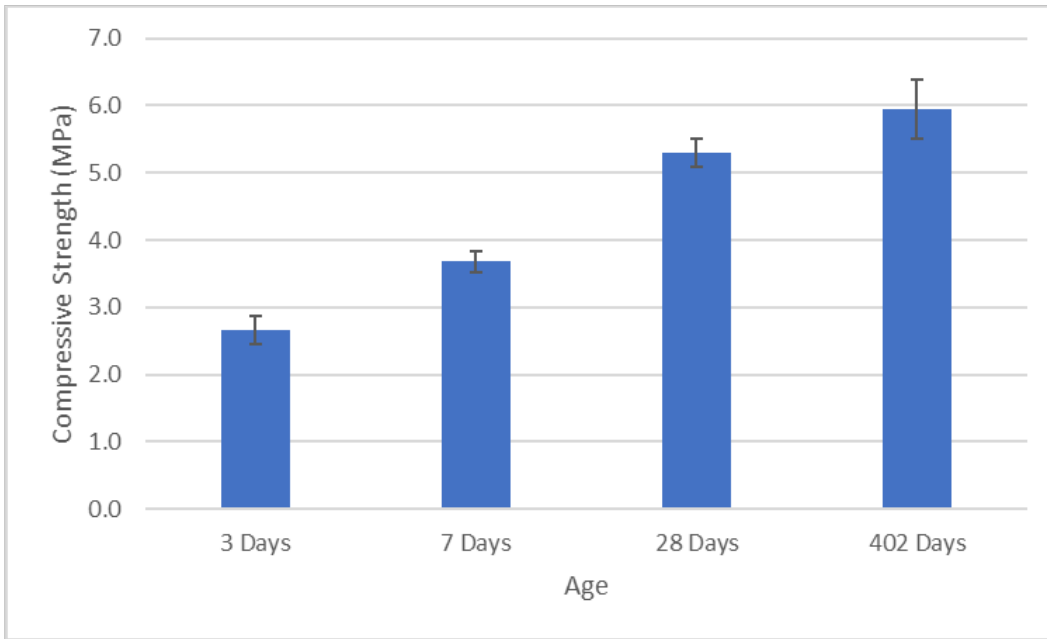


Figure 7-12. LCB compressive strength results

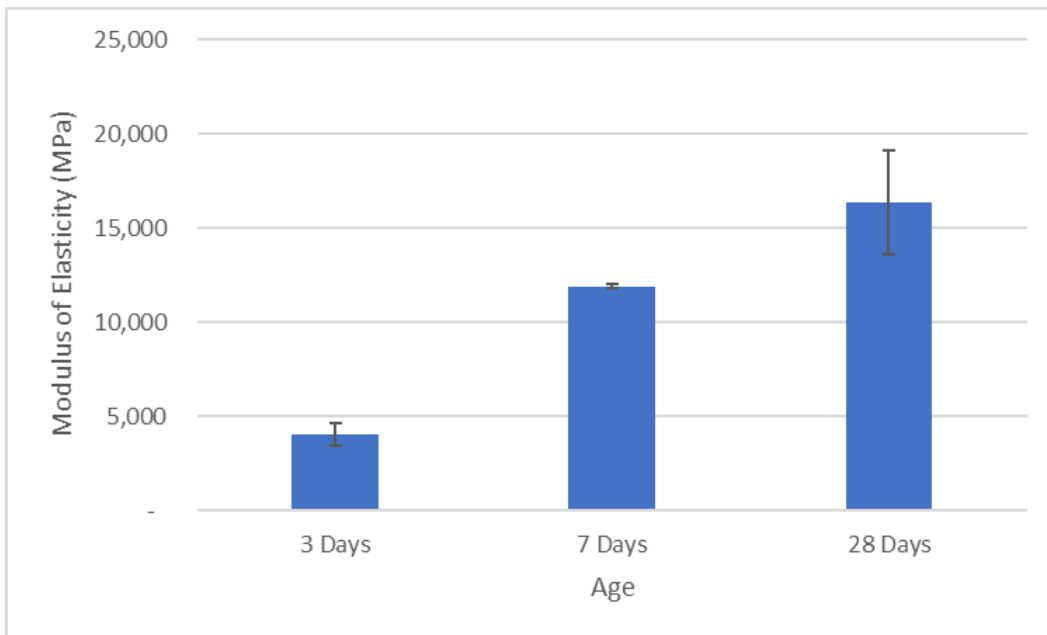


Figure 7-13. LCB modulus of elasticity results

7.5.2 Summary Results for PLC

The summary of the laboratory testing results done for the PLC is shown in Figure 7-14, Figure 7-15, and Figure 7-16 for compressive strength, modulus of elasticity, and modulus of rupture (MOR), respectively. The 1-year MOE testing was performed at 443 days due to machine complications. According to Caltrans, the compressive strength requirement is 27.6 MPa (4,000 psi) at 28 days. The mix used for this project reached 33.55 MPa (4,865 psi) at 28 days.

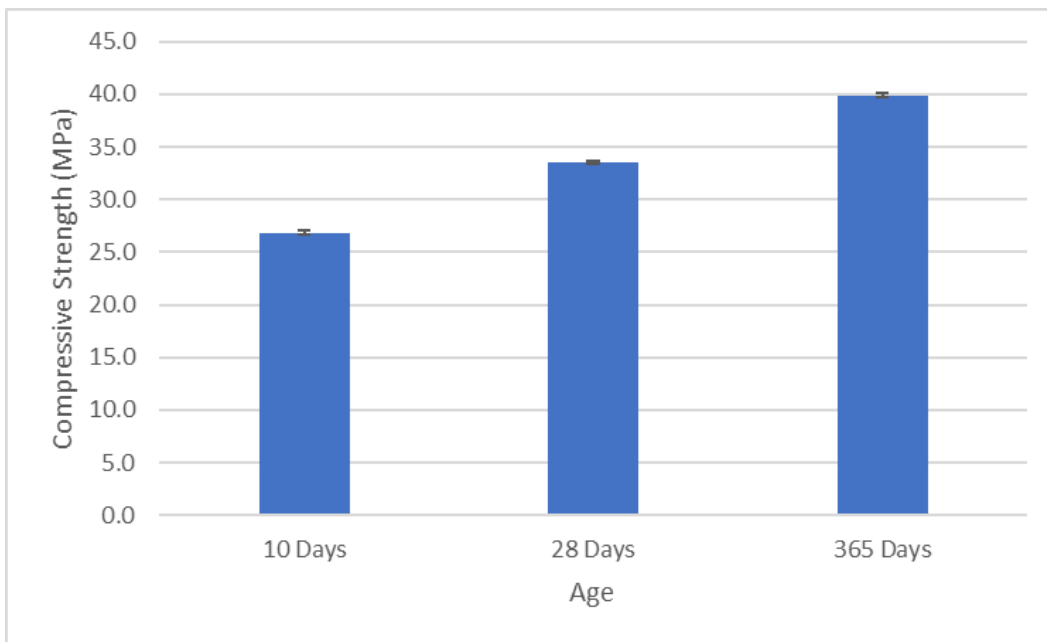


Figure 7-14. PLC compressive strength results

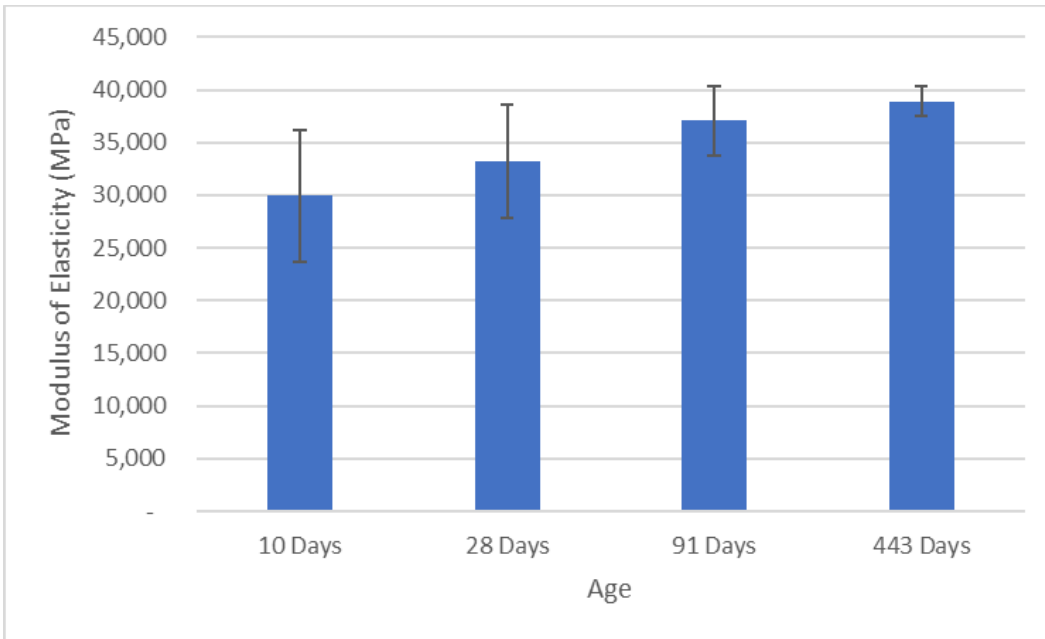


Figure 7-15. PLC modulus of elasticity results

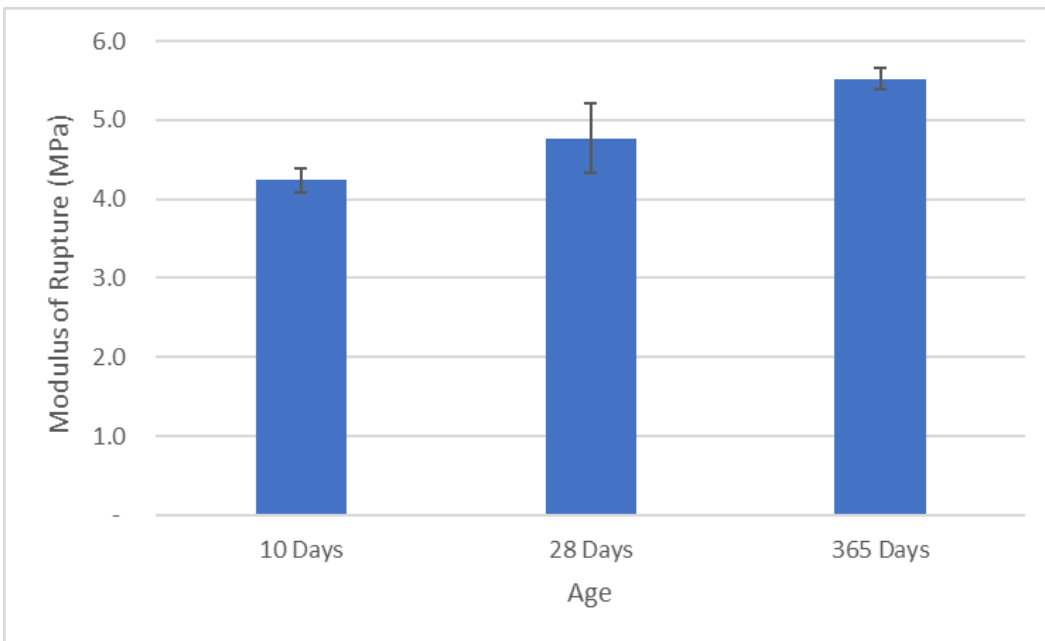


Figure 7-16. PLC modulus of rupture results

7.6 Test Track Monitoring

7.6.1 Slabs Curling/Warping

The strain data collected by the VWSG sensors in the slabs were used to calculate the mean and the differential strains, ϵ_{MEAN} and ϵ_{DIFF} . The strain ϵ_{MEAN} is the average of the strain measured at the top and bottom of the slabs; ϵ_{MEAN} quantifies mean slab expansion/contraction. The strain ϵ_{DIFF} is the difference between the strain measured at the top and bottom of the slabs; ϵ_{DIFF} quantifies slab curling/warping. See ϵ_{MEAN} and ϵ_{DIFF} calculation formula in Figure 7-17.

The strains measured at the corners are analyzed in this report. At the corners, there is no restriction to slab expansion/contraction, and neither to curling/warping and consequently, no section-to-section differences are expected. The average of all VWSG strains (two instrumented corners per section, four sections) at the top and bottom of the slabs were used to calculate ϵ_{MEAN} and ϵ_{DIFF} .

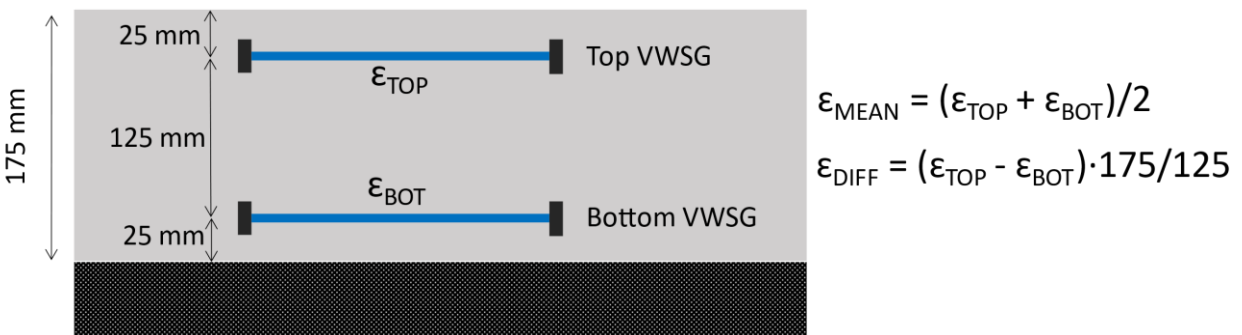


Figure 7-17. Calculation of ϵ_{MEAN} and ϵ_{DIFF}

The strains ϵ_{MEAN} and ϵ_{DIFF} throughout the evaluation period presented in this report are shown in Figure 7-18. A "field setting time" of 4 hours, measured from the ready-mix truck batching, has been adopted as a reference for strain calculation (ϵ is set to zero at the "field setting time"). The

adoption of 4 hours is based on the set time testing according to ASTM C403 [55]. The initial set time, when it reached a penetration resistance of 3.45 MPa (500 psi), was 3 hours and 25 minutes, while the final set time, when it reached a penetration resistance of 27.5 MPa (4000 psi), was 4 hours and 30 minutes, counted from the ready-mix truck batching. The penetration resistance is measured with a needle that penetrates to a depth of 25 ± 2 mm (1 +1/6 in.) of a specimen that has a height of at least 140 mm (5.5 in.) Figure 7-18 also shows rain events, and it is observed a direct relationship between rain events and concrete swelling (increase in the ϵ_{DIFF}).

The negative sign of ϵ_{MEAN} indicates contraction, while the negative sign of ϵ_{DIFF} indicates that the slabs' curvature is concave upwards. The mean strain reached values as low as $-700 \mu\epsilon$ (contraction); the lowest mean strain (maximum contraction) occurred during winter-time due to the low temperature. The differential strain reached values as low as $-550 \mu\epsilon$ (concave upwards); the lowest differential strain (maximum concave upwards curvature) occurred during summer-time due to the differential drying shrinkage (the top of the slab dries more than the bottom). Figure 7-19 shows an example of the daily variations of the strain and temperature.

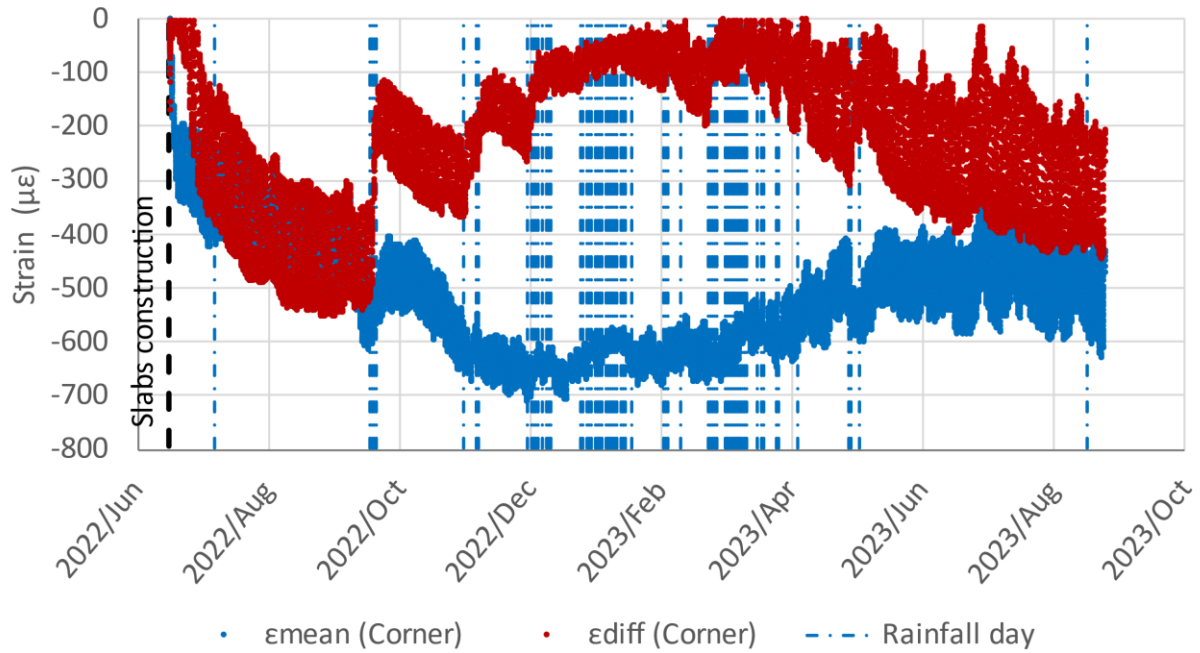
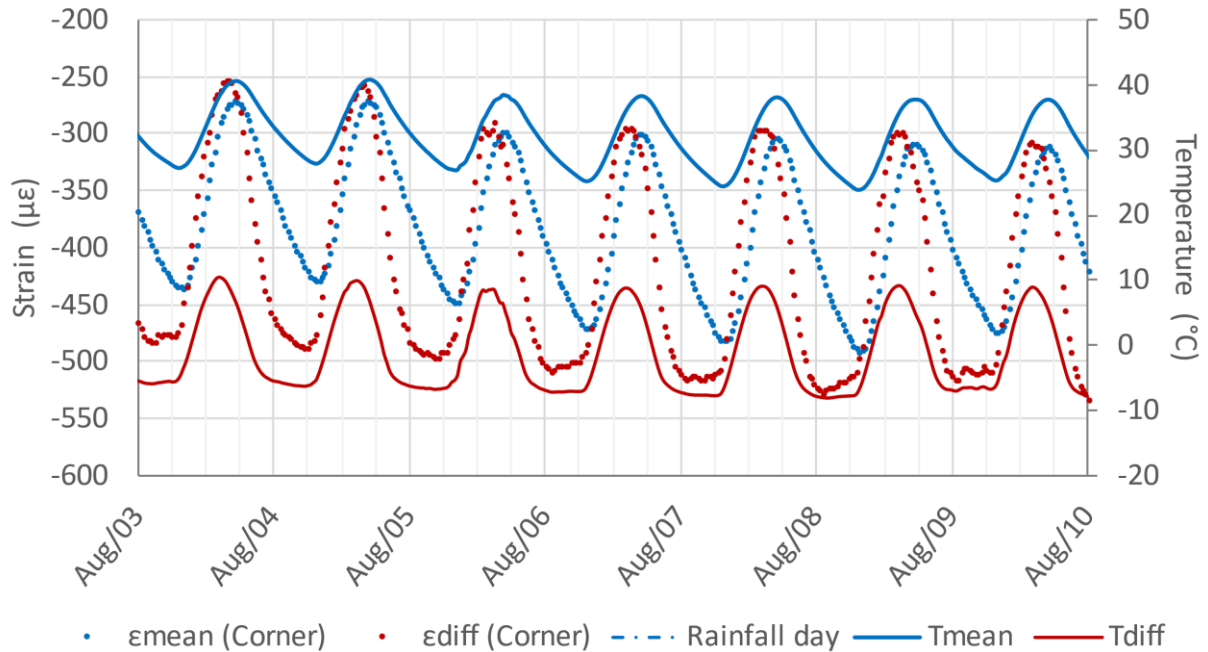


Figure 7-18. Strain ϵ_{MEAN} at the corner of the slabs



Note: Tmean is the average of the top and bottom of the slab temperatures; Tdiff is the top minus bottom of the slab temperatures

Figure 7-19. Example of daily variation of strain and temperature at the corners of the slabs

The curvature of the slabs is expected to impact the deflection measured at the corner with the FWD. As the corner lifts due to the curvature (curling and warping), the slab loses support below the corner, and consequently, the deflection produced by the FWD loading increases. While this is expected to impact all sections regardless of the base type and interlayer, the magnitude of the impact is expected to be different from one section to another. The impact is presented in Section 7.6.2.

7.6.2 FWD Deflections

The sections were periodically evaluated with the FWD. The goal of the FWD evaluations was to determine how the corner deflection changes versus the curvature of the slab and how the change varies from section to section. The curvature of the slab changes daily and through the year depending on the environment loads. Temperature and humidity changes determine the magnitude of the environmental loads, which are critical loads for the pavement structures, as was shown in Figure 1-6. The type of base and interlayer was expected to play a key role in the slab curvature versus corner deflection relationship.

Each slab was evaluated at the center and corners, as shown in Figure 7-20, twice a day (morning and afternoon). Four evaluations were conducted: Jun-28, 2022; Aug-19, 2022; Nov-10, 2022; and Feb-2, 2023. The curvature of the slabs varied considerably from one date to another and also from morning to afternoon. Three FWD load levels were applied: 30, 50, and 70 kN (6,750, 11,250, and 15,750 lbf) to capture the relationship between load level and stiffness of the structure. It is assumed that the curvature of the concrete slab causes the corner to be as a cantilever, therefore the stiffness at lower FWD loads should be lower and increase with the

increase of the load since it is ensured that a bigger portion of the corner is in contact with the base.

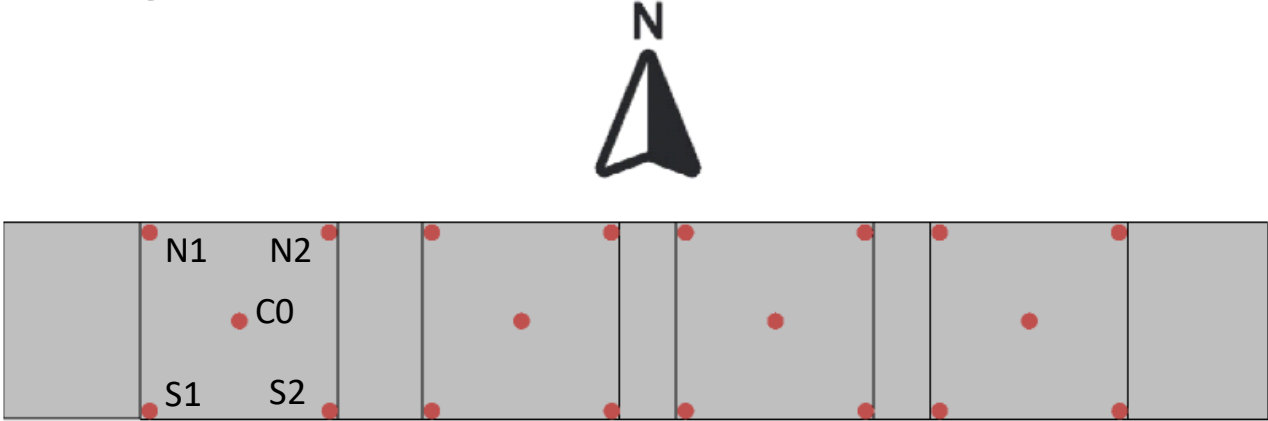
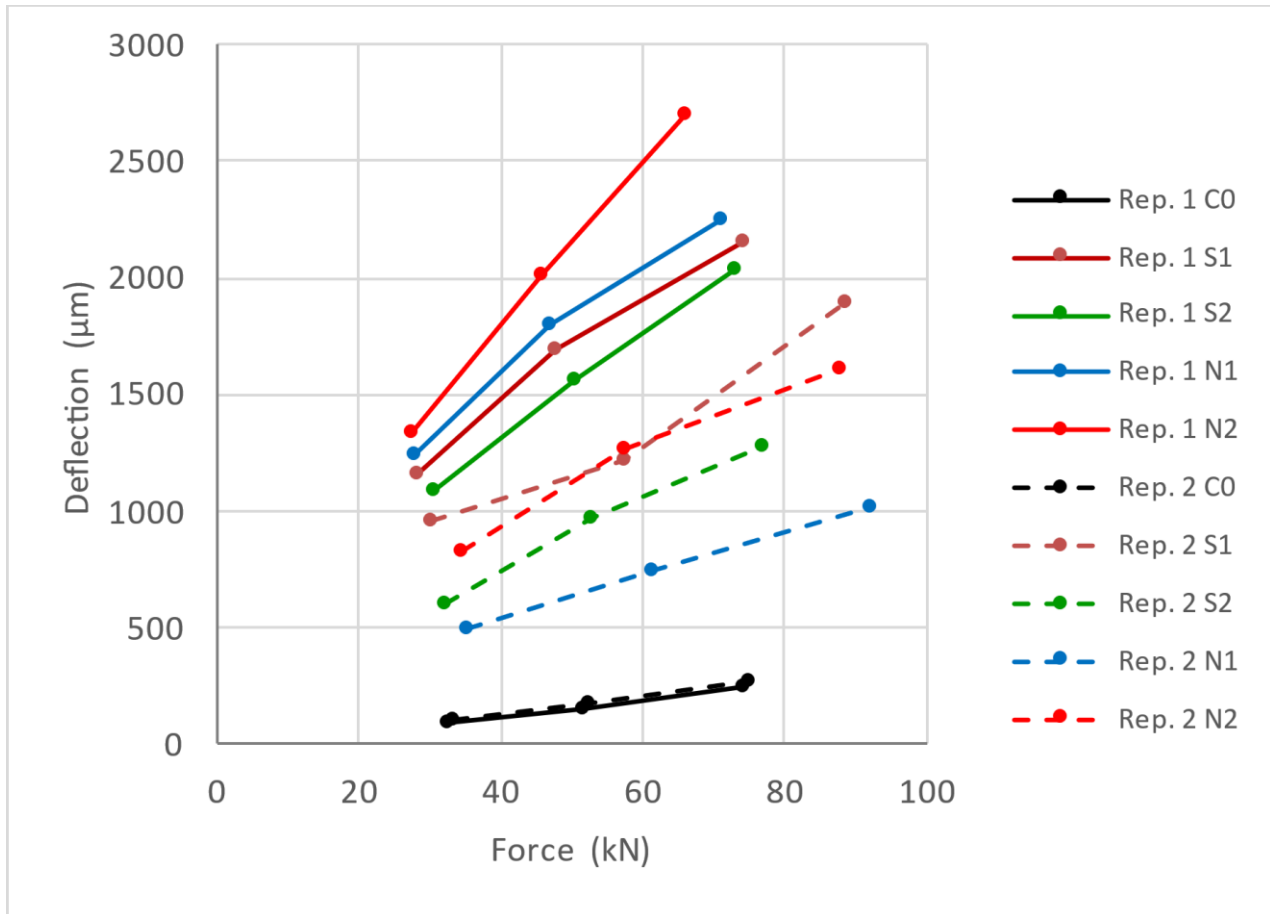


Figure 7-20. FWD evaluation locations

As an example, the deflections measured in the section with curing compound in the evaluation conducted on Aug. 19, 2022, are shown in Figure 7-21. The lower deflection at the center of the slab compared to the corner is evident in the figure. The higher corner deflection in the morning (Replicate 1) compared to the afternoon (Replicate 2) is also evident in the figure. The latter outcome is due to the higher curvature (in absolute value) in the morning compared to the afternoon, which is due to more negative thermal gradients (the colder temperature at the top of the concrete layer) in the morning compared to the afternoon. Considerable corner to corner variability is also evident in the figure.



Notes: Replicate 1 (Rep. 1) @morning; Rep. 2 @afternoon. C0, N1, N2, S1, and S2 locations shown in Figure 7-20

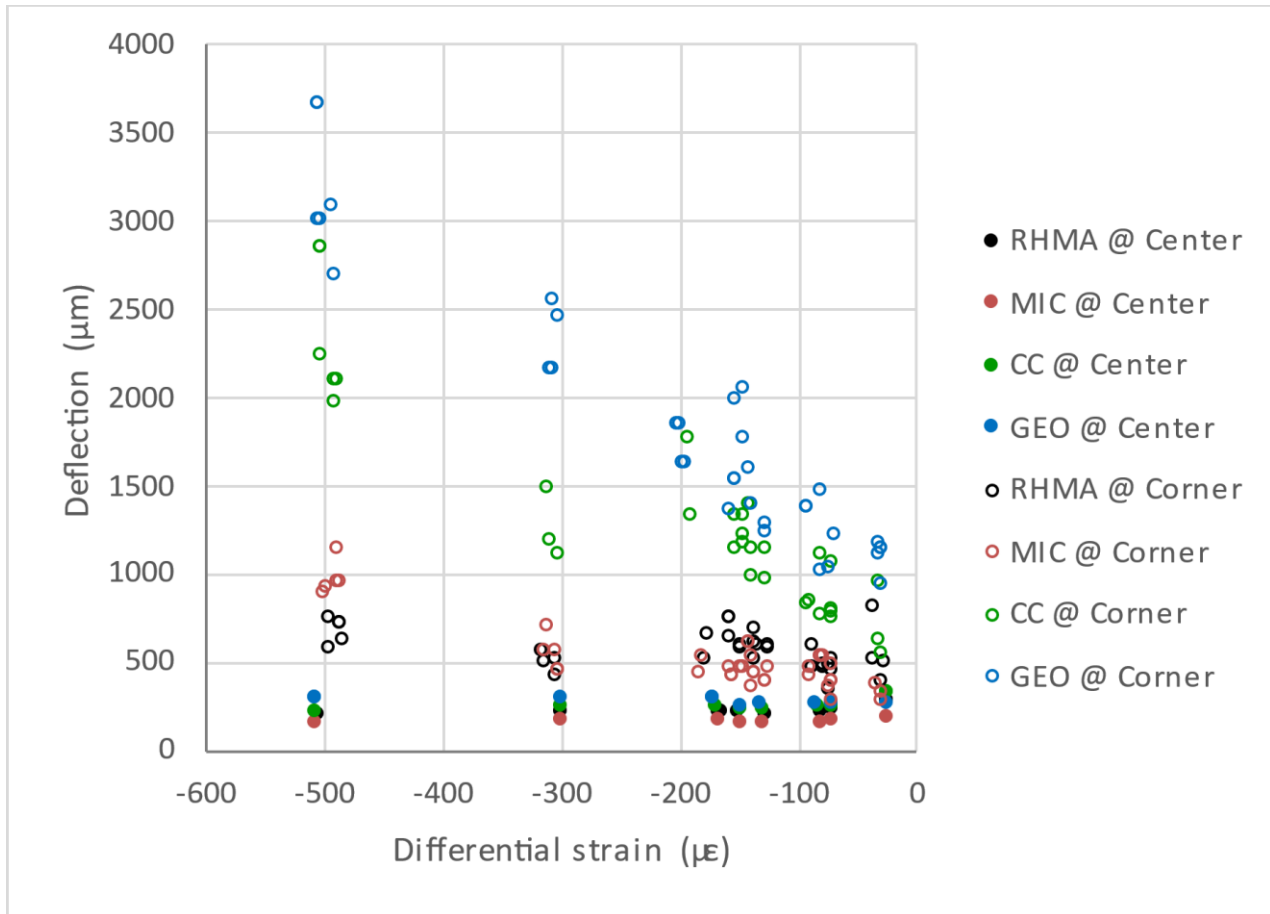
Figure 7-21. Example of FWD evaluation @ Section with Curing Compound; Aug-19, 2022

The summary of the four evaluations is presented in Figure 7-22. This figure shows the corner (average of four corners per section) and center deflection under 70 kN (15,750 lbf) FWD loading.

Several conclusions can be extracted from this figure:

- While the deflection at the center of the slab remains stable versus time and varies little from section to section, the deflection at the corner increases between two to five times through time, depending on the section. It ranges between 800 µε to 3700 µε from one section to another during the last FWD evaluation.

- As expected, the corner deflection increases as the magnitude of the differential strain (ϵ_{DIFF}) increases.
- The relationship between corner deflection and slab curvature strongly depends on the type of base and interlayer.
- The corner deflection in the section with LCB and curing compound interlayer versus slab curvature is more susceptible to change than in the section with RHMA-G base. In the summer evaluations, the corner deflection in the section with LCB and curing compound is up to three times the corner deflection in the section with RHMA-G base. This outcome agrees with the worse cracking performance of JPCP with LCB compared to JPCP with asphalt concrete base.
- The geotextile did not improve but diminished the performance of the section with curing compound interlayer based on the corner deflections measured over time. The corner deflections in the geotextile section were 25 to 65 percent more than the deflections in the curing compound section.
- The introduction of the microsurfacing interlayer considerably improved the performance of the section with curing compound interlayer based on the corner and center deflections when compared against the geotextile and curing compound interlayers. In fact, the corner deflection in the section with the microsurfacing interlayer and LCB barely increased 2.8 times versus slab curvature, and it was similar to the corner deflection in the section with RHMA-G base, which increased 2.1 times versus lab curvature.



Note: RHMA=rubberized hot mix asphalt, MIC=microsurfacing, CC=curing compound, and GEO=geotextile

Figure 7-22. Summary of FWD evaluations @ 70 kN (15,750 lbf) loading

7.6.3 Coring of Microsurfacing Section

A coring campaign was conducted on the microsurfacing section after analyzing the results obtained from the FWD testing. Initially, cores were extracted from the transition slab between the microsurfacing and the RHMA-G section to not core in the section itself. The microsurfacing thicknesses that were observed on the field while coring the transition slab had a big variability, as will be seen below, so it was also decided to core the corners and the center of the actual test slab to determine the thicknesses in those five locations. Figure 7-23 shows the section layout

and the location for each of the cores. Cores 1 through 8 were the first ones to be extracted, followed by cores A through F. As a reminder, this section consisted of a 175 mm (7 in.) concrete slab over a 105 mm (4.2 in.) LCB layer. The microsurfacing was the interlayer in this section and had an approximate thickness of 10 mm (0.2 in.). The section layout was shown previously in Figure 7-1.

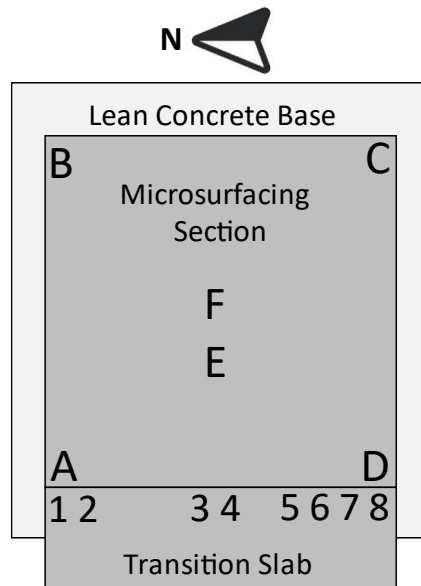


Figure 7-23. Core locations in the microsurfacing section

The extracted cores from the transition slab and the actual slab are shown in Figure 7-24 and Figure 7-26, respectively. None of the extracted cores had all three layers bonded together, which is the reason why each core has two parts to it, the tall section corresponds to the PCC layer, while the thinner section is the LCB. From visual observation, it was clear that there is a thickness variation of the microsurfacing between the different cores. The microsurfacing thickness was measured for each of the cores and reported as the summation of two parts: the side bonded to the PCC and the side bonded to the LCB. The recorded thicknesses are shown in Figure 7-25 and

Figure 7-27. The LCB side of Core 6 could not be extracted; hence, there is no microsurfacing thickness reported on the LCB side.



a) Cores 1 through 4



b) Cores 5 through 8

Figure 7-24. Close up pictures of cores 1 through 8

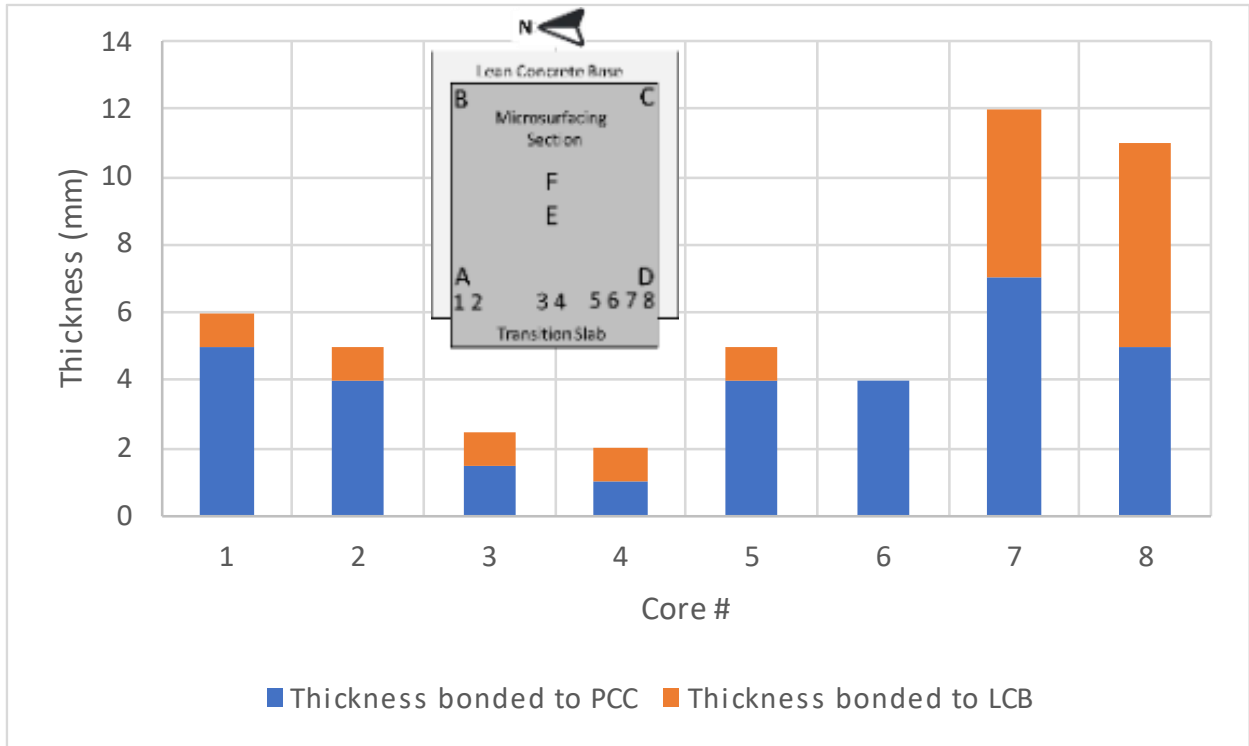


Figure 7-25. Microsurfacing thickness, cores 1 through 8 from transition slab



Core A



Core B



Core C



Core D



Core E



Core F

Figure 7-26. Close up pictures of cores A through F

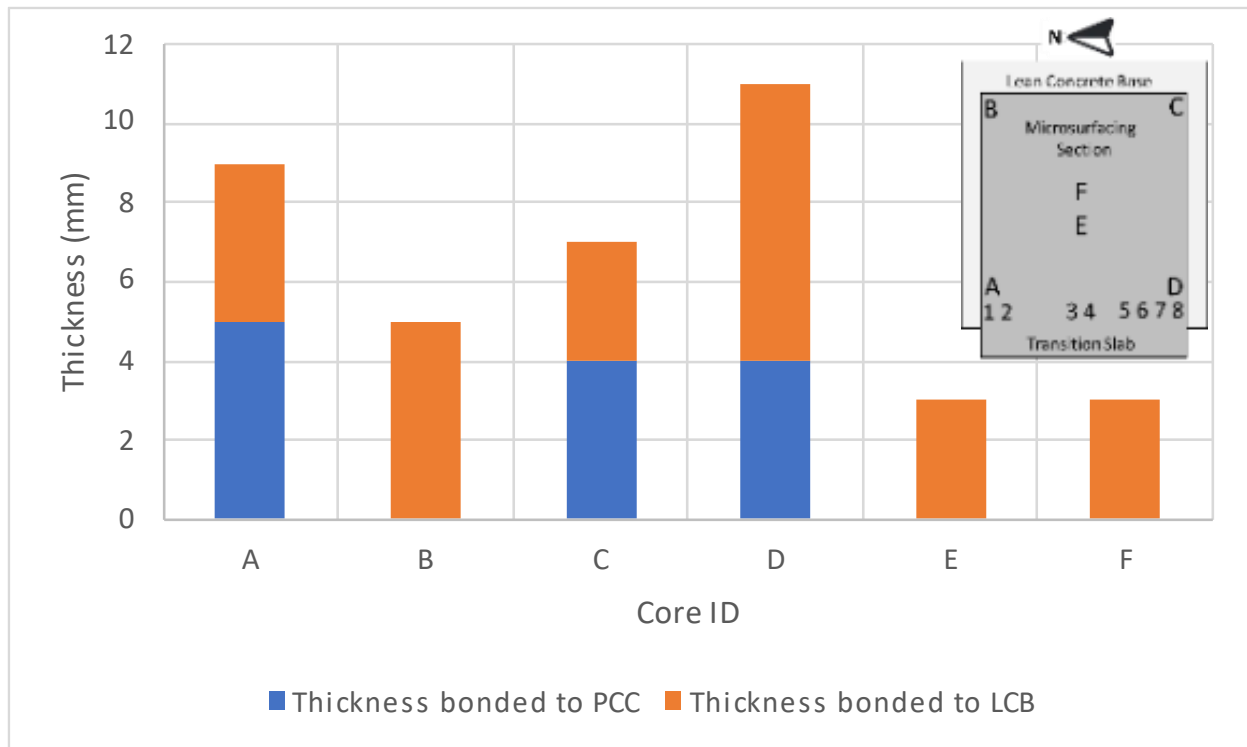


Figure 7-27. Microsurfacing thickness, cores A through F from test slab

7.6.3.1. Summary of Findings

- Corner cores have a microsurfacing thickness 2 to 6 times more than the center cores. Thickness variation from the center of the slab and corners was likely to occur due to microsurfacing migration from the center to the corners due to the concrete slab's daily curling and warping combined with the long-term effect of the shrinkage. The flow of material was observed in both the transition slab and the test slab.
- The microsurfacing texture of the specimens in the center of the slab has a crushed, thin, over-compacted microsurfacing layer with a lack of coarser aggregate. The specimens in the corners have a rich, thick microsurfacing layer with the presence of coarser aggregate.

The sinking of the slab in the center was a possible cause of the crushing and displacement of the microsurfacing.

- Microsurfacing placing issues could have added to the differences in the thickness of the microsurfacing, but the condition of the microsurfacing in the center (crushed without coarse aggregate) discards such initial thought and supports the likely migration of material from the center to the corners due to the combined effect of shrinkage and daily variation of the environment loads.
- Bonding between the microsurfacing and the PLC and LCB is proven to be adequate. Only one core (E) had no microsurfacing bonded to the PCC, and only one core had no microsurfacing bonded to the LCB. Hence, there is no difference in the bonding between the microsurfacing and both layers, even though the LCB had curing compound applied twice right after construction.
- The microsurfacing thickness difference between the four corners of the slab did not cause a noticeable difference in the corner deflections that were measured with the FWD testing at four different ages.

8. MODELING FRAMEWORK

8.1 Goal and Objectives

The goal of this chapter was to model the observed field behavior of the JPCP test sections presented in Chapter 7 and use the viscoelastic properties obtained from the tensile hanging damage and shear ramp tests presented in Chapter 5. A finite element model (FEM) was developed for each section type of JPCP pavement with their corresponding field description and measured material properties. The FEM software Abaqus was employed for this task. A detailed description of the material model implementation of the asphalt concrete in Abaqus is presented before the models.

The tensile cracking failure of the asphalt base near the interphase presents different mechanisms, mainly associated with delamination of the old HMA layer (as shown in Figure 2-9e) and with non-localized failures of RHMA-G mixes (as shown in Figure 2-9d). The failure for both cases was usually a band zone close to the interphase. Therefore, a cohesive damage model was defined for both cases, assuming that the failure occurs near the interphase, represented by a finite-thickness layer. A layer of cohesive elements, with a viscoelastic traction-separation law, was defined between the HMA and the JPCP.

8.2 Constitutive parameters

The material damage and separation (or failure) were assumed to be limited in a discrete plane, represented by the cohesive elements. The constitutive behavior of the cohesive model was determined by a traction-separation law (TSL) relating the traction (T) with the separation (δ) between the extreme planes defining the cohesive layer. Two TSLs were defined, one for axial

direction and one for shear direction. In the axial model, no damage was caused by compression; the damage was only associated with tension.

The material initiates its damage when the separation reaches an initial value δ_0 , corresponding to the maximum stress T_0 defined in the TSL. After going over this maximum, the interphase stress decreases gradually, and it fails when the separation reaches a final value δ_f , for which the related stress is 0. Different TSLs can be defined for a particular material and Figure 8-1 shows schematically three evolution laws that were considered when defining the research approach: linear, bilinear, and exponential approaches. The figure presents the T- δ relationship for traction and perpendicular separation variables, but the same evolution laws were used for shear stress and transverse separation.

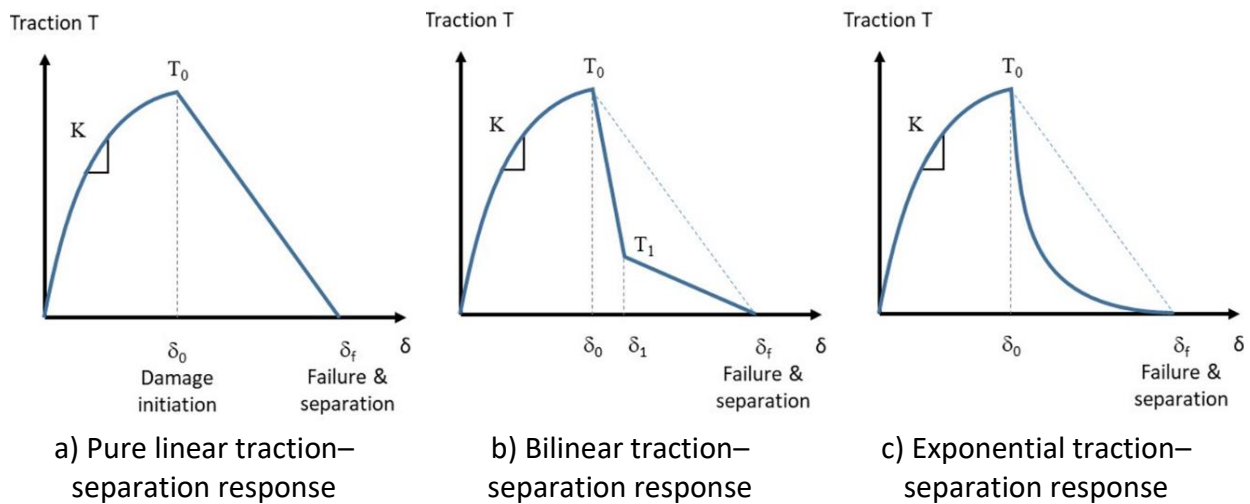


Figure 8-1. Traction-separation evolution laws of the cohesive element considered in this research

The evolution laws can be easily defined with linear equations for cases a) and b) in Figure 8-1.

The exponential variation of the damage shown in Figure 8-1c corresponds to the following equation:

$$D = 1 - \left\{ \frac{\delta_0}{\delta} \right\} \left(1 - \frac{1 - \exp \left(-\alpha \left(\frac{\delta - \delta_0}{\delta_f - \delta_0} \right) \right)}{1 - \exp(-\alpha)} \right)$$

The basic material properties of the cohesive elements were defined from the viscoelastic properties of the 3D continuum. The instantaneous elastic properties are the normal stiffness (K_{nn}) and the transverse stiffness along both transverse directions (K_{ss} and K_{tt} , respectively). Those represent the instantaneous relationship between stress and relative displacement on the cohesive nodes, thus being thickness-dependent:

$$K_{nn} = \frac{E}{h}, K_{ss} = \frac{G}{h}, K_{tt} = \frac{G}{h}$$

Where E and G are the Young's elastic modulus and the transverse elastic modulus, respectively.

The cohesive layer thickness is h. These properties are presented in Table 8-1.

Table 8-1. Elastic properties of the cohesive elements

Material	Isotropic			Thickness	Cohesive		
	E, MPa (ksi)	Poisson's ratio	G, MPa (ksi)	h, mm (in.)	K_{nn} , MPa/mm (ksi/mm)	K_{ss} , MPa/mm (ksi/mm)	K_{tt} , MPa/mm (ksi/mm)
Yol113	22,454 (3,257)	0.1	10,206 (1,480)	10 mm (0.4)	2,245 (325)	1,020 (148)	1,020 (148)

Relaxation and creep viscoelastic properties are considered using a Prony series expansion obtained from the testing done in Chapter 5. The Prony series parameters for each term i , g_i , k_i ,

and τ_i (relaxation, creep, and time coefficient of the series) were defined directly in the model, assuming an expansion of 20 terms as was mentioned in section 5.3.6.

Abaqus provides four different damage initiation criteria based either on displacements or stress. This research used the displacement approach. The initiation of the failure occurs when the maximum nominal strain ratio reaches the value of 1:

$$MAX \left\{ \frac{\langle \varepsilon_n \rangle}{\varepsilon_n^{max}}, \frac{\varepsilon_s}{\varepsilon_s^{max}}, \frac{\varepsilon_t}{\varepsilon_t^{max}} \right\} = 1 \quad \text{Equation 15}$$

Alternatively, it can be formulated considering a quadratic interaction function, initiating the failure when the addition of the squared nominal strain ratios reaches one:

$$\left\{ \frac{\langle \varepsilon_n \rangle}{\varepsilon_n^{max}} \right\}^2 + \left\{ \frac{\varepsilon_s}{\varepsilon_s^{max}} \right\}^2 + \left\{ \frac{\varepsilon_t}{\varepsilon_t^{max}} \right\}^2 = 1 \quad \text{Equation 16}$$

In which ε_n , ε_s , and ε_t are the nominal strains in the normal direction, first and second shear directions, respectively. ε_n^{max} , ε_s^{max} , and ε_t^{max} are the individual initiation strains in the corresponding directions. Equation 16 was decided to be used in this research because it considers the influence of both tension and shear in the failure initiation.

8.3 Cohesive elements

The cohesive elements are frequently used to model an interphase between two surfaces that may experience damage with consequent separation. The interphase may have no thickness when the problem studied corresponds to pure delamination or may have an actual volume when

the problem is not localized. Nevertheless, the cohesive width should be small in relation to the model dimensions since the objective is not to study the stress characterization but the separation between the surfaces.

A sensitivity study was performed for different interphase widths (2, 10, and 20 mm [0.08, 0.4, and 0.8 in.]), applied to the tensile hanging damage and shear ramp tests that were performed in the laboratory to compare their behavior. When using a 2 mm (0.08 in.) interphase width, it was difficult to replicate the laboratory test behavior, while when using a 20 mm (0.8) interphase width, it was suspected that it was too thick of a layer, although an adequate result was obtained. A 10-mm (0.4 in.) width replicated the test behavior and was adopted for the cohesive interphase in this research, defined with 8-node three-dimensional cohesive elements (COH3D8 element from Abaqus). The main variables of the cohesive element are the deformation in the normal mode and two transverse shear modes (Abaqus manual [56], 1.3.45 Cohesive elements). The model is dynamic/explicit and uses cohesive elements (instead of cohesive surface contact pairs) because it is the only solution in Abaqus that supports viscoelastic behavior with damage.

8.4 Material parameters obtained from testing

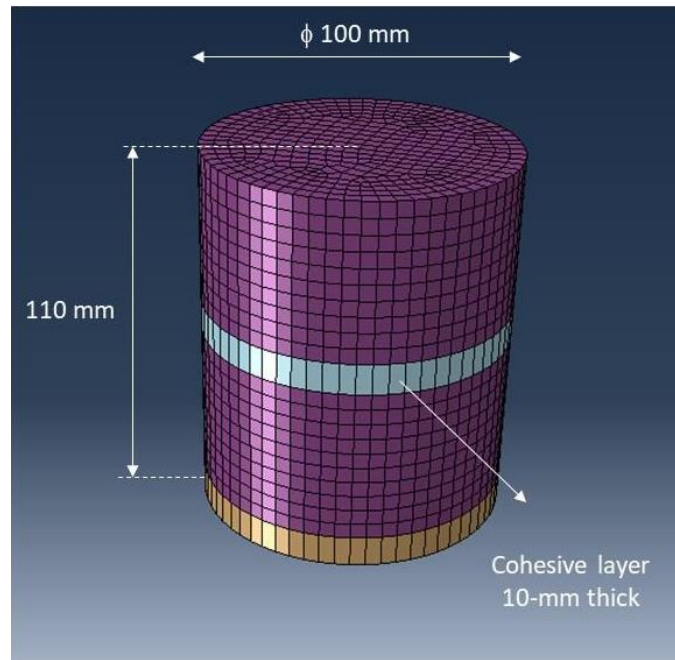
The material behavior observed in the tensile hanging damage and shear ramp tests of the asphalt materials was used to obtain the parameters to characterize the traction-separation law of the cohesive elements. A description of the process for each of the tests is shown in the following subsections.

8.4.1 Tensile Hanging Damage test

The tensile hanging damage test represented the normal behavior under tension of the asphalt for very low loading frequencies. This was the behavior needed to study the delamination of the asphalt-concrete interphase due to shrinkage and temperature-related loads that take place over long periods of time, which can range from a day to several months. Figure 8-2 shows the test setup and the corresponding model of the specimen in Abaqus. The specimen height is 200 mm (8 in.), and the diameter is 100 mm (4 in.). The model height corresponds to the LVDT span, which was 110 mm (4.4 in.).



a) Hanging test setup



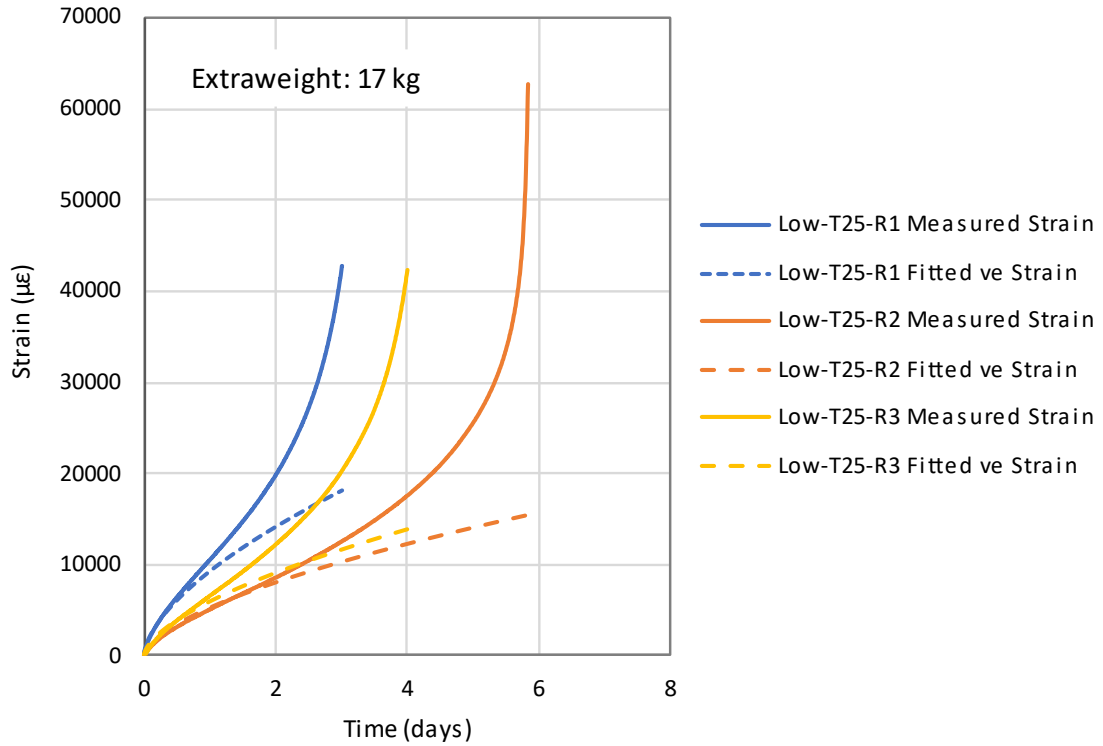
b) Hanging test model in Abaqus with a 10 mm cohesive layer in the middle of the specimen

Figure 8-2. Hanging test setup and model

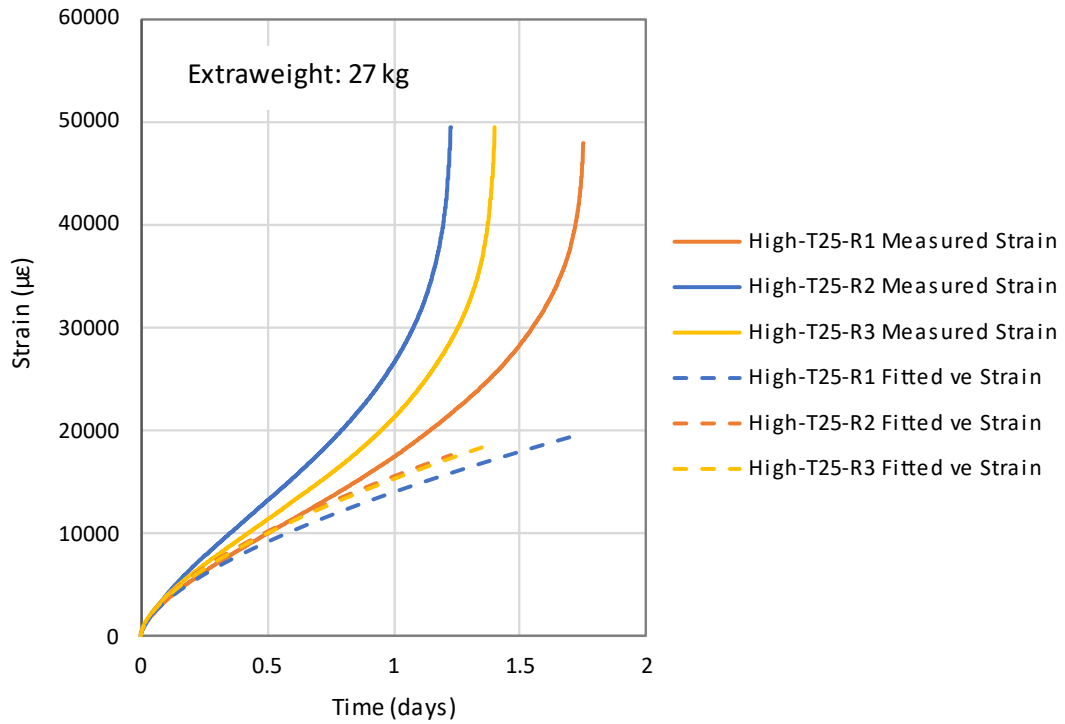
The parameters defining the traction-separation law were determined using values back-calculated to match the behavior of the RHMA-G specimens in the hanging test. It is important

to note that the damage is extended to the whole specimen, while in the FEM model, it was restricted to the cohesive layer with a predefined width and position. Hence, the layer width has a considerable influence since it needs to represent damage that spreads over a larger volume. Therefore, since the model tries to represent the overall behavior of the specimen under damage, identifying the specific failure position is not relevant.

The process of identification of the damage model properties started by reviewing the model behavior without damage. There was a considerable dispersion between the hanging test results, even for the same materials and loads (series of 3 tests). Figure 8-3 presents the test results for two series of 3 tests fabricated with Yol113RHMA-G, each one using a different hanging load. The figure shows the measured strain from each of the tests and the fitted veStrain that was introduced in Section 5.4 which corresponds to a model that describes the undamaged part of the test.



a) Test 1: Low, with 17 kg (37.5 lb) extra weight



b) Test 2: High, with 27 kg (59.5 lb) extra weight

Figure 8-3. Dispersion of hanging test results for two sets of Yo113RHMA-G tests

The viscoelastic model in Abaqus uses a unique Prony series that was fitted for the full frequency range, using the different laboratory tests available, which were explained in Chapter 5. Consequently, differences may be expected when a single series is used to represent the hanging test results. The adopted procedure assumed that the Prony series behavior was a good approach for the actual viscoelastic behavior if the model results were within the laboratory test variability. Since the viscoelastic behavior was assumed correct, the laboratory test results may need to be scaled to be coincident with the FEM results before the damaged interval. The adjustment coefficient may be required since the FEM result is done using average values obtained across multiple specimens. Hence, the model cannot explain every single laboratory test. Then, the FEM damage properties were tuned until the FEM results fit the scaled laboratory results. In this research, the R3 test from Figure 8-3a fitted well with the viscoelastic model and no scaling was necessary, as can be seen in Figure 8-4.

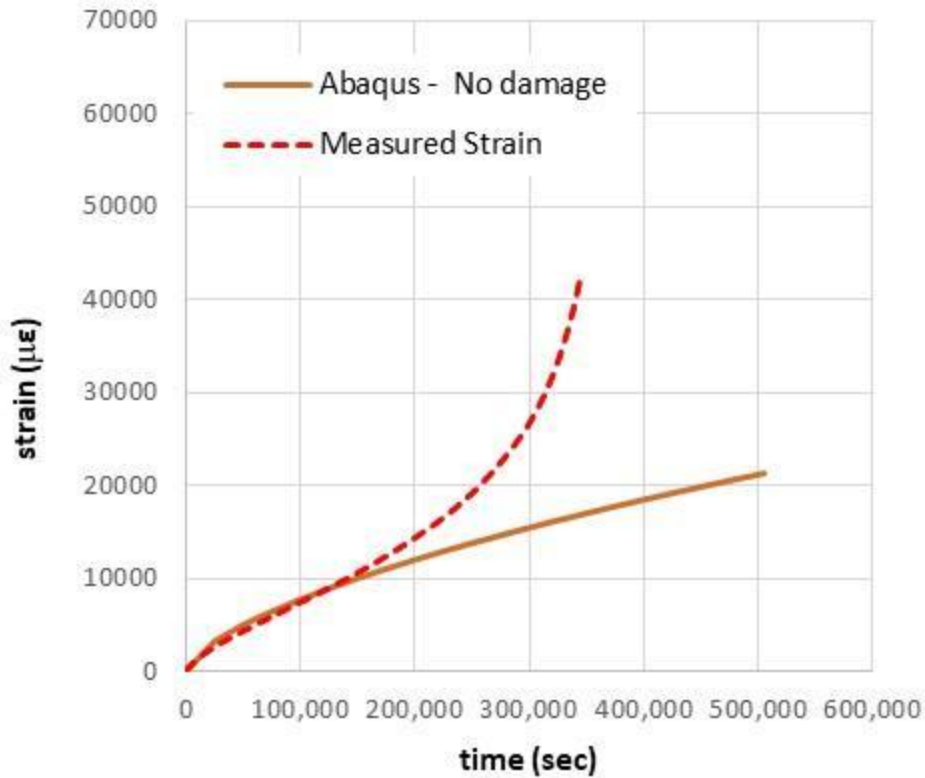


Figure 8-4. Damage properties fitting. R3 case (no need of scaling)

The most critical parameter in damage modeling is the damage initiation. Figure 8-5 shows three FEM approaches with different initiation values compared to the lab-measured strain of an RHMA-G specimen. As observed, the fit of the model behavior to the hanging test results was very good for a 10 mm (0.4 in.) cohesive layer with a linear damage evolution, with initiation at $\epsilon = 0.065$. The damage evolution was important because it controls the damage increase with the load and can be defined as linear, tri-linear, or exponential. In this specific case, a linear evolution with a separation displacement of 5 mm (0.2 in.) measured from the damage initiation position fits the data well. It was found that the linear evolution in Abaqus coincides well with the exponential function of zero order.

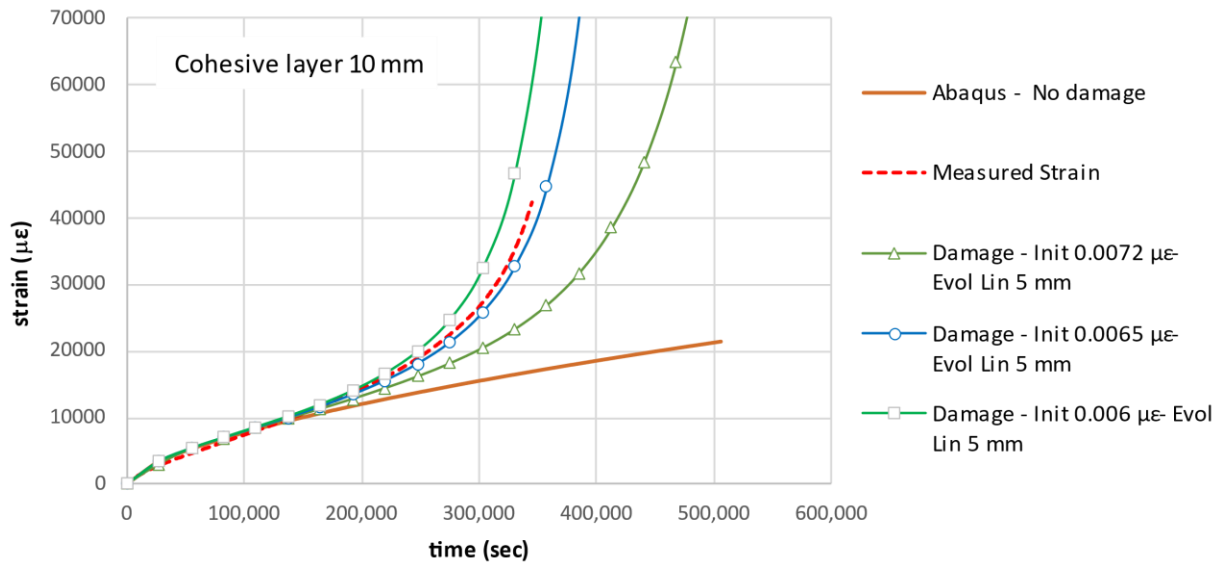


Figure 8-5. Yol113RHMA-G tensile hanging damage test compared to different damage models, cohesive layer thickness of 10 mm

Since the damage behavior was localized in the cohesive layer, it was expected that different cohesive layer thicknesses need distinct damage properties to represent the same specimen failure. Various cohesive layer thicknesses were considered when repeating the previous fitting process, obtaining the damage models detailed in Table 8-2 for the tension behavior of the RHMA-G mix. All of them can represent the specimen behavior adequately.

Table 8-2. Cohesive damage approaches to the hanging test

Cohesive layer thickness, mm (in.)	Traction Initiation, $\mu\epsilon$	Evolution law	Parameters	
			Damage %	Displacement T_{mf} , mm (in.)
2 (0.08)	0.005	Linear	100	5 (0.2)
10 (0.4)	0.065	Linear	100	5 (0.2)
20 (0.8)	0.075	Linear	100	5 (0.2)
35 (1.4)	0.085	Linear	100	5 (0.2)

Figure 8-6 shows the representation of this approach among the dispersed results obtained from the hanging test. As can be seen, the behavior obtained using the damage model from Abaqus accurately describes the test results and proves to be adequate.

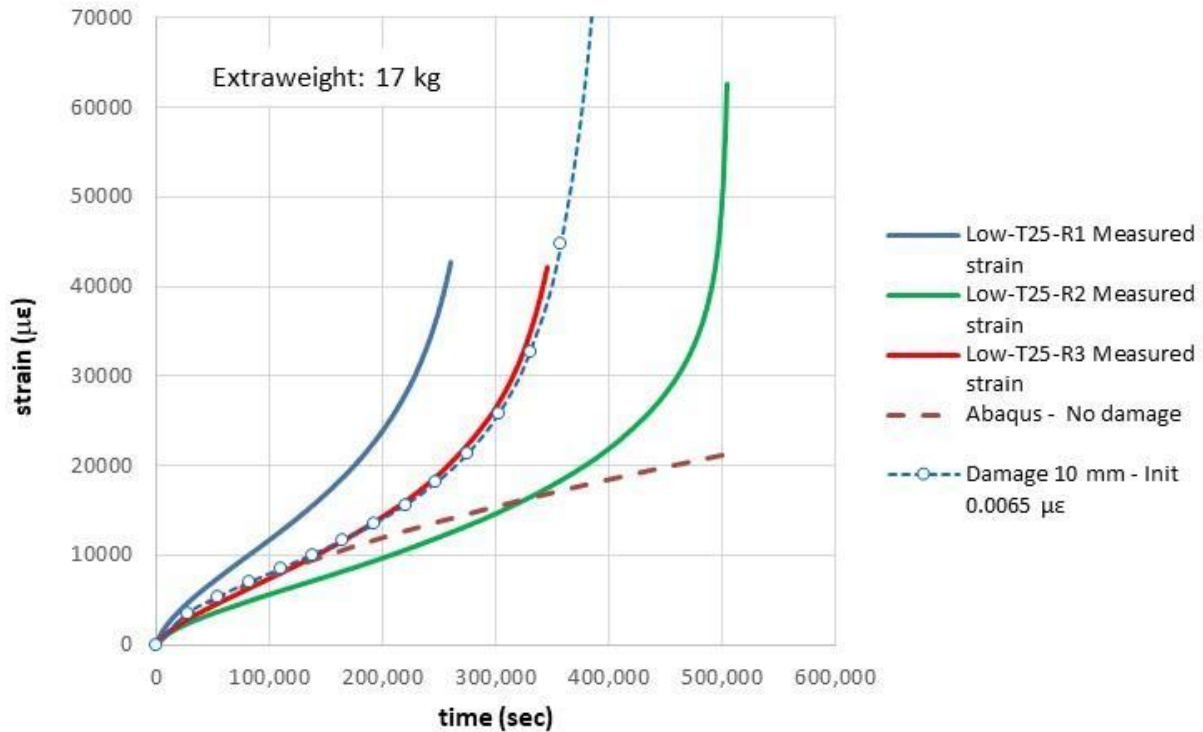
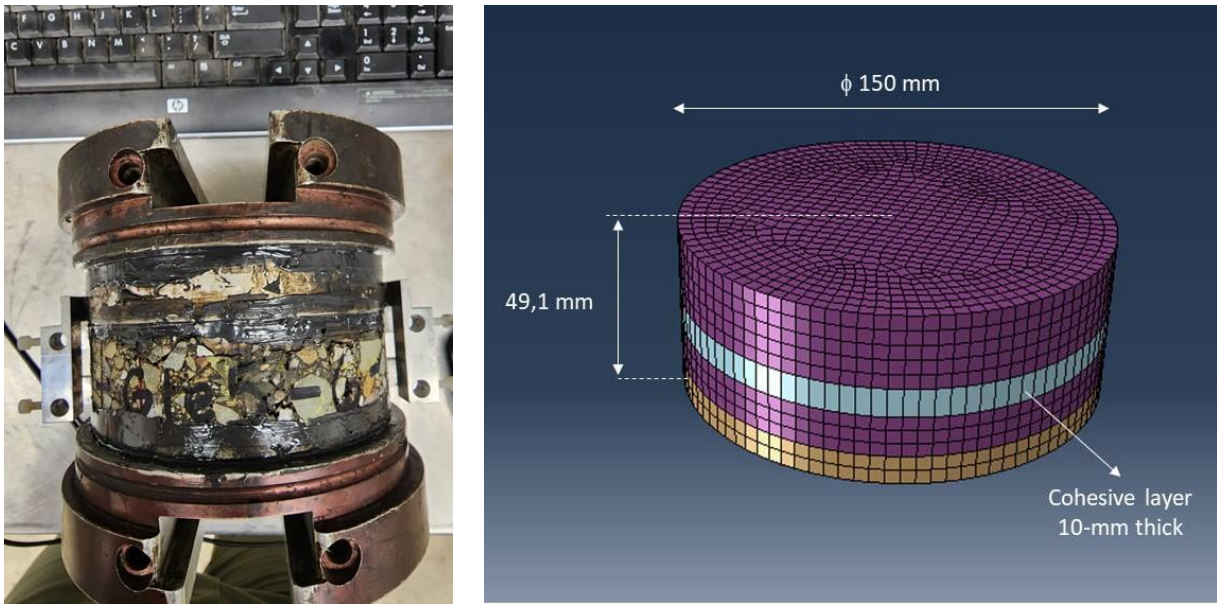


Figure 8-6. Tensile hanging damage test results compared to Abaqus viscoelastic and damage model, cohesive layer thickness of 10 mm

8.4.2 Shear Ramp Test

The shear ramp test studied the shear behavior of the specimen under a monotonic increasing displacement at the extreme faces, maintaining a constant normal load. The specimen was tested under constant shear strain for nearly 35,000 seconds. This was the slowest shear test setup available and was used to characterize the traction-separation law for shear.

Figure 8-7 presents the test setup and corresponding model. The specimen in the model has the same height as in the actual test. The cohesive layer was placed at a vertically intermediate position. This position has no significance since the results were checked for the whole specimen, measuring the total displacements of the base platen.



a) Shear test setup

b) Shear test model in Abaqus with 10 mm cohesive layer at an intermediate position of the specimen

Figure 8-7. STT shear test setup and model

The cohesive layer thickness had a relevant influence on the results, as in the hanging test case, because the damage in the asphalt is extended to the whole specimen. However, the FEM model focuses the damage behavior at the cohesive layer, which should be capable of representing the overall shear performance of the specimen. The layer width influence is conceptually represented in Figure 8-8, showing that different layer thicknesses would need distinct damage parameters. A greater thickness allows the specimen to reach a total strain with smaller damage strains at the cohesive layer, while a thinner layer allows higher cohesive damage strains.

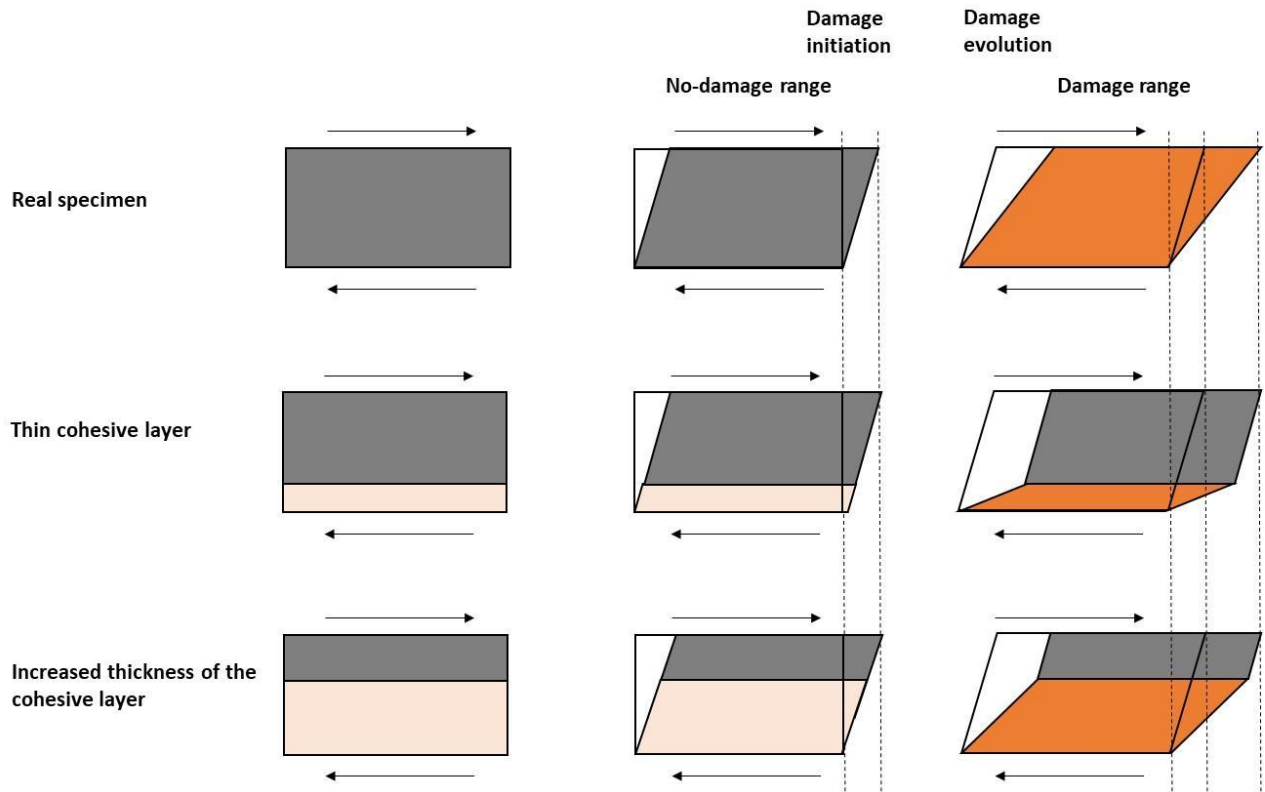


Figure 8-8. Conceptual behavior of different cohesive layer thicknesses in the damage range

The results from the shear ramp test showed dispersion; however, one of the tests provided complete and reliable results. This test result was selected as a reference to build the Abaqus approach. Figure 8-9 shows the comparison between the measured strains and the viscoelastic model results without damage. No significant scaling was necessary in this case.

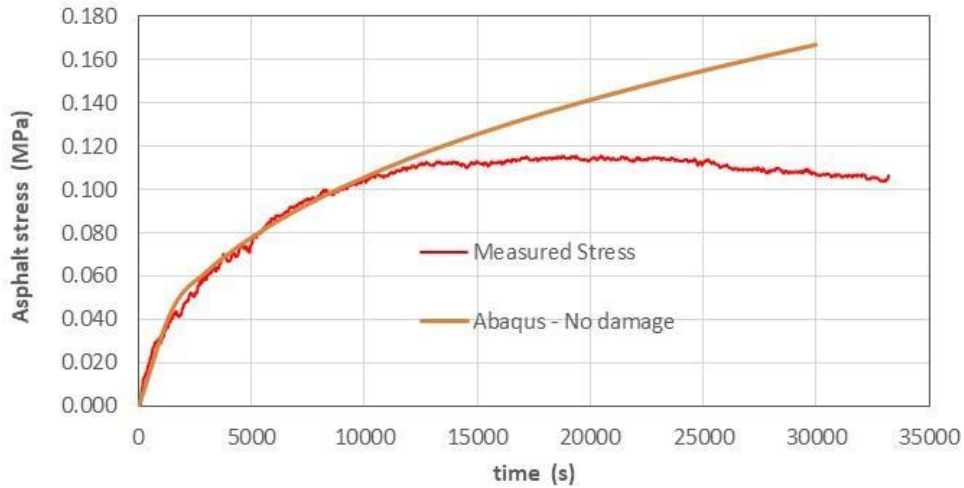


Figure 8-9. Shear stress-time results to be used as a reference for the damage properties fitting

Thicknesses of 35, 20, 10, and 2 mm (1.4, 0.8, 0.4 and 0.08 in.) were considered to study the variability. Although the first two were too thick, the four thicknesses can correctly model the problem if the properties are adequately tuned. Table 8-3 shows the best damage model approaches using different traction-separation laws. The accuracy for each approach is graphically presented in Figure 8-10. A bilinear evolution law fitted well for thicker layers, but an exponential law was needed for the 2 mm (0.08 mm) one.

Table 8-3. Cohesive damage approaches to SST shear test

Cohesive layer thickness, mm (in.)	Shear Initiation, $\mu\epsilon$	Evolution law	Parameters	
			alpha	displacement δf , mm (in.)
2	0.012	exponential	-15	3
			Damage %	displacement δf , mm (in.)
10	0.003	bilinear	0.5	0.35
			1	1.5
20	0.003	bilinear	0.4	0.8
			1	2.5
35	0.003	bilinear	0.35	1.4
			1	4

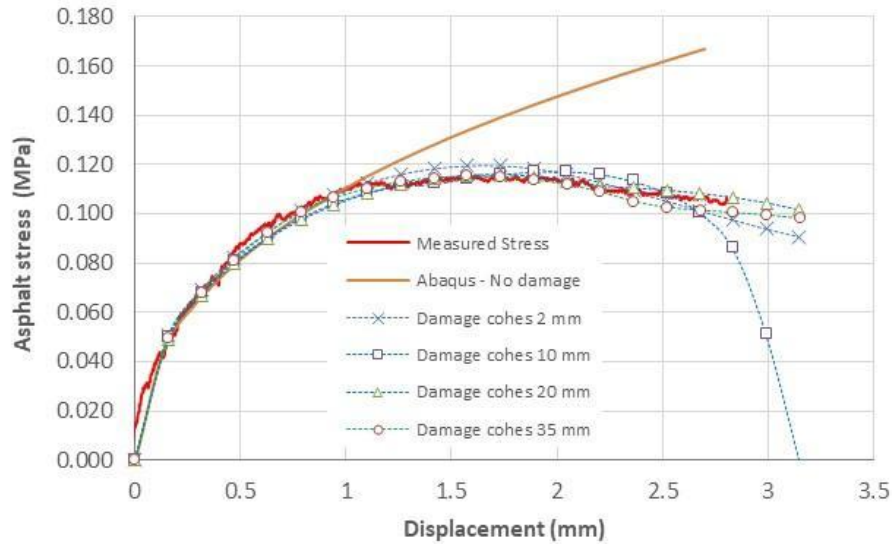


Figure 8-10. Shear stress-displacement results for different cohesive layer thickness

8.4.3 Full model damage properties

The damage properties obtained previously correspond to a particular cohesive layer of a specimen with a defined height. As explained above, the fact that the cohesive layer has the damage behavior makes the model thickness dependent. However, the test damage behavior always showed the same results, independently of the specimen height, when the variation was represented using a non-dependent parameter on the specimen size. Additionally, when testing the tensile ramp of asphalt and composite specimens in Section 6.4, it was observed that both sets of specimens had the same deformation level envelope. However, the distance over which they were measuring was 100 mm for asphalt specimens and 50 mm for composite specimens. This behavior can be proven using the measurements obtained at different specimen heights for both the hanging and the shear tests. This fact is described in Figure 8-11 for the tensile hanging damage test and in Figure 8-12 for the shear ramp test.

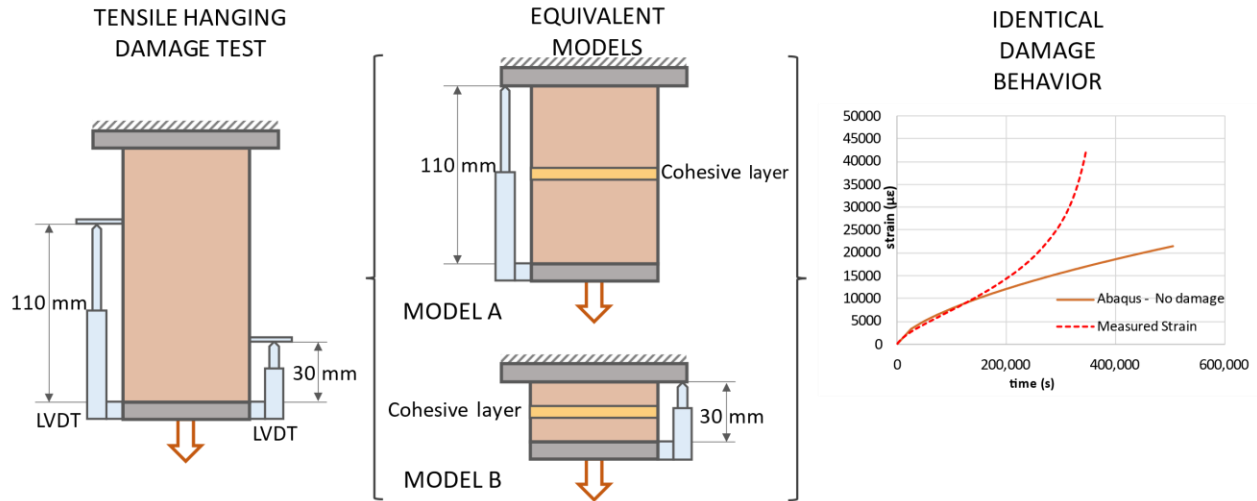


Figure 8-11. Hanging test strain-time results for different specimen thicknesses

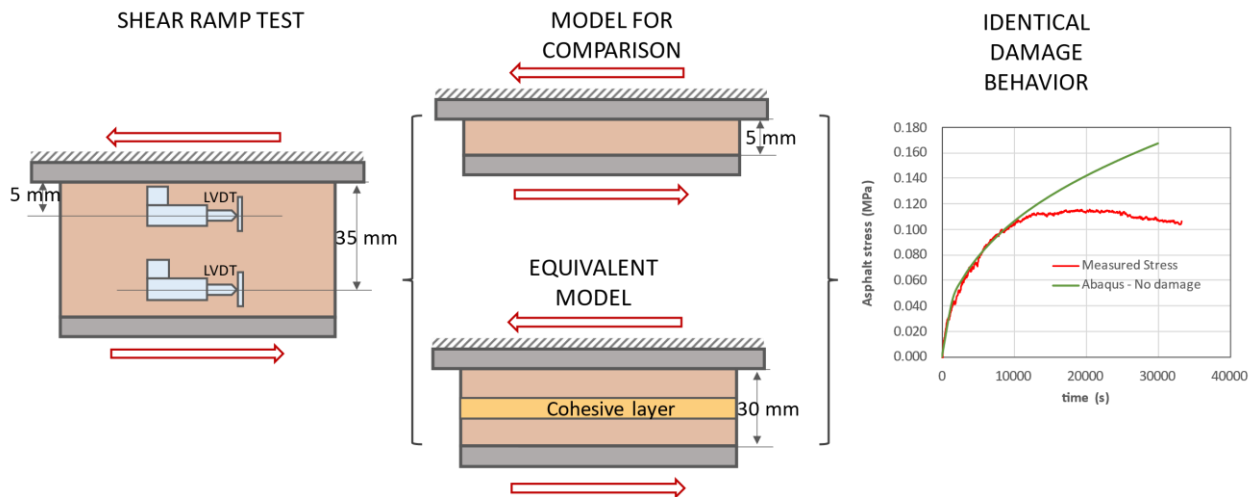


Figure 8-12. Shear test stress-time results for different specimen thicknesses

Consequently, it was assumed that a theoretical specimen with the same height as the pavement asphalt layer would also have the same damage behavior. Then, the FEM model damage properties of the pavement can be assumed using the models of the theoretical specimen and fitting its damage behavior as was explained in the previous section. This procedure was applied to obtain the final damage properties of the complex model, which are presented in Table 8-4.

Table 8-4. Cohesive damage approaches for the complex model of asphalt

Damage mechanism	Specimen height, mm (in.)	Cohesive layer thickness, mm (in.)	Damage initiation, $\mu\epsilon$	Evolution law	Parameters	
					Damage %	Failure displacement δf , mm (in.)
Tension	76 (3)	10 (0.4)	6.8E-03	Linear	100	5 (0.2)
Shear	76 (3)	10 (0.4)	7.2E-03	Bi-linear	0.65	0.35 (0.014)
					1	2.3 (0.09)

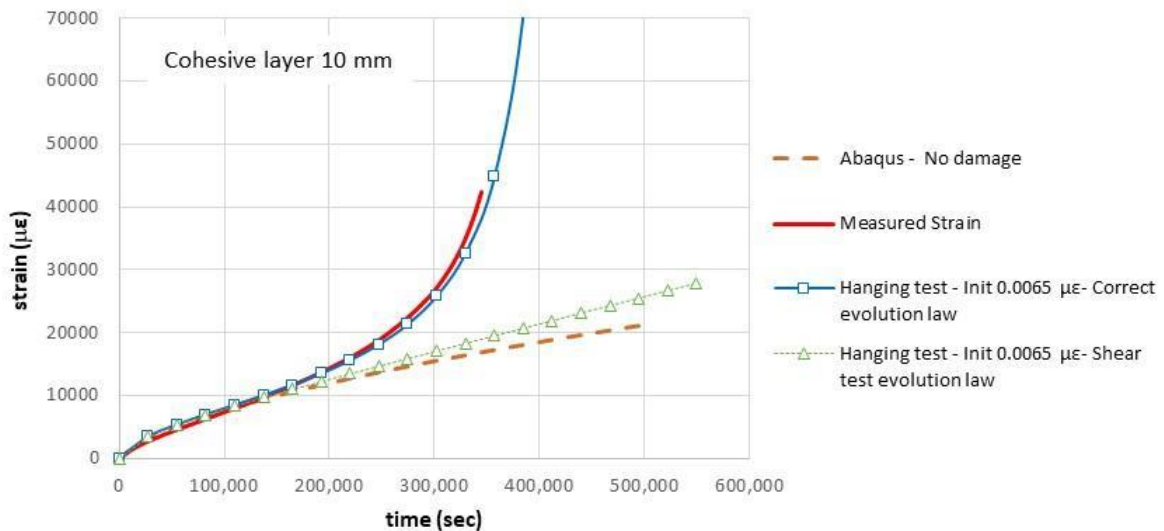
8.4.4 Combined model for tension and shear damage

As explained above, a good fit was obtained for the tensile hanging damage and shear ramp tests independently, using proper damage models. However, the evolution parameters fitting the tensile hanging damage test did not coincide with those matching the shear ramp test. Abaqus allows separate initiation strains for normal and shear displacements, but it has a built-in limitation that it only allows one damage evolution law for both simultaneously. Thus, an agreement needed to be achieved when modeling the pavement structures, and two possible approaches can be used:

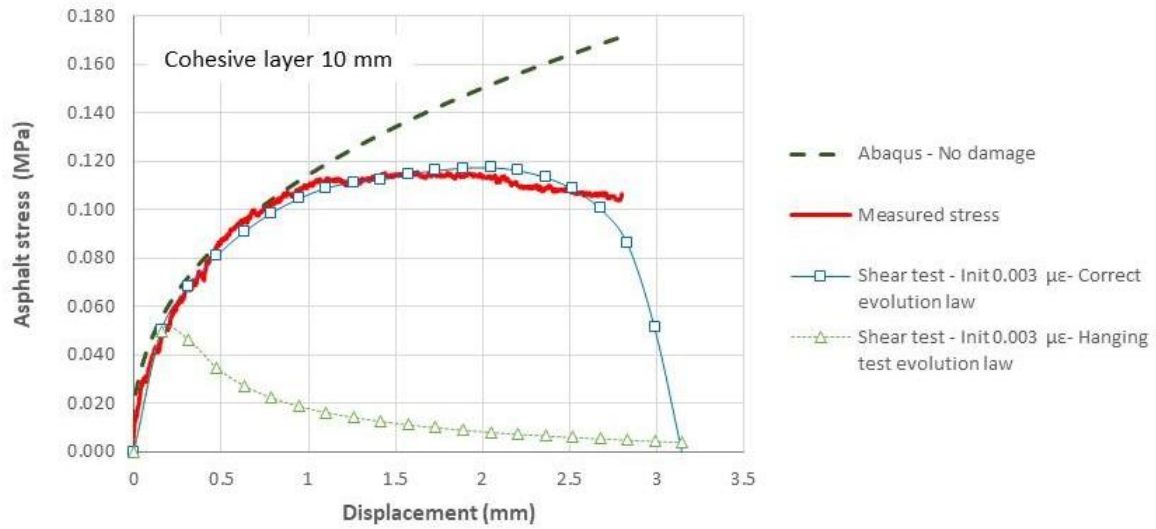
- The first approach was to study in advance the damage mechanisms of tension and shear independently, identifying the most likely to happen and using its initiation criteria. This was the solution chosen in this research, with the squared addition criteria (defined in Equation 16).
- The second approach was to define independent cohesive layers, one for tension behavior and another one for shear behavior, assuming that each one reaches failure independently. The layers would be defined one on top of the other, so if one of them fails, the system fails. This approach considered that both damage behaviors act

independently and without mutual interaction. The initiation law for this case was like the one defined in Equation 15. The law defined in Equation 16 was not possible with this model.

It should be noted that the use of a single cohesive layer with a common evolution law for tension and shear without previous analysis of their respective influence might lead to significant errors, which can cause the failure to either never initiate or to initiate too soon. Figure 8-13a shows the tensile hanging damage test specimen behavior with the damage evolution law from the shear test analysis with almost no damage. Figure 8-13b presents the behavior of the shear ramp test specimen with the evolution law from the hanging test showing a very early failure.



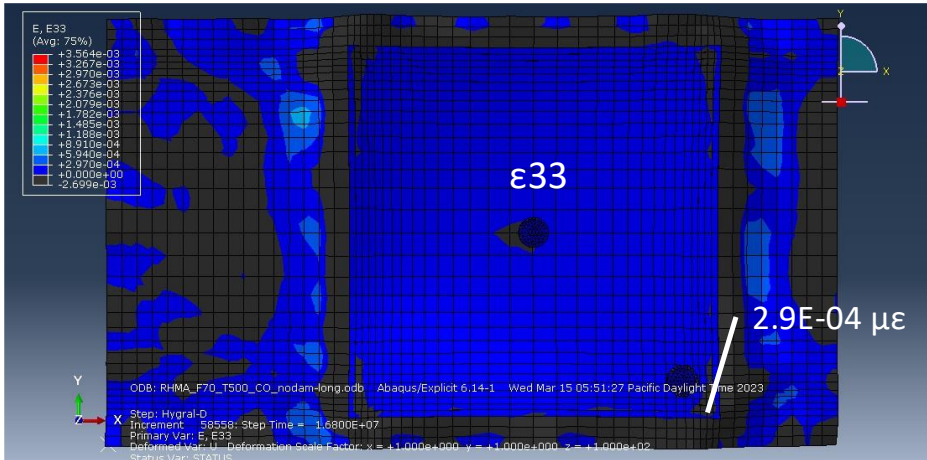
a) Hanging test plot with 10 mm (0.4 in.) cohesive layer



b) Shear test plot with 10 mm (0.4 in.) cohesive layer

Figure 8-13. Comparison of model results interchanging damage evolution laws for hanging and shear tests

Since only one damage evolution law can be input in the software, independent case analyses were performed to determine which is the critical failing criteria in the pavement structure. An undamaged model was analyzed to determine whether the modeled tensile and shear strains would reach the respective damage initiation values shown in Table 8-4. The model results and strain values are shown in Figure 8-14. The modeled maximum vertical strain was $2.9\text{E-}04 \mu\epsilon$, which was below the damage initiation of $6.8\text{E-}03 \mu\epsilon$, and the modeled maximum shear strain (vectorial summation of shear in both directions) was $9.0\text{E-}02 \mu\epsilon$, which was around ten times over the damage initiation of $7.2\text{E-}03 \mu\epsilon$. Therefore, the critical failing criteria in the structure is shear and corresponds to the damage evolution law that should be used.

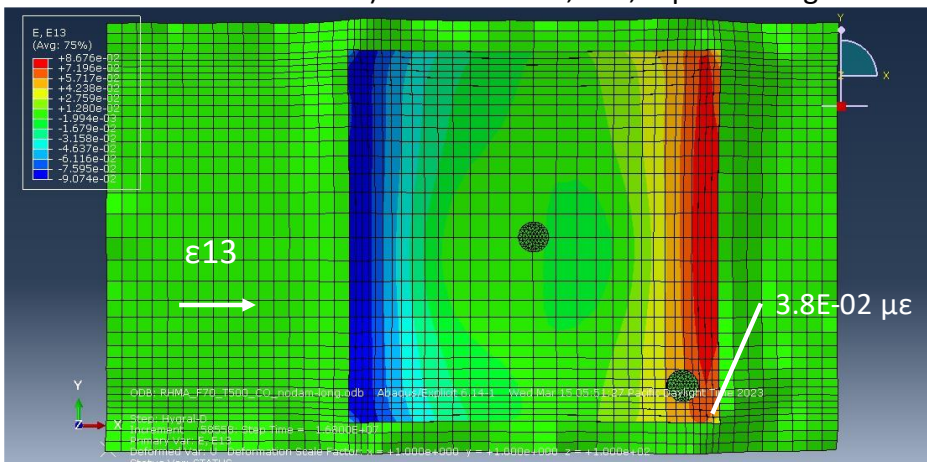


Maximum vertical strain: $2.9E-04 \mu\epsilon$

Damage initiation strain: $6.8E-03 \mu\epsilon$

→ No failure

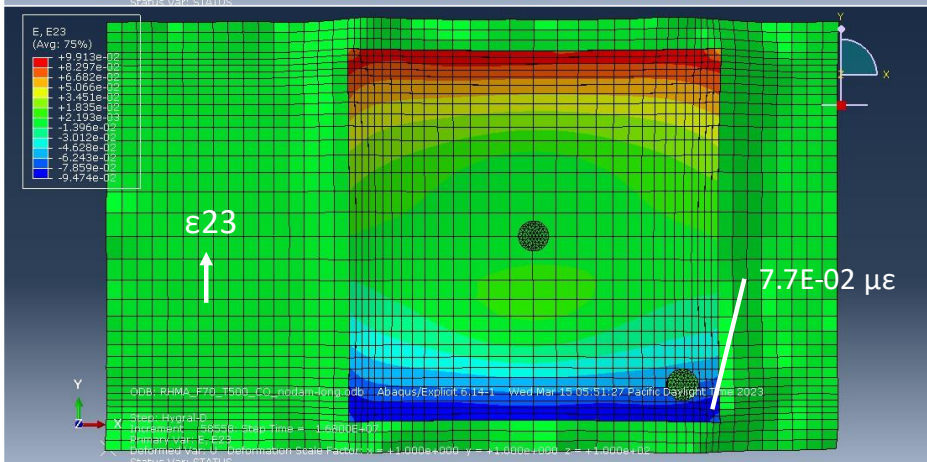
a) Vertical strain, ϵ_{33} , top view diagram



Maximum shear strain: $9.0E-02 \mu\epsilon$

Damage initiation strain: $7.2E-03 \mu\epsilon$

→ Failure



b) Shear strain, ϵ_{13} and ϵ_{23} , top view diagrams

Figure 8-14. Tensile and shear strain comparison for determining the critical damage initiation law

8.4.5 Compression model for the viscoelastic solids

A couple of challenges were faced when defining the compression model for the viscoelastic solids. First, the viscoelastic nature of the model presented high strength for fast loads and a low strength for slow loads. For example, loads applied over long periods, like the pavement self-weight, would tend to sink in the underlayer viscoelastic solid. Second, a non-zero thickness cohesive layer under alternating tension and compression also presented a problem. Tension may completely damage the layer material, causing separation of the adjacent solid and leaving the cohesive element without strength. Afterward, the overlaying solid can re-contact the damaged layer, and assuming zero compression strength would be unrealistic.

To avoid these undesired behaviors in compression, each viscoelastic solid should have a minimum compression strength that is not significant compared to the reference strength so that the response to faster loading is not changed. Having a viscoelastic model and a minimum compression strength simultaneously is not compatible with any predefined model in Abaqus and can only be achieved by programming a subroutine. However, an alternative way to solve the problem was to define a twin elastic solid, coincident in shape and place with the viscoelastic one, with the desired compression properties. An elastic modulus of 200 MPa (29,000 psi) was assigned to this elastic solid in this research project, having as a reference that the RHMA-G has a Young's modulus at an infinite frequency of 22,454 MPa (3,256,677 psi). Figure 8-15 presents an ideal scheme of the twin solids, viscoelastic and elastic, where the twin elastic solid is drawn separately for easy understanding. Figure 8-16 shows the application of this technique to the FEM model structure.

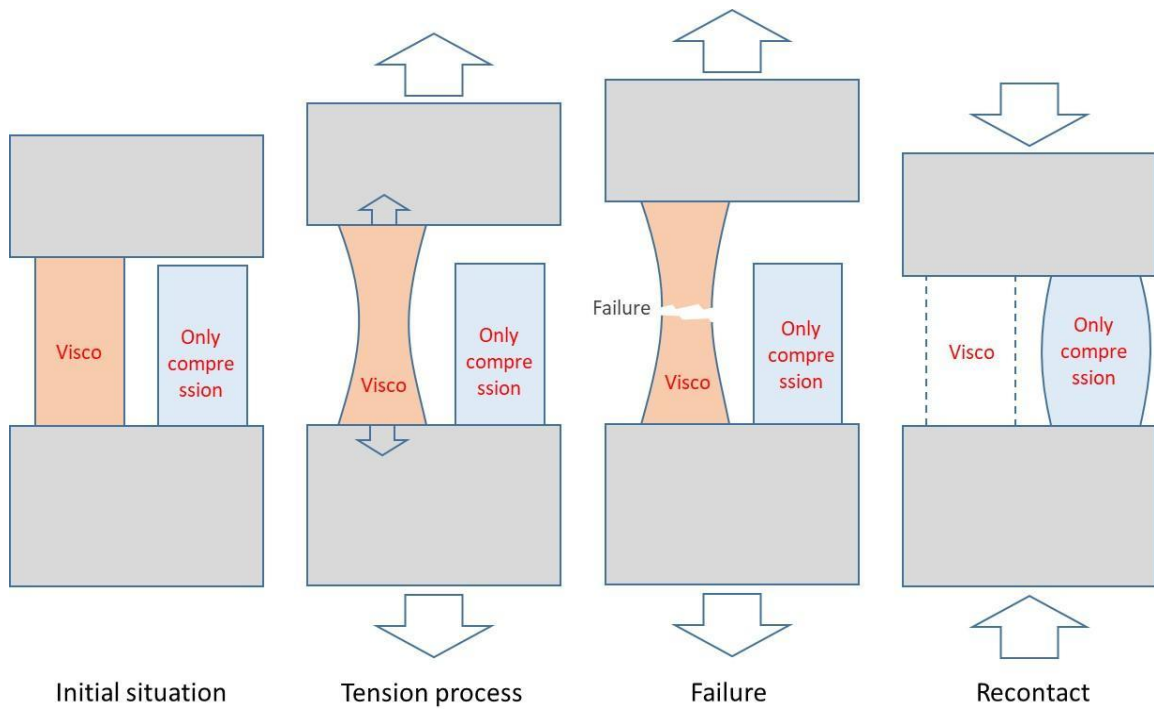


Figure 8-15. Simplified process of the tension failure of the viscoelastic solid and later re-contact with the elastic twin solid under compression

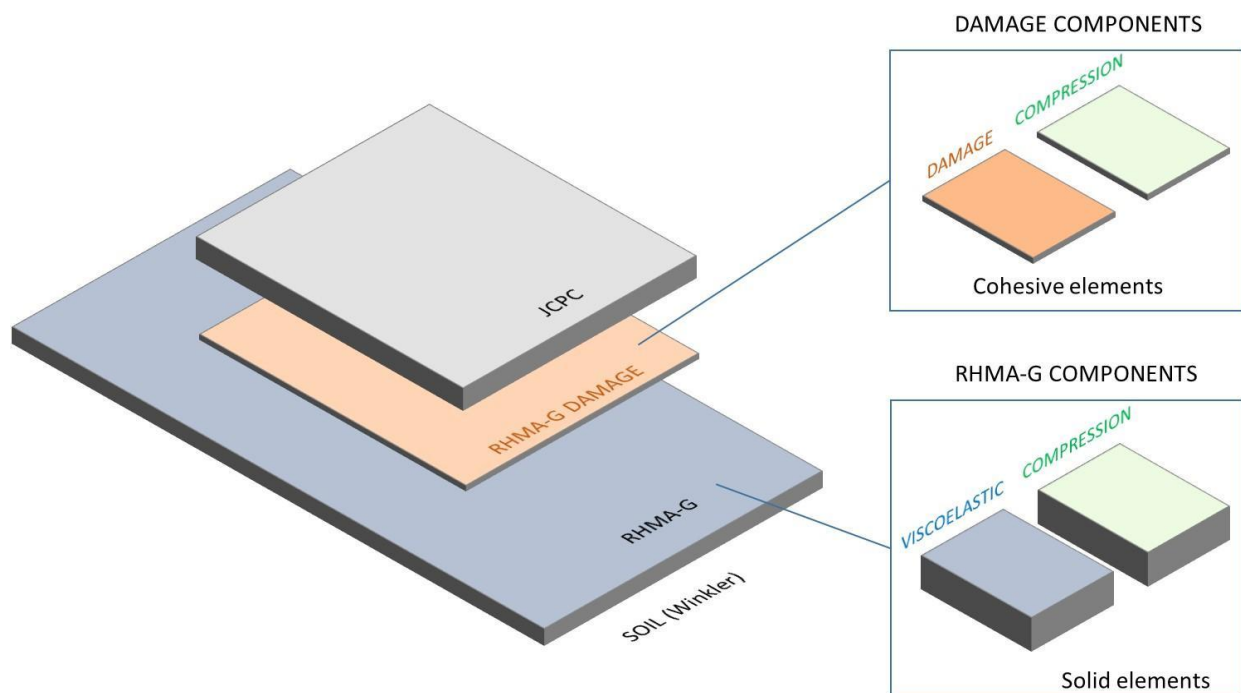


Figure 8-16. Schematic of the pavement model section including the different cohesive layers and coincident minimum-compression components

8.5 Models

Two main loads were considered acting on the pavement beside the self-weight: traffic loads and environmental loads, including shrinkage and temperature changes. Both types of loads have different loading times. Ambient loads are long-term loads, with cycles extending over several months for shrinkage or one day for temperature. However, traffic loads are short-term, with time periods shorter than 1 second.

The different nature of the loads suggested that two different models may be convenient:

- A complex dynamic model including asphalt viscoelastic behavior, long-term action of ambient loads, and the subsequent progressive damage on the interphase between the asphalt base and the PCC slab. The expected cycles of curling and warping created by shrinkage and temperature changes were considered, followed by re-contact produced by traffic loads. No dynamic load applied by traffic or FWD tests were considered in this model.
- A simplified static model with elastic materials behavior, a preestablished debonding between asphalt base and PCC slab, and equivalent static loads applied by the traffic and the FWD tests.

The different features of the models are described in the following subsections, first defining the complex and simplified model structures and then detailing the material properties. Lastly, the detailed application of the models to the 4.76B full-scale test track shown in Chapter 7 is presented, including the characterization of the loads applied.

8.5.1 Complex model

The complex model aims to represent the debonding phenomenon that occurs at the interphase between the concrete slab and the base. The concrete slab tends to separate from the asphalt base due to ambient loads that produce curling in the concrete slab. The base follows the concrete as long as the bonding at the interphase remains intact. When the interphase does not have adhesive properties, both layers would separate from each other. However, if adhesion exists and curling is significant, the asphalt material near the concrete will experience damage in the areas under higher stresses, reducing its strength progressively and creating debonding bands along the slab edges.

An explicit-dynamic model was developed in Abaqus FEM, including linear viscoelastic behavior for the asphalt, viscoelastic damage of the asphalt-concrete interphase, and may also represent transient dynamic loads due to traffic loads and FWD test load. The pavement structure was made of multiple parts, including concrete slab, interphase, base (asphalt concrete or lean concrete base), and subgrade.

The basic element considered in the solid parts of the model was an 8-node linear brick element with incompatible modes and second-order accuracy (C3D8I). This element was used to model the concrete slab, the asphalt, and the LCB. A Winkler-type interaction between the base and the subgrade represented the pavement foundation. The subgrade was idealized by a fixed shell with a 4-node doubly curved thin 10 mm (0.4 in.) shell, with reduced integration (S4R). This shell interacts with the LCB slab with a linear pressure-overclosure normal stiffness of 0.10 MPa/mm (363 psi/in.), obtained from the FWD tests shown in Chapter 7. The definition of the interphase

between the base and concrete slab depends on each model. The pavement structures and the interphase are detailed in the following subsections.

8.5.1.1. *Curing compound section*

The structure included the concrete slab, curing compound interphase treatment, and lean concrete base slab. The geometrical properties of the model are shown in Figure 8-17, and an image of the model as disassembled parts can be seen in Figure 8-18. The curing compound does not produce adhesion between the LCB and the concrete slab. Consequently, the concrete slab will curl and separate from the LCB base when the ambient loads act on the pavement.

There is no specific model of the interphase beyond the definition of the bonding properties between the RHMA-G layer and the concrete layer. Since no adhesive behavior has been detected in this material, the model only defines a hard-type contact in the normal direction and a very small stiffness in the tangential direction (to ensure horizontal stability).

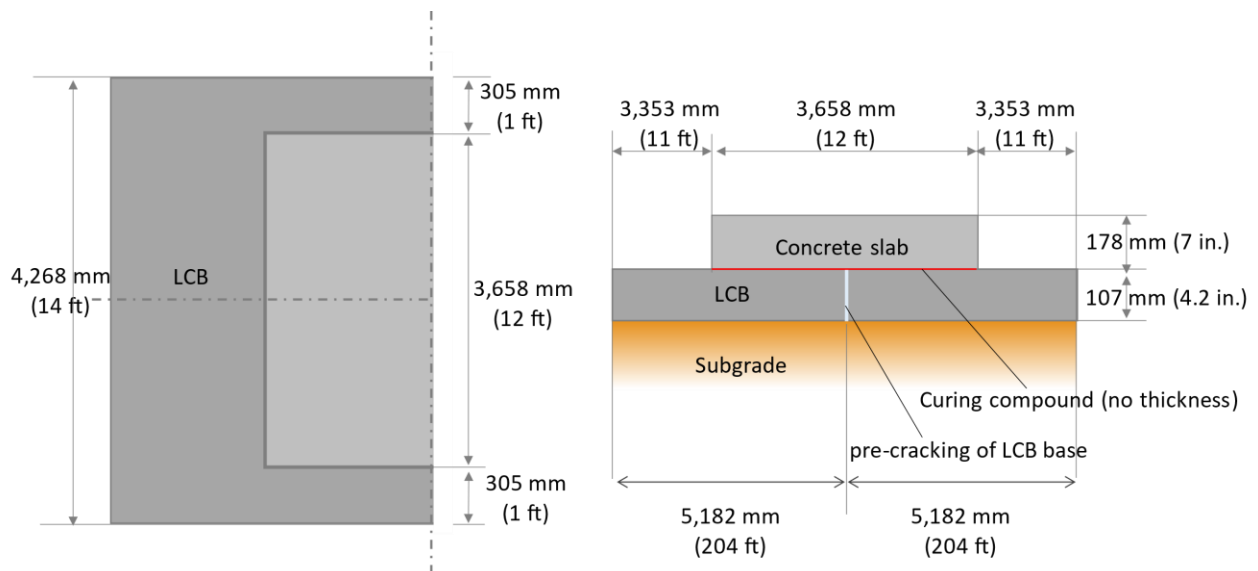


Figure 8-17. Description of the JPCP over LCB section (unscaled)

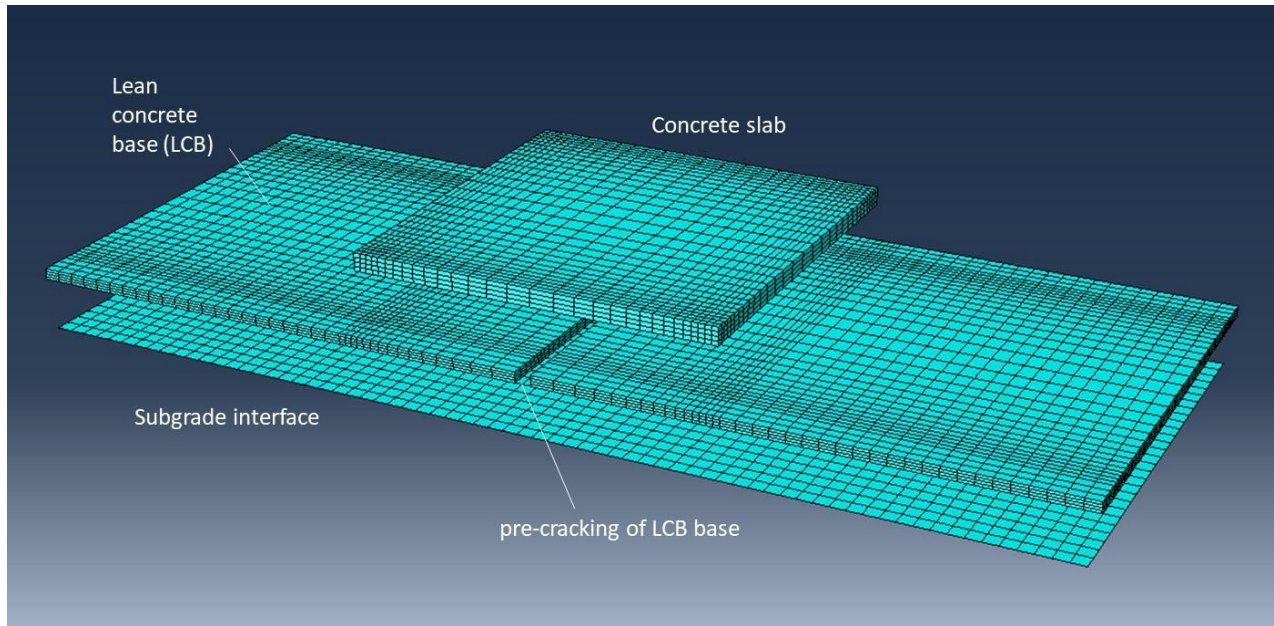


Figure 8-18. Disassembled representation of the 3D finite element model of the JPCP LCB section

It is important to note that since neither specific contact behavior nor viscoelastic material properties were defined, this complex model does not present any differences from the simplified model of the curing compound section.

8.5.1.2. RHMA-G section

The RHMA-G section included the concrete slab, asphalt layer, and subgrade. As explained before, when the concrete slab curling increases, the asphalt material near the concrete will experience progressive damage, reducing its strength and creating a delamination band along the slab edges. The behavior of the layer closer to the interphase that gets damaged was modeled using a layer of cohesive finite elements, traditionally used to study fracture and delamination processes. This layer was considered as an independent part of the RHMA-G base, having the same viscoelastic behavior but including damage. The geometrical properties of the model are

shown in Figure 8-19. The 3D finite element model and its parts are shown in Figure 8-20, with a disassembled representation for a better understanding.

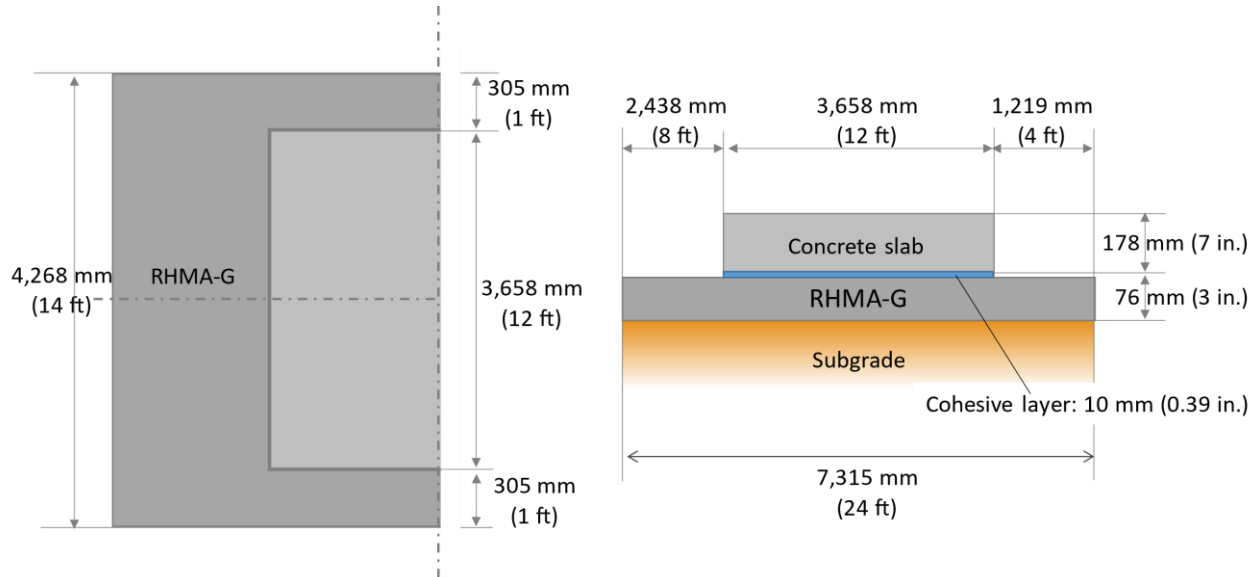


Figure 8-19. Description of the JPCP over RHMA-G section (unscaled)

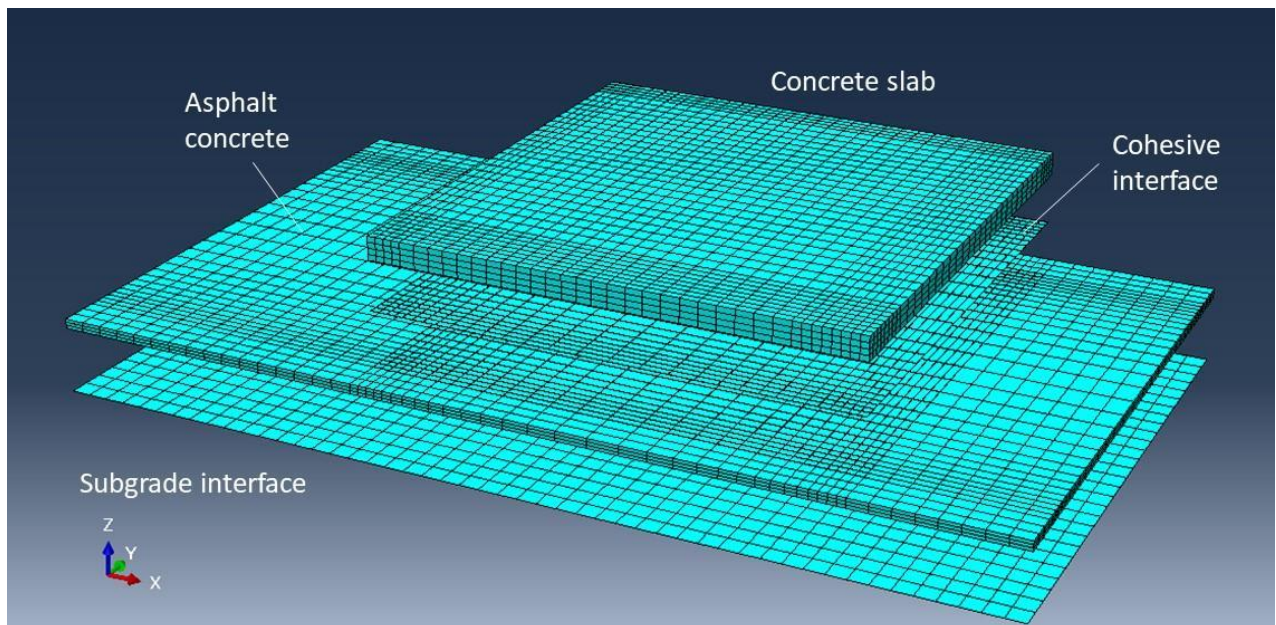


Figure 8-20. Disassembled representation of the 3D finite element model of the JPCP over RHMA-G section

The interphase layer between HMA and PCC was represented using 8-node three-dimensional cohesive elements (COH3D8) that, in explicit models, can simultaneously include damage and viscoelastic behavior, which is not possible for implicit models. The cohesive element transverse dimension was comparatively small compared to the two in-plane dimensions, acting similarly to a two-dimensional plane domain. In this case, a 10 mm (0.4 in.) thickness was adopted for the cohesive layer, reducing the asphalt thickness from 76 to 66 mm (3 to 2.60 in.) in the model for the overall viscoelastic behavior of the ensemble to be preserved.

8.5.2 Simplified debonded model

The complex models explained above were used to analyze the pavement behavior under ambient loads, considering the dynamic effect related to the variation of the loading rate and the damage produced in the interphase between the concrete slab and the base. A simplified model was defined, assuming a pseudo-static loading rate, for the calculation of the effect of the FWD and traffic loads. This model has the advantages of considerably reducing the computational load and avoiding the consideration of the dynamic load effects.

8.5.2.1. *Curing compound section*

As explained before, there is no difference between complex and simplified models in configuration or structure for the curing compound sections because the parts and interactions are the same. The difference is the static nature of the simplified model that ignores the dynamic loading. However, considering that no viscoelastic properties are assumed for the concrete, both simulations reproduce the same behavior. Consequently, only the simplified model of the curing compound section was used in this research.

8.5.2.2. *RHMA-G section*

Contrary to the complex model, the asphalt and concrete slabs were defined as linear elastic materials in the simplified model. The layers were connected by a cohesive interphase that had already suffered uniform delamination around the perimeter. The debonding width was deduced from the results obtained in the complex model analysis and from the sensitivity studies using the simplified method. These studies compared the results with different debonding-width bands against the FWD test measurements. To allow maximum simplicity in the geometric definition of the interphase, the connection was built in the model with a cohesive interphase of negligible thickness that acted as a fixed bonded surface that did not experience damage. This interphase defined the bonding area, which was extended only to the connected part between asphalt and concrete slabs, as shown in Figure 8-21. A disassembled 3D view of the FEM model can be seen in Figure 8-22. The asphalt and PCC layers are not connected in the delaminated zone.

It is important to consider that the curled concrete slab can re-contact the asphalt when the load is applied, and then a normal interaction between both interphases should be defined in the model.

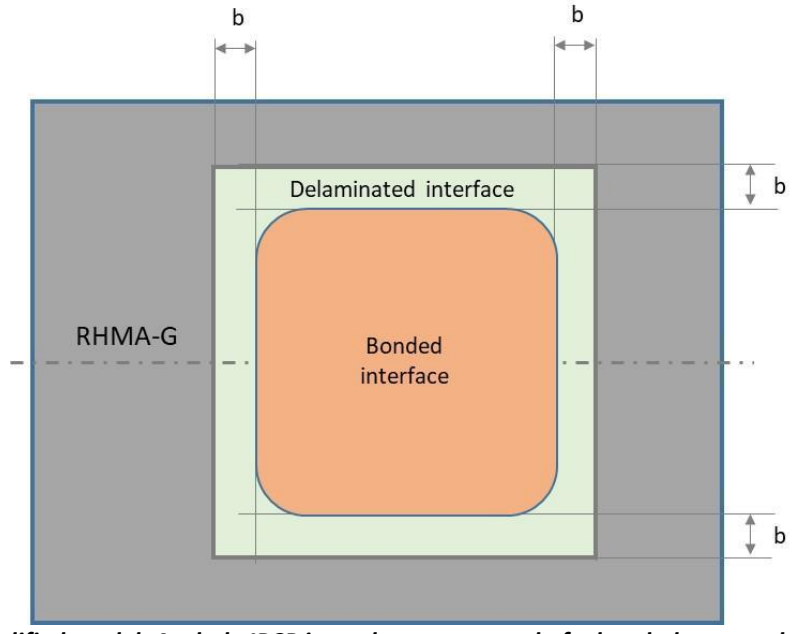


Figure 8-21. Simplified model. Asphalt-JPCP interphase composed of a bonded zone and a b-wide debonded band

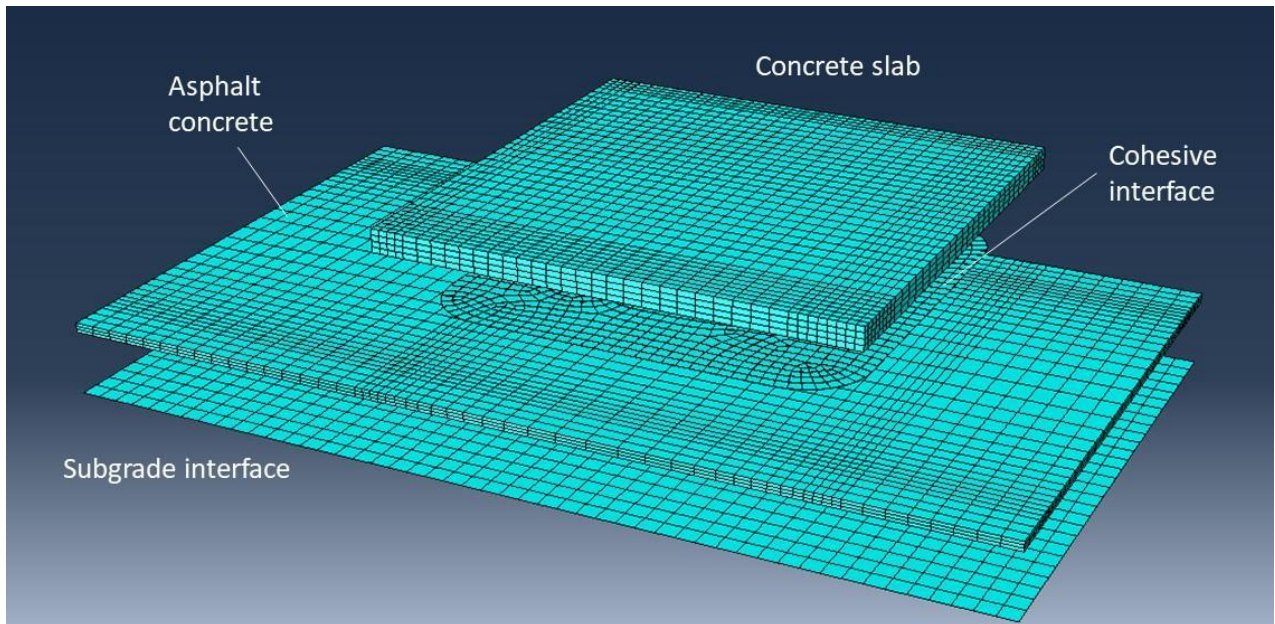


Figure 8-22. Disassembled representation of the 3D simplified finite element model of the JPCP over RHMA-G section

8.5.3 Material model properties

The properties of the elements for both models are summarized in Table 8-5 and explained below. The values are given in SI units, and an English unit version of the table is provided in Appendix D. The simplification of the second model consisted mainly of using simpler material models and behaviors for the viscoelastic elements and the damage definition.

Table 8-5. Material properties of the elements in the pavement models

			Complex model			Simplified model		
Element	Material type	Density (kg/m ³)	Material model	Parameters	Value	Material model	Parameters	Value
JPCP slab	Concrete	2,400	Elastic	E (MPa)	35,000	Elastic	E (MPa)	35,000
				ν	0.2		ν	0.2
Lean concrete base (LCB)	Concrete	2,400	Elastic	E (MPa)	24,000	Elastic	E (MPa)	24,000
				ν	0.2		ν	0.2
RHMA-G	Asphalt	2,400	Viscoelastic	Instant E_0 (MPa)	22,454	Elastic	E (MPa)	5,000
				ν	0.1		ν	0.1
				Prony series coefficients	20			
RHMA-G (interphase)	Asphalt	2,400	Cohesive viscoelastic with damage	E_{nn} (MPa)	22,454	Elastic with no damage	E (MPa)	5,000
				E_{ss} (MPa)	10,206		ν	0.1
				E_{tt} (MPa)	10,206			
				Damage initiation	Table 8-4			
				Damage evolution	Table 8-4			
Curing compound	Surface treatment	None	Hard contact			Hard contact		
Subgrade	Granular subgrade	1,800	Winkler subgrade reaction	Normal stiffness (N/m)	0.1	Winkler	Normal stiffness (N/m)	0.1
				Tang. stiffness (N/m)	0.001		Tang. stiffness (N/m)	0.001

The concrete was represented in the FEM model as an elastic material with an elastic modulus of 35,000 MPa (5,076 ksi), Poisson's ratio 0,2, and coefficient of thermal expansion (CTE) of $10^{-5} \text{ } ^\circ\text{C}^{-1}$ ($5.55 \cdot 10^{-6} \text{ } ^\circ\text{F}^{-1}$).

Asphalt concrete was defined as a viscoelastic material with properties depending on temperature and time-load rate. This behavior was included in the model using a Prony series expansion of the dimensionless relaxation modulus obtained from the different laboratory test results. The Prony series infinite elastic modulus was 22,545 MPa (3,270 ksi), and a Poisson's ratio of 0.1 was assumed. It is known that the Poisson's ratio of a viscoelastic material like asphalt varies with temperature and frequency of loading; it has a value close to 0.3 at intermediate frequencies of loading, such as traffic loading, and close to 0.5 at low frequencies. Therefore, at high frequencies, it is safe to assume that the Poisson's ratio is around 0.1. The models were also analyzed at a Poisson's ratio of 0.2 without noticing any difference since the model is not used at such a high frequency, so the end result does not depend on this particular ratio determined for when the material is infinitely elastic.

The asphalt-PCC interphase was modeled independently from the asphalt slab underneath, defining a thin layer of cohesive elements with a material having viscoelastic properties (the same as the material below) and which also has damage properties in it (even though the damage was produced in the whole asphalt slab).

In the model, the damage was restricted to the cohesive layer between asphalt and concrete, assuming a viscoelastic traction-separation law before the failure. The failure was then assumed to be a progressive degradation of the cohesive stiffness from the damage initiation point until

the complete separation, following a law obtained experimentally. That law may change depending on whether it is a tension or shear failure and can be linear, bilinear, or exponential, among other types of variation.

8.6 FEM modeling application to a full-scale test track

A FEM model with properties shown in Section 8.1 was developed for each JPCP section, matching the pavement layout in the full-scale test track shown in Chapter 7. The results obtained in the model were compared to those of the test track for the two following configurations:

- Interphase debonding under ambient loads for the RHMA-G sections with a detailed debonding model.
- Structural response under FWD loading with a simplified previously-debonded model for the RHMA-G and curing compound sections.

Both models are explained below.

8.6.1 Complex model: Structural response under ambient loading

This model corresponds to the complex dynamic model introduced in section 8.5.1, which considered the viscoelastic properties of the asphalt concrete. It was intended to study the debonding in the section with the RHMA-G as a base. The main parameter analyzed was the width of the delamination band of the interphase along the edges of the concrete slab for different sections and curvature levels. This parameter was not measured in the field test track, and therefore, the model results cannot be directly validated.

Different combinations of shrinkage and temperature values were defined. In the model, a single simplified load scheme was adopted, which is coherent with the field measurement shown in Figure 8-23. A total differential strain of $500 \mu\epsilon$ was assumed at the concrete slab, composed of $300 \mu\epsilon$ corresponding to long-term shrinkage and $200 \mu\epsilon$ corresponding to daily variations.

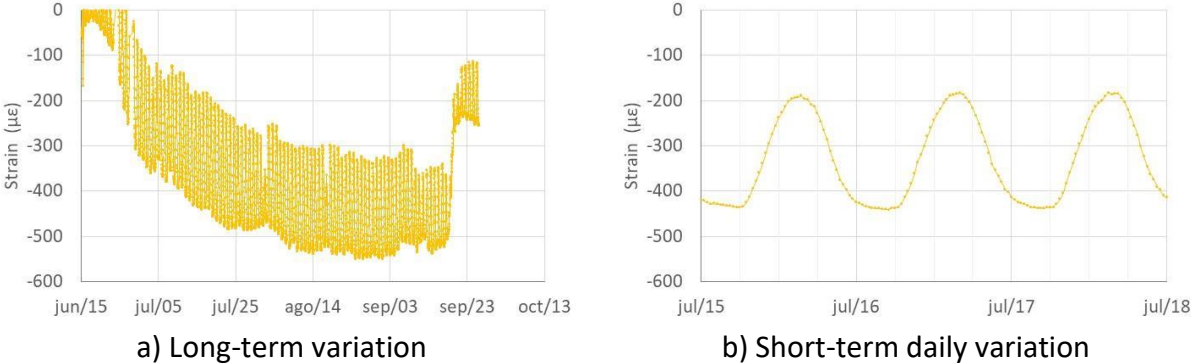


Figure 8-23. Strain variation at the corner of the concrete slab

In this model, the three loads were applied sequentially: self-weight, seasonal shrinkage, and daily temperature changes. Shrinkage was modeled as an equivalent temperature change in the concrete section, and both shrinkage and temperature were introduced as a slab equivalent linear temperature difference (ELTD) between the top and bottom of the slab. The $300 \mu\epsilon$ and $200 \mu\epsilon$ previously mentioned correspond to a $30 \text{ }^\circ\text{C}$ and $20 \text{ }^\circ\text{C}$ ELTD, respectively. The loading process is presented in Figure 8-24. A predefined smooth transition was considered to avoid dynamic instabilities.

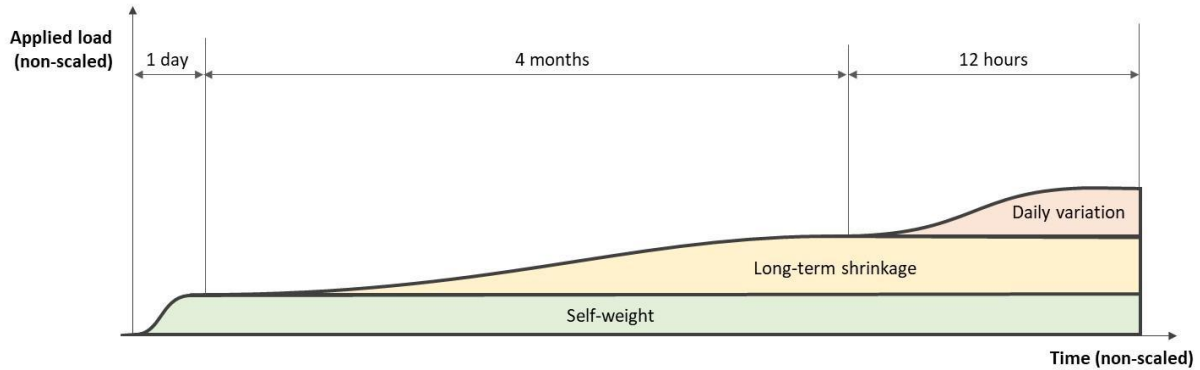


Figure 8-24. Time variation of applied loads to the model

The main results obtained with this model were related to the debonding process experienced by the interphase between the asphalt and the PCC slab for the RHMA-G section. No results are shown for the curing compound section since there was no bonding between LCB and PCC with the curing compound.

8.6.1.1. RHMA-G section

The concrete slabs experienced curling when the environmental loads were applied. The curling caused tension at the interphase since the concrete pulled the asphalt up and simultaneously caused shear due to the bottom concrete fiber elongation. The asphalt followed the concrete along its curling until the stresses and strains at the interphase exceeded the limit for the damage initiation. It also may produce delamination if the strain reaches the separation limit.

Figure 8-25 shows the evolution of the damage variable (scalar stiffness degradation, SDEG in Abaqus) along the loading process. The damage initiated early at the shrinkage step, reducing the asphalt interphase strength to about 75 percent, with the remaining loss caused by the temperature load until the final reduction of about 90 percent.

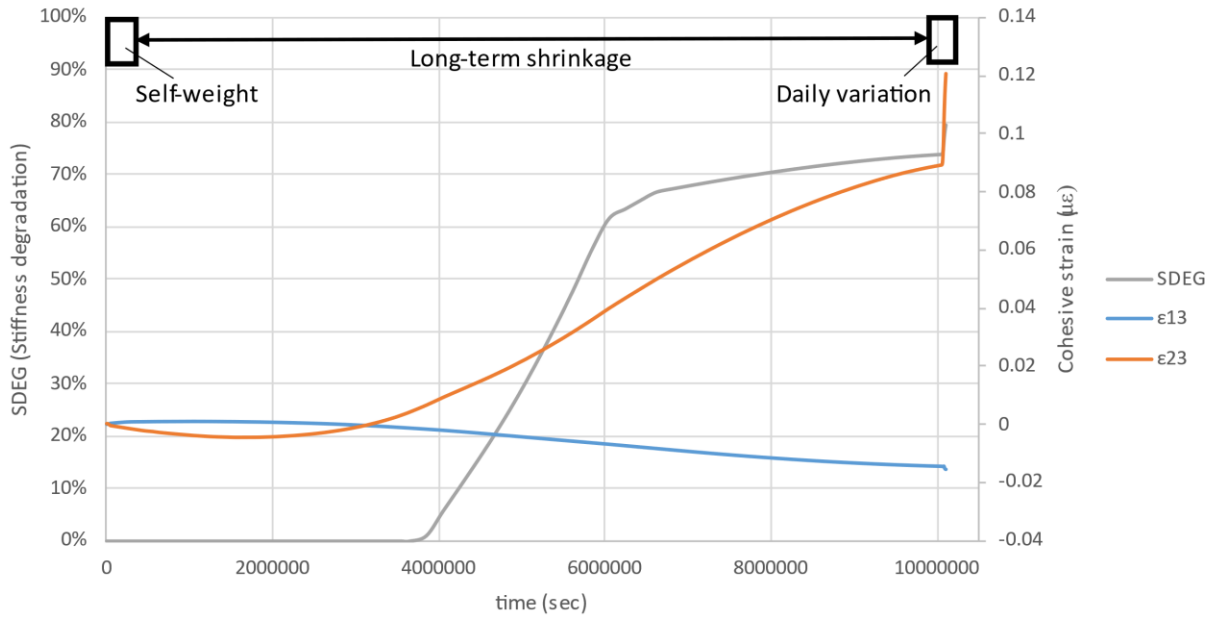


Figure 8-25. Evolution of the damage through the scalar stiffness degradation of the interphase, considering the application of self-weight, long-term shrinkage, and daily temperature variation. Center node of the frontal edge. RHMA-G section

At the end of the loading process, the interphase stiffness was damaged from 50 percent up to nearly 90 percent along a perimeter strip of about 200 mm (8 in.), depending on the assumed hypothesis, and maintained more than 50 percent of its strength in the inner zone. Figure 8-26 presents the interphase and the degradation bands obtained at the final step. It was noticed that the degradation was produced as a combination of the tension and shear strains when the model considers this damage approach, but the main cause appeared to be the shear strain, being less important the tension produced by the curling upward movement, which is relatively small enough to not initiate the damage by itself.

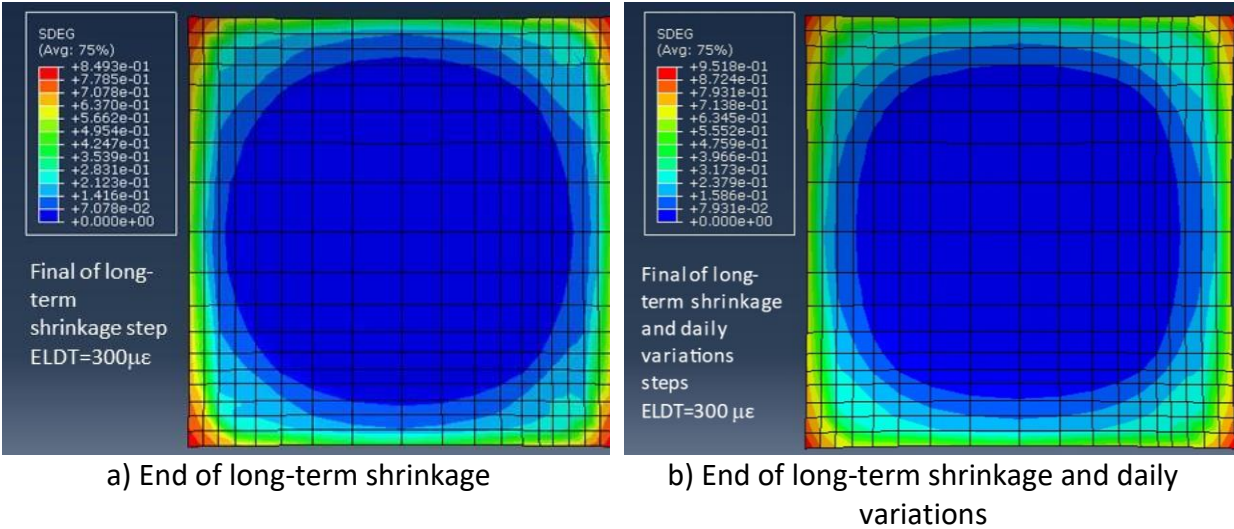


Figure 8-26. Stiffness degradation bands in RHMA-G section with constant curvature

8.6.2 Simplified debonded model: Structural response under FWD loading

This model assumed that the debonding described in the previous section had already taken place. The objective was to provide a simpler model to calculate the pavement responses without the complexity of a dynamic viscoelastic model with damage that requires many hours of computational time.

The assumptions were that the materials have an equivalent elastic behavior, that a previously defined delamination between asphalt and concrete exists depending on the interphase type, and that the dynamic effects are negligible. The section cases studied with this model were:

- Curing compound section.
- RHMA-G section.

The concrete slabs suffered curling and warping due to shrinkage and temperature changes. These environmental loads were represented in the model as a slab equivalent linear temperature difference (ELTD) applied only to the PCC slab, resulting in an imposed slab

curvature. Four different levels of equivalent differential strain were applied: $50 \mu\epsilon$, $150 \mu\epsilon$, $300 \mu\epsilon$, and $500 \mu\epsilon$, matching the levels seen during FWD tests.

Different distribution schemes of this curvature can be assumed along the slab. The simpler one was to define a constant curvature. However, previous research [21] showed that the curvature varies from the center of the slab with no curvature to a maximum at the corners. Three different variations of slab curvature were considered in this model, from the center to the edge of the slab: constant curvature, linear curvature, and parabolic curvature. These different curvatures would provide different support areas on the base, as shown in Figure 8-27.

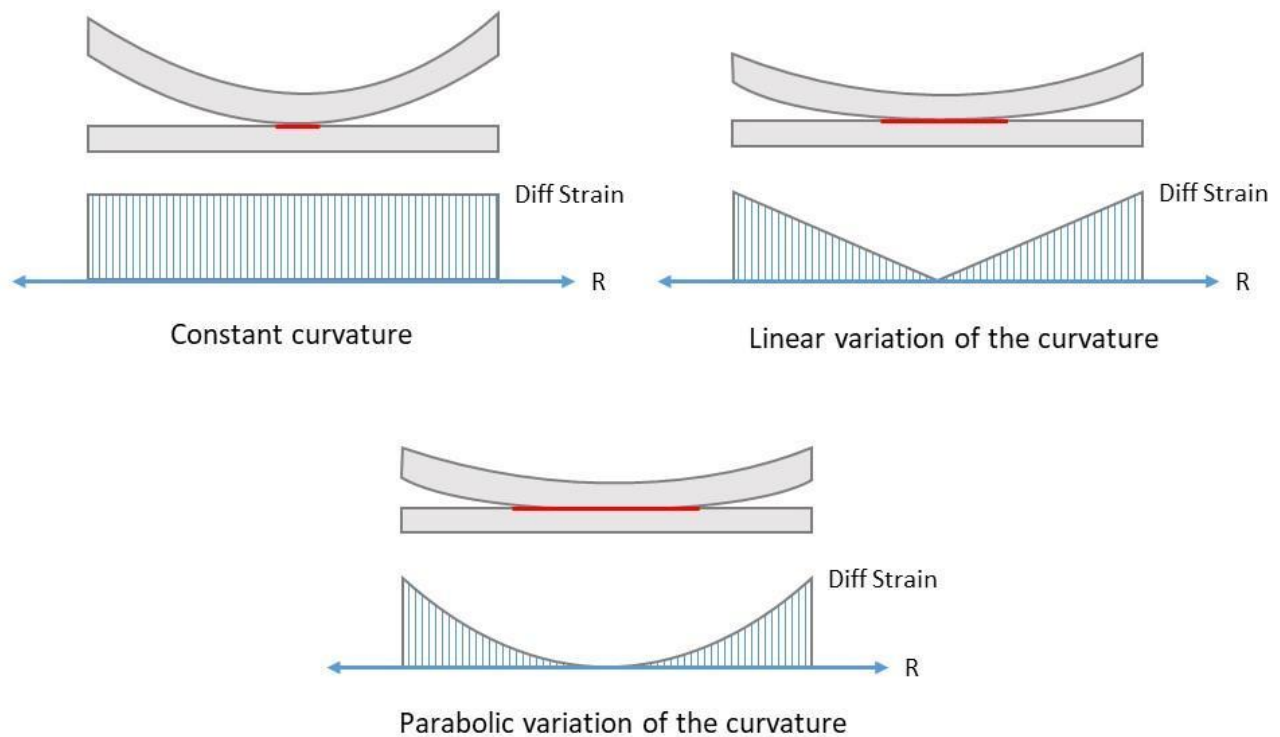


Figure 8-27. Assumed laws of slab curvature variation: constant, linear, and parabolic curvatures

The FWD tests were performed at the center and corners of the slab. The results at different corners were grouped as only one type of result due to the symmetry of the slabs. The figures in the following subsections show the modeled results compared to the FWD results.

8.6.2.1. Curing compound section

The interphase in this section was prepared with a single application of a standard curing compound on the lean concrete base right before the JPCP was built directly over it. The main assumption in this model was that there is no connection between LCB and JPCP, and the interphase behaves as completely delaminated.

Figure 8-28 shows FWD and modeling comparison for a test conducted at the corner. It is observed that the constant curvature was a good approach for low differential strain but became progressively inaccurate at values higher than $200 \mu\epsilon$. The curvature produced high deflections at corners and a considerably reduced support area. On the contrary, the parabolic distribution of curvature showed very low deflections at the corners, meaning that the support area was excessive. The best approach seemed to be the model with linear curvature variation. It matched very well the FWD results. Deviation was observed for the $-150 \mu\epsilon$ and $-30 \mu\epsilon$ cases but did not seem to be related to the model, as will be analyzed later.

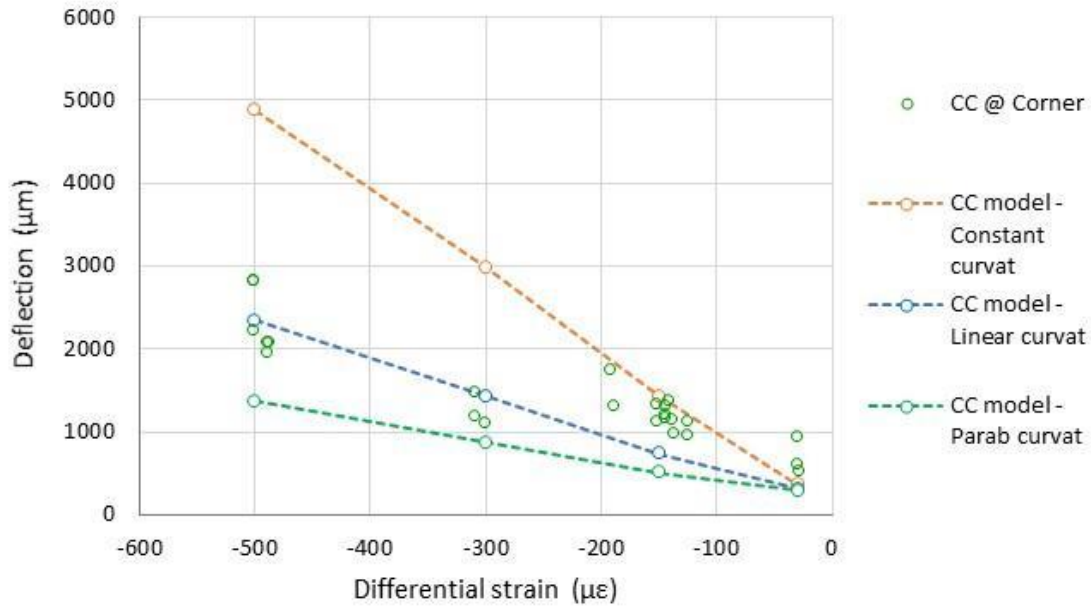


Figure 8-28. FWD and modeling comparison, curing compound section, $F=70$ kN (15,750 lbf) FWD at slab's corner

A similar analysis was conducted with the FWD load positioned in the center of the slab. The findings are displayed in Figure 8-29. The results indicated a satisfactory match (a little low values) for the linear and parabolic curvature cases. However, the constant curvature produced exaggerated outcomes as the differential strain rises.

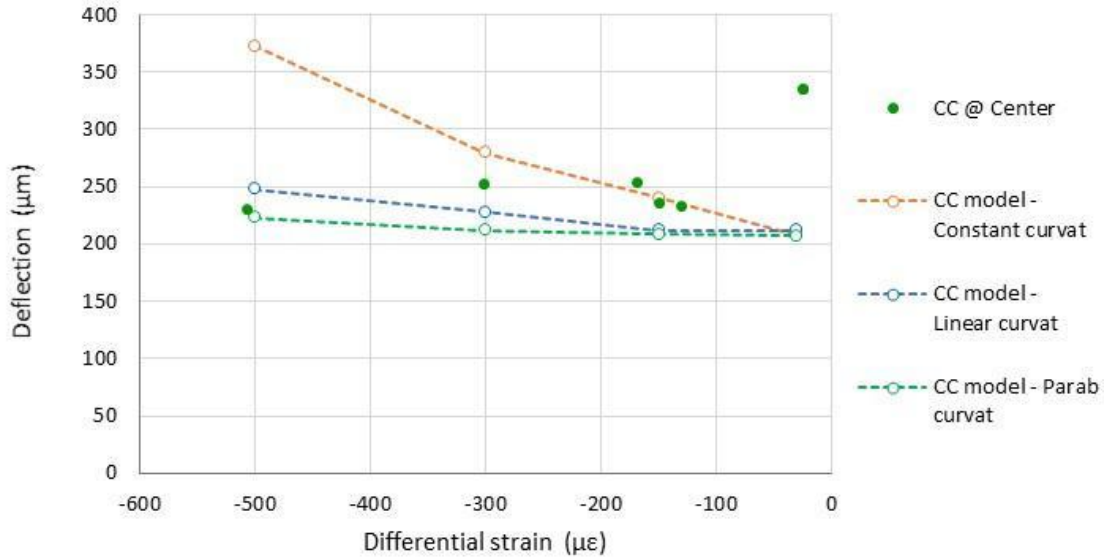


Figure 8-29. FWD and modeling comparison, curing compound section, $F=70$ kN (15,750 lbf) FWD at slab's center

8.6.2.2. RHMA-G section

As explained in section 8.5.1.2, the interphase between the RHMA-G and the concrete JPCP was divided into two separate zones, one central zone completely bonded and one band strip along the perimeter completely debonded. High strength was assigned to the center of the interphase to ensure perfect bonding, and no node connection was defined along the perimeter strip area.

8.6.2.2.1. Influence of the variation of curvature

Assuming a delamination bandwidth of 200 mm (8 in.), Figure 8-30 presents the analysis of the influence of the JPCP curvature variation on the FWD deflection, comparing the modeled results to the FWD testing measurements.

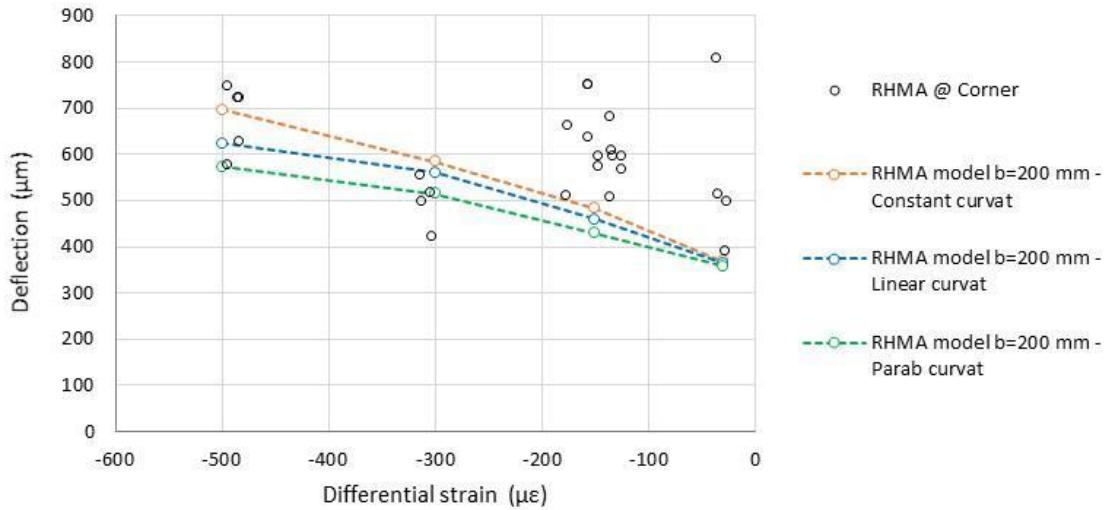


Figure 8-30. FWD and modeling comparison, RHMA-G section, F=70 kN (15,750 lbf) FWD at slab's corner

There seems to be little significant difference between the three curvature models. The constant one seemed to overestimate the deflection for differential strains higher than $-150 \mu\epsilon$. The linear and parabolic approaches showed both good matches with the FWD testing, but the linear one appeared to be more aligned with the test results, which is why it is recommended for future calculations.

Figure 8-31 presents a similar comparison for the case of FWD testing on the center of the slab, considering constant and linear curvature variations and $F=70 \text{ kN}$ (15,750 lbf). The results show a similar trend as the test results but shifted vertically, presenting a null influence of the ambient load, meaning that relatively small changes in the support contact area with the subgrade were irrelevant. This can be produced by the approximate estimation of the Winkler stiffness of the subgrade. Neither the debonded bandwidth (changes in the support area) nor the variation of the curvature seemed to have any influence on the results.

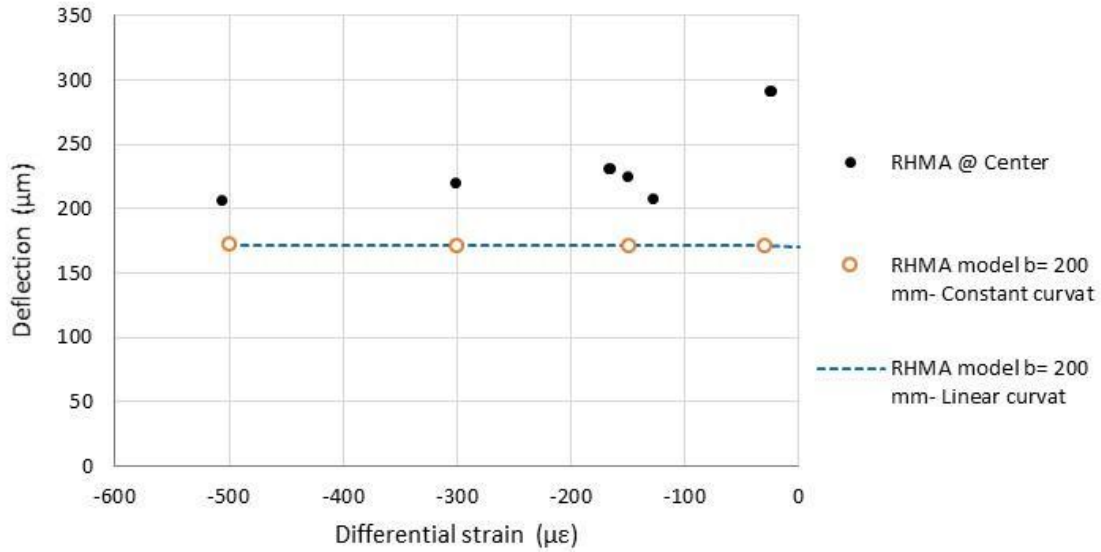


Figure 8-31. FWD and modeling comparison, RHMA-G section, F=70 kN (15,750 lbf) FWD at slab's center

8.6.2.2.2. Influence of the debonded band width

A sensitivity study analyzed the influence of the debonded bandwidth, assigning values of 0, 100, 200, and 300 mm (0, 4, 8, and 12 in.) to the b-parameter shown in Figure 8-21. This value range is consistent with the results of the complex model, which showed a reduction of 50 percent of the cohesive layer strength over a perimeter band of 200 mm (8 in.). The results are presented in Figure 8-32, assuming initially, a linear variation of the curvature of the JPCPC slab due to ambient loads.

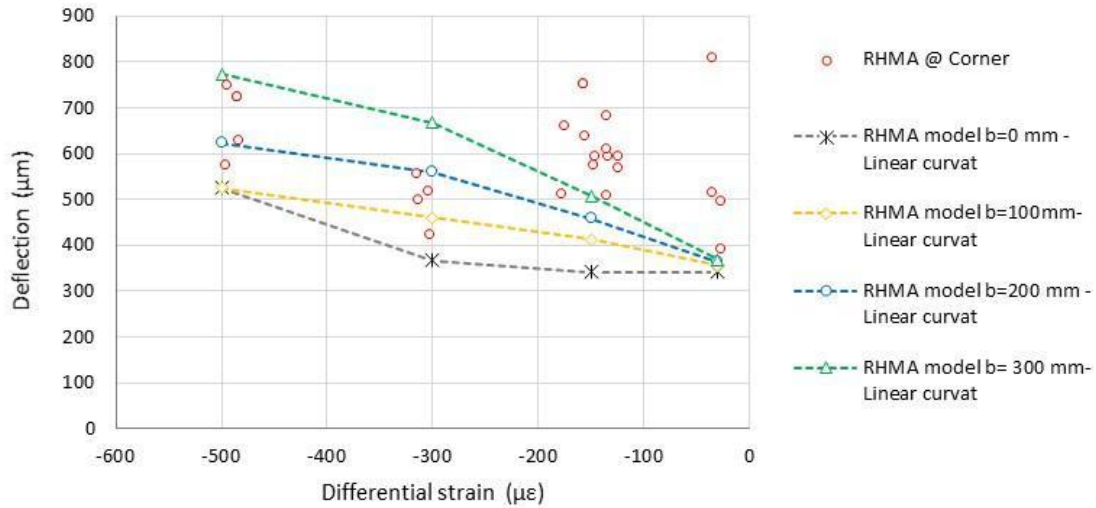


Figure 8-32. Sensitivity analysis of the FWD test with different debonding bandwidths. RHMA-G section with linear curvature. FWD at slab's corner. F=70 kN (15,750 lbf)

A relatively good agreement with the FWD test results was obtained with the model using debonded band widths ranging from 100 to 300 mm (4 to 12 in.). Better model performance can be observed for the b=200 mm (8 in.) case. Thus, it will be used as the reference case for later comparisons. The usual practice of assuming full bonding and no damage leads to poorer results compared to the field measurements, underpredicting the corner slab deflection along all the differential strain range.

The model did not capture the higher deflections measured when the differential strain was within $-150 \mu\epsilon$ and $-30 \mu\epsilon$. To study the behavior of the model in more detail, Figure 8-33 presents the deflection variation at the main steps of the loading process: self-weight, ambient loads, and FWD.

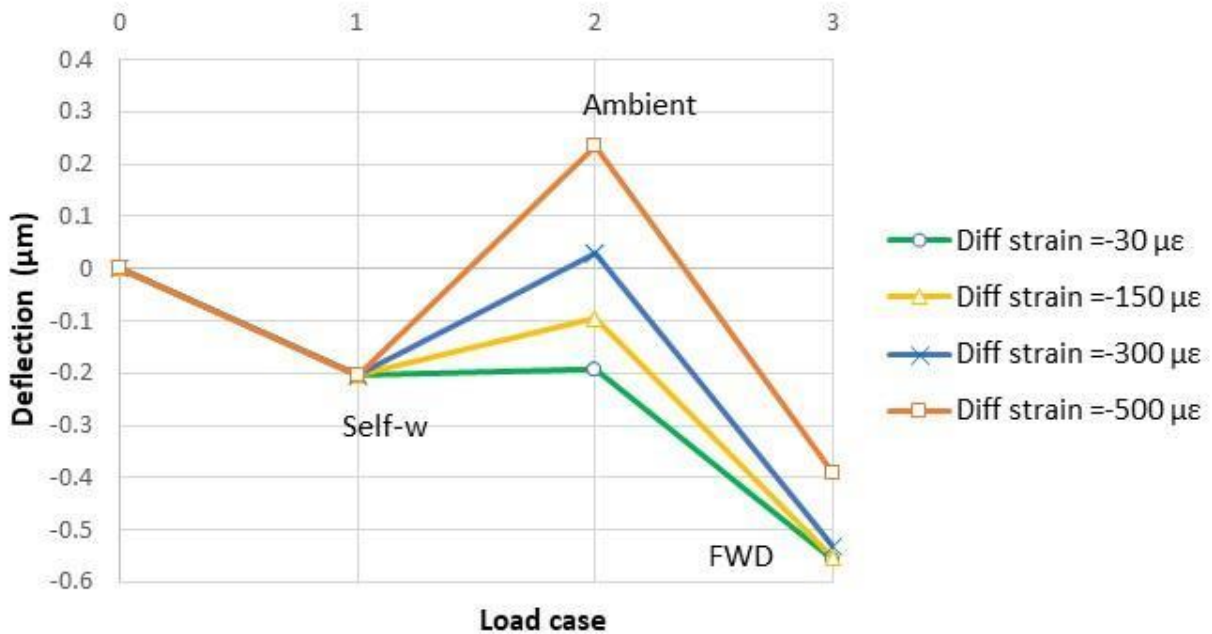
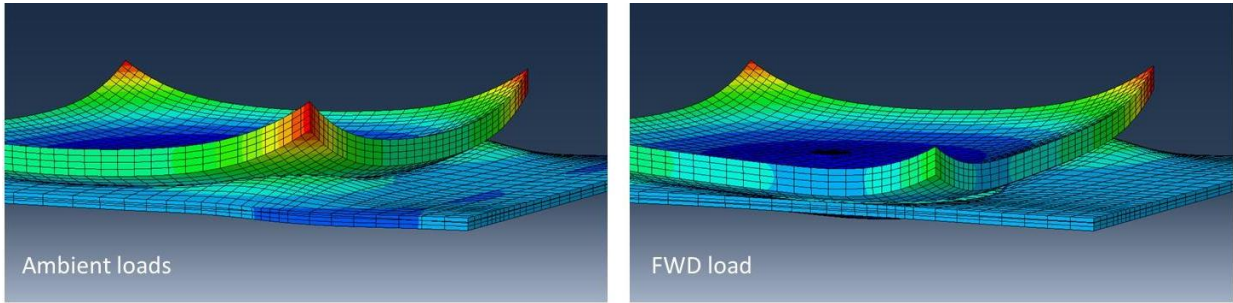


Figure 8-33. Deflection evolution with different loading steps and comparison of different ambient load magnitudes. RHMA-G section, $b=200$ mm (8 in.), with linear curvature. FWD at slab's corner. $F=70$ kN (15,750 lbf)

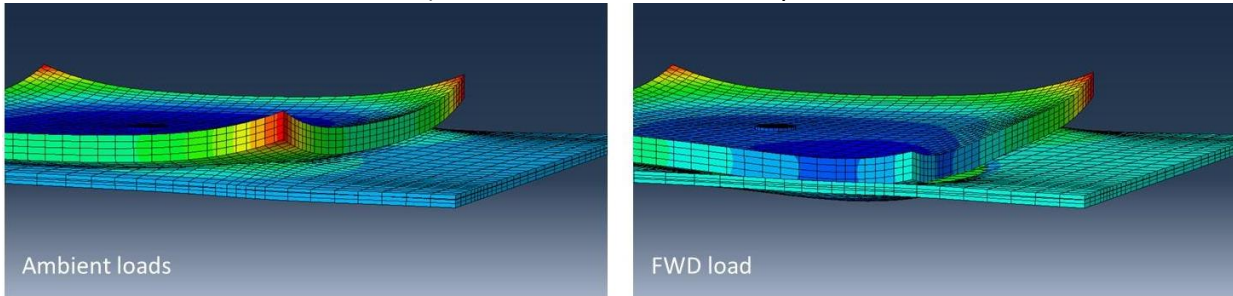
As observed, a higher differential strain produced an increased deflection in the ambient load step, associated with more curling of the concrete slab. The higher the elevation of the JPCP corner area, the larger the deflection when applying the FWD in the new step because the slab would work as a cantilever without the support of the asphalt base. An additional deflection would be produced by an easier rocking of the slab around its reduced support. This support would be recovered progressively along the FWD step as the JPCP base recontacts the asphalt, occurring earlier in the step for the smaller differential strain cases and consequently producing lower deflections in these cases.

No explanation was found in the model for the anomalous behavior of the cases with differential strain between -150 µε and -30 µε. They maintain the previously explained increasing deflections when changing from -30 µε to -150 µε but shifted to higher deflections. Since the FWD tests for

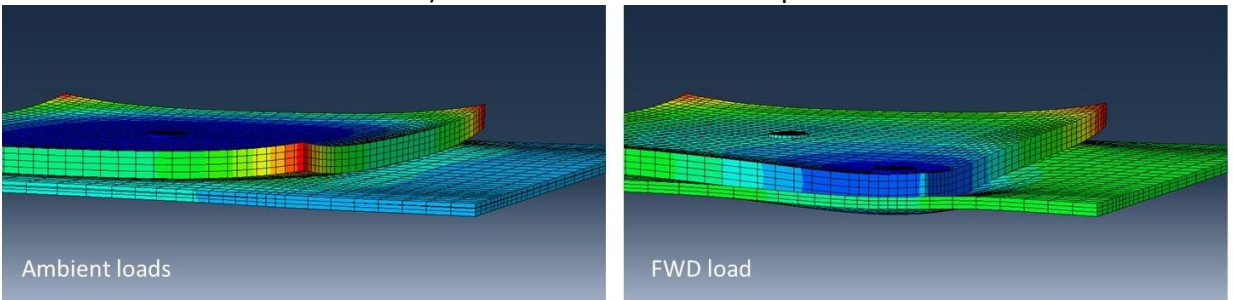
these cases (tests 1 and 2) were performed at the beginning of the test-track life (28/06/2022), a lower concrete stiffness might be expected. However, performing the calculation with a lower concrete stiffness did not offer any significant variation in the results. Since the same unexpected differences were observed for other FWD tests with loads of 30 and 50 kN (6,750 and 15,750 lbf) and also in the curing compound section results, it can be assumed that the deviation is due to issues in the testing itself. The previously explained variation in the FWD deflection is illustrated in Figure 8-34 with the images from the FEM model, considering only the end of the ambient load step and the FWD step. It can be seen that the contact of the JPCP with the RHMA-G after ambient loads was relevant mainly for differential strain cases c) and d) with $-150 \mu\epsilon$ and $-30 \mu\epsilon$, respectively.



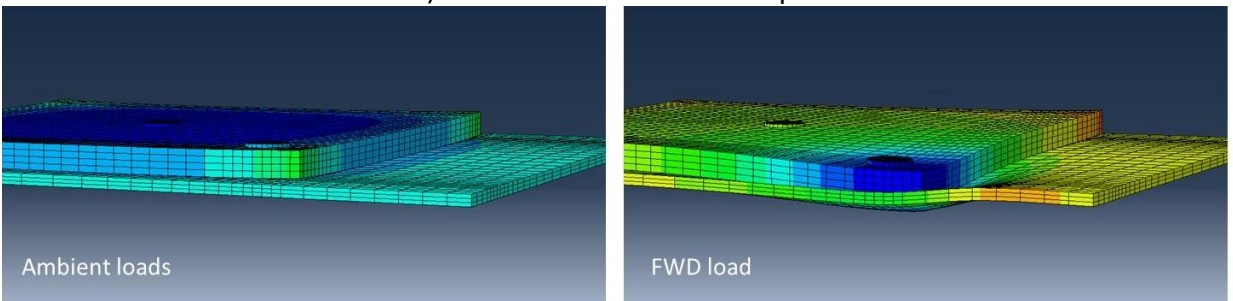
a) Differential strain of $-500 \mu\epsilon$



b) Differential strain of $-300 \mu\epsilon$



c) Differential strain of $-150 \mu\epsilon$



d) Differential strain of $-30 \mu\epsilon$

Figure 8-34. Deflection evolution of different load cases and load magnitudes. RHMA-G section, $b=200 \text{ mm}$ (8 in.), with linear curvature

8.6.2.2.3. Influence of the FWD load magnitude

The influence of the FWD load magnitude on the model accuracy is shown in Figure 8-35. The model described the pavement behavior properly, assuming a debonded band of $b=200$ mm (8 in.) and linear curvature variation. The previously mentioned deviation of the test results for the differential strain range between $-150 \mu\epsilon$ and $-30 \mu\epsilon$ was also observed here for $F=50$ kN (11,250 lbf) but to a lesser degree, and it almost disappeared for $F=30$ kN (6,750 lbf).

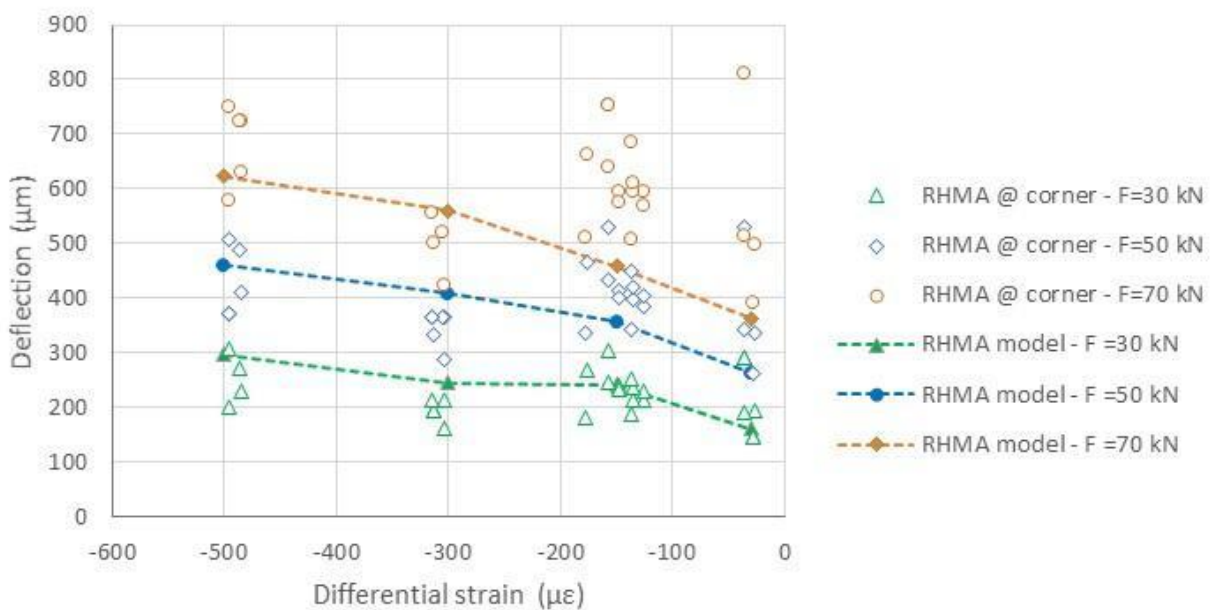


Figure 8-35. Sensitivity analysis of the FWD test with different FWD load magnitudes. RHMA-G section with linear variation of curvature. FWD at slab's corner

9. CONCLUSIONS AND RECOMMENDATIONS

9.1 Summary of Completed Tasks

This study performed a mechanical characterization of asphalt base materials under conditions relevant to use under concrete slabs and of slab/base interactions for concrete pavement structures. Laboratory specimens and full-scale slabs were performed to analyze and characterize different base materials and interlayers that are currently used or can potentially be used as bases for concrete pavements. FEM models to replicate laboratory testing were performed to extract material properties and behavior which were later applied to full-scale slabs to understand the behavior of the field slabs better. The following tasks were completed:

- 1- Ideal properties under different load conditions for base material for JPCP and SJPCP-COA pavements were determined.
- 2- A set of applicable laboratory test methods and analysis procedures for asphalt and composite specimens were determined.
- 3- Asphalt specimens made of HMA and RHMA-G were prepared and tested under various conditions using an extensive set of laboratory test methods that replicated field loading conditions caused by environmental and traffic loads.
- 4- A reduced testing protocol for the characterization of material and bonding properties was established based on the extensive set of laboratory test methods.
- 5- Asphalt specimens made of HMA and RHMA-G and composite specimens with PCC cast on top of asphalt materials were tested and analyzed under the reduced testing protocol for material and bonding characterization.

- 6- Four full-scale instrumented concrete sections were built following current Caltrans design approaches and possible base alternatives for improving the performance of JPCP and SJPCP-COA pavements.
- 7- Data from concrete sensors, FWD testing, and coring was collected on full-scale sections to understand better the behavior and performance of the slab/base interaction.
- 8- Laboratory specimen behavior was replicated using FEM to obtain material properties that were required for the full-scale section models.
- 9- A complex viscoelastic FEM model with damage properties was developed to study the debonding process of composite pavement structures due to environmental loads.
- 10- A simplified elastic FEM model with a predefined debonding was developed to study the effect of the FWD testing.
- 11- Conclusions and recommendations for implementation were provided, and future research needs were identified.

9.2 Contributions to Knowledge

Several gaps and questions about slab/base interactions for concrete pavements were proposed to be answered with this study. The findings are applicable to thinner concrete overlays as well as concrete pavements in general. The following questions were answered:

- 1- Which are the available tests for asphalt materials to characterize them for use as bases for concrete pavement? Can the same tests be applicable to composite specimens?
 - a. A set of 8 laboratory tests were used for the initial testing of asphalt specimens for material characterization (Sections 5.3 and 5.4). The shear frequency sweep

test and compressive dynamic modulus already had a testing protocol and were ready to be done. Shear creep, shear ramp, tensile creep, and tensile ramp tests were testing procedures developed under the current research project using available testing machines. The tensile creep and ramp tests were performed in a universal testing machine (UTM), which is quite common in laboratories; the shear testing was performed in a less common testing device, which contributed to the idea of not including those tests from the final testing protocol. The tensile hanging creep and tensile hanging damage tests were fully developed under this project, which intends to test material and bonding properties under slow-loading scenarios to replicate the effect of environmental loads. All the testing procedures can potentially be applied to composite specimens, but in this particular case, only the tensile ramp test was performed on asphalt and composite specimens simultaneously.

- 2- Is there any set of tests that can characterize the material properties without having to do a full testing factorial? Can these tests be easily replicated by any other testing laboratory or agency?
 - a. Three testing methods out of the eight initially used were determined to measure relevant properties under time and temperature conditions expected in the pavement without the need to run all eight (Sections 6.3 and 6.4). Compressive dynamic modulus, tensile ramp, and tensile hanging creep were the tests defined for characterizing the material and slab/base properties. Any well-established laboratory or agency can easily replicate the first two tests with typical laboratory

equipment: an asphalt mixture performance tester (AMPT) and a universal testing machine (UTM). The tensile hanging creep is a test that was entirely developed under this project, but it would not be complicated to replicate it since the testing frame and data acquisition system are not complex. In the last testing phase, it was recommended to include a test able to analyze the water-induced damage in the specimens. The indirect tensile cracking test (IdealCT) under dry and wet conditions was selected, and the moisture conditioning was done with a moisture-induced stress tester (MiST) device.

- 3- Which is the effect of temperature and humidity on the material and slab/base interaction properties? What variables control the material properties and slab/base interaction?
- a. As it was suspected, temperature and humidity negatively impact the strength of the base materials (Sections 5.4, 6.4 and 6.5), and by extension, it will also impact the slab/base interaction. Moisture conditioning specimens at 60 °C (140 °F) can decrease the strength of the asphalt material by 11% for HMA specimens and 16% for RHMA-G specimens. Laboratory strength tests conducted at different temperatures determined that increases in temperature reduce the material strength and cause the material to behave softer, which increased the deformation to reach a 50 percent integrity between 40 and 100 percent more when testing at 40 °C than when testing at 25 °C.
 - b. New alternatives for interlayers can improve the slab/base interaction, as was seen in the FWD deflections of the slab with microsurfacing as an interlayer

(Section 7.6). On the other hand, certain interlayers that are currently being used will prevent the layers from bonding and will not work as a soft interlayer that absorbs the slab deformations, which causes less area of the slab to be in contact with the base, increasing the amount of the slab that is in a cantilever condition, therefore reducing tensile stresses

4- What is the performance of the currently allowed bases? Is there any other base material or interlayer that can be used to increase the performance of concrete pavements?

- a. Lean concrete base does not perform well compared to hot mix asphalt when used as a base for concrete pavements (Section 7.6). There is literature that supports this fact [6, 20] but none of them had done an experimental demonstration of what was really happening in a JPCP section with LCB as a base. This project performed several full-scale test sections with different bases and concluded that the common practice of applying curing compound on top of the lean concrete base, which happens twice after construction of the base and once right before the casting of the concrete slabs, acts as a debonding agent causing both layers to be completely separated and will not work as a soft interlayer that absorbs the slab deformations. Hence, concrete distresses are expected to occur at a faster rate in the sections built over lean concrete bases than in the sections built over asphalt materials. Based on FWD testing performed in the test sections, the deflections of JPCP over LCB were three times more than the deflections of JPCP over RHMA-G, which results in a poorly supported concrete slab which, with the addition of traffic loads, will increase the cracking potential of the structure.

- b. Using geotextile as an interlayer between the lean concrete base and concrete layer in structures with thin concrete under 175 mm (7 in.), even though it is widely used, is not recommended since it does not provide a cushioning effect to absorb the slab deformations and it will prevent bonding between the two layers (Section 7.6). The lack of bonding, similar to the use of curing compound, will increase the tensile stress in the slab, leading to cracking. The use of geotextile as a debonding agent for thicker concrete structures over lean concrete base or as an interlayer between concrete layers requires further investigation to determine if it provides any benefit to the structures.
 - c. Using RHMA-G as a base for concrete pavements and using a microsurfacing interlayer between the PCC and the LCB were two alternative recommendations from this research project to be analyzed. Both pavement structures provided a very positive outcome, as shown in the laboratory testing (Sections 5.3, 5.4, 6.3, and 6.4) and field test slabs (Section 7.6). Question 6 provides more insight on this topic.
- 5- Can a FEM model explain SJPCP-COA performance? How is the debonding influencing the performance of the SJPCP-COA under environmental and FWD loads?
- a. The material FEM models developed in Abaqus accurately replicated the behavior of the viscoelastic asphalt materials with damage in both tensile hanging damage and shear ramp tests (Section 8.5). The ability of the models to replicate the behavior of the materials allowed the development of two full pavement models. The models used material properties obtained from the test models, including

asphalt stiffness variation with the loading rate as it occurs with the ambient loads and the degradation of the asphalt-concrete interphase due to stress created by the curling of the concrete leading to damage and separation.

- b. The complex pavement FEM model with asphalt viscoelastic behavior and long-term action of ambient loads predicted the damage that may occur in the pavement due to a delamination band around the concrete-asphalt interphase perimeter (Section 8.6). Field evaluation of damage was not conducted, but the simplified model gave reliable results through indirect checking.
 - c. The simplified FEM model with elastic material behavior and a preestablished debonding area consistently reproduced the FWD results obtained in the field, assuming some hypotheses of material behavior and interphase delamination (Section 8.6). FWD evaluations performed under different environmental conditions suggest the environmental loads damaged the interphase of the structure, which resulted in higher FWD deflections. Higher deflections result from curled concrete slabs with less base support, which will increase the tensile strains at the bottom and, therefore, increase the cracking potential of the slabs.
- 6- Based on laboratory testing, real-scale slabs, and modeling, which are the ideal base materials and/or surface preparation techniques for concrete structures?
- a. Based on corner deflections from full-scale test sections (Section 7.6.2) and laboratory testing (Sections 5.3, 5.4, 6.3, and 6.4), it is concluded that gap-graded rubberized hot mix asphalt (RHMA-G) can be used as a base layer for concrete pavements. This will expand the list of bases that Caltrans currently has for

concrete pavements, which is limited to only lean concrete base (LCB) and hot mix asphalt (HMA). An additional benefit of using this type of mix as a base is to fulfill Caltrans' desire of using rubber in the paving industry. As of right now, it is only used in the surface layer, but the use of rubber can also be expanded to base layers of concrete pavements. From the laboratory experimental design, it was seen that the interphase in both RHMA-G and HMA composite specimens is not the weakest point in the structure. The failure of the composite specimens happened due to cracking of the base material.

- b. Placing microsurfacing between the lean concrete base and concrete slabs is considered to be an ideal interlayer (Section 7.6.2). It provides the road paving industry with a new material to be used as an interphase when dealing with concrete pavements, but further investigation in field pilot projects should be conducted. It is an alternative that is cheaper to place than widely used geotextile and produces almost the same behavior as having a gap-graded rubberized asphalt base. This outcome is ideal since it still supports the use of lean concrete bases in concrete pavements since they can use the same paving equipment and plants but causes the section to perform similarly to concrete pavements placed on top of asphalt bases. Allowing structures with lean concrete bases to perform similarly to sections with asphalt layers may be a solution to the current issues faced in the state of California, where concrete over lean concrete base sections is cracking, longitudinally and transverse, at a much faster rate than concrete pavements placed over asphalt layers.

9.3 Recommendations for Future Work

The following recommendations for future research include, but are not limited to:

- 1- In the near future, it is important to finalize improvements in the tensile hanging data acquisition system and finalize the remaining RHMA-G testing that could not be performed.
- 2- Additional full-scale instrumented sections with thicker PCC layers and recycled base materials should be developed following laboratory experiments that are currently being conducted.
- 3- The next step towards the slab/base interaction research is the construction of a pilot project to test the full-scale section findings under real traffic loading for an extended period of time. Sections with an RHMA-G base and a section with a microsurfacing interlayer between the PCC and LCB should be analyzed.
- 4- Laboratory specimens with microsurfacing should be prepared and tested to characterize the material properties. Complications may be encountered when replicating the mixing process in the laboratory. Extracting cores from the field could be another approach for obtaining specimens, but the coring process would probably damage the bond.
- 5- Modeling of a microsurfacing section after obtaining the laboratory properties to understand better the mechanism causing a good performance is recommended to be conducted.

REFERENCES

1. Federal Highway Administration. 2020. Highway Statistics 2020, Table HM-12. Retrieved from: <https://www.fhwa.dot.gov/policyinformation/statistics/2020/hm12.cfm>
2. Cheng, D., and Hicks, R.G. 2012. Life-Cycle Cost Analysis Comparison of Rubberized and Conventional Hot-Mix Asphalt in California. *Transportation Research Record, Journal of the Transportation Research Board, No. 0895(12)*. Washington, DC: National Academy of Sciences, Engineering, Medicine.
3. Kim, Y.R. 2009. Modeling of asphalt concrete. ASCE Press, McGraw-Hill, New York
4. Caltrans. 2015. Caltrans Concrete Pavement Guide, Chapter 120. Sacramento
5. Caltrans. 2020. Caltrans Highway Design Manual, Chapter 620. Sacramento
6. Saboori, A., Lea, J., Harvey, J., Lea, J., Mateos, A., and Wu, R. 2021. Pavement ME JPCP Transverse Cracking Model Calibration and Design Catalog Framework (Version 2.5.5). (Research Report: UCPRC-RR-2020-02). Davis and Berkeley, CA: University of California Pavement Research Center.
7. Yildirim, Y., Smit, A.D.F., and Korkmaz, A. 2005. Development of a laboratory test procedure to evaluate tack coat performance. *Turkish Journal of Engineering and Environmental Sciences, 29(4)*. Turkey. (pp 195-205)
8. Leng, Z., Ozer, H., Al-Qadi, I.L., and Carpenter, S.H. 2008. Interphase bonding between hot-mix asphalt and various Portland cement concrete surfaces: laboratory assessment. *Transportation Research Record, Journal of the Transportation Research Board, No. 2057(1)*. Washington, DC: National Academy of Sciences, Engineering, Medicine. (pp 46-53)
9. Trevino, M., Kim, S. M., Smit, A., McCullough, B. F., and Yildirim, Y. 2004. Asphalt Concrete Overlays on Continuously Reinforced Concrete Pavements: Decision Criteria, Tack Coat Evaluation, and Asphalt Concrete Mixture Evaluation (No. FHWA/TX-05/0-4398-3).
10. Darter, M.I., and Barenberg, E.J. 1976. Zero-Maintenance Pavements: Results of Field Studies on the Performance Requirements and Capabilities of Conventional Pavement. Washington, DC: Federal Highway Administration. (FHWA-RD-76-105)

11. Rasmussen, R.O., and Rozycki, D.K. 2004. Thin and ultra-thin whitetopping: A synthesis of highway practice. Vol. 338: Transportation Research Board.
12. Vandenbossche, J., and Sachs, S. 2013. Guidelines for Bonded Concrete Overlays of Asphalt: Beginning with Project Selection and Ending with Construction. Technical Note
13. Yu, H.T., and Tayabji, S. 2007. Thin Whitetopping—the Colorado Experience. Washington, DC: Federal Highway Administration. (FHWA-HIF-07-025)
14. Mateos, A., Harvey, J.T., Wu, R., Paniagua, F., and Paniagua, J. 2018. Development of Improved Guidelines and Designs for Thin Whitetopping: HVS testing of Full-Scale BCOA Sections. (Research Report: UCPRC-RR-2017-XX). Davis and Berkeley, CA: University of California Pavement Research Center. (In progress)
15. Mu, F., and Vandenbossche, J.M. 2011. Development of Design Guide for Thin and Ultra-Thin Concrete Overlays of Existing Asphalt Pavements, Task 2: Review and Selection of Structural Response and Performance Models. University of Pittsburgh. (MN/RC 2001-25)
16. Winkelman, T.J. 2005. Whitetopping Construction and Early Performance in Illinois. Illinois Department of Transportation, Bureau of Materials and Physical Research. (No. FHWA/IL/PRR 144)
17. Sheehan, M. J., Tarr, S. M., and Tayabji, S. D. 2004. Instrumentation and Field Testing of Thin Whitetopping Pavement in Colorado and Revision of the Existing Colorado Thin Whitetopping Procedure. Colorado Department of Transportation, Denver. (Report CDOT-DTD-R-2004-12).
18. Ayers, M., Cackler, T., Fick, G., Harrington, D., Schwartz, D., Smith, K., Snyder, B., and Van Dam, T. (2018). Guide for concrete pavement distress assessments and solutions: identification, causes, prevention, and repair.
19. Harrington, D., and Fick, G. 2014. Guide to concrete overlays: sustainable solutions for resurfacing and rehabilitating existing pavements. 3rd Edition, National Concrete Pavement Technology Center.
20. Xu, C., and Cebon, D. 2017. Analysis of Cracking in Jointed Plain Concrete Pavements: [summary report] (No. FHWA-HRT-16-073). United States. Federal Highway Administration. Office of Research, Development, and Technology.
21. Mateos, A., Harvey, J., Paniagua, F., Paniagua, J., and Wu, R. 2017. Development of Improved Guidelines and Designs for Thin Whitetopping: Construction and Initial Environmental

- Response of Full-Scale BCOA Sections. (Research Report: UCPRC-RR-2017-02). Davis and Berkeley, CA: University of California Pavement Research Center.
22. Pouteau, B., Chabot, A., and De Larrard, F. 2002. Essai accéléré de durabilité du collage blanc sur noir dans une chaussée composite. 17e Congrès Français de Mécanique. (pp 21-25)
 23. Mateos, A., Harvey, J., Paniagua, F. Paniagua, J., and Wu, R. 2017 Development of Improved Guidelines and Designs for Thin Whitetopping: Moisture-Related Shrinkage Response of Full-Scale BCOA Sections. (Research Report: UCPRC-RR-2017-05). Davis and Berkeley, CA: University of California Pavement Research Center.
 24. Mu, F., and Vandebossche, J.M. 2011. Development of Design Guide for Thin and Ultra-Thin Concrete Overlays of Existing Asphalt Pavements, Task 1: Compilation and Review of Existing Performance Data and Information. University of Pittsburgh.
 25. Rasmussen, R.O., McCullough, B.F., Ruiz, J.M., Mack, J., and Sherwood, J.A. 2002. Identification of pavement failure mechanisms at FHWA accelerated loading facility ultrathin whitetopping project. *Transportation Research Record, Journal of the Transportation Research Board, No. 1816(1)*. Washington, DC: National Academy of Sciences, Engineering, Medicine. (pp 148-155)
 26. Heath, A. C., and Roesler, J. R. 1999. Shrinkage and thermal cracking of fast-setting hydraulic cement concrete pavements in Palmdale, California. Pavement Research Center, Institute of Transportation Studies, University of California, Berkeley.
 27. Brand, A.S., and Roesler, J.R. 2017. Bonding in cementitious materials with asphalt-coated particles: Part I—The interfacial transition zone. *Construction and Building Materials 130*. (pp 171-181)
 28. Brand, A.S., and Roesler, J.R. 2017. Bonding in cementitious materials with asphalt-coated particles: Part II—Cement-asphalt chemical interactions. *Construction and Building Materials 130*. (pp 182-192)
 29. Mindess, S., Young, F.J., and Darwin, D. 2003. Concrete 2nd Edition. Technical Documents.
 30. Sadd, M.H., Subramaniam, V.K., Shukla, A., and Lee, W. 2007. Interfacial Failure Behavior of Concrete-Asphalt Bi-Materials. *Insem annual conference and exposition on experimental and applied mechanics*. (pp 1421-1430)

31. Nelson, P.K., and Rasmussen, R.O. 2002. Delamination stresses at the interphase of bonded concrete overlays. *Proceedings of 81st Transportation Research Board Meeting*. Washington DC, US.
32. Mu, F. 2014. Laboratory and numerical investigation of interphase debonding of bonded concrete overlay of asphalt and its effect on the critical stress in the overlay. University of Pittsburgh.
33. Roesler, J.R., Bordelon, A.C., Ioannides, A., Beyer, M., and Wang, D. 2008. Design and concrete material requirements for ultra-thin whitetopping. Illinois Center for Transportation, Illinois.
34. Tarr, S.M., Sheehan, M.J., and Okamoto, P.A. 1998. Guidelines for the thickness design of bonded whitetopping pavement in the State of Colorado. Colorado Department of Transportation Denver, CO. (CDOT-DTD-R-98-10)
35. Trevino, M., McCullough, F., and Fowler, W. 2002. Techniques and procedures for bonded concrete overlays. Center for Transportation Research, Texas. (FHWA/TX-05/0-4398-2)
36. Cable, J.K., Hart, J.M., and Ciha, T. 2001. Thin Bonded Overlay Evaluation. Department of Civil and Construction Engineering, Iowa State University.
37. Chabot, A., Balay, J.M., Pouteau, B., and de Larrard, F. 2008. FABAC accelerated loading test of bond between cement overlay and asphalt layers. *Proceedings of the Sixth International RILEM Conference on Cracking in Pavements*. Chicago, US.
38. Pouteau, B., Chabot, A., and de Larrard, F. 2002, October. Etude en laboratoire du collage béton hydraulique sur matériau bitumineux. *Matériaux 2002*. France.
39. Mahdi, M., Wu, Z., and Rupnow, T. 2014. Evaluation of bonded concrete overlays over asphalt under accelerated loading: research project capsule (No. 14-4C). Louisiana Transportation Research Center. (FHWA/LA.19/622)
40. Applied Research Associates, Inc. 2016. Integrating the Bonded Concrete Overlay of Asphalt (BCOA-ME) Design Procedure into the AASHTOWare Pavement ME Software.
41. Khazanovich, L., and Tompkins, D. 2017. Incorporating Slab/Underlying Layer Interaction into the Concrete Pavement Analysis Procedures. (No. NCHRP Project 01-51).

42. Caltrans. Caltrans Pavement Climate Regions Map. Retrieved from: <https://dot.ca.gov/programs/maintenance/pavement/concrete-pavement-and-pavement-foundations/climate>
43. Lea, J.D., and Harvey, T.J. 2012. The Simplified Thermal Modeling Approach Used in CALME. *Transportation Research Record, Journal of the Transportation Research Board, No. 2938(12)*. Washington, DC: National Academy of Sciences, Engineering, Medicine.
44. American Society of Testing and Materials. 2020. ASTM D7870/D7870M-20: Standard Practice for Moisture Conditioning Compacted Asphalt Mixture Specimens by Using Hydrostatic Pore. West Conshohocken, PA.
45. American Association of State Highway and Transportation Officials. 2020. AASHTO T320-07: Standard Method of Test for Determining the Permanent Shear Strain and Stiffness of Asphalt Mixtures Using the Superpave Shear Tester (SST). Washinton, DC.
46. American Association of State Highway and Transportation Officials. 2022. AASHTO T378-22: Standard Method of Test for Determining the Dynamic Modulus and Flow Number for Asphalt Mixtures Using the Asphalt Mixture Performance Tester (AMPT). Washinton, DC.
47. American Society of Testing and Materials. 2019. ASTM D8225-19: Standard Practice for Determination of Cracking Tolerance Index of Asphalt Mixture Using the Indirect Tensile Cracking Test at Intermediate Temperature. West Conshohocken, PA.
48. Mateos, A. 2003. Modeling the Structural Response of Flexible Pavements from Full Scale Test Track Experimental Data. PhD Thesis, Technical University of Madrid (publication in Spanish).
49. American Society of Testing and Materials. 2019. ASTM C309-19: Standard Specification for Liquid Membrane-Forming Compounds for Curing Concrete. West Conshohocken, PA.
50. American Society of Testing and Materials. 2021. ASTM C595/C595M-21: Standard Specification for Blended Hydraulic Cements. West Conshohocken, PA.
51. American Society of Testing and Materials. 2022. ASTM C989/C989M-22: Standard Specification for Slag Cement for Use in Concrete and Mortars. West Conshohocken, PA.
52. American Society of Testing and Materials. 2021. ASTM C39/C39M-21: Standard Test Method for Compressive Strength of Cylindrical Concrete Specimens. West Conshohocken, PA.

53. American Society of Testing and Materials. 2021. ASTM C78/C78M-21: Standard Test Method for Flexural Strength of Concrete (Using Simple Beam with Third-Point Loading). West Conshohocken, PA.
54. American Society of Testing and Materials. 2022. ASTM C469/C469M-22: Standard Test Method for Static Modulus of Elasticity and Poisson's Ratio of Concrete in Compression. West Conshohocken, PA.
55. American Society of Testing and Materials. 2008. ASTM C403/C403M-08: Standard Test Method for Time of Setting of Concrete Mixtures by Penetration Resistance. West Conshohocken, PA.
56. Smith, M. 2009. ABAQUS/standard user's manual, version 6.14. Accessed online: <http://130.149.89.49:2080/v6.14/>

APPENDIX A

ADDITIONAL TESTING PROCEDURES

The FEM models that are discussed when determining testing parameters always follow the convention shown in Figure A- 1. The longitudinal joints are along the x-axis while the transverse joints are along the Y axis. X, Y, and Z correspond to the directions 1, 2, and 3, respectively.

Whenever shear strain is mentioned, it corresponds to the vectorial addition of ϵ_{13} and ϵ_{23} such

$$\text{as: } \tau = \sqrt{\epsilon_{13}^2 + \epsilon_{23}^2}.$$

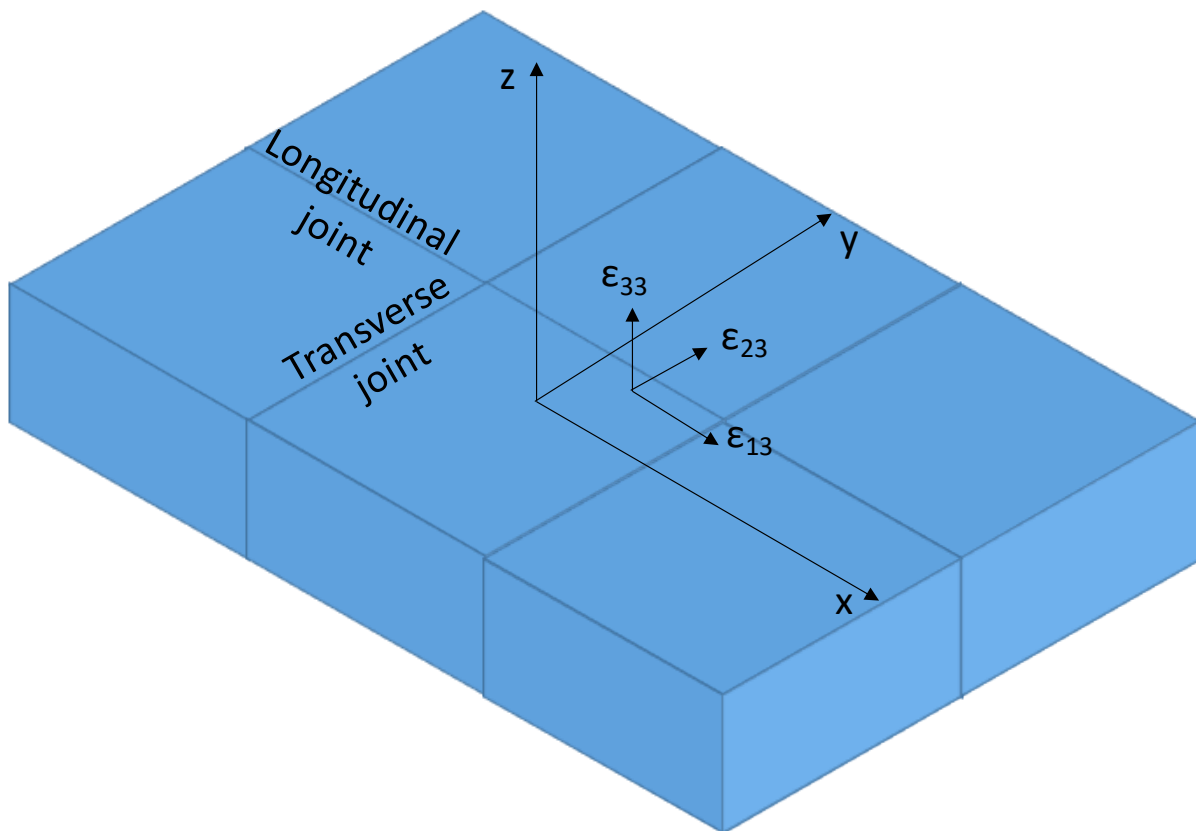


Figure A- 1. FEM models axis representation

Shear Fatigue

The shear fatigue test is performed in the SST machine. It is a deformation-controlled test used to characterize the fatigue life of SJPCP-COA specimens after a specific amount of shear loading cycles are applied. Besides characterizing the damage, the test can also be used to characterize the nonlinear viscoelastic behavior of the structure under high strain levels.

A diagram for the test is shown in Figure A- 2. A 0.1 kN (22.5 lbf) compressive load is used in order to ensure no tension will be applied to the specimen through the test. Four LVDTs are used to track displacements in the interphase and at the asphalt structure; one of the last ones is used to control the deformation level required for the test.

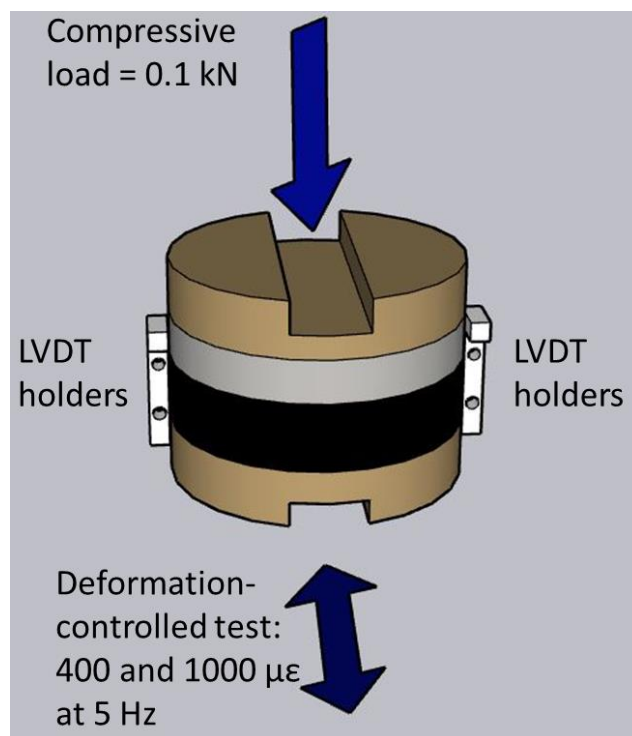


Figure A- 2. Shear fatigue test diagram

Input Parameters

The test requires the input of the frequency and strain level. The shear strain levels were obtained from modeling SJPCP-COA sections under HVS loading. The modeling is required because the instrumented SJPCP-COA sections only provide tensile and compressive strains.

The test is done at three temperatures: 15, 25, and 40 °C (59, 77 and 104 °F).

From 4.58B HVS Sections:

Since HVS data was recorded during the HVS testing at a speed of 8 km/h (5 mph) and during the manual testing at 2 km/h (1.2 mph), a representative frequency can be calculated for each of the loading speeds. Figure A- 3 shows the deflection influence line under a moving load of 2 km/h (1.2 mph), and at the top, the influence distance is labeled. On average, such distance varies between 2.8 and 3.6 m (9.2 and 12 ft), and it takes the HVS 5.0 - 6.5 seconds, which corresponds to a frequency of approximately 0.175 Hz for the 2 km/h (1.2 mph) evaluation.

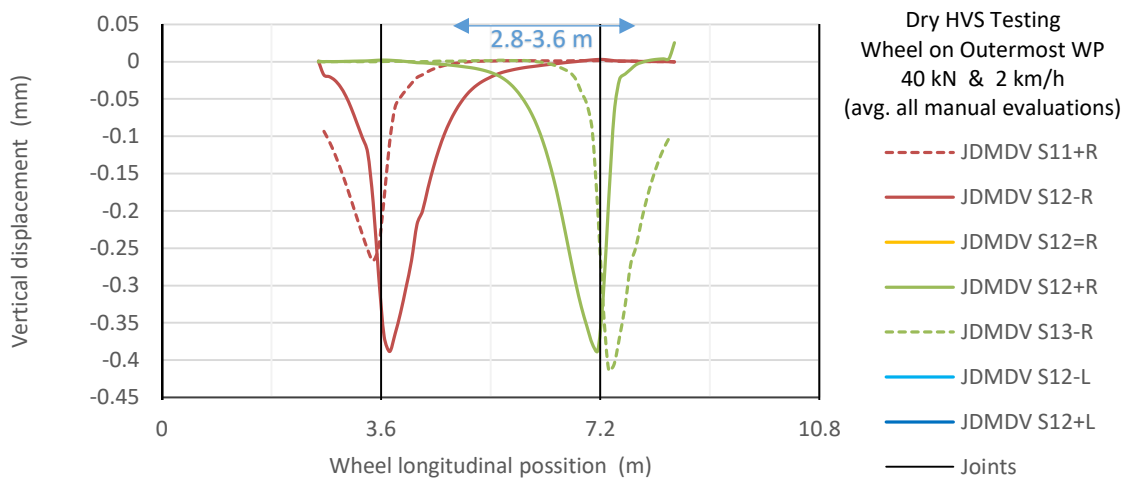


Figure A- 3. Deflection influence lines under the HVS wheel

Therefore, a speed of 8 km/h (4.8 mph) corresponds to a frequency of 0.70 Hz. Since real traffic speed is intended to be simulated and there is limited time and resources for laboratory testing, a frequency of 10 Hz is proposed for the fatigue test. Using the previous correlation, a speed of 104 km/h (65 mph) corresponds to a frequency of 9.1 Hz, so it is reasonable for this test to be rounded up to 10 Hz.

From Modeling

Since the instrumentation placed on the SJPCP-COA sections does not provide shear strain, the sections were modeled under traffic loads to try to match the tensile and compressive strain levels that were obtained in the HVS sections. The finite element method (FEM) model of a 1.8 x 1.8 m (6 x 6 ft) slab section is shown in Figure A- 4. Since it is a high-frequency fatigue test, the analysis was done only under traffic loading of a fully bonded SJPCP-COA section that consisted of six concrete slabs placed on top of an HMA layer. The HMA layer was modeled as separated slabs since, from field observations, the concrete cracks were propagated all the way into the asphalt mixture layer. The loading was a 40 kN (9,000 lbf) half axle (half of the maximum legal axle load in California), which is applied in two square loading areas, and it was an elastic analysis in which the HMA stiffness for 20 °C (68 °F) was used: 3450 MPa (500,000 psi). Three SJPCP-COA sections with a 112.5 mm (4.5 in.) thick PCC with different slab sizes were analyzed: the 1.8 x 1.8 m (6 x 6 ft) slab section previously detailed, a section with a widened 1.8 x 2.4 m (6 x 8 ft) slab in the exterior side of the lane and a 3.6 x 3.6 m (12 x 12 ft) slab section. The goal of the widened slab is to keep traffic loads off the edges of the slab, which will reduce stresses and strains in those areas. These two slab sizes were analyzed since those are the recommended slab configurations to be used from previous experience [14].

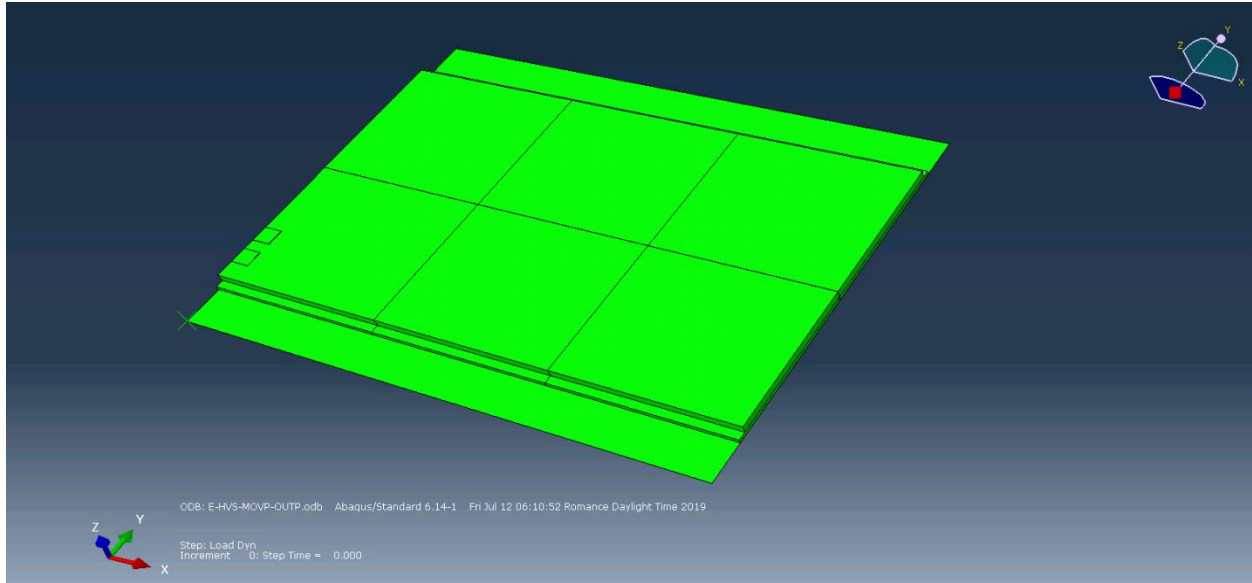


Figure A- 4. Undeformed SJPCP-COA section of 1.8 x 1.8 m (6 x 6 ft) slabs

Figure A- 5 shows the maximum shear strain under a moving load along two adjacent slabs. The data for the 1.8 x 1.8 m (6 x 6 ft) slabs is shown in the green curve, the widened slab [1.8 x 2.4 m (6 x 8 ft)] in the dashed brown line and the 3.6 x 3.6 m (12 x 12 ft) slabs in the blue line. The asphalt under the concrete transverse joint is under the highest shear strain, being the corner, the most critical location, as can be seen in the figure. There is a considerable reduction in the shear strain when the load is kept off the edge of the slab. If the load is on the edge of the slab (edge of the outside tire at 220 mm (8.5 in.) from the edge of the slab), the shear maximum peak-to-peak strain ($\tau = \sqrt{\epsilon_{13}^2 + \epsilon_{23}^2}$) is 675 $\mu\epsilon$, but if the load is kept two feet apart from the joint (edge of the outside tire at 820 mm (32 in.) from the edge of the slab), it is reduced to approximately 325 $\mu\epsilon$.

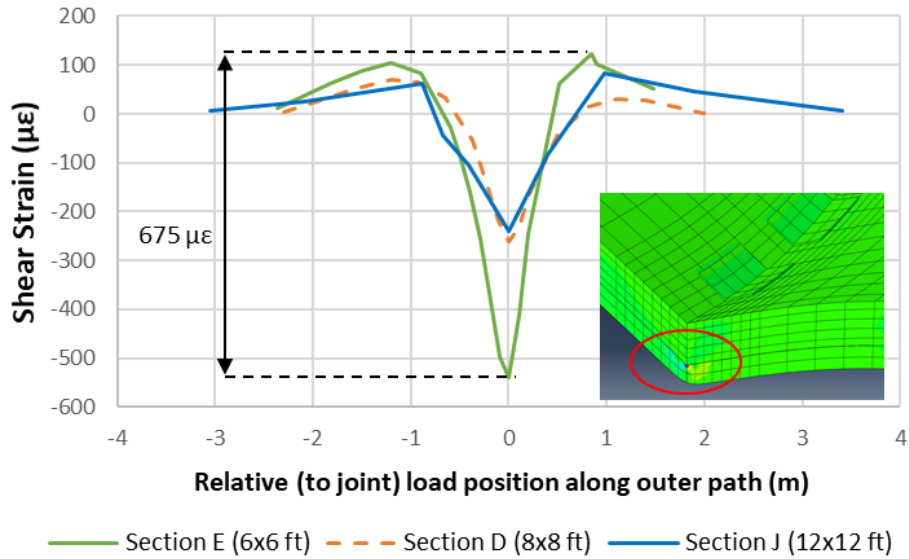


Figure A- 5. Shear strain under moving load for SJPCP-COA sections, 0 m corresponds to the joint

A temperature susceptibility analysis was done for the 1.8 x 1.8 m (6 x 6 ft) slab section, which consisted of running the model with a temperature value added to the concrete layer. Five cases were analyzed in addition to the one shown in the previous figure. The first three cases were performed at the temperatures at which the laboratory tests are conducted: 15, 25, and 40 °C (59, 77, and 104 °F) constant throughout the structure. The results for these three cases are shown in Figure A- 6 and are compared against the previous case. Both the strain level and differential strain under the wheel displacement increased when the temperature in the structure was increased from 15 to 40 °C (59 to 104 °F). Two additional cases with a positive and negative temperature gradient in the concrete were analyzed in which the concrete surface remained at 25 °C (77 °F). The temperature gradient was +9 °F and -9 °F which means that the interphase between the concrete and the asphalt was at 20 and 30 °C (68 and 86 °F). The strain level did not differ much from the scenario with a constant temperature gradient, but the

differential shrinkage under the load movement did have some changes. When the concrete surface was at 25 °C (77 °F) and the interphase at 20 °C (68 °F), the differential shrinkage was 650 $\mu\epsilon$. On the other hand, when the interphase was at 30 °C (86 °F), the differential shrinkage was 790 $\mu\epsilon$.

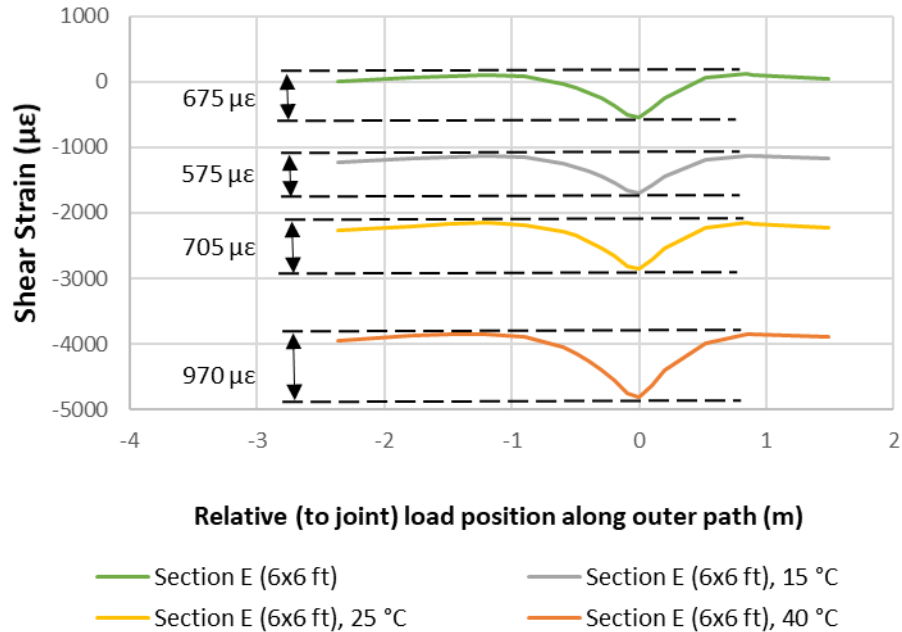


Figure A- 6. Shear strain under moving load in a 1.8 x 1.8 m (6 x 6 ft) section, 0 m corresponds to joint

In order to determine if the strains shown in Figure A- 5 and Figure A- 6 correspond to a localized stress concentration point or to an accurate representation of what is happening in the slab, the shear strain along the transverse joint was calculated for the case without temperature change of the 1.8 x 1.8 m (6 x 6 ft) section. Since the actual transverse position of where the load is going to be on the field is unknown, different loading positions were analyzed, and a strain envelope for all the curves was obtained. The shear strain envelope along the transverse joint for a 1.8 x 1.8 m (6 x 6 ft) slab sections in Figure A- 7 shows that the shear strain remains over 500 $\mu\epsilon$ along

30 cm (11.8 in.) of the transverse joint with a maximum strain level of 675 $\mu\epsilon$. Such high strains at the top of the asphalt layer are prone to cause damage to the asphalt layer.

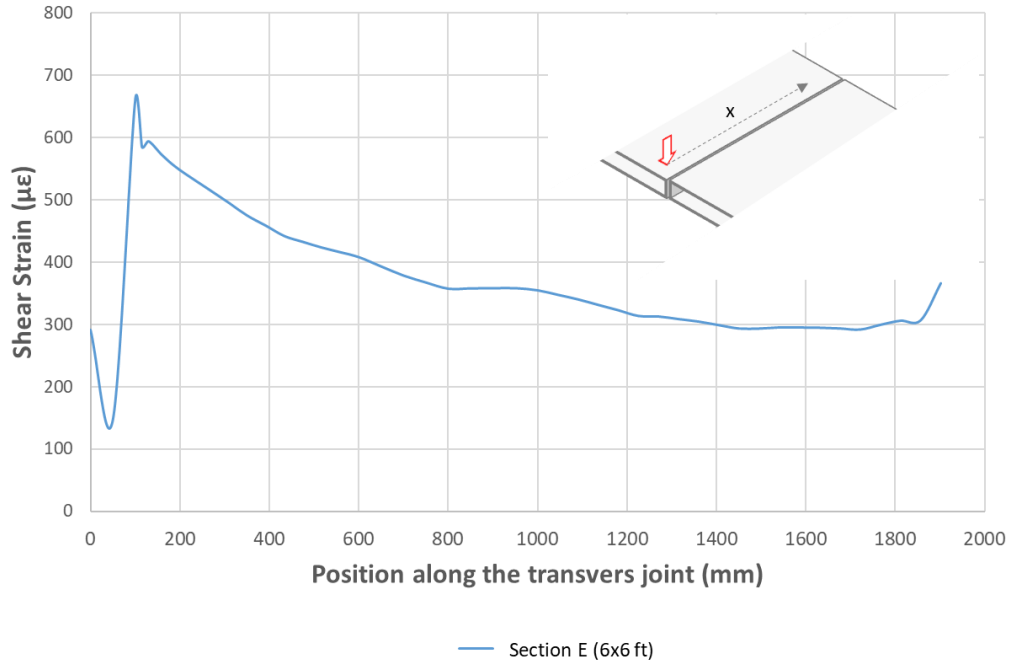
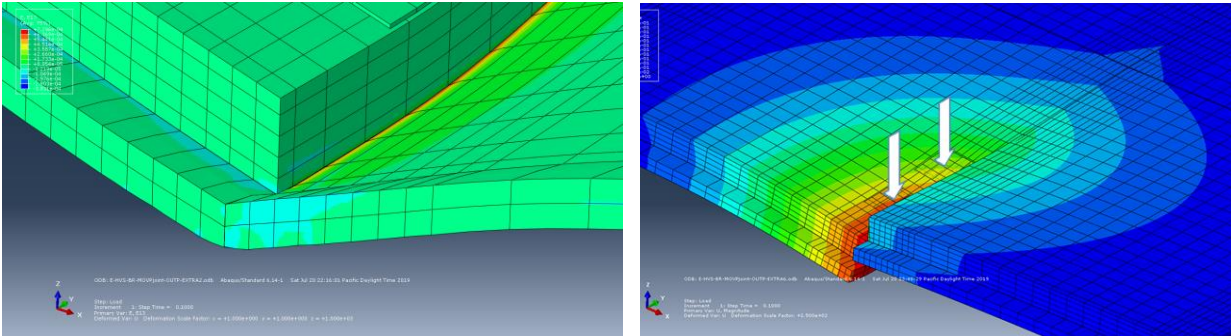


Figure A- 7. Shear strain envelope along transverse joint, 1.8 x 1.8 m (6 x 6 ft) slab. 0 mm corresponds to edge

Based on field data of SJPCP-COA sections with different slab sizes, it was observed that shear strains in the order of 500 to 700 $\mu\epsilon$ in sections with 1.8 x 1.8 m (6 x 6 ft) slabs were likely to damage the asphalt underneath the transverse joint. Such damage was reflected as a crack propagation into the asphalt, which would cause a considerable increase in the shear strain levels due to the reduction of support under the joint. The damaging process can be summarized in two separate mechanisms. First, a punching mechanism (a) will cause the crack to start propagating into the asphalt due to the increased shear stress and strain under the concrete slab joints. Then, a second mechanism in which two adjacent slabs do not carry the load simultaneously causes a ‘scissors’ (b) effect whenever the loads are moving from one slab to the next. Both mechanisms

are shown in Figure A- 8. Shear stress is shown in the punching mechanism, while vertical displacement is shown in the ‘scissors’ mechanism.



a) Punching mechanism, shear stress modeled

b) ‘Scissors’ mechanism, vertical displacement modeled

Figure A- 8. Damaging mechanisms under the concrete joint

Performing a similar analysis as the one in Figure A- 7, but adding a new variable, different scenarios were analyzed, which included crack propagations of lengths along the transverse joint varying from 0 to 1,450 mm (0 to 57 in.) to determine the shear strain increase if the crack is propagated into the asphalt layer. Figure A- 9 summarizes the shear strain envelopes for the eight crack propagation lengths analyzed. From the FEM results, it was defined that the punching mechanism occurs up to a crack propagation length of 500 mm (20 in.), in which the shear strain level was always under $650 \mu\epsilon$. Whenever the crack propagation length goes beyond 500 mm (20 in.), there is a considerable increase in shear strain due to the effect of the ‘scissors’ mechanism, causing the asphalt under two adjacent slabs to carry the loads independently due to the lack of connection caused by the crack propagation.

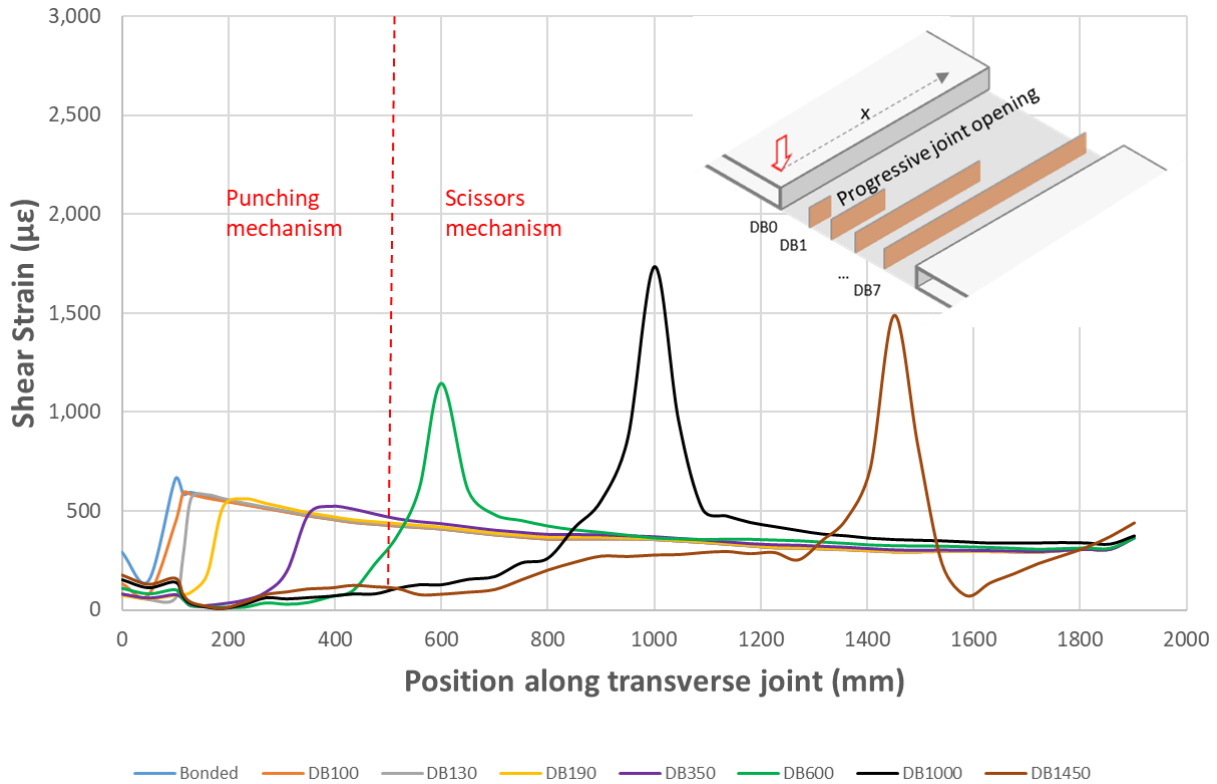


Figure A- 9. Summary of shear strain envelope along transverse joint for 1.8 x 1.8 m (6 x 6 ft) slab

Since the fatigue life of the asphalt is highly dependent on the strain level, the testing was conducted at two strain levels. Performing tests at two strain levels enables extrapolation or interpolation to other strain levels. Based on the information shown above, one strain level should be over the 675 µε that was provided by the modeling of a 1.8 x 1.8 m (6 x 6 ft) section (Figure A- 5) and another one that is under this value. The low strain level test is defined to be performed at 400 µε. The high deformation level, which will cause the fatigue life to shorten, was chosen as 1200 µε, which corresponds to the strain level recorded when a crack propagation length of 600 mm (24 in.) occurred (first case or ‘scissors’ mechanism in Figure A- 9).

Summary

The shear fatigue test will be performed at:

- Frequency: 10 Hz
- Strain level:
 - o 400 $\mu\epsilon$ for the low deformation testing
 - o 1200 $\mu\epsilon$ for the high deformation testing
- Temperatures: 15, 25, 40 °C (59, 77 and 104 °F). 1200 $\mu\epsilon$ only done at 25 °C (77 °F).

Shear Sine-Ramp

The shear sine-ramp test is performed in the SST machine. It is a deformation-controlled test used to replicate the field loading of SJPCP-COA sections by simulating daily and yearly environmental loads occurring in the pavement structure. The test consists of an increasing sinusoidal ramp, which replicates the daily temperature variation happening in the structure and the shrinkage effect occurring on the field over 6 months. Figure A- 10 shows how the data looks for this test. A simplification in the testing procedure has been made by grouping five sine cycles followed by one ramp.

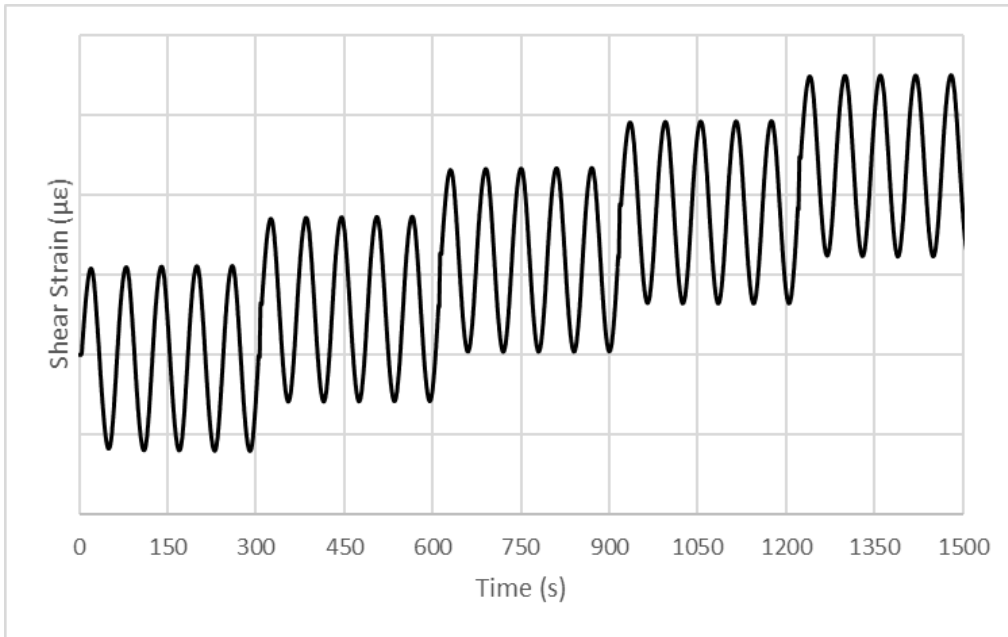


Figure A- 10. Sine-Ramp stress vs time plot

Figure A- 11 shows a diagram for the shear sine-ramp. One of the asphalt LVDTs controls the deformation level of the test. A 0.1 kN (22.5 lbf) vertical load is applied during the test to ensure that the specimen is under slight compression.

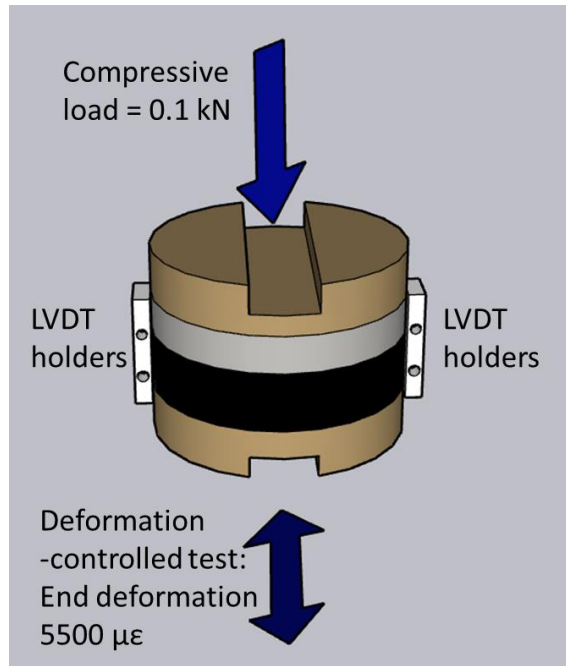


Figure A- 11. Shear sine-ramp test diagram

Input Parameters

The test requires three parameters: end strain level, cyclic strain variation, and length of test. The two first parameters are obtained from modeling a SJPCP-COA structure under maximum contraction produced by thermal gradients. Even though the testing will replicate the loading that occurred in SJPCP-COA sections over six months, the testing times must be reduced considerably. Three times are used to allow extrapolation to real loading time in the slabs.

From Modeling

SJPCP-COA sections of 3.6 x 3.6 m (12 x 12 ft) slabs and 1.8 x 1.8 m (6 x 6 ft) slabs were modeled in Abaqus to determine which is the typical strain level the structures will have under environmental loading. The model for the 3.6 x 3.6 m (12 x 12 ft) slab section is shown in Figure A- 12. It consisted of three slabs on top of an AC layer, which is supported on a continuous

aggregate base, and complete bonding is assumed. The model assumes no crack propagation into the asphalt layer based on what was observed in test sections.

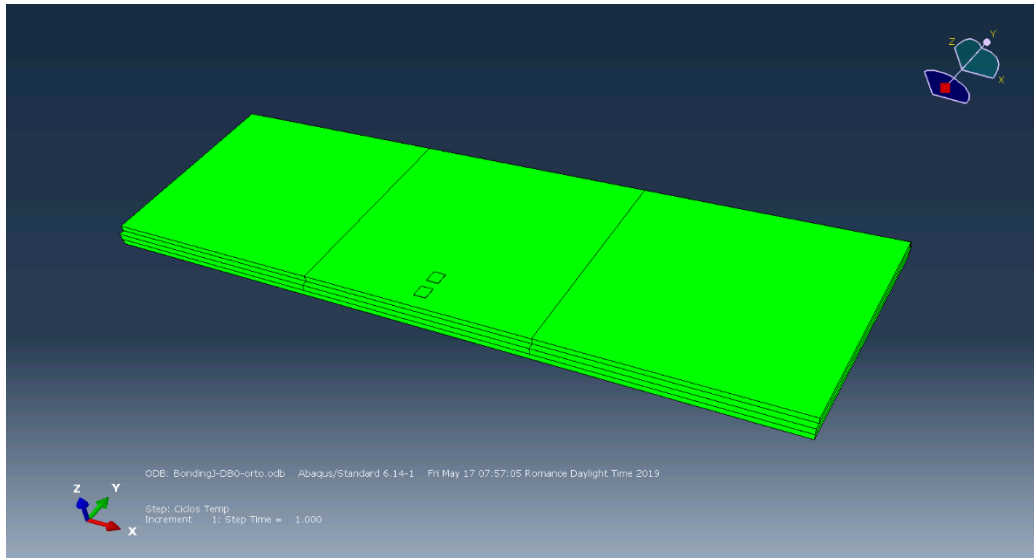


Figure A- 12. Undeformed SJPCP-COA section of 3.6 x 3.6 m (12 x 12 ft) slabs

This analysis was done for the maximum contraction values that were observed in the field in a 3.6 x 3.6 m (12 x 12 ft) slab size SJPCP-COA section on July 19th, 2016. On this day, the maximum bending that occurred due to temperature and shrinkage corresponds to a temperature difference of -60 °C (-108 °F) between the top and bottom of the slab. On that day, a uniform contraction corresponding to a uniform temperature of -42 °C (-76 °F) due to temperature and shrinkage also happened, this value was rounded to -45 °C (-81 °F). In this case, traffic load was not applied since it was solely an environmental analysis. When the structure is modeled under those ambient conditions, it deforms as shown in Figure A- 13. The point of interest is at the corner next to the transverse joint in the asphalt layer (red dot), which is why the concrete layer is hidden in the second and third slabs.

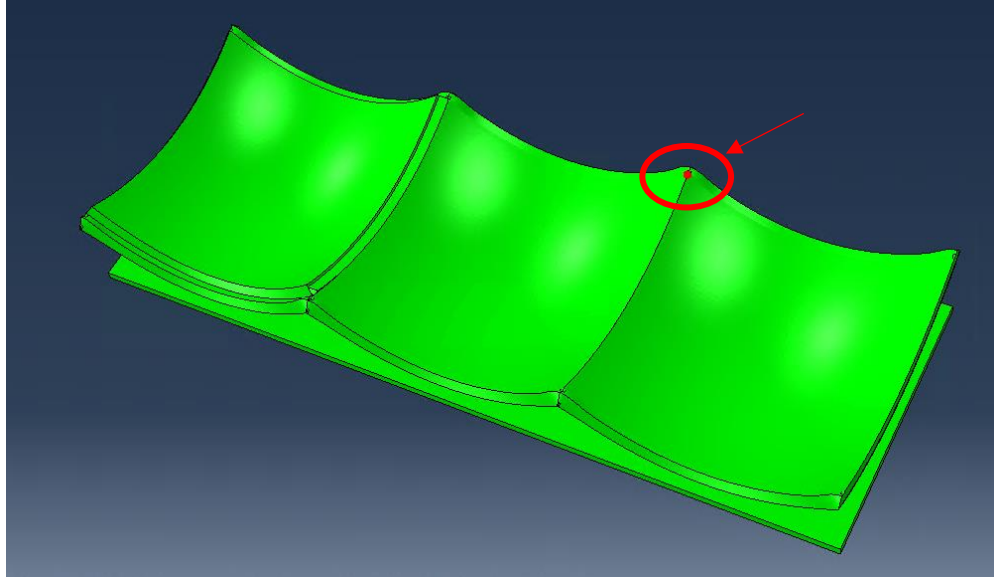


Figure A- 13. Deformed SJPCP-COA section under environmental loads

Focusing only on the node of interest, the model provides the strain data that is summarized in Table A- 1. The total shear strain is defined as vector summation of ϵ_{13} and ϵ_{23} , which are the two components that cause shear strain in the note of interest. The sum given by $\tau = \sqrt{\epsilon_{13}^2 + \epsilon_{23}^2} = \sqrt{(-7,354)^2 + (35)^2}$ adds up to 7,354 $\mu\epsilon$. For this test, the value is going to be rounded up to 7500 $\mu\epsilon$ and will be used as the end strain level for the test.

Table A- 1. Strain values at the point of maximum shear strain in slab 3.6 x 3.6 m (12 x 12 ft)

Strains ($\mu\epsilon$)		
ϵ_{33}	ϵ_{13}	ϵ_{23}
359	-7,354	35

The cyclic strain variation that occurs due to daily changes in temperature and humidity in the structure is obtained from the same analysis as was explained before. As it was stated, -60 °C (-108 °F) is the temperature difference corresponding to the maximum bending that occurred in one day. To determine the maximum daily variation, the minimum bending on that same day was

calculated and corresponded to a temperature value of -40 °C (-72 °F). The total shear strain for these two temperatures along two sides of the slab is shown in Figure A- 14. The strain difference between both analyzed temperatures is approximately 1,918 $\mu\epsilon$, which corresponds to the total daily temperature variation. From this analysis, it is determined that the peak-to-peak strain to account for daily temperature changes pertains to 2,000 $\mu\epsilon$ or a sine semi-amplitude of 1,000 $\mu\epsilon$.

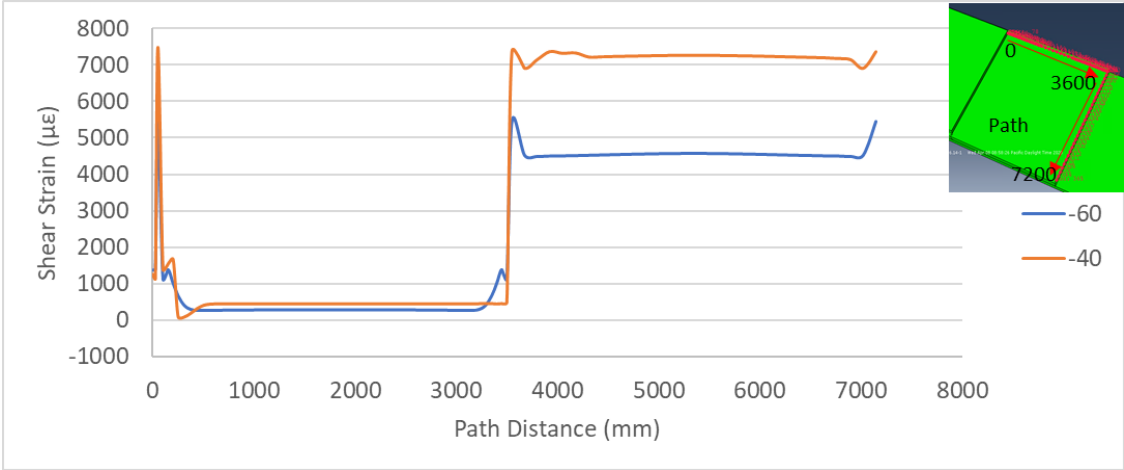


Figure A- 14. Total shear strain along critical path, slab 3.6 x 3.6 m (12 x 12 ft)

The same procedure was done on a 1.8 x 1.8 m (6 x 6 ft) slab section, which is the recommended slab size to be used in California. The model consisted of 6 slabs (Figure A- 4) and had the same properties as the previous one in order to have comparable results. In this case, the maximum shear strain had a value of 5,329 $\mu\epsilon$, which occurred in the same location near the corner of the concrete slab and was calculated by the vector summation of ϵ_{13} and ϵ_{23} . As a simplification, the value will be rounded up to 5,500 $\mu\epsilon$. The strain data for such node is summarized in Table A- 2. The cyclic strain variation caused by the temperature differences throughout the day corresponded to a peak-to-peak deformation of 491 $\mu\epsilon$. The deformation is rounded to 500 $\mu\epsilon$.

or a sine semi-amplitude of 250 $\mu\epsilon$. Figure A- 15 shows both the maximum shear strain and the cyclic variation for the 1.8 x 1.8 m (6 x 6 ft) model.

Table A- 2. Strain values at the point of maximum shear strain in slab 1.8 x 1.8 m (6 x 6 ft)

Strains ($\mu\epsilon$)		
ϵ_{33}	ϵ_{13}	ϵ_{23}
491	-4,731	2,452

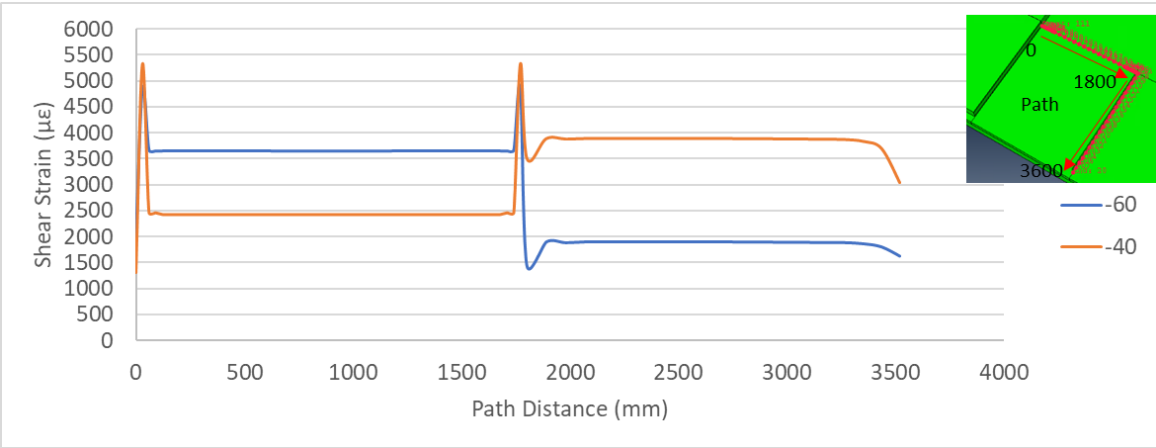


Figure A- 15. Total shear strain along critical path, slab 1.8 x 1.8 m (6 x 6 ft)

The previous results indicate that higher deformation levels were experienced in the larger slab sections. Even though a higher deformation will cause a more critical testing condition, for this case, the deformation level of the 1.8 x 1.8 m (6 x 6 ft) slabs is recommended for the majority of the tests since it is the slab dimension that is being used the most in the state of California. Additionally, a few specimens will be tested at the deformation levels provided from the analysis of the 3.6 x 3.6 m (12 x 12 ft) slabs to obtain valuable results that can be compared to those obtained in the 1.8 x 1.8 m (6 x 6 ft) section or to be used by any project that decides to build bigger sized slabs.

From SJPCP-COA sections that were exposed only to environmental loads, it is known that debonding had occurred in all the sections before six months. Since six months of testing is impossible to replicate in the laboratory, the test is performed at three different reduced time periods to be able to extrapolate the findings. The tests have the same strain levels and amount of loading cycles, the only difference is the length of each of the loading cycles. The shortest test is done in 3 hours, the most extended test takes 3 days, and an intermediate time of 1 day is also analyzed. The length of one loading cycle for each of the test durations (3 hours, 1 day and 3 days) is 1 minute, 8 minutes and 24 minutes, respectively.

Summary

The shear sine-ramp testing will be performed at:

- Daily strain: $5,500 \mu\epsilon / 180 \text{ days} = 30 \mu\epsilon$
- Cyclic strain variation: $500 \mu\epsilon$
- Time: 3 hours, 1 day and 3 days

Tensile Sine-Ramp

The tensile sine-ramp test is performed in the UTM machine. It is a deformation-controlled test used to replicate the behavior of field SJPCP-COA sections by simulating daily and yearly environmental loads occurring in the pavement structure. The test consists of an increasing sinusoidal ramp, which replicates the daily temperature variation happening in the structure and the shrinkage effect. Figure A- 10 shows a sample result of a sine-ramp test that can be either in tension or shear.

A diagram for the test is shown in Figure A- 16. The tensile sine-ramp is different from the shear sine-ramp test in two main ways. The deformation-controlled test is done in the vertical direction, and the horizontal actuator applies no load. Additionally, a vertical LVDT is included in the test, which controls the deformation level through the test. The other three LVDTs remain in the horizontal direction.

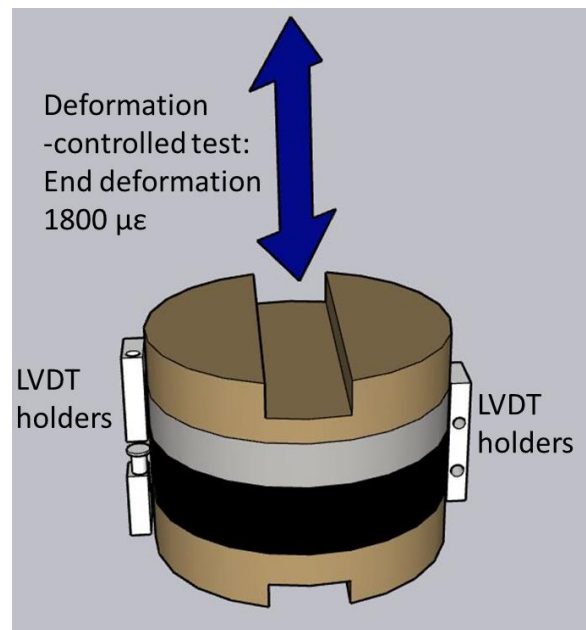


Figure A- 16. Tensile sine-ramp test diagram

Input Parameters

The test requires three parameters: end strain level, cyclic strain variation, and length of test. The two first parameters are obtained from modeling a SJPCP-COA structure under maximum contraction produced from uniform and thermal gradients. Even though the testing will replicate the loading that occurred in SJPCP-COA sections over six months, the testing times must be reduced considerably. Three times will be used to allow extrapolation to real loading time in the slabs.

From Modeling

The same two slab size sections that were modeled in Abaqus for the shear sine-ramp test were used to obtain the results for the tensile sine-ramp test. Vertical strains (ϵ_{33}) were obtained from the 3.6 x 3.6 m (12 x 12 ft) slabs SJPCP-COA section shown in Figure A- 12. The maximum vertical strain along the analyzed path is 2,000 $\mu\epsilon$ and Table A- 3 shows the strain summary.

Table A- 3. Strain values at the point of maximum vertical strain in slab 3.6 x 3.6 m (12 x 12 ft)

Strains ($\mu\epsilon$)		
ϵ_{33}	ϵ_{13}	ϵ_{23}
2,000	777	-29

The process to obtain the cyclic strain variation that occurs due to daily changes in temperature and humidity in the structure is obtained in the same way as was done for the shear sine ramp test. Having a maximum and minimum bending corresponding to $-60\text{ }^{\circ}\text{C}$ and $-40\text{ }^{\circ}\text{C}$ (-108 and $-72\text{ }^{\circ}\text{F}$), respectively, the strain difference of these two scenarios determines the maximum daily variation happening in the slab. Figure A- 17 shows the vertical strain along two sides of the slab for both scenarios.

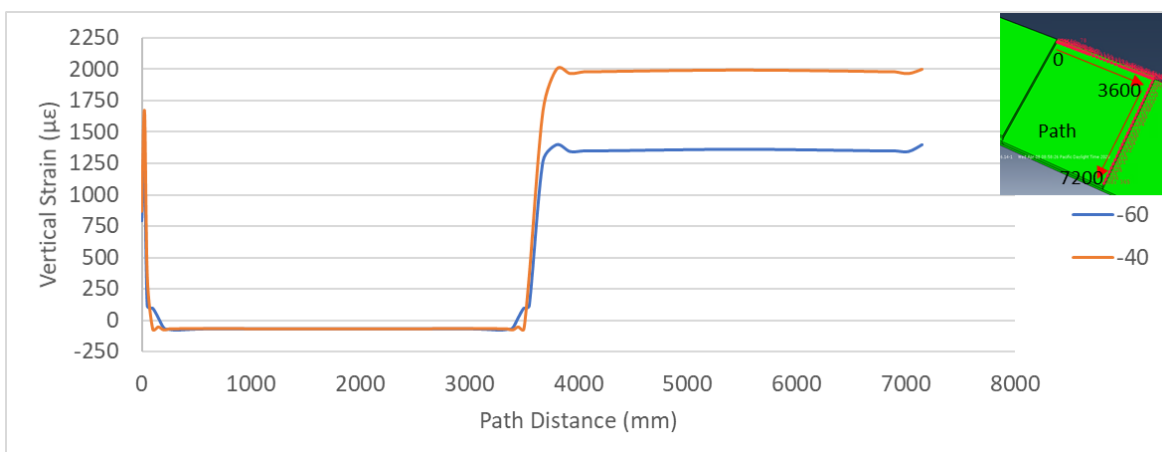


Figure A- 17. Total vertical strain along critical path, slab 3.6 x 3.6 m (12 x 12 ft)

From this analysis, it is determined that the peak-to-peak strain to account for daily changes corresponds to approximately 600 $\mu\epsilon$ or a sine semi-amplitude of 300 $\mu\epsilon$.

A similar analysis was made on a 1.8 x 1.8 m (6 x 6 ft) slab section, the recommended slab size to be used in California. The model had the same exact properties as the previous one to have comparable results. In this case, the maximum tensile strain had a value of 1,802 $\mu\epsilon$, which occurred in the same location near the corner of the concrete slab and is rounded to 1800 $\mu\epsilon$. The strain data for such node is summarized in Table A- 4. The cyclic strain variation caused by the temperature differences throughout the day corresponded to a peak-to-peak deformation of approximately 390 $\mu\epsilon$. As a simplification, the deformation level will be assumed as 400 $\mu\epsilon$ or a sine semi-amplitude of 200 $\mu\epsilon$. Figure A- 18 shows a plot in which can be seen both the maximum shear strain and cyclic variation for the 1.8 x 1.8 m (6 x 6 ft) model.

Table A- 4. Strain values at the point of maximum vertical strain in slab 1.8 x 1.8 m (6 x 6 ft)

Strains ($\mu\epsilon$)		
ϵ_{33}	ϵ_{13}	ϵ_{23}
1802	-1,177	-577

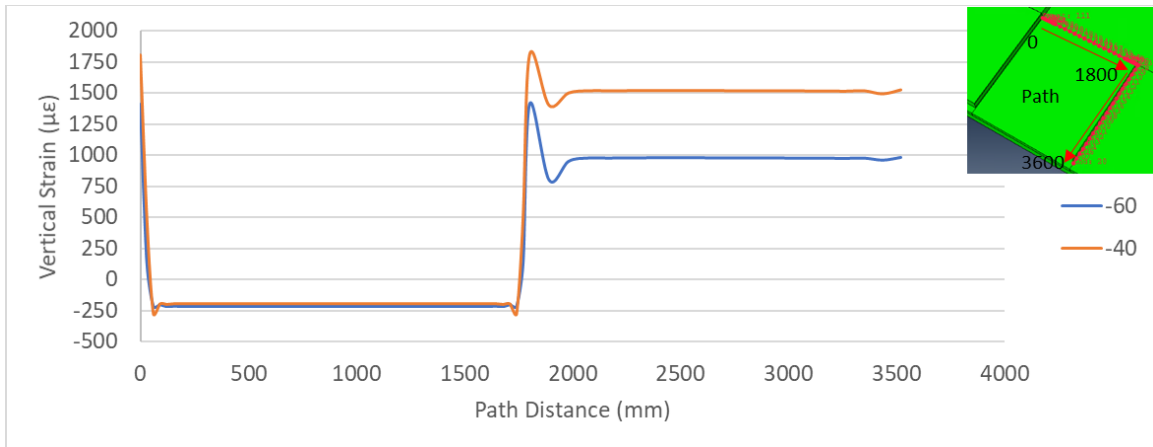


Figure A-18. Total vertical strain along critical path, slab 1.8 x 1.8 m (6 x 6 ft)

The previous results indicate that higher cyclic variation was experienced in the larger slab sections. Higher deformations cause a more critical testing condition, for this case, the deformation level of the 1.8 x 1.8 m (6 x 6 ft) slabs is also recommended for the majority of the tests since it is the slab dimension that is being used the most in the state of California. Additionally, a few specimens will be tested at the deformation levels provided from the analysis of the 3.6 x 3.6 m (12 x 12 ft) slabs to obtain valuable results that can be compared to those obtained in the 1.8 x 1.8 m (6 x 6 ft) section or to be used by any project that decides to build bigger sized slabs.

The same three testing times that were suggested for the shear sine-ramp test are used for the tensile sine-ramp test: 3 hours, 1 day and 3 days.

Summary

The tensile sine-ramp testing will be performed at:

- Daily strain: $1,800 \mu\epsilon / 180 \text{ days} = 10 \mu\epsilon$

- Cyclic strain variation: 400 $\mu\epsilon$
- Time: 3 hours, 1 day and 3 days

Combined Sine-Ramp

The combined sine-ramp test is performed on the SST machine. Since the SJPCP-COA structure is simultaneously under shear and tensile loads, it is important to analyze the effect of both loads acting at the same time in a combined sine-ramp test. Initially, it was performed one test under tensile and one test under shear load to determine if one of the two scenarios was clearly predominant.

A diagram for the test is shown in Figure A- 19. The combined sine-ramp is a deformation-controlled test in the vertical and horizontal direction. The test setup requires a horizontal and a vertical LVDT controlling the deformation level of the test in each direction. This means that one LVDT is placed in the vertical direction while the other three LVDTs remain in the horizontal direction.

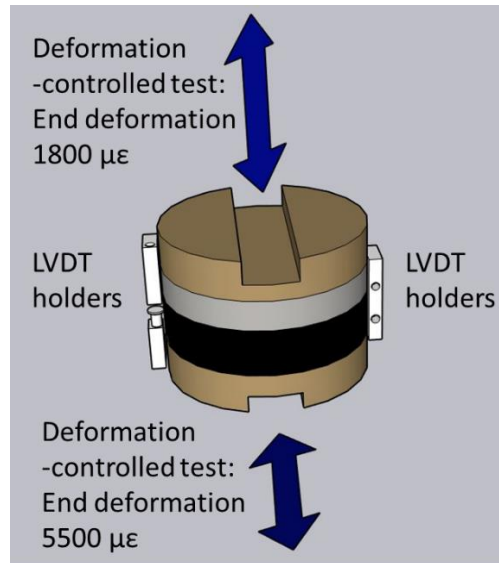


Figure A- 19. Combined sine-ramp test diagram

Input Parameters

The test requires three parameters for each loading direction: end strain level, cyclic strain variation, and length of the test. The values used in the combined test are the same ones that were used for the individual sine-ramp tests that were mentioned before. The testing times also remain the same.

Summary

The combined sine-ramp testing will be performed at:

In horizontal direction


- Daily strain: $5,500 \mu\epsilon / 180 \text{ days} = 30 \mu\epsilon$
- Cyclic strain variation: $500 \mu\epsilon$
- Time: 3 hours, 1 day and 3 days

In vertical direction


- Daily strain: $1,800 \mu\epsilon / 180 \text{ days} = 10 \mu\epsilon$
- Cyclic strain variation: $400 \mu\epsilon$
- Time: 3 hours, 1 day and 3 days

APPENDIX B

Gle5: HMA with 19 mm aggregate and PF64-16 binder


UCPRC LABORATORY							 <small>UNIVERSITY OF CALIFORNIA PAVEMENT RESEARCH</small> <small>Center for Research and Education</small>	
Work Sheet For:		Add a Mix Design			V20190701			
Project ID:		Task ID:						
Project Description:								
Mix Design ID:	MD-GLENS	Mix Design Title:			3/4" HMA RAP15	Mix Design Type:	AC	
Mix Design Description: 3/4" HMA-SP RAP15 Type A PG 64-16 supplied for 03-OF3704 near Orland (03-Gle5-R24,8/R28,6)								
Developed By: Knife River Orland							Plant BarCode:	002-20210413-0001
Asphalt Concrete Mix Design Basic Information								
Mix Type:	HMA	NMAS:	3/4" (19 mm)	Binder Final PG Grade:	PG 64-16	Knows Proportion:	Yes	
Asphalt Binder ID:	VB-PNO-PG6416	Additive ID:						
Comp. TWM% =>	Virg. Binder:	3,85	Virg. Aggregate:	11,18	RAP:	14,97	Additive:	0,00
Total Binder Content (%TWM)=>		From JMF:		From UCPRC:		Value for Production:		4,49
Virgin Binder Content (%TRA)=>		From JMF:		From UCPRC:		Value for Production:		4,00
RAP Aggregate Contents (%TRA):		15,00	Total RAP Aggregate Contents (%TRA):			15,00	=< Gradation proportions	
Asphalt Concrete Compaction Information								
Compaction Temperature (°C):		138	Need Gyrotory Compaction?:		Yes			
RICE Value from JMF:		2,556						
UCPRC RICE Values=>		From FMFC:		From FMLC:		From LMLC:		
Production RICE Values=>		For FMFC:		For FMLC:		For LMLC:		
For Gyrotory Compaction=>		Compressive Pressure (kPa):			600	Hold Time (minutes):		15
Other Instruction:								
Material Proportion and Pre-Conditioning Temperature and Duration for Production								
Plant ID	Raw Material Group	Raw Material ID	% TWM	Pre-Conditioning (i.e. Mixing) Temp. (°C)		Pre-Conditioning Duration (Hours)	Material BarCode	
				Minimum	Maximum			
Pacific Northwest Oil	Virgin Binder	VB-PNO-PG6416	3,85	163	163	2	061-20210413-0001	
	Additive							
	Additive							
Knife River Orland	Virgin Aggregate	VA-GLENS 3/4"	11,46	163	163	4	061-20210413-0002	
Knife River Orland	Virgin Aggregate	VA-GLENS 1/2"	21,01	163	163	4	061-20210413-0003	
Knife River Orland	Virgin Aggregate	VA-GLENS 3/8"	12,415	163	163	4	061-20210413-0004	
Knife River Orland	Virgin Aggregate	VA-GLENS Dust	12,415	163	163	4	061-20210413-0005	
Knife River Orland	Virgin Aggregate	VA-GLENS Washed Dus	23,88	163	163	4	061-20210413-0006	
	Virgin Aggregate							
Knife River Orland	RAP	RAP-GLENS RAP	14,97	110	110	1,5	061-20210413-0007	
	RAP							
	RAP							
Check Total (%)			100,00	=< Must be 100				
Mix Design Documents								
Document #1:								
Document #2:								
Document #3:								
RAP Binder Contents (% RAP):	4,3							
Binder Contents from RAP (%):	0,64371			Binder Content From RAP TWM (%):	0,64371			
RAP Aggregate (% TWM):	14,32629			Total RAP Aggregate (% TWM):	14,32629	Virgin and RAP Aggregate (% TWM):	95,50629	

Yol113: RHMA-G with 12.5 mm aggregate and PG64-16 w/CRM binder


UCPRC LABORATORY							 <small>UNIVERSITY OF CALIFORNIA Pavement Research Center</small>			
Work Sheet For:		Add a Mix Design		V20190701						
Project ID:				Task ID:						
Project Description:										
Mix Design ID:	MD_YOL113		Mix Design Title:	1/2" RHMA-G RAP0		Mix Design Type:	AC			
Mix Design Description: JMF for the Woodland 113 BCOA pilot project										
Developed By: Granite Bradshaw Plant							Plant Barcode:	002-20200629-0001		
Asphalt Concrete Mix Design Basic Information										
Mix Type:	RHMA-G		NMAS:	1/2" (12,5 mm)		Binder Final PG Grade:	PG 64-16 w/ CRM			
Asphalt Binder ID:	VB-YOL113-APS-RB		Additive ID:						Knows Proportion:	Yes
Comp. TWM% =>	Virg. Binder:	7,50	Virg. Aggregate:	92,50	RAP:	0,00	Additive:	0,00		
Total Binder Content (%TWM)=>		From JMF:		7,5	From UCPRC:	7,5	Value for Production:			
Virgin Binder Content (%TRA)=>		From JMF:		8,11	From UCPRC:	8,11	Value for Production:			
RAP Aggregate Contents (%TRA):				Total RAP Aggregate Contents (%TRA):			<= Gradation proportions			
Asphalt Concrete Compaction Information										
Compaction Temperature (°C):		152		Need Gyrotory Compaction?:		Yes				
RICE Value from JMF: 2,49										
UCPRC RICE Values=>		From FMFC:		From FMLC:		2,479		From LMLC:		
Production RICE Values=>		For FMFC:		For FMLC:		2,479		For LMLC:		
For Gyrotory Compaction=>		Compressive Pressure (kPa):			825		Hold Time (minutes):		60	
Other Instruction:										
Material Proportion and Pre-Conditioning Temperature and Duration for Production										
Plant ID	Raw Material Group	Raw Material ID	% TWM	Pre-Conditioning (i.e. Mixing) Temp. (°C)		Pre-Conditioning Duration (Hours)	Material Barcode			
				Minimum	Maximum					
American Pavement S	Virgin Binder	VB-YOL113-APS-RB	7,5	185	195	-1	061-20210525-0006			
	Additive									
	Additive									
Granite Bradshaw Vine	Virgin Aggregate	VA-YOL113-1/2"	18,5	163	163	-1	061-20210525-0002			
Granite Bradshaw Vine	Virgin Aggregate	VA-YOL113-3/8"	45,324	163	163	-1	061-20210525-0003			
Granite Bradshaw Vine	Virgin Aggregate	VA-YOL113-1/4"xDust	16,85	163	163	-1	061-20210525-0004			
Granite Bradshaw Vine	Virgin Aggregate	VA-YOL113-1/4" Washed	12,025	163	163	-1	061-20210525-0005			
	Virgin Aggregate									
	Virgin Aggregate									
	RAP									
	RAP									
	RAP									
Check Total (%)			100,00	<= Must be 100						
Mix Design Documents										
Document #1:										
Document #2:										
Document #3:										
RAP Binder Contents (% RAP):										
Binder Contents from RAP (%):				Binder Content From RAP TWM (%):						
RAP Aggregate (% TWM):				Total RAP Aggregate (% TWM):		Virgin and RAP Aggregate (% TWM)				

APPENDIX C

4.88HMA: HMA with 19 mm aggregate and PG64-10 binder

UCPRC LABORATORY							 <small>UNIVERSITY OF CALIFORNIA Pavement Research Center</small>		
Work Sheet For:		Add a Mix Design			V20190701				
Project ID:	4.88 CR in JPCP Bases			Task ID:	4.88 Lab Testing				
Project Description: Use of Cold Recycling in JPCP Bases									
Mix Design ID:	Teichert HMA-4.88			Mix Design Title:	Teichert HMA-4.88		Mix Design Type:	AC	
Mix Design Description: Teichert HMA (3/4 in.) with 13% RAP & PG 64-10 used as reference HMA in 4.88 Project								Plant Barcode:	002-20200609-0003
Developed By: Teichert Perkins Plant									
Asphalt Concrete Mix Design Basic Information									
Mix Type:	HMA	NMAS:	3/4" (19 mm)	Binder Final PG Grade:	PG 64-10		Knows Proportion:	Yes	
Asphalt Binder ID:	VB-Valero PG 64-10		Additive ID:						
Comp. TWM% =>	Virg. Binder:	4,21	Virg. Aggregate:	82,83	RAP:	12,96	Additive:	0,00	
Total Binder Content (%TWM)=>		From JMF:		From UCPRC:		Value for Production:			
Virgin Binder Content (%TRA)=>		From JMF:		From UCPRC:		Value for Production:			
RAP Aggregate Contents (%TRA):				Total RAP Aggregate Contents (%TRA):		<= Gradation proportions			
Asphalt Concrete Compaction Information									
Compaction Temperature (°C):		141		Need Gyrolatory Compaction?		Yes			
RICE Value from JMF:		2,541							
UCPRC RICE Values=>		From FMFC:		From FMLC:		2,552			
Production RICE Values=>		For FMFC:		For FMLC:					
For Gyrolatory Compaction=>		Compressive Pressure (kPa):		600		Hold Time (minutes):			
Other Instruction:									
Material Proportion and Pre-Conditioning Temperature and Duration for Production									
Plant ID	Raw Material Group	Raw Material ID	% TWM	Pre-Conditioning (i.e. Mixing) Temp. (°C)		Pre-Conditioning Duration (Hours)	Material Barcode		
				Minimum	Maximum				
Valero Benicia	Virgin Binder	VB-Valero PG 64-10	4,21	148	154	2	061-20210824-0009		
	Virgin Aggregate								
	Additive								
	Additive								
Teichert Perkins Plant	Virgin Aggregate	VA-4.88-3/4" MA	18,09	158	164	12	061-20200609-0007		
Teichert Perkins Plant	Virgin Aggregate	VA-US50-1/2"	16,18	158	164	12	061-20220601-0003		
Teichert Perkins Plant	Virgin Aggregate	VA-US50-3/8"	15,23	158	164	12	061-20220601-0004		
Teichert Perkins Plant	Virgin Aggregate	VA-US50-Dust	19,05	158	164	12	061-20220601-0005		
Teichert Perkins Plant	Virgin Aggregate	VA-US50-Washed Dust	14,28	158	164	12	061-20220601-0006		
	Virgin Aggregate								
	Virgin Aggregate								
	Virgin Aggregate								
Teichert Perkins Plant	RAP	RAP-4.76A-3/8" RAP	12,96				061-20221031-0006		
	RAP								
	RAP								
Check Total (%)			100,00	<= Must be 100					
Mix Design Documents									
Document #1:									
Document #2:									
Document #3:									
RAP Binder Contents (% RAP)									
Binder Contents from RAP (%)			Binder Content From RAP TWM (%)						
RAP Aggregate (% TWM)			Total RAP Aggregate (% TWM)		Virgin and RAP Aggregate (% TWM)				

4.76BRHMA-G: RHMA-G with 19 mm aggregate and PG64-16 w/CRM binder

UCPRC LABORATORY							 <small>UNIVERSITY OF CALIFORNIA PAVEMENT RESEARCH</small> <small>Center - Berkeley CENTER</small>	
Work Sheet For:		Add a Mix Design			V20190701			
Project ID:		Task ID:						
Project Description:								
Mix Design ID:		Teichert-GG-4.76B		Mix Design Title:		Teichert-GG-4.76B		Mix Design Type:
Teichert RHMA-G mix (3/4 in.) used for building 4.76B Test Track on May-2022								
Developed By:							Teichert Perkins Plant	Plant Barcode:
002-20200609-0003								
Asphalt Concrete Mix Design Basic Information								
Mix Type:	RHMA-G	NMAS:	3/4" (19 mm)	Binder Final PG Grade:	PG 64-16 w/ CRM	Knows Proportion:	Yes	
Asphalt Binder ID:	MB-US50-AR-2022	Additive ID:						
Comp. TWM% =>	Virg. Binder:	7,50	Virg. Aggregate:	82,50	RAP:	0,00	Additive:	
							0,00	
Total Binder Content (%TWM)=>		From JMF:		From UCPRC:		Value for Production:		
						7,50		
Virgin Binder Content (%TRA)=>		From JMF:		From UCPRC:		Value for Production:		
						8,11		
RAP Aggregate Contents (%TRA):				Total RAP Aggregate Contents (%TRA):		<= Gradation proportions		
Asphalt Concrete Compaction Information								
Compaction Temperature (°C):		160		Need Gyrotory Compaction?:		Yes		
RICE Value from JMF:		2,484						
UCPRC RICE Values=>		From FMFC:		From FMLC:		From LMLC:		
				2,482				
Production RICE Values=>		For FMFC:		For FMLC:		For LMLC:		
				2,482				
For Gyrotory Compaction=>		Compressive Pressure (kPa):		825		Hold Time (minutes):		
						45		
Other Instruction:								
Material Proportion and Pre-Conditioning Temperature and Duration for Production								
Plant ID	Raw Material Group	Raw Material ID	% TWM	Pre-Conditioning (i.e. Mixing) Temp. (°C)		Pre-Conditioning Duration (Hours)	Material Barcode	
				Minimum	Maximum			
Teichert Perkins Plant	Virgin Binder	MB-US50-AR-2022	7,5	148	154	2	061-20220601-0001	
	Additive							
	Additive							
Teichert Perkins Plant	Virgin Aggregate	VA-US50-3/4"	17,575	158	164	12	061-20220601-0002	
Teichert Perkins Plant	Virgin Aggregate	VA-US50-1/2"	16,850	158	164	12	061-20220601-0003	
Teichert Perkins Plant	Virgin Aggregate	VA-US50-3/8"	26,825	158	164	12	061-20220601-0004	
Teichert Perkins Plant	Virgin Aggregate	VA-US50-Dust	7,400	158	164	12	061-20220601-0005	
Teichert Perkins Plant	Virgin Aggregate	VA-US50-Washed Dust	19,425	158	164	12	061-20220601-0006	
Teichert Perkins Plant	Virgin Aggregate	VA-US50-5/16" Chips	4,625	158	164	12	061-20220601-0007	
	RAP							
	RAP							
	RAP							
Check Total (%)			100,00	<= Must be 100				
Mix Design Documents								
Document #1:								
Document #2:								
Document #3:								
RAP Binder Contents (% RAP):								
Binder Contents from RAP (%):				Binder Content From RAP TWM (%):				
RAP Aggregate (% TWM):				Total RAP Aggregate (% TWM):		Virgin and RAP Aggregate (% TWM)		

PCC: Portland limestone cement (PLC), 550 psi flexural strength at 10 days

Mix with Slag-PLC CONCRETE MIX BATCHING										
INFORMATION	DATE:	3/21/2022	NOTES:			No. SPECIMEN	4" x 8" Cylinder	0		
	PROJECT	4.76B-4.88					6" x 12" Cylinder	0		
	MIX NO.						Flexure Beams	0		
	DESIGN VOLUME	27	cu.ft.				Shrinkage Beams	0		
	DESIGN SLUMP	4	inch				TC Beams	0		
	DESIGN AIR CONTENT	1.5	%				Batch Size (ft ³)	5.00		
	DESIGN UNIT WEIGHT	151.33	lb/cf				Batch Waste	20%		
	DESIGN STRENGTH	4000 @ 28 D	<input type="checkbox"/> FLEX	<input checked="" type="checkbox"/> COMP	psi		Batch Factor	0.22		
TECHNICIAN (S)	Fabian Paniagua					Batch (ft ³)	6.00			
Material Description	Designed Weights	Units	Batch Weights	Units	Moisture/Water Content (%)	Absorption (%)	Adjusted Weights	Units		
PLC Cement CEMEX	413.0	lbs	91.78	lbs			91.8	lbs		
Water (Split 2/3 & 1/3)	283.6	lbs	63.01	lbs			73.4	lbs		
CA: Perkins 1" x #4	1900.0	lbs	422.22	lbs		1.20%	417.2	lbs		
IA	0.0	lbs	0.00	lbs		1.20%	0.0	lbs		
FA: Perkins Conc. Sand	1312.0	lbs	291.56	lbs		2.00%	285.8	lbs		
Slag (GGBF)	177.0	lbs	39.33	lbs			39.3	lbs		
Glenium 7500	23.6	oz	5.24	oz	100.00%		155.1	mL		

APPENDIX D

Table 8-5 conversion to English units.

Table D- 1. Material properties of the elements in the pavement models, English units

			Complex model			Simplified model		
Element	Material type	Density (lb/ft ³)	Material model	Parameters	Value	Material model	Parameters	Value
JPCP slab	Concrete	150	Elastic	E (ksi)	5075	Elastic	E (ksi)	5075
				v	0.2		v	0.2
Lean concrete base (LCB)	Concrete	150	Elastic	E (ksi)	3475	Elastic	E (ksi)	3475
				v	0.2		v	0.2
RHMA-G	Asphalt	150	Viscoelastic	Instant E ₀ (ksi)	3250	Elastic	E (ksi)	725
				v	0.1		v	0.1
				Prony series coefficients	20			
RHMA-G (interphase)	Asphalt	150	Cohesive viscoelastic with damage	E _{nn} (ksi)	3475	Elastic with no damage	E (ksi)	725
				E _{ss} (ksi)	1475		v	0.1
				E _{tt} (ksi)	1475			
				Damage initiation	Table 8-4			
				Damage evolution	Table 8-4			
Curing compound	Surface treatment	None	Hard contact			Hard contact		
Subgrade	Granular subgrade	112	Winkler subgrade reaction	Normal stiffness (lbf/ft)	6.85E-03	Winkler	Normal stiffness (lbf/ft)	6.85E-03
				Tang. stiffness (lbf/ft)	6.85E-05		Tang. stiffness (lbf/ft)	6.85E-05